

2013-09-13

Triaxial Compression Strength of Methane Hydrate-Bearing Sediments

Jaysinghe, Anuruddhika

Jaysinghe, A. (2013). Triaxial Compression Strength of Methane Hydrate-Bearing Sediments (Doctoral thesis, University of Calgary, Calgary, Canada). Retrieved from <https://prism.ucalgary.ca>. doi:10.11575/PRISM/28526
<http://hdl.handle.net/11023/973>
Downloaded from PRISM Repository, University of Calgary

UNIVERSITY OF CALGARY

Triaxial Compression Strength of Methane Hydrate-Bearing Sediments

by

Anuruddhika Ganganie Jayasinghe

A THESIS

SUBMITTED TO THE FACULTY OF GRADUATE STUDIES
IN PARTIAL FULFILMENT OF THE REQUIREMENTS FOR THE
DEGREE OF DOCTOR OF PHILOSOPHY

DEPARTMENT OF CIVIL ENGINEERING

CALGARY, ALBERTA

SEPTEMBER, 2013

© Anuruddhika Ganganie Jayasinghe 2013

Abstract

Hydrate-bearing sediments are characterized as soils in which the pore space is partially or fully occupied by ice-like crystalline solid consisting of hydrogen bonded water lattices encapsulating guest gas molecules, mostly methane in natural environments. These sediments are found along marine continental margins and in permafrost regions. The main focus of this thesis is to investigate the behaviour of hydrate-bearing sediments subject to triaxial compression. The work presented includes (1) an investigation into the formation process dependency of hydrate growth habit, spatial distribution, and saturation (the key deterministic factors of the physical behaviour), (2) a novel formation methodology to isolate the effects of formation habit from those of spatial variation in hydrate distribution, (3) an investigation into the accurate estimation of hydrate saturation, (4) and a comprehensive series of tests to investigate the initial effective confining stress and hydrate saturation dependent stress-strain behaviour, strength, and stiffness, (5) a comparison of present results with previous work published in literature to investigate the differences in strength/stiffness behaviour between different formation habits. The results of the study reveal that the stress-strain behaviour is affected by hydrate added cohesion (or cementation), the failure strength at low saturations is controlled by frictional resistance at mineral grain contacts, the failure strength at high saturations is determined predominantly by hydrate-mineral bonding strength or intact hydrate breakage strength while the residual strength is determined by the hydrate saturation, stiffness is controlled predominantly by formation habit while hydrate saturation acts as a factor of secondary importance, and the effects of initial effective confinement on the strength/stiffness behaviour is significant only at low hydrate

saturations. Additionally, an increased dilative tendency, reflected in strongly negative pore pressure development was observed in the hydrate-bearing specimens under constant mass shearing. Comparison of our results of the experimental program with theoretical predictions generates a good match, which indicates that theoretical modeling of the strength gain due to the presence of gas hydrates is possible. The knowledge generated in this research is essential in evaluating the potential risks associated with drilling and methane production, reservoir subsidence, and dissociation induced submarine slope instability.

Acknowledgements

I would like to take this opportunity to thank those who led and accompanied me in this journey of success.

First and foremost, I would like to express my sincere gratitude to my supervisor, Dr. Jocelyn Grozic, for her continuous support and guidance without which this work would not have been possible. Dr. Grozic, being a true mentor, inspired me to explore all arenas of gas hydrates research. I am privileged to have worked with you. I should also mention the opportunities that you had provided me with for sharing ideas and research know-how with the other academics through attending various conferences. I will carry with me the impression you have created in me as a true teacher and a researcher for the rest of my life.

I would like to thank Dr. Ron Wong and Dr. Richard Wan for the invaluable knowledge and research expertise they offered through graduate courses and research meetings. Critical comments made, the insightful questions raised, and the invaluable advice, feedback, and suggestions provided by the duo helped immensely to shape my research.

I gratefully acknowledge Dr. Matthew Clarke and Dr. Pooladi-Darvish for the advice, and suggestions received. I should also mention the positive learning experience I enjoyed in attending Dr. Achari's graduate courses.

I thank the technical staff of the Department of Civil Engineering for providing me with the technical support and advice at various stages of the experimental program.

I gratefully acknowledge the financial contributions from Natural Sciences and Engineering Research Council (NSERC) of Canada, Geological Society of Canada (GSC) - Natural Resources Canada. I also acknowledge the Department of Civil Engineering, University of Calgary for the financial assistance I received through teaching assistantships.

I would now like to take this opportunity to thank my colleagues and friends who helped me stay sane through difficult years. Their support and care helped me overcome setbacks and stay focused on my studies. I greatly value their friendship and I deeply appreciate their belief in me.

Most importantly, none of this would have been possible without the love, support and patience of my family. I must express my gratitude to my parents and sister for their silent wish for my success and the motivation throughout. I thank my husband who stood by me in my joys and sorrows both. Last but not least I should also mention our son, Charana, who brought smiles and happiness even at hard times.

Dedication

This thesis is dedicated to my parents for their constant love, endless support and encouragement.

Amma and Appachchi, without you this journey would never have started.

Table of Contents

Abstract	i
Acknowledgements	iii
Dedication	v
Table of Contents	vi
List of Tables	x
List of Figures	xii
Nomenclature	xv
CHAPTER ONE: INTRODUCTION	1
1.1 Introduction	1
1.2 Human interest in gas hydrates	2
1.3 Problem statement – The importance and the challenges in assessing geomechanical properties of hydrate-bearing sediments	3
1.4 Research objectives	4
1.5 Scope of investigation	5
1.6 Organization of the thesis	5
CHAPTER TWO: METHANE HYDRATES IN POROUS SOIL MEDIA - A REVIEW	9
2.1 Introduction	9
2.2 Methods of laboratory synthesis of artificial hydrate-bearing sediments	9
2.2.1 Dissolved gas method	10
2.2.2 Partial water saturation method	11
2.2.3 Ice-seeding method	12
2.2.4 Hydrate pre-mixing method	13
2.3 Natural gas hydrates	13
2.3.1 Hydrate growth morphologies	14
2.3.2 Pore scale hydrate growth habits	15
2.3.2.1 Pore filling habit	16
2.3.2.2 Load bearing habit	16
2.3.2.3 Grain cementing and/or coating habit	16
2.3.3 Controls on pore scale hydrate growth morphologies and habits	17
2.3.4 Classification of natural hydrate accumulations	19
2.4 Hydrate growth habit dependency of physical properties	20
2.5 Hydrate spatial distribution dependency of physical properties	20
2.6 Hydrate saturation dependency of physical properties	21
2.7 Hydrate formation method dependency of growth habit, spatial distribution, and hydrate saturation	22
2.7.1 Growth habit	22
2.7.2 Spatial distribution	22
2.7.3 Hydrate saturation	23

2.8 Formation “Method” versus Formation “Process”	24
2.8.1 Implications of the primary formation method	25
2.8.2 Implications of different approaches for forming a partially water saturated specimens	27
2.8.3 Effects of freezing and thawing.....	29
2.8.4 Effects of water migration during formation of hydrate	31
2.8.5 Effects of formation P/T conditions and subsequent changes to formation P/T conditions	32
2.8.6 Effects of post formation water saturation	33
2.8.7 Intact strength of hydrate	34
2.8.8 Hydrate former	36
2.9 Discussion.....	37

CHAPTER THREE: LABORATORY SYNTHESIS OF METHANE HYDRATE-BEARING SEDIMENT

3.1 Introduction.....	46
3.1.1 A novel procedure for hydrate synthesis – hydrate formation from water rich gaseous methane	46
3.1.2 Potential hydrate growth habit.....	49
3.1.3 Implications of hydrate growth habit on the strength and stiffness of the sediments.....	49
3.2 The experimental procedure	49
3.2.1 Materials	50
3.2.1.1 Sand	50
3.2.1.2 Water.....	50
3.2.1.3 Hydrate former.....	50
3.2.2 Methods	51
3.2.2.1 Specimen preparation	51
3.2.2.2 Hydrate formation.....	52
3.3 The concept – Hydrate formation from water saturated gaseous methane.....	54
3.4 Estimation of hydrate quantities formed from isobaric cooling of water saturated vapour	58
3.5 Hydrate growth habit and distribution deduced from subsequent strength testing of hydrate-bearing specimens.....	59
3.6 Discussion.....	60

CHAPTER FOUR: ESTIMATING PORE SPACE HYDRATE SATURATION USING DISSOCIATION GAS EVOLUTION MEASUREMENTS (DGEM)

4.1 Introduction.....	74
4.2 Hydrate saturation dependency of physical properties	76
4.2.1 Effective medium models of pore scale hydrate growth habit.....	78
4.3 Techniques for determination of the hydrate saturation	79

4.4 Laboratory testing of artificial hydrate-bearing specimens and application of DGEM method for hydrate saturation estimation	84
4.4.1 Measured parameters	89
4.4.2 Estimates of volumetric parameters	90
4.4.3 Estimates of methane density and volume of hydrate bond water	93
4.5 A sensitivity analysis for DGEM.....	104
4.5.1 Sensitivity of hydrate saturation to direct temperature measurements, absolute pre and post-dissociation pressures and estimates of volumetric parameters	105
4.5.2 Sensitivity to estimates of methane density.....	107
4.5.2.1 Methane density of the hydrate phase - Hydrate number n_k	107
4.5.2.2 Methane density of vapour phase under the H-V equilibrium at pre-dissociation conditions M_{Go}	108
4.5.2.3 Methane density of vapour phase under Lw-V equilibrium at post-dissociation conditions at the gas/water collector M_{Gf}	109
4.5.2.4 Methane density of vapour phase under the Lw-V equilibrium for the material mass present within total volume of hydrate forming gas filled elements external to the immediate boundaries of the specimen M_{Gext}	110
4.6 Discussion.....	111
CHAPTER FIVE: TRIAXIAL COMPRESSION STRENGTH OF METHANE HYDRATE-BEARING COURSE GRANULAR MEDIA.....	126
5.1 Introduction.....	126
5.2 Geomechanical properties of hydrate-bearing sediments and the characterisation.....	127
5.2.1 Early investigations of geomechanical properties of hydrate-bearing sediments	128
5.3 Experimental procedure	130
5.3.1 Specimen consistency immediately prior to shearing	131
5.3.2 Shearing at constant mass under triaxial compression conditions	131
5.4 Pore fluid pressure response and volume change during undrained shearing of water saturated soil specimens.....	133
5.4.1 Pore fluid pressure response	133
5.4.2 Volume change	136
5.5 Pore fluid pressure response and volume change during shearing of hydrate-bearing soil specimens under constant mass conditions	136
5.5.1 Biot's effective stress parameter α for hydrate-bearing soil.....	137
5.5.1.1 The aggregated compressibility of the solid constituents C'_s	137
5.5.1.2 The compressibility of the soil skeleton (or the hydrate-cemented solid framework) C_c	139
5.5.1.3 An effective stress law for hydrate-bearing soils.....	141
5.5.2 Pore pressure coefficient B for hydrate-bearing soil.....	142

5.5.3 Pore pressure coefficient A for hydrate-bearing soils	143
5.5.4 Experimental measurement of volume change in response to shearing	145
5.5.5 Predicting volume change response to shearing for hydrate-bearing soil	146
5.6 Undrained response of water saturated specimens –observations and analysis	148
5.6.1 Typical behaviour of undrained water saturated specimens.....	148
5.6.2 Observations and analysis of undrained response of water saturated specimens	149
5.7 Response of hydrate-bearing specimens to shearing under constant mass - observations and analysis	151
5.7.1 Observations of hydrate-bearing sediment behaviour in summary	153
5.7.2 Response of hydrate-bearing specimens at low hydrate saturations (< 40%) consolidated at 500 kPa initial effective confining stress to shearing at constant mass.....	155
5.7.3 Response of hydrate-bearing specimens at low hydrate saturations (< 40%) consolidated at 1000 kPa initial effective confining stress to shearing at constant mass.....	156
5.7.4 Response of hydrate-bearing specimens at high hydrate saturations (> 40%) to shearing at constant mass.....	158
5.7.5 End of test visual observations of test specimens	162
5.8 The stress path plots.....	164
5.8.1 The definition of stress path	164
5.8.2 $p' - q$ plots for hydrate-bearing specimens	164
5.9 Results.....	165
5.9.1 Strength and stiffness dependency on initial effective confining stress.....	166
5.9.2 Strength and stiffness dependency on hydrate saturation.....	168
5.9.3 Comparison to previous work	169
5.10 Behaviour of hydrate-cemented soils in summary	173
5.11 Remarks	176
 CHAPTER SIX: CONCLUSIONS AND RECOMMENDATIONS	 222
6.1 Conclusions.....	222
6.2 Significance	226
6.3 A path forward	227
 REFERENCES	 229

List of Tables

Table 2.1: Impact of formation process elements on the growth habit and hydrate distribution during laboratory synthesis of hydrate-bearing soil specimens	44
Table 3.1: Possible combination of number of co-existing phases (P) and number of independent variables (F) for a two component systems in accordance with Gibbs Phase Rule	70
Table 3.2: Experimentally measured values for water content in methane under Lw-V equilibrium	70
Table 3.3: Experimentally measured values for water content in methane under H-V equilibrium	71
Table 3.4: References for determination of input parameters of the hydrate quantity estimation	71
Table 3.5: Estimated hydrate quantity per known volume of water saturated methane under L-V equilibrium	72
Table 3.6: Laboratory test results for vapour phase hydrate formation with and without initial water content	73
Table 4.1: References for experimental determination of hydrate number, n_k	115
Table 4.2: Hydrate saturation estimation with the use of simple and complex primary estimates at measured P/T conditions	116
Table 4.3: Resources for determination of hydrate bond water and methane concentration.....	119
Table 4.4: Sensitivity of hydrate saturation to direct temperature measurements, absolute pre and post-dissociation system pressures, and estimates of volumetric parameters:.....	123
Table 4.5: Sensitivity of hydrate saturation to the choice of vapour phase EoS under pre-dissociation conditions at H-V equilibrium	124
Table 4.6: Sensitivity of hydrate saturation to the choice of vapour phase EoS under post-dissociation conditions at Lw-V equilibrium.....	124
Table 4.7: Sensitivity of hydrate saturation to the choice of vapour phase EoS at Lw-V equilibrium for quantity of gas present within such elements external to the immediate	

boundaries of the specimen for which the material present within is forced into the gas/water collector during collection of dissociation products	125
Table 5.1: Test conditions for water saturated non-hydrated specimens and hydrate-bearing specimens	212
Table 5.2: Skempton's pore pressure parameters A and B for water saturated specimens.....	213
Table 5.3: Biot's Effective stress coefficient for hydrate-bearing specimens	214
Table 5.4: Typical values of constituent compressibility	215
Table 5.5: The calculated values of pore pressure coefficient B for hydrate-bearing specimens	216
Table 5.6: The calculated values of pore pressure coefficient A for hydrate-bearing specimens at low hydrate saturations (< 40%)	217
Table 5.7: Triaxial compression strength of non-hydrated and hydrated specimens at different initial effective confining stress and hydrate saturations	218
Table 5.8: Summary results for water saturated specimens.....	220
Table 5.9: Mobilised friction angle and the measured inclination of the shearing plane	221

List of Figures

Figure 2.1: Different hydrate growth morphologies found in natural hydrate-bearing sediments (Hydrate in white)	39
Figure 2.2: Pore-scale hydrate growth habits for unconsolidated packing of mineral grains.....	40
Figure 2.3: Solubility of methane in pure water	41
Figure 2.4: Classification of hydrate-bearing sediments	42
Figure 2.5: The general association between the four primary methods of hydrate laboratory synthesis and hydrate growth habits	43
Figure 3.1: X-ray MicroCT imagery showing the distribution of different phases within hydrated sediment	62
Figure 3.2: Growth habit and growth habit transition; (a) initial conversion of capillary held water into hydrate leading to grain cementing hydrate habit and (b) further hydrate growth from condensing water leading to grain coating hydrate habit.....	63
Figure 3.3: Triaxial gas hydrate testing system	65
Figure 3.4: The PT Diagram for isobaric cooling of water rich gaseous methane (vapour) into the hydrate stability zone	66
Figure 3.5: Temperature-Composition (T-X) diagram for methane-water binary system at fixed pressure	67
Figure 3.6: The reduction in the water content of gaseous methane associated with isobaric cooling.....	68
Figure 3.7: Schematic diagram showing application of mass balance for methane and water between the two stages; (1) the system consisting of water saturated gaseous methane (vapour) at Lw-V equilibrium and (2) the system consisting of hydrate and vapour in H-V equilibrium	69
Figure 4.1: Hydrate formation in gas-rich environment, subsequent testing, and measurements to facilitate application of DGEM for hydrate saturation estimation.....	113
Figure 4.2: System consistency at pre and post-dissociation conditions	114
Figure 5.1: High pressure and low/high temperature capable triaxial soil testing apparatus	178

Figure 5.2: Phase transformation and steady states during undrained shear	179
Figure 5.3: (a) Deviator stress and axial strain and (b) pore fluid pressure response to deviatoric loading as measured on water saturated sand specimens at different initial effective confining stresses	180
Figure 5.4: The identity of the friction angle mobilized at undrained phase transformation and at the friction angle mobilized at steady state	181
Figure 5.5: $p' - q$ plots for water saturated sand specimens at different initial effective confining stresses [$q = (\sigma'_1 - \sigma'_3)/2$ and $p' = (\sigma'_1 + \sigma'_3)/2$]	182
Figure 5.6: Grain scale mechanisms governing stress-strain behaviour of hydrate-bearing sediments.....	183
Figure 5.7: (a) Deviator stress and axial strain and (b) pore fluid pressure response to deviatoric loading as measured on hydrate-bearing specimens at low hydrate saturations (<40%) at 500 kPa initial effective confining stress	185
Figure 5.8: Hydrate saturation dependency of deviator stress at failure at different initial effective confining stress (ECS)	186
Figure 5.9: Hydrate saturation dependency of secant stiffness at different initial effective confining stress (ECS), and (b) hydrate saturation dependency of initial tangential stiffness at different initial effective confining stress (ECS)	187
Figure 5.10: (a) Deviator stress and axial strain, (b) pore fluid pressure response and (c) volume change behaviour in response to deviatoric loading as measured on hydrate-bearing specimens at low hydrate saturations (<40%) at 1000 kPa initial effective confining stress	188
Figure 5.11: Deviator stress and excess pore fluid pressure for test MH 007 (at hydrate saturation of 46.3%) during shearing at 500 kPa initial ECS	189
Figure 5.12: Deviator stress and excess pore fluid pressure for test MH 008 (at hydrate saturation of 51.3%) during shearing 500 kPa initial ECS	190
Figure 5.13: Deviator stress and excess pore fluid pressure for test MH 009 (at hydrate saturation of 53.6%) during shearing at 500 kPa initial ECS	191
Figure 5.14: Deviator stress and excess pore fluid pressure for test MH 010 (at hydrate saturation of 45.9%) during shearing at 1000 kPa initial ECS	192

Figure 5.15: Deviator stress and excess pore fluid pressure for test MH 011 (at hydrate saturation of 56.1%) during shearing at 1000 initial ECS	193
Figure 5.16: Deviator stress and excess pore fluid pressure for test MH 012 (at hydrate saturation of 61.5%) during shearing at 1000 kPa initial ECS	194
Figure 5.17: Deviator stress and excess pore fluid pressure for test MH 013 (at hydrate saturation of 80%) during shearing at 1000 kPa initial ECS	195
Figure 5.18: Hydrate saturation dependency of failure stress and residual strength	196
Figure 5.19: Photographs of sheared specimens and deformation band scars left on specimen membrane.....	197
Figure 5.20: The stress path plot and the Mohr-Coulomb failure criterion	199
Figure 5.21: $p' - q$ plots for hydrate-bearing specimens.....	203
Figure 5.22: Comparison of hydrate saturation dependency of failure strength of the present study for cementing habit of hydrates (solid circles and squares) with that of Yun et al. [2007] for pore-filling to load bearing habit of hydrates (open circles and squares).....	205
Figure 5.23: Comparison of strength-stiffness correlation for the present study for cementing habit of hydrates (solid circles and squares) with that obtained by Yun et al. [2007] for pore-filling to load bearing habit of hydrates (open circles and squares).....	206
Figure 5.24: Comparison of shear strength at constant mass obtained in the present study (solid circles) with the data of Yun et al. [2007] (open circles).....	207
Figure 5.25: The predicted undrained strength by Santamarina and Ruppel [2008] model versus measured strength of present study (solid circles) and measured undrained strength of Yun et al. [2007] (open circles)	208
Figure 5.26: Comparison of measured shear strength of present study (solid circles) with that predicted by Santamarina and Ruppel [2008] model with a and b parameters obtained by fitting to data of present study	209
Figure 5.27: The predicted strength by Santamarina and Ruppel [2008] model versus the measured strength of present study (solid circles)	210
Figure 5.28: The predicted strength by Santamarina and Ruppel [2008] model versus the measured strength of present study (solid circles).....	211

Nomenclature

$[a]$	Lattice parameter
a, b	Model coefficients of Santamarina and Ruppel (2008)
a_o	Lattice parameter at a reference temperature, T_o
a_1, a_2, a_3	Lattice constants
A, B	Skempton`s pore pressure coefficients
C_c	Compressibility of the soil structure
C_g	Compressibility of pore gas
C_H	Compressibility of hydrate
C_s	Compressibility of the soil mineral
C'_s	Aggregated compressibility of the solid constituents
C_v	Compressibility of the pore fluid
C_w	Compressibility of pore water
E	Young`s modulus
G	Shear modulus
K_i	Bulk modulus of the i^{th} constituent ($i =$ soil mineral or hydrate)
K_c	Bulk modulus or the (skeletal stiffness) of the soil framework
K'_s	Aggregated bulk modulus of the solid constituents

M_{Go}	Moles of methane present per unit volume of vapour phase under pre-dissociation conditions
M_{Gf}	Moles of methane present per unit volume of vapour phase under post-dissociation conditions
M_{Gext}	Moles of methane present per unit volume of vapour phase volume V_{ext} under Lw-V equilibrium
M_H	Moles of methane present per unit volume in hydrate phase
M_{wo}	Moles of methane present per unit volume of aqueous liquid under pre-dissociation conditions
M_{wf}	Moles of methane present per unit volume of aqueous liquid under post-dissociation conditions
M_{Wext}	Moles of methane present per unit volume of aqueous phase volume V_{ext} under Lw-V equilibrium
MV_{Lw}	Molar volume of aqueous liquid
MV_v	Molar volume of vapour
n	Total number of gas moles present within the volume V_{ext}
N	Number of distinct solid constituents (= 2 including soil mineral and hydrate)
n_{ext}	Porosity of the soil material

n_{Gf}	Total number of gas moles present within the gas/water collector ($n_{Gf(GWC)}$) less the total number of gas moles present within the connection tubing (n_{ext})
$n_{Gf(GWC)}$	Total number of gas moles present within the gas/water collector at post-dissociation conditions
n_k	Hydrate number
P	Pressure
q_h	Hydrate strength
q and p'	Stress path parameters
S_g	Degree of gas saturation
S_h	Degree of hydrate saturation
S_u	Undrained shear strength
S_w	Degree of water saturation
T	Temperature
u	Pore pressure
Δu_a	Pore pressure development during application of all around confining stress
Δu_d	The pore pressures development during deviatoric loading stage of the test

V	Volume
V_{ext}	Volume of hydrate forming gas filled elements external to the immediate boundaries of the specimen for which the material mass within is forced into the gas/water collector during collection of dissociation products
V_d	Volume change in the gas phase due to gas dissolution in the aqueous phase under pre-dissociation conditions
V_d'	Volume change in the aqueous phase due to gas dissolution in the aqueous phase under pre-dissociation conditions
V_e	Volume of hydrate lattice per mole of water at pre-dissociation conditions
V_g	Pore gas volume
V_{Go}	Volume of water saturated gaseous methane (vapour) present within the system under pre-dissociation conditions
V_{Gf}	Volume of water saturated gaseous methane (vapour) corresponding to the number of gas moles n_{Gf} under post-dissociation conditions
$V_{Gf(GWC)}$	Total volume of gas collected at the gas/water collector under Lw-V equilibrium at post-dissociation conditions
V_{GH}	Volume of gas consumed for hydrate formation

V_{GTot}	Total volume of gas available for hydrate formation under pre-dissociation conditions
V_H	Volume of hydrates under pre-dissociation conditions
V_l	Partial molar volume of water in the solution at pre or post-dissociation conditions
V_m	Molar volume of methane under given temperature/pressure conditions
V_{Mext}	Molar volume of methane under Lw-V equilibrium at pressure/temperature conditions (i.e., pre-dissociation pressure and room temperature) corresponding to the vapour volume V_{ext}
V_{Mf}	Molar volume of methane under Lw-V equilibrium at post-dissociation conditions
V_s	Volume of solid soil (constant under pre and post-dissociation conditions)
V_{wo}	Volume of (gas dissolved) water present within the system under pre-dissociation conditions
V_{wf}	Volume of (gas dissolved) water present within the system under post-dissociation conditions
V_{wH}	Volume of water generated due to hydrate dissociation or consumed in hydrate formation
V_{wTot}	Total volume of water available for hydrate formation under pre-dissociation conditions
V_{wv}	Volume change in the gas phase due to the presence of moisture

V'_{wv}	Volume change in the aqueous phase due to the moisture loss into the gas phase
V_{vo}	Initial volume of voids under pre-dissociation conditions
v_p	Compression wave velocity
v_s	Shear wave velocity
x_{CH_4}	Mole fraction of methane in aqueous liquid
y_{CH_4}	Mole fraction of methane in vapour phase
α	Biot's effective stress coefficient
θ	Inclination of the shearing plane to the direction of minor principal stress
μ	Poisson's ratio
ρ	Mass density of the soil-hydrate medium
σ_1	Major principal stress
σ_3	Minor principal stress
$(\sigma'_3)_0$	Initial effective confining stress
ϕ	Friction angle
ϕ'	Effective friction angle
ψ_i	Volumetric fraction of the i^{th} constituent in the solid phase ($i = \text{soil mineral or hydrate}$)

Chapter One: Introduction

1.1 Introduction

Gas clathrate hydrates (herein called “hydrate” or “hydrates”) are non-stoichiometric compounds where guest gas molecules are encapsulated within hydrogen bonded lattice cages of water. Two common molecular structures into which the hydrates of most non-polar and some weakly polar gases are formed are known as Structure I and Structure II [van der Walls and Platteeuw, 1959], where, Structure I is the most commonly found in nature [Kvenvolden, 1993]; and methane, a low carbon number hydrocarbon, is the most commonly found hydrate former in natural systems. However, many naturally occurring gases such as low-carbon-number hydrocarbons, carbon dioxide, and hydrogen sulphide have molecular sizes suitable to form hydrates.

Gas hydrates received attention in the 1930s when hydrate formations were discovered to cause pipeline blockage during transmission of natural gas [Hammerschmidt, 1934]. Natural gas hydrates were first discovered in the Siberian Messoyakha gas field in 1960s [Makogon, 1981]. In the 1970s they were found to occur in deep water sediments [Claypool & Kaplan, 1974]. Since then, evidence of their existence in deepwater marine sediments and in permafrost regions have been recorded abundantly where appropriate pressure/temperature (P/T) conditions and sufficient methane flux exist.

1.2 Human interest in gas hydrates

Gas hydrates capture human interest (1) as a potential energy resource, (2) as a submarine geo-hazard and, (3) as a factor in global climate change [Kvenvolden, 1993]. On one hand, the large quantities of organic carbon present in the concentrated form of hydrates [Kvenvolden, 1993] leading to greater energy density of reservoir rock compared to other conventional and unconventional sources of gas (e.g. coal beds, tight sands, and black shales) [MacDonald, 1990] explains the popularity of such gas hydrate-bearing sediments as potential sources of energy. On the other hand, the link to submarine geo-hazards, drilling and methane production related failures, and climate change issues that are associated with hydrated sediments require engineering evaluation. The slides and slumps on the continental slope and rise of South West Africa, slumps on the U. S. Atlantic continental slope, and submarine slides on the Norwegian continental margin are among much historical evidence that exhibit a possible connection between hydrate boundaries and geo-hazards [Grozić, 2010]. The possible mechanisms that lead to the observed behaviour of dramatic loss of strength and stiffness in these sediments are discussed by Nixon and Grozić [2007] and Sultan et al. [2004]. The role of gas hydrate as an influential factor controlling climate change is discussed by many including Majorowicz et al. [2012], Regan et al. [2011], Regan and Moridis [2007], and Ruppel [2011].

1.3 Problem statement – The importance and the challenges in assessing geomechanical properties of hydrate-bearing sediments

Knowledge of the mechanical properties of hydrate-bearing sediments is important in evaluating the potential risks associated with short and long term sediment behaviour related to drilling and methane production, reservoir subsidence, and mechanisms that lead to slope instability issues associated with shallow hydrated sediments. The mechanical properties of these sediments are determined either by non-destructive field measurements including seismic and electric methods, direct sampling and subsequent laboratory measurements of natural hydrate-bearing cores, or laboratory tests on artificially synthesised hydrate-bearing specimens.

A variety of factors including host sediment properties, pore fluid consistency, hydrate saturation, distribution and growth habit [Spangenberg and Kulenkampff, 2006; Priest *et al.*, 2005, 2009] affect the seismic and electric properties of these sediments and hence the reliability of field measurements. Direct sampling is significantly affected by the alterations to in-situ stress conditions and hydrate dissociation related issues during sampling and core transfer [Waite *et al.*, 2009; Yun *et al.*, 2006]. As such laboratory synthesis and subsequent testing of hydrate-bearing sediments is an important method of gaining fundamental knowledge about these complex materials. However, synthesis of artificial hydrates at the laboratory and the subsequent testing are very challenging. The greatest difficulty exists with the synthesis to form representative growth habits of natural systems. It is believed that in many natural environments hydrates form from dissolved methane in water [buffet and Zatsepina, 2000]; in certain other natural

environments hydrates form in the presence of free gas. Replicating the spatial variability of hydrate distribution is also equally challenging. Waite *et al.* [2009] presents a vivid illustration of the special variability in hydrate sediments “from the scale of gas hydrate-bearing reservoirs to the submicron scale”. Therefore, there exists a need to further our investigation of geomechanical properties while paying attention to the details of formation process of synthetic hydrate cores. The results can later be aggregated and adjusted to develop better models of natural environments.

1.4 Research objectives

This research of geomechanical properties of hydrate-bearing sediments was carried out with the following objectives:

- (a) To introduce a novel formation procedure to artificially synthesise representative hydrate-bearing sediments at the laboratory.
- (b) To investigate the triaxial compressive strength of hydrate-bearing sediments; specifically to investigate:
 - a. The hydrate saturation dependency of strength and stiffness
 - b. The initial effective stress dependency of strength and stiffness
 - c. Pore-scale hydrate growth habit dependency of strength and stiffness

1.5 Scope of investigation

Our attempt to accomplish the above objectives is set within the scope defined by the following tasks:

- (a) Investigating the factors governing the physical properties of natural hydrate-bearing sediments; specifically the geomechanical properties
- (b) Investigating the methods for laboratory synthesis of hydrate-bearing sediments and the impact on physical properties
- (c) Introducing a novel formation method to form methane hydrate in the presence of free gas within particulate granular soil material
- (d) Investigating a method of accurate estimation of hydrate saturation
- (e) Testing of hydrate-bearing soil specimens under triaxial compression conditions at constant strain rate and constant mass
- (f) Analysis of test results for general stress-strain behaviour and correlation between hydrate saturation/initial effective confining stress and strength/stiffness
- (g) Comparison of test results with previously published work to identify the pore-scale growth habit dependency of the strength/stiffness behaviour

1.6 Organization of the thesis

The main aim of this research has been to investigate the strength of hydrate-bearing sediments.

The work carried with this focus is presented within the thesis as explained below.

Identifying the impacts of the process of laboratory synthesis of gas hydrate on the physical properties of hydrate-bearing sediments – Chapter 2

The Chapter identifies that the physical properties of hydrate-bearing sediments are governed by the growth habit, spatial distribution, and hydrate saturation. It also identifies that the growth habit, spatial distribution, and hydrate saturation are formation method dependent. Hence it concludes that the physical properties of hydrate-bearing sediments are governed by the method of laboratory synthesis of hydrates. Four primary formation methods are brought in to detailed discussion to identify the variations in the formation procedures for a given primary formation method adopted at various laboratories. The important impacts of different process elements of these procedures include the effects of freezing and thawing, water migration during formation, effects of formation P/T conditions and subsequent changes to the conditions, and effects of post formation water saturation. The study adds to current knowledge by reviewing in detail the aforementioned effects for possible impacts on the growth habit and spatial distribution of hydrates. The Chapter emphasises on the need to direct our attention not only toward the “method” but also toward the formation “process” and provides insight into planning the laboratory formation methodology for this research.

Synthesising artificial hydrate-bearing sediments at the laboratory – Chapter 3

The previous discussion on controls of geomechanical properties of hydrate-bearing sediments indicates the need to isolate these effects in testing for physical properties of these sediments. This study is focused on hydrate formation in the presence of a free gas phase and attempts to

isolate the impact of formation habit on the geomechanical response from the impacts of spatial variability in distribution. A novel formation procedure which is based on the partial water saturation method and extended to form hydrates from water saturated methane was introduced. The methodology is detailed in Chapter 3.

Identifying the need to perform accurate estimations of hydrate saturation – Chapter 4

Many methods of hydrate saturation estimation (including acoustic wave speed measurements, measurement of electrical properties such as resistivity and dielectric constant) suffer from dependency of those measured parameters on:

- Host sediment characteristics such as porosity, porosity distribution, geological features such as fractures and fracture orientation, intact properties of the soil grains, and stress state
- Pore space consistency (such as existence of free gas) and pore fluid characteristics (such as salinity and presence of other solutes)
- Hydrate growth habit and distribution

This study explores the applicability of dissociation gas evolution measurements (DGEM) as an alternative to the aforementioned; the DGEM is attractive for the following reasons; (1) it is based on fundamental physics and chemistry, (2) the estimation depends only on the bulk hydrate filled pore volume fraction, and (3) it can be used to calibrate most other aforementioned methods. The Chapter emphasizes the need to determine hydrate saturation accurately and links to

available resources that are valuable in the accurate determination of the input parameters required for the DGEM. Additionally, this Chapter explores the sensitivity of hydrate saturation to the accuracy with which the input parameters are measured or estimated. The work contributes to the main focus of the research by providing insight as to the degree of care that we need to exert in relevance to laboratory measurements and by providing guidance as to the choice of mathematical model in the parameter estimation.

Investigating the triaxial compression strength of hydrate-bearing sediments – Chapter 5

The Chapter 5 serves the main purpose of the thesis. It presents the results of the laboratory investigation carried out to investigate the behaviour of hydrate-bearing sediments. The Chapter focuses mainly on the initial effective confining stress, hydrate saturation, and pore scale hydrate growth habit dependency of strength and stiffness of hydrated sediments.

Conclusions – Chapter 6

The main conclusions derived from the study are presented in Chapter 6. This Chapter also presents recommendations as to potential future research.

Chapter Two: Methane Hydrates in Porous Soil Media - A Review

2.1 Introduction

Presence of hydrate within soil pore space is well known to affect the physical properties of such sediments and the geomechanical properties are no exclusion. It may well be hypothesised that these effects are of three folds: (1) effects of hydrate growth habit, (2) effects of spatial distribution of hydrates, and (3) the effects of the degree of hydrate saturation. At a given degree of hydrate saturation, the method of hydrate synthesis within host sediment certainly is one of the major deterministic factors of pore scale hydrate growth habit and distribution. Therefore, it is one of the most influential factors governing the way in which the sediment responses to various loading applied on it. As such, this Chapter is organized to identify four different primary methods of hydrate formation, to identify the growth morphologies and habits encountered in nature, to discuss the relations between physical properties and growth habit, spatial distribution, and hydrate saturation, to discuss the relation between formation method and growth habit, spatial distribution, and hydrate saturation. More importantly, this Chapter reviews in detail the possible outcomes of important hydrate formation process elements emphasizing on the need to view hydrate formation as a “process” and not a “method”.

2.2 Methods of laboratory synthesis of artificial hydrate-bearing sediments

There are four commonly used primary methods of laboratory hydrate synthesis:

- (1) dissolved gas method;

- (2) partial water saturation method;
- (3) ice-seeding method; and
- (4) hydrate pre-mixing method.

However, quite a number of differences are found among the exact formation processes employed at various laboratories for a given primary formation method. These particulars will later be discussed in Section 2.9.1. The following details the four primary formation methods.

2.2.1 Dissolved gas method

The dissolved gas method involves circulation of methane dissolved water through a porous specimen [Ghiassian and Grozic, 2011; Spangenberg et al., 2005, 2008]. Hydrate is expected to form within porous media as methane dissolved water at high pressure cools into the hydrate stability zone. Methane depleted water leaving the specimen enters a source chamber within which high aqueous methane concentration is re-established. The interplay of pressure, temperature, and dissolved methane concentration as driving forces of hydrate formation is well described by Zatsepina and Buffett [1997] and Davie et al. [2004]. The rate of hydrate formation is limited by solubility of methane in water [Ghiassian and Grozic, 2011; Priest et al., 2009; Spangenberg et al., 2005; Waite et al., 2009; Yun et al., 2005], and whether the flow conditions are static or dynamic [Tohidi et al., 2001]. Some attempts to promote formation from dissolved phase are given by Waite et al. [2008a] and Zhong and Rogers [2000]. The dissolved gas method mostly results in hydrate and gas dissolved water in (H-L) equilibrium at the end of formation stage as achieving 100% hydrate filled pore-space is unlikely due to decrease in fluid

permeability caused by growing hydrate saturation [Spangenberg et al., 2005]. The difficulties related to formation of methane hydrate from dissolved gas have led researchers to use other hydrate formers such as carbon dioxide (CO₂) and tetrahydrofuran (THF) as proxies for methane. Formation with CO₂ involves a similar procedure to that of formation with methane, and the details are presented by Buffett and Zatsepina [2000] and Tohidi et al. [2001]. In the case of THF, known amount of THF and water are pre-mixed to obtain a solution of predetermined concentration; the porous specimen is saturated with the solution, and then forced in to the hydrate stability field to allow formation of hydrate [Yun et al., 2007]. The hydrate saturation is fixed by the concentration of THF-water solution and the desired pore contents can be easily arrived at. Particularly, the uncertainties related to hydrate saturation estimation can be eliminated. However, there are concerns related to the use of THF to mimic natural hydrates of methane. Different forms of “excess water” methods [Eaton et al., 2007, 2009; Madden et al., 2009; Priest et al., 2009] which appear to be, however, different from what is generally termed “dissolved gas method” could also be found in literature.

2.2.2 Partial water saturation method

The partial water saturation method involves hydrate growth within gas-rich environment, and hence hydrate is formed in the presence of free gas. A partially water saturated host specimen is created and forced into the hydrate stability field. Two different approaches are generally used to form a partially water saturated specimen; (1) moist tamping of a pre-mixed soil-water mixture [Ebinuma et al., 2005; Hyodo et al., 2007, 2009, 2011; Priest et al., 2011; Rees et al., 2011;

Waite et al., 2008b; Winters et al., 2007; Yoneda et al., 2011] and (2) partially draining of an initially fully water saturated specimen [Ghiassian and Grozic, 2011; Grozic and Ghiassian, 2010; Masui et al., 2005a, 2005b; Miyasaki et al., 2008, 2010a, 2010b, 2011; Winters et al., 2004]. Upon complete formation of hydrate, both the methods are expected to produce hydrate and vapour in (H-V) equilibrium. Although both the approaches may expect to generate hydrate specimens of similar “consistency”, whether they would produce specimens of similar “distribution” of pore contents is uncertain. Also, it is appropriate to expect some quantity of unreacted water to be present in the pores at the apparent end of formation (indicated by insignificant gas consumption rates or pressure reduction rates), particularly at higher degree of initial (pre-formation) water saturations [Kneafsey et al., 2007; Spangenberg et al., 2005; Yun et al., 2007]. Upon hydrate formation, the test specimens are sometimes brought to H-L equilibrium by water saturating the specimens [Ebinuma et al., 2005; Hyodo et al., 2007, 2009, 2011; Masui et al., 2005a, 2005b; Miyasaki et al., 2008, 2010a, 2010b, 2011; Yoneda et al., 2011].

2.2.3 Ice-seeding method

This method involves pre-mixing of ice and cooled sand grains, tamping the mixture into a mould to construct the testing specimen, and then establishing the P/T conditions suitable for hydrate formation while ice is forced to melt producing liquid water required in the progression of the hydrate formation reaction. The details of the methodology are presented by Stern et al. [1996, 1998]. Masui et al. [2005a, 2005b] and Ebinuma et al. [2005] employ this methodology in the specimen preparation for geomechanical testing of hydrated sediments. Ice-seeding method

results in H-V equilibrium within the soil specimen upon complete conversion of melt water into hydrate. However, sometimes the test specimens are brought to H-L equilibrium by water saturating the specimen at the end of formation [Masui et al., 2005a, 2005b].

2.2.4 Hydrate pre-mixing method

Similar to ice-seeding method, hydrate granules are mixed with sand grains and formed into a test specimen at low temperatures, pressurized, and brought to an elevated temperature while the P/T conditions are maintained within hydrate stability field. Hyodo et al. [2005] uses hydrate pre-mixed specimens in testing for geomechanical properties. The hydrate granules are formed by mixing misted water with pure methane gas under hydrate forming conditions [Hyodo et al., 2005]. Similar to ice-seeding method, pore space of such hydrate pre-mixed specimens consists of hydrate and vapour in (H-V) equilibrium.

2.3 Natural gas hydrates

Natural gas hydrates are generally found beneath the permafrost and in deep oceanic sediments. The upper hydrate boundary is found at typical water depths of 300-800 m conditioned by the local bottom water temperature in oceanic environments [Koh and Sloan , 2007]. Most hydrate occurrences are reported in continental shelves and enclosed seas where rapid organic carbon accumulation takes place, adequate methane flux exists (due to bacterial methanogenesis of organic carbon), and suitable P/T conditions exist. Natural gas hydrate is usually thought to have

formed from gas dissolved aqueous solutions except within such regions where free gas is present [Buffett and Zatsepina, 2000].

2.3.1 Hydrate growth morphologies

Natural hydrates are found to occur in varying forms (or growth morphologies) within different types of Earth's sediments [Boswell and Collett, 2006; Collett, 2002]:

- (1) disseminated hydrate growth within the pore space of coarse granular particulate sediments; and
- (2) nodules, laminae, and growth within cracks and fissures particularly associated with fine grained sediments.

According to the summaries of Waite et al. [2009], Mackenzie Delta and Nankai Trough sediments contain sand and gravel and are characterized as coarse grained sediments. Lesser amounts of disseminated hydrates are also found in fine grained sediments consisting of clay and silt of Blake Ridge, Gulf of Mexico, Hydrate Ridge, and Offshore India although nodule or layered hydrate formations within these sediments are the major contributors to the total hydrate saturation of such sediments [Waite et al., 2009]. The Figure 2.1 illustrates some of these various growth habits.

2.3.2 Pore scale hydrate growth habits

Presently, our understanding of porous media hydrate growth (although not extensive) is limited to disseminated pore space hydrate growth within sediments of coarse granular particle assemblies of varying nature while, other hydrate growth forms such as nodules, laminae, and growth within cracks and fissures particularly associated with fine grained sediments awaits proper attention. The disseminated form of growth is generally categorized in to a number of different pore scale growth habits. A number of studies including but not limited to those carried out by Kleinberg et al. [2003], Murray et al. [2006], Winters et al. [2004] agree upon model developed by Helgerud [2001] or similar effective medium models for pore scale hydrate growth habit. Helgerud [2001] approach is based on four distinct hydrate habit models for explaining soil hydrate interaction for unconsolidated packing of mineral grains (Figure 2.2). According to Helgerud [2001] (a) hydrate grows without significant interaction with the frame as a pore filling substance, (b) hydrate grows in the interior of the pores as a part of the load bearing frame, (c) hydrate forms preferentially at grain contacts, acting as cement between particles, and (d) hydrate coats grains more or less uniformly, progressively cementing them as the hydrate volume increases. The hydrate habits models of Winters et al. [2004] treat the two models of Helgerud [2001] (c) hydrate formation at grain contacts and (d) hydrate formation coating the grains as one model of cementation habit. As such it is appropriate to present the pore scale hydrate growth categorized in to three habits as follows.

2.3.2.1 Pore filling habit

The pore filling habit refers to the growth form where hydrate exists within the pore space without significant interaction with the soil skeleton. Hydrate does not bridge sediment grains together. Heterogeneous nucleation (i.e., hydrate nucleation occurring on mineral surfaces) or homogeneous nucleation (i.e., hydrate nucleation occurring spontaneously within fluid phase away from mineral boundaries as shown in Figure 2.2(a)) may take place conditioned by various factors [Katsuki et al., 2006, 2007; Ohmura et al., 2004; Spangenberg et al., 2008; Tohidi et al., 2001; Yun and Santamarina, 2011]. Further details can be found in Section 2.8.1.

2.3.2.2 Load bearing habit

The load bearing habit refers to the growth form where hydrate acts as a part of the soil skeleton providing mechanical stability to the structure. The load bearing habit is considered to be as resulting from continuous growth of pore filling hydrates to reach the mineral boundaries of a pore (as shown in Figure 2.2(b)). Further growth may even displace the mineral grains in loose unconsolidated sediments. The load bearing habit may be expected when hydrate saturations exceed 25-40% [Berge et al., 1999; Yun et al., 2005, 2007]

2.3.2.3 Grain cementing and/or coating habit

This growth form refers to hydrate growth at grain contacts acting as cement between particles (as shown in Figure 2.2(c)) or hydrate growth coating the sediment grains more or less uniformly

progressively cementing the grains as the hydrate volume increases (as shown in Figure 2.2(d)).

This form of hydrate growth generally takes place when free gas is present within the sediments.

2.3.3 Controls on pore scale hydrate growth morphologies and habits

The hydrate growth morphologies and habits found in natural sediments are mainly determined by (1) permeability and permeability distribution within the sediment which is determined by pore size and porosity distribution within the sediment [Nimblett and Ruppel, 2003; Waite et al., 2009], (2) methane solubility which is determined by the temperature, pressure, salinity, and capillary pressure and pore size [Clennell et al., 1999; Davie et al., 2004; Sun and Duan, 2007; Zetsepina and Buffett, 1998], and (3) availability of methane flux. Kleinberg et al. [2003] also suggests variety of other factors including “sediment mineralogy and texture, other solutes such as biosurfactants, gas composition”, and “annealing effects” as deterministic of hydrate growth morphology and habit.

Course grained sediments, which are highly permeable compared to fine grained sediments, are generally associated with disseminated form of hydrate growth in sediment pore space. Within fine grained sediments, hydrates tend to occur in cracks and fissures where methane flux to hydrate nucleation sites (either in dissolved form or in free gas form) is less restricted and capillary inhibition of hydrate formation (detailed below) is less significant. Methane solubility in water increases with decrease in temperature, however, in the presence of hydrate methane solubility decreases with decrease in temperature [Davie et al., 2004; Zetsepina and Buffett,

1998] (Figure 2.3). In absence of hydrates methane solubility increases with increasing pressure, however, in the presence of hydrate, solubility decreases slightly with increasing pressure [Davie et al., 2004; Zetsepina and Buffett, 1998] (Figure 2.3). The aforementioned indicates that greater the temperature and pressure at the base of the HSZ, the higher the tendency for hydrates to form from dissolved phase upon pressure temperature decrease within the HSZ while the available methane flux (which is mostly determined by the geologic setting of the region) compared to the solubility limit under the prevailing P/T conditions and the rate of methane dissolution determines if free gas is present within the HSZ. Continuous sedimentation and resulting warming at the base of HSZ may also cause hydrate dissociation at the base and subsequent migration of free gas into the HSZ [Rempel and Buffett, 1997]. As would be later discussed in greater detail, whether or not hydrate is formed in the presence of free gas in tern determines the formation habit. The presence of salt in pore water results in decreased methane solubility both in the presence and absence of hydrates; however, the effect is not as significant as that of other factors. Within fine grained sediments, high capillarity affects growth in two ways: (a) capillarity increases methane solubility in water [Clarke et al., 1999; Sun and Duan, 2007; Waite et al., 2009] and (b) capillarity favors hydrate formation in larger pores within the sediment and smaller pores are invaded later [Kneafsey et al., 2007]. Thus, provides a secondary reason for hydrates to occupy features of high porosity such as cracks and fissures within fine grained sediments. The underlying physical laws governing the aforementioned behavior are explained elsewhere [Clennell et al., 1999; Davie et al., 2004; Waite et al., 2009; Zetsepina and Buffett, 1998].

In the context of laboratory synthesis of hydrate-bearing sediment, for given sediment exposed to particular gas water chemistry, the pore scale hydrate distribution is most preferably governed by the formation procedure or more specifically, the sequential events during the formation stage. Apart from formation procedure, the pre-formation water saturation is the most deterministic factor of hydrate growth habit and the fact is reflected in the experimental results of Howard et al. [2011] and Minagawa et al. [2009] (Section 4.3).

2.3.4 Classification of natural hydrate accumulations

The natural hydrate accumulations of disseminated hydrate growth morphology (at temperatures above the freezing point of water and overlain by a cap rock) are further categorized into three types by Moridis and Collett [2003] (Figure 2.4):

- (1) Class I with underlying free gas,
- (2) Class II with underlying free water, and
- (3) Class III located between impermeable formations.

Class I accumulations consists of hydrate and free gas (Class IG) or hydrate and free water (Class IW) within the reservoir pore space of the hydrate stability zone (HSZ). These accumulations are underlain by a region where the sediment pore space is occupied by water and free gas. Class II and Class III reservoirs are associated with complete pore space hydrate occupancy within the HSZ.

2.4 Hydrate growth habit dependency of physical properties

The growth habits are known to result in “different macro-scale behaviour of seemingly identical” host “sediments” [Ghiassian and Grozic, 2011] and changes in acoustic and geomechanical properties are among many such properties that are affected.

The pore filling habit alters the bulk stiffness of the pore fluid of host sediments [Yun et al., 2005] while, the cementation habit alters both the bulk stiffness of the pore fluid and the skeletal stiffness [Dvorkin et al., 2000; Yun et al., 2005]. Therefore the acoustic properties of hydrate-bearing sediments are affected by hydrate growth habit as the wave propagation speeds are controlled by the sediment’s bulk modulus (which is determined by bulk stiffness of the pore fluid and the skeletal stiffness [Waite et al., 2009]) and the shear modulus (which is determined by several factors including the nature of inter-granular contacts and hence by growth habit [Santamarina et al., 2001]). The differences in sediment strength properties between different growth habits are highlighted in Winters et al. [2002] and Ghiassian and Grozic [2011] with observations of stronger and stiffer response for cementing habits compared to that of pore filling or load bearing habits.

2.5 Hydrate spatial distribution dependency of physical properties

The effects of spatial distribution of hydrate on the geomechanical properties have not been studied comprehensively. However, the anisotropies caused by variations in hydrate distribution can very well be anticipated to define the physical properties including the geomechanical

properties of these sediments. Studies such as Waite et al. [2008b] indicate the changes in peak strength caused by the changes in distribution.

2.6 Hydrate saturation dependency of physical properties

Of the three controls, it is the effects of hydrate saturation that has mostly been a research focus. Many evidence can be found in literature for hydrate saturation dependency of geomechanical properties (Ebinuma et al., 2005; Hyodo et al., 2007, 2009, 2011; Kuniyuki et al., 2010; Masui et al., 2005a, 2008a, 2008b; Miyazaki et al., 2008, 2010, 2011; Ghiassian and Grozic, 2011; Winters et al., 2002, 2007; Yun et al., 2007), acoustic wave speeds [Chand et al., 2006; Howard et al., 2011; Kleinburg et al., 2003; Priest et al., 2005, 2009; Waite et al., 2008b, 2009; Winters et al., 2004], electrical properties (such as resistivity and dielectric constant) [Kilner and Grozic, 2006; Spangenberg and Kulenkamff, 2006], and thermal properties (such as thermal conductivity) [Waite et al., 2002, 2007, 2009]. A detailed explanation of the relationship between these factors and hydrate saturation is presented in Chapter 4.

The Sections 2.5, 2.6, and 2.7 conclude that the physical properties of hydrate-bearing sediments are governed by the growth habit, spatial distribution, and hydrate saturation.

2.7 Hydrate formation method dependency of growth habit, spatial distribution, and hydrate saturation

2.7.1 Growth habit

Different methods of hydrate synthesis result in different formation habits [Ebinuma et al., 2005; Grozic and Ghiassian, 2010; Priest et al., 2009; Spangenberg et al., 2005; Waite et al., 2009; Winters et al., 2004; Yun et al., 2007; Zhong and Rogers, 2000]. The Figure 2.5 presents the ***general association*** between the four primary methods of hydrate laboratory synthesis (Section 2.2) and hydrate growth habits. As can be seen, the dissolved gas method results in pore filling growth habit with hydrates nucleating on mineral surfaces [Katsuki et al., 2006, 2007; Ohmura et al. 2004; Spangenberg et al., 2008; Tohidi et al., 200] and subsequent growth in to the pore space (Figure 2.5(a)). However, with continuous hydrate growth, load bearing habit can well be anticipated. The partial water saturation method is associated with grain cementing hydrate habit with hydrate formation at grain contacts (Figure 2.5(b)). The ice-seeding method either results in cementing or load bearing habit, while hydrate pre-mixing habit results in load bearing habit (Figure 2.5(c)) depending upon hydrate saturation and the relative size of the hydrate and sediment grains.

2.7.2 Spatial distribution

The formation method dependency of hydrate spatial distribution has received attention only lately. Kneafsey et al. [2010] investigate the possible means of obtaining uniform pore space distribution of hydrate for variety of formation procedures based on the primary method of

partial water saturation, while Minagawa et al. [2009] examines the hydrate spatial distribution for different formation procedures based on the primary methods of partial water saturation and ice-seeding. Both studies observe differences in hydrate spatial distribution between different formation procedures and provide evidence of hydrate formation method dependency of hydrate spatial distribution. Also, the aforementioned studies reveal the challenges that exist with the attempts to obtain uniform hydrate distributions at the laboratory which can be used as representative of a given hydrate habit in the study of physical behaviours associated with the hydrate habit.

2.7.3 Hydrate saturation

The hydrate saturations obtained in the laboratory is often constrained by the challenges associated with different formation methods. The dissolved gas method has only shown limited success due to low solubility of methane in water and hydrate plugging of fluid circulation lines. Conceptually, it is envisaged that the method can yield up to 60-70% before pore fluid circulation is severely restricted [Waite et al., 2009]. A highest saturation of 95% after 50 days of formation had been reported by Spangenberg et al. [2005]. The partial water saturation method allows hydrate saturations up to about 60%. The full conversion of water into hydrate becomes challenging as the initial water saturation increases. Thus, higher hydrate saturations obtained with this method are associated with limited reliability. Ice-seeding and hydrate pre-mixing methods has been used to generate hydrate saturations up to about 50% [Masui et al., 2005; Hyodo et al., 2005]. Similar to partial water saturation method the hydrate saturations achievable

using ice-seeding method is restricted by the issues related to full conversion of ice or melt water into hydrate. The hydrate pre-mixing method may conceptually used to achieve 100% hydrate saturation.

The Sections 2.7.1, 2.7.2, and 2.7.3 allows us to conclude that growth habit, spatial distribution, and hydrate saturation are formation method dependent. As such, based on our previous conclusions on growth habit, spatial distribution, and hydrate saturation dependency of physical properties it can now be deduced that the physical properties of hydrate-bearing sediments are governed by the method of laboratory synthesis of hydrates. The four primary formation methods are, in fact, consists of various formation process elements and are employed with significant differences in procedures at different laboratories. Considering the dependence of physical properties on the formation method and the differences in formation procedures employed, it is of immense importance to investigate the implications of different formation process elements in detail. The Section 2.8 serves this purpose.

2.8 Formation “Method” versus Formation “Process”

When laboratory synthesis of hydrate-bearing sediment is considered, we tend to perceive hydrate formation in porous media as a result of a mere method of distinctive end product. We highlight the need to propel our observations towards greater details viewing hydrate formation as a “process” of which the end product carries the signatures of several process elements. Evidence can be presented from literature that paying attention to different formation “process

elements” is much needed as those different process elements may have significant control over the hydrate growth habit and the pore space hydrate distribution of the synthesised specimens thus governing the physical properties. The notion of forming “representative samples” of natural hydrate-bearing sediments includes two key components; (1) forming a representative growth habit and (2) forming a representative pore space distribution of hydrate. It can be noticed that either one of the components often receive attention at a time while the other remains unnoticed. Kneafsey et al. [2010] and Minagawa et al. [2009] investigate the possible means of obtaining uniform pore space distribution of hydrate by employing various formation processes while the general associations between growth habit and primary formation method are assumed to be applicable. The following sections look into the possible implications of various process elements over the representative nature of the resulting specimens and thus serve a long awaited need. Other than the formation process elements (including freezing and thawing, water migration during hydrate formation, formation P/T conditions and subsequent changes of conditions on the hydrates of a particular primary formation method), the impact of the factors; intact strength of hydrate and hydrate former are also discussed.

2.8.1 Implications of the primary formation method

The hydrate growth habit is thought to be predominantly governed by the primary formation method. According to Waite et al., [2009], and Yun and Santamarina, [2011], when hydrates are formed from gas dissolved water, heterogeneous nucleation tend to occur on mineral surfaces. Heterogeneous nucleation is also supported by Katsuki et al. [2006, 2007] and Ohmura et al.

[2004], however, different macroscopic hydrate morphologies and different hydrate-sediments bonding characteristics are reported at different sub-cooling during hydrate formation. In contrast to above observations, with regard to “excess water” method of hydrate formation, which is a variation of dissolved gas method, hydrates nucleate in the pore space with no contact with mineral surfaces [Spangenberg et al., 2008; Tohidi et al., 2001]. In all cases, subsequent hydrate growth in water-rich environment results in non-cementing hydrate habit [Spangenberg et al., 2008]; particularly, pore filling habit of hydrate growth at low hydrate saturations and the load bearing habit at higher saturations are observed [Yun et al., 2007; Priest et al., 2009].

Partial water saturation method, due to pre-formation water accumulation at grain contacts, however, produces cementation habit of hydrate growth with hydrate formation initiating at grain contacts [Chuvilin et al., 2003; Ebinuma et al., 2005; Klapproth et al., 2007; Kneafsey et al., 2005, 2007; Kono and Budhijanto, 2002; Masui et al., 2005a; Priest et al., 2005]. As hydrate formation proceeds, the growth may result in coating the sediment grains entirely.

According to Waite et al. [2009] it appears that a mixed habit of cementing and load bearing nature can be expected for specimens created with ice-seeding method. The cementing nature of the habit is due to preferential melt water accumulation at grain contacts. This form of growth can particularly be expected at low initial ice to sediment volume fraction. Whether or not the formation would continue to grow into a load bearing habit is seemingly determined by combined effect of several factors including the initial (pre-formation) ice to sediment volume fraction, relative size of mineral and ice grains (which determines if the ice grains filled the

sediment pores or acted as a part of the pre-formation sediment frame as a load bearing element), and the pace at which the melt-water conversion into hydrate takes place relative to the possible sediment consolidation that may take place as the melting of (load bearing) ice occurs.

The hydrate premixing method essentially results in a load bearing growth habit and the “load distribution within the sediment depends on the relative size of the hydrate granules and sediment grains” [Waite et al., 2009].

The above summarises the general associations between the primary formation methods and the pore scale hydrate growth habits. The exact form of growth habit and hydrate distribution depends on several other factors which are discussed in the following sections. The knowledge presented in the following sections may even lead us to question the validity of the aforementioned associations.

2.8.2 Implications of different approaches for forming a partially water saturated specimens

Mainly two different approaches are employed to form partially water saturated specimen; (1) moist tamping of a pre-mixed soil-water mixture and (2) partially draining of an initially fully water saturated specimen.

With the use of moist tamping of pre-mixed soil-water mixture, an approximately uniform initial water distribution can be expected within the specimen. During the time between specimen

preparation and hydrate nucleation some water re-distribution within the specimen can also be expected for reasons such as gravity effects. According to our observations with 20/30 grading Ottawa sand, however, at least for low water saturations (up to a water saturations of about 25%) of compact grain arrangements the gravity effects cause minimal or negligible changes in water migration over time spans of multiple hours as capillary effects helps holding water at grain contacts acting against gravity. If the formation procedure consists of freezing and thawing of the partially saturated specimen, significant degree of water redistribution should be expected.

As opposed to the use of moist sand, partially draining of an initially water saturated specimen may result in high water saturations predominantly closer to the drainage end of the specimen. Introducing hydrate forming gas as a bubble form into the specimen with reversed flow direction may help obtaining a better water distribution. Significant improvements of initial water distribution can be achieved by subjecting the specimen to a series of sudden pressure pulses following draining of excess water. Therefore, in either case of (1) use of moist sand, and (2) partially draining, whether or not a uniform distribution of hydrates would result depends on the initial water distribution (if not altered by subsequent freezing and thawing) and the very nature of the hydrate nucleation and growth process. For example, rapid formation with simultaneous nucleation at multiple sites may result in greater uniformity as opposed to slow formation with limited number of nucleation sites. Hydrate formation itself can causes non-uniformities within a specimen [Kneafsey et al., 2010] particularly when the slow formation takes place with water migration towards a small number of nucleation sites.

2.8.3 Effects of freezing and thawing

The effects of freezing and thawing can be discussed in relation to both laboratory synthesised specimens and natural hydrate-bearing core samples as a factor which affects (1) hydrate distribution and (2) possible mineral grain re-distribution and preservation of the sediment pore structure. In the case of laboratory synthesis of hydrate-bearing specimens, the issues of hydrate distribution appears to be more prominent. In the case of natural core samples the issues of mineral grain re-distribution and the preservation of the sediment pore structure appear to be prominent. The following discussion, however, omits the discussion of effects on natural core samples as the focus of this Chapter is to investigate the process of synthesising artificial hydrate-bearing specimens at the laboratory. Many laboratories [Hyodo et al., 2007, 2009, 2011; Masui et al., 2005a; Miyasaki et al., 2008, 2010a, 2010b, 2011] follow hydrate formation processes consisting of freezing and thawing with respect to initially partially water saturated specimens. Once the specimens are transferred into strength testing apparatus, such frozen specimens are then thawed under pressure to reach a temperature outside the hydrate stability zone [Hyodo et al., 2011] prior to subsequent cooling and formation. In other cases the frozen specimens are only thawed to facilitate ice melting but temperature is maintained within the hydrate stability region [Hyodo et al., 2007, 2009; Masui et al., 2005a; Miyasaki et al., 2008, 2010a, 2010b, 2011] facilitating hydrate formation as water-ice melts.

Freezing initiates at surfaces where heat is removed; in the case of cylindrical specimen subjected to radial heat transfer freezing initiates at the outer radii and then draws water towards

the freezing front [Kneafsey et al., 2010, Kneafsey and Nakagawa, 2011]. However, the degree of water movement is apparently governed by the degree of initial water saturation, the type of soil, and rate of freezing [Kneafsey et al., 2010]. According to the observations of Kneafsey et al. [2010] little change in water movement could be expected upon freezing of sand with lower packing density and high roughness of the grains at low water saturation. Rapid freezing could also help maintaining uniform ice distribution [Kneafsey et al., 2010]. However, the correlations do not appear clear and ample room exists for further research.

Irrespective of initial water saturation and the type of soil, thawing seems to be re-establishing the initial water distribution resulting in fairly uniform water distribution [Kneafsey et al., 2010]. However, whether or not uniformly distributed hydrate formation would result depends on the subsequent procedures followed in an experiment. From the aforementioned it could be deduced that controlled slow thawing of a specimen (previously subjected to rapid freezing) under hydrate forming gas pressure could be used to create more uniform hydrate distribution as opposed to rapid melting and lagged initiation of hydrate formation as hydrate formation itself affects water distribution. As the thawing progresses the system temperature may preferably maintained within the hydrate stability zone.

In addition to water change characteristics, freezing/thawing can also cause mineral grain redistribution within unconsolidated sediment although the effects can be minimized at higher confining stresses [Kneafsey et al., 2011]. The mineral grain redistribution is more prominent in

fine grained sediments than in course grained sediments and is also freezing rate dependent [Winters et al., 1999; Winters et al., 2008]. Rapid freezing in liquid Nitrogen does not appear to disrupt the sediment as severely as slow freezing as extensive grain movement with ice-lens formation due to “pore water migration towards freezing fronts” associated with slow freezing [Winters et al., 2008] is avoided.

2.8.4 Effects of water migration during formation of hydrate

The effect of water migration during hydrate formation is discussed below in relevance to hydrate formed within partially water saturated granular media. Evidence can be cited in literature for observed water migration towards hydrate nucleation sites creating un-evenness in water distribution [Guptha et al., 2008; and Kneafsey et al., 2007; and Kneafsey and Nakagawa, 2011]. Capillary pressure changes takes place within porous medium as hydrate formation narrows the pores [Guptha et al., 2008; Kneafsey et al., 2007, Kneafsey and Nakagawa, 2011] and water tends to flow into narrower pores and hence, a growing hydrate front drags a region of high water saturation along [Kneafsey et al., 2007, 2010]. Water migration and hydrate formation can result even in grain-redistribution particularly in unconsolidated sediments as explained previously with relevance to freezing and ice-lens formation. If facilitated, rapid hydrate formation upon establishing hydrate stability conditions with simultaneous nucleation at multiple sites could be expected to create lesser degree of water migration. Low initial water saturation could also be expected to promote simultaneous multiple nucleation.

2.8.5 Effects of formation P/T conditions and subsequent changes to formation P/T conditions

The effects of formation P/T conditions are barely but addressed in literature with regard to (1) intact hydrate characteristics of microscopic nature which is later discussed under “intact strength of hydrate” [Huo et al., 2003; Sloan, 2003], (2) macroscopic morphology of hydrate crystal growth [Katsuki et al., 2006, 2007; Ohmura et al., 2004], (3) consequent hydrate-sediment interaction [Katsuki et al., 2006, 2007], and (4) strength properties of granular hydrate assemblies [Hyodo et al., 2002; Nabeshima et al., 2005; Song et al., 2010]. An unmistakable dependency of above on formation P/T conditions could be identified.

Macroscopic morphology of hydrate crystal growth is known to be governed by the degree of sub-cooling which is the difference between the enforced formation temperature and the equilibrium H-L-V three-phase temperature corresponding to the system pressure [Katsuki et al., 2006, 2007; Ohmura et al., 2004]. It is interesting to note that those different hydrate morphologies interact with sediment grains in different ways and hence affect the geomechanical properties of hydrate-bearing sediment to a varying degree. The type of hydrate morphology observed at low sub-cooling (faceted crystals) exhibits stronger bonding with the sediment grains [Katsuki et al., 2006, 2007]. The hydrate morphology observed at high sub-cooling (dendritic crystals) tends to change to crystals of particulate nature with aging and appears to have no cementation effect on the sediment grains [Katsuki et al., 2006, 2007].

Effects of subsequent changes to formation P/T has been reported external to the crystallographic scale. Dramatic increase in hydrate formation rate is induced by the “reduction of driving force” (by means of reducing pressure towards the equilibrium pressure at a given temperature or by increasing the temperature towards the equilibrium temperature at a given pressure), possibly due to (1) formation of isolated pockets of water containing dissolved methane and the over-pressurization as gas pressure declines or temperature increases, consequent breakage of surrounding hydrate walls of these pockets, and resulting improved communication between water and gas phases, (2) methane super-saturation of pore water and consequent gas ex-solution in response to pressure drops [Kneafsey et al., 2007].

2.8.6 Effects of post formation water saturation

Many specimen preparation processes subjected to our review of hydrate synthesis for geomechanical testing of specimens include post formation water saturation of hydrated specimens consisting of free gas phase within the pore space at the end of formation phase. Due to the altered pore contents such a specimen should be expected to exhibit different geomechanical behaviour with respect to a non-water saturated specimen consisting of hydrate and vapour. Seismic resonance frequency measurements of Kneafsey et al. [2010] reveals a reduction of specimen stiffness and therefore, indicates possible de-bonding of hydrate from mineral surfaces upon post formation water saturation. This important observation suggests a change in the hydrate habit from grain cementation to pore filling, although little evidence can be cited in literature to support this observation. Issues such as water saturation induced possible

hydrate re-formation or dissolution due to possible methane concentration differences between flood water and the equilibrium methane concentration at corresponding system temperature and pressure awaits attention.

2.8.7 Intact strength of hydrate

The effects of intact strength of hydrate are expected to have significant control on the overall strength of hydrate-bearing sediment particularly at high hydrate saturations exceeding approximately 80% of pore space saturation as illustrated in Waite et al. [2009]. Triaxial compression tests of Hyodo et al. [2002], Nabeshima et al. [2005], and Song et al. [2010] on strength of methane hydrate are seemingly non-representative of particular growth morphologies formed under the applied formation conditions, but appear to be altered by the respective testing procedure. Whether or not the P/T conditions are maintained constant between formation and subsequent testing is not clear. Particularly, some procedures [Nabeshima et al., 2005, Song et al., 2010] involve compaction of hydrate formed from powdered ice in forming triaxial test specimens. Therefore, the specimens represent an assembly of hydrate granules of certain growth morphology with seemingly different crystal-crystal interactions at the inter-granular contacts to intact bonds between crystals within the undisturbed core of individual granules.

However, the reported strength of these granular hydrate assemblies shows increased strength at cooler temperatures and higher pressures [Hyodo et al., 2002; Nabeshima et al., 2005; Song et al., 2010] and interestingly shows a clear correlation with the relative location of test P/T

conditions in the P-T space for methane-water system with respect to the three phase hydrate-aqueous liquid-vapour (H-Lw-V) boundary [Hyodo et al., 2002]. These observations are signs of microscopic level response of hydrate to different environmental conditions and subsequent changes in such environmental conditions.

As presented earlier, hydrate crystal morphology at least depends on applied sub-cooling during hydrate formation [Katsuki et al., 2006, 2007; Ohmura et al., 2004]. Therefore, it is prudent to assume that strength of hydrate as relevant to its contribution to the strength of hydrated sediment to be affected by many factors both known and unknown including the intact single crystal hydrate strength. On one hand, Katsuki et al. [2006] in relevance to their examination of sub-cooling dependency of morphology assume the mechanical properties of hydrate crystals are independent of the degree of sub-cooling during formation. On the other hand, Raman Spectroscopy experiments of Huo et al. [2003] prove non-stoichiometric existence of methane hydrate unit cell at partial cage occupancy and the cage occupancies are governed by the pressure, temperature and the overall methane composition of a given system [Sloan, 2003a, 2003b]. In fact, hydrates grown at vapour-liquid interface tends to exhibit greater cage occupancy than dendritic crystals grown into liquid phase [Huo et al., 2003]. It is therefore, not inappropriate to question if the intact single crystal strength itself could be considered independent of formation conditions. As such it is evident that the strength of aggregated hydrate is governed by complex interplay of variable factors and our present knowledge is apparently inadequate in predicting its contribution to the overall strength of hydrated sediments.

2.8.8 Hydrate former

Carbon dioxide (CO₂) and tetrahydrofuran (THF) are often used as proxies for methane with the intention of avoiding the difficulties associated with methane hydrate formation. According to the previous discussion, not only the way that hydrate interacts with sediment grains at macro level but also the properties of intact hydrate at micro level too can be considered as influential over the overall geomechanical behaviour of hydrate-bearing sediment. Therefore, it is important that our choices as to the alternative hydrate formers to methane are based on sound scientific facts. “CO₂ hydrate yields the same hydrate structure as the CH₄ hydrate” [Buffett and Zatsepina, 2000] and leaves researchers with the ease of working at low pressures still offering greater solubility in water compared to methane. CO₂ is generally considered as a “useful analog to naturally occurring hydrates” [Buffett and Zatsepina, 2000] and we do not wish to further our discussion in this regard as geomechanical testing of hydrated specimens reported in literature do not include hydrates formed from CO₂. The differences between THF and CH₄ hydrates are discussed, the issues are raised, and their impacts over the mechanical strength are addressed by Lee et al. [2007]. Waite et al. [2009] summarises the THF related issues and highlights the relative advantages of the use of THF as a hydrate former. The argument remains that the overall hydrate-bearing sediment behaviour is more reflective of the hydrate formation process (i.e., the primary formation method and the subsequent process elements of macro scale impacts) than it would be of the micro scale differences of THF and methane hydrates.

2.9 Discussion

The results of our above investigation of hydrate formation process are summarized in Table 2.1. The present success with dissolved gas method remains with the use of proxies for methane such as tetrahydrofuran (THF). Uncertainties though exist as to whether nucleation takes place on mineral grains or in pore water with no grain contact. The formation P/T conditions particularly, the degree of sub-cooling during formation appear to have an impact over the cementing or non-cementing nature of formation. However, observations of sediment physical properties to date do not support the cementing habit of hydrates but pore filling and load bearing hydrates.

Hydrate-bearing sediment formed with initially partial water saturated specimens are generally associated with grain cementation hydrate habit at low saturations and grain coating hydrate habit at high saturations. However, when the impact of various process elements during formation are carefully considered, it appears that there exists a possibility of obtaining pore filling and load bearing hydrate habits which are more representative of natural hydrates. Evenness of hydrate distribution can be expected in specimens prepared at low initial water saturations forced to rapid formation with simultaneous nucleation at multiple sites. If freezing and thawing are involved in the formation process, rapid freezing followed by slow thawing with temperatures and pressures maintained within hydrate stability zone would result in preservation of initial water distribution within the specimen. High sub-cooling during formation and post formation water saturation of the specimen are known to result in hydrate de-bonding

from mineral surfaces and such specimen could be expected to exhibit physical properties characteristic to pore filling or load bearing hydrate habits.

However, in both the cases of ice-seeding and hydrate pre-mixing processes, the mineral grain assembly itself become non-representative of natural sediments as the packing density is determined by ice-to-sediment or hydrate-to-sediment volume ratio but not by the very nature of the mineral grains and the consolidation process.

From the above it is evident that our understanding of natural hydrates as well as of forming representative samples at the laboratory is incomplete. However, compiling the knowledge generated through various researches (as we have attempted within the scope of this Chapter) provides guidance for further research. As such, with inputs from above investigation, we explore a novel method for forming representative samples of grain cementing and/or coating habit of hydrates to study the behaviour of hydrates formed in the presence of free gas phase. Our objective is to achieve uniform hydrate distributions at both low and high saturations. The details are presented in Chapter 3.

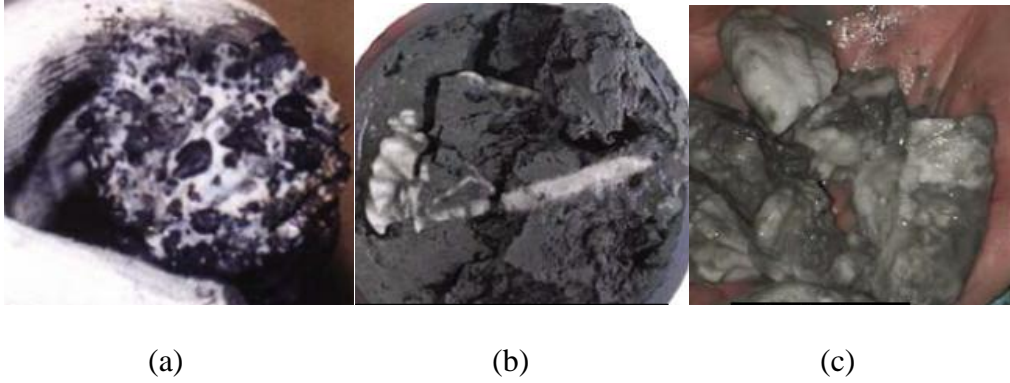


Figure 2.1: Different hydrate growth morphologies found in natural hydrate-bearing sediments (Hydrate in white)

- (a) Disseminated form of hydrate growth in coarse grained soils from 1998 Mallik 2L-38 hydrate research well, (b) Veined hydrate formation in fine grained sediments from Krishna Godavari Basin, offshore India, and (c) Sediment coated hydrate chunks in fine grained sediments of Gulf of Mexico. (Modified from Waite et al. [2009])

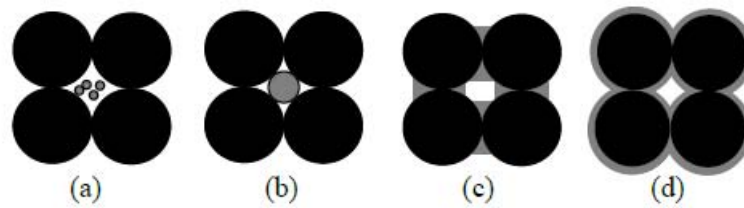


Figure 2.2: Pore-scale hydrate growth habits for unconsolidated packing of mineral grains

- According to Helgerud [2001], hydrate growth can be categorized into different habits as follows: (a) hydrate grows without significant interaction with the frame as a pore filling substance, (b) hydrate grows in the interior of the pores as a part of the load bearing frame, (c) hydrate forms preferentially at grain contacts, acting as cement between particles, and (d) hydrate coats grains more or less uniformly, progressively cementing them as the hydrate volume increases.

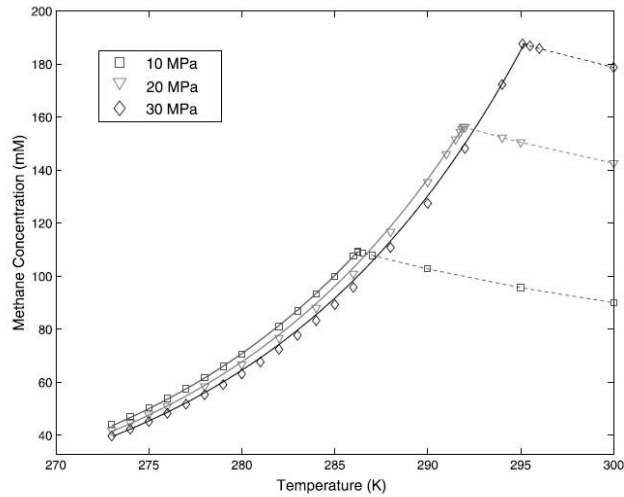


Figure 2.3: Solubility of methane in pure water

- Methane solubility in water increases with decrease in temperature, however, in the presence of hydrate methane solubility decreases with decrease in temperature. In the absence of hydrates methane solubility increases with increasing pressure, however, in the presence of hydrate, solubility decreases slightly with increasing pressure (Adopted from Davie et al. [2004]).

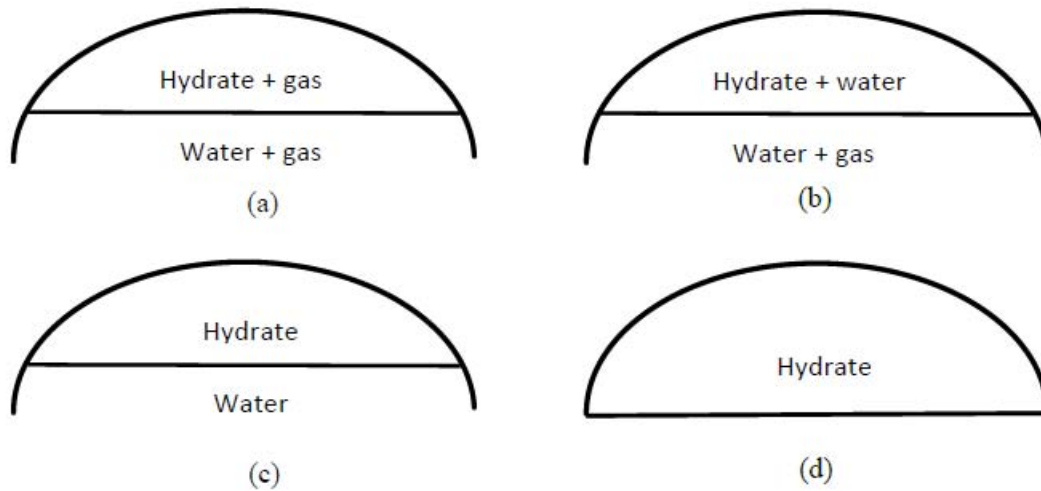


Figure 2.4: Classification of hydrate-bearing sediments

- Class I accumulations are underlain by free gas and are classified in to two sub categories based on the pore space consistency within the hydrate stability zone (HSZ) (a) Class IG with free gas and hydrate within HSZ and (b) Class IW hydrate and water within HSZ. (c) Class II accumulations are underlain by free water, and (d) Class III accumulations are located between impermeable formations (illustration after Sia [2013]).

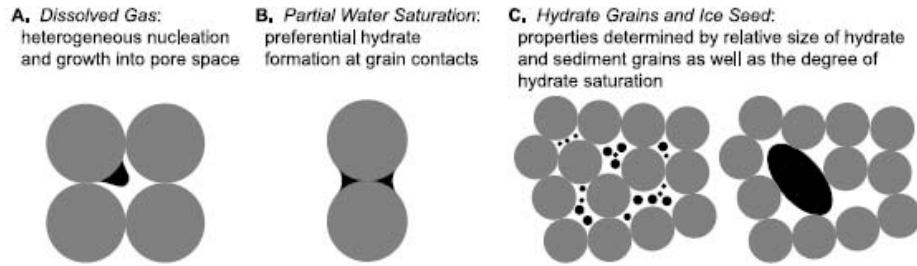


Figure 2.5: The general association between the four primary methods of hydrate laboratory synthesis and hydrate growth habits

- (a) the dissolved gas method results in pore filling growth habit with hydrates nucleating on mineral surfaces and subsequent growth in to the pore space, (b) the partial water saturation method is associated with grain cementing hydrate habit with hydrate formation at grain contacts, and (c) the ice-seeding method either results in cementing or load bearing habit, while hydrate pre-mixing habit results in load bearing habit depending upon hydrate saturation and the relative size of the hydrate and sediment grains (Adopted from Waite et al. [2009])

Table 2.1: Impact of formation process elements on the growth habit and hydrate distribution during laboratory synthesis of hydrate-bearing soil specimens

Formation process elements	Laboratory synthesis of disseminated hydrate in particulate granular media			
Primary formation method	Dissolved gas method – nucleation on mineral surface and subsequent growth into pore space OR nucleation in pore water with no grain contact?	Partial water saturation method – nucleation and growth at grain contacts	Ice seeding method – melt water is converted to hydrates	Hydrate premixing method
General associations between the hydrate formation methods and pore space hydrate growth habits	Pore filling hydrate habit at low hydrate saturations Load bearing hydrate habit at high hydrate saturations	Grain cementation hydrate habit at low hydrate saturations grain coating habit at high hydrate saturations	Grain cementation hydrate habit (at low initial ice to sediment volume ratio) OR Load bearing hydrate habit (Whether or not the load bearing hydrate habit would exist depends upon several factors as presented in Section 2.8.1.	Load bearing hydrate habit
Use of moist sand specimen versus partially draining a water saturated specimen to obtain a partially water saturated specimen	NA	Use of moist sand – fairly uniform initial distribution of water Partially draining a saturated specimen – tendency for uneven initial distribution of water	NA	NA
Freezing – associated with water migration and pore water volume expansion	NA	Mild water migration observed with: Rapid freezing Low packing density of mineral grains High roughness of mineral grains and Low initial water saturation (Caution: Greater tendency for mineral grain re-distribution exists with lower packing density) (The adverse impact is not as severe as in the case of natural core samples of no free gas as the pore volume is much compressible)	NA	NA

Formation process elements	Laboratory synthesis of disseminated hydrate in particulate granular media			
Thawing to reach out of stability region conditions OR thawing to reach a set temperature within hydrate stability zone	NA	Thawing seems to be re-establishing the initial water distribution (Slow thawing of a specimen with fairly uniform ice distribution with temperatures and pressures maintained within hydrate stability zone to facilitate quick conversion of melt water into hydrate may help avoiding water migration during hydrate formation)	Slow thawing of a specimen with fairly uniform ice distribution with temperatures and pressures maintained within hydrate stability zone to facilitate quick conversion of melt water into hydrate may help avoiding water migration during hydrate formation	NA
Hydrate formation – associated with water migration towards hydrate formation front	NA	Rapid formation with simultaneous nucleation at multiple sites may help minimize water migration	Rapid formation with simultaneous nucleation at multiple sites may help minimize water migration	
Formation P/T conditions	Low sub-cooling: resulting in faceted crystals with strong bonding between hydrate and sediment grains High sub-cooling: resulting with dendritic crystals with weak bonding between hydrate and mineral grains, de-bonding with aging, and pore filling hydrate habit Load bearing hydrate habit may be expected at high saturations			NA
post formation water saturation	NA	Possible de-bonding of hydrate from grain contacts resulting in pore filling habit	Possible de-bonding of hydrate from grain contacts resulting in pore filling habit	NA – Reported procedures in literature on geomechanical testing of such specimen do not include a post formation water saturation element

Chapter Three: Laboratory Synthesis of Methane Hydrate-Bearing Sediment

3.1 Introduction

The details of common methods for laboratory synthesis of methane hydrate-bearing sediments, namely; (1) dissolved gas method, (2) partial water saturation method (3) ice-seeding method and (4) hydrate pre-mixing method [Waite et al., 2009] were presented in Chapter 2. Further, investigation into the hydrate growth habit, spatial distribution, and saturation dependency of physical properties including geomechanical properties has illustrated that the laboratory synthesis method of hydrate-bearing sediments plays an influential role in determining the physical behaviour of such sediments. Existing hydrate formation methodologies are incapable of producing representative specimens of a given hydrate habit [Kneafsey et al., 2007; Waite et al., 2008b] as the behaviour is influenced by the specimen non-uniformities resulting from uneven hydrate distribution [Waite et al., 2008b]. Therefore, one focus of this research has been to develop a laboratory procedure to obtain a more uniform hydrate distribution, particularly at higher hydrate saturations, within particulate granular soil media.

3.1.1 A novel procedure for hydrate synthesis – hydrate formation from water rich gaseous methane

A novel hydrate formation procedure, based on the partially water saturated method, is thus proposed. The method extends the partial saturation concept to continue hydrate formation in a second phase where the formation occurs from water saturated gaseous methane (vapour). The hydrate formation mechanisms in the second (vapour) phase are very similar to hydrate plug formation, which occurs in natural gas transmission pipelines.

Partial water saturation method, due to pre-formation water accumulation at grain contacts, produces cementation habit of hydrate growth with hydrate formation initiating at grain contacts [Chuvilin et al., 2003; Ebinuma et al., 2005; Kneafsey et al., 2005, 2007; Priest et al., 2005, 2009; Waite et al., 2008b; Waite et al., 2009]. Uniform hydrate distributions can be achieved with this methodology at low initial water saturations (or at low hydrate saturations) provided that pre-formation water menisci are uniformly distributed within the media.

However, at higher hydrate saturations, the specimen non-uniformities, originating mainly from non uniform distribution of pre-formation water, result in altered physical behaviours as evidenced by Kneafsey et al. [2010]. When high hydrate saturations are to be achieved, high initial water saturation is required, which may lead to existence of saturated granular clusters (or “aggregates of sand grains connected by a patch of pore fluid” [Kneafsey and Nakagawa, 2011]) resulting in occurrences of un-reacted water pockets within the hydrated sediment and not achieving expected hydrate saturations. The hydrate formation in partially water saturated sand and measurement of acoustic properties [Kneafsey et al., 2011] at 39% initial degree of water saturation (which is considered a relatively high water saturation) provides an explanation. According to Kneafsey et al. [2011], hydrate growth initiates at gas-water interface followed by “needle like crystal” growth in to the water phase from “diffusion of methane molecules through the hydrate film and the water”. This growth model is applicable to (a) conversion of capillary held water at single grain to grain contact (in the case of low initial water saturations) or (b) conversion of capillary held water at outer surface of a saturated granular cluster. It is reasonable that at low water saturations, there exists a greater probability of full conversion of capillary held water at single grain to grain contacts in to hydrate before the thickness of the growing hydrate

mass significantly hinders methane diffusion through the hydrate mass. In contrast, at high initial water saturations there exists a greater probability for unreacted water to be present in the core of a saturated granular cluster by the time methane diffusion through the growing hydrate film is apparently blocked. As should be expected, the observations related to tests of Kneafsey et al. [2011] at 39% water saturation fit with the latter case indicating the possible existence of unreacted water pockets within the hydrate mass. The X-ray MicroCT imagery (Figure 3.1) of laboratory formed hydrate sediments by Jin et al. [2006] also provide visual evidence for existence of unreacted water. Such irregularities can significantly alter the geomechanical behaviour of sediment as over-pressurization of trapped water may lead to hydrate fracturing [Kneafsey et al., 2007] as the soil-hydrate medium deforms due to applied loading particularly when excess negative bulk pore pressures develop within dense soil medium under undrained conditions or when bulk pore fluid pressure dissipation takes place under drained conditions.

The developed hydrate formation procedure thus aims at eliminating the difficulties associated with partial water saturation method and begins by forming a partially water saturated soil specimen with a known initial water content, kept low enough (15-20% water saturation) to ensure uniform pre-formation water distribution. Kneafsey et al. [2010] reports on difficulties in maintaining uniform water distribution arising around water saturations of 35%. At low water saturations, uniform water distribution can be achieved as capillary effects force water to reside at grain contacts, thereby negating gravity effects. However, it should be noted that capillary held water distribution within granular soil media is fundamentally governed by the pore size (radius) distribution within the media. As such the uniform water distribution within specimens should be expected for such grain assemblies where reasonably uniform pore size distribution is

expected. Hydrate saturations higher than that could be expected by mere conversion of capillary held free water are obtained by allowing the specimen to enter a secondary formation phase where accumulated hydrate growth takes place from conversion of vapour phase moisture into hydrate. The theoretical background is presented in Section 3.3.

3.1.2 Potential hydrate growth habit

Within the specimens prepared with some initial water saturation, hydrate formation will begin at the gas water interface leading to grain cementing hydrate habit (Figure 3.2(a)). As the growth proceeds to the secondary phase where formation takes place from water vapour preferably condensing on the mineral surfaces, the formation can be expected to coat the mineral grains (Figure 3.2(b)). When the vapour phase is used with initially dry specimens, it is anticipated that the hydrate will nucleate at the grain surfaces and grow coating the grain surfaces, and eventually into the pore space.

3.1.3 Implications of hydrate growth habit on the strength and stiffness of the sediments

Grain cementing and grain coating hydrate habits are known to particularly increase the skeletal stiffness [Fernandez and Santamarina, 2001; Priest et al., 2009; Waite et al., 2009]. Also, host sediments indicate greater shear strength in the presence of hydrates.

3.2 The experimental procedure

The experimental procedure consists of three important stages, namely; (1) preparation of the host specimen for hydrate synthesis, (2) hydrate formation, and (3) triaxial compression testing of the hydrated specimen. The following is focused on the details of stages (1) and (2). The

details of stage (3) – the triaxial compression testing procedure are presented in Chapter 5 with summary information of stages (1) and (2). A detailed diagram of experimental set-up is presented in Figure 3.3.

3.2.1 Materials

3.2.1.1 Sand

Ottawa sand of uniform grain distribution (20/30, with mean particle size of 0.72 mm and coefficient of uniformity of 1.2) [Cho et al., 2005] was used for preparation of host specimens for laboratory synthesis of methane hydrate. The maximum and minimum void ratios of Ottawa sand are 0.742 and 0.502 respectively [Cho et al., 2005]. According to ASTM C-778-12, Ottawa sand has a specific gravity of 2.65.

3.2.1.2 Water

De-aired water was used in the testing process for specimen saturation and hydrate formation as the presence of dissolved gases in water hinders methane dissolution in water and consequently delays the hydrate nucleation process.

3.2.1.3 Hydrate former

Laboratory grade high purity (99.7%) methane was used as the hydrate former. The presence of impurities in methane is known to affect the equilibrium P/T conditions of the methane-water binary system.

3.2.2 Methods

3.2.2.1 Specimen preparation

A typical methane hydrate host specimen of cylindrical geometry was prepared by dry pluviation of sand into a latex membrane fixed to the bottom cap of the triaxial assembly and supported by a cylindrical split mould. A vacuum applied between the mould and the membrane ensures tight contact between the membrane and the wall of the cylindrical mould during dry pluviation. The specimen top cap was then set into place. All test specimens were constructed at an approximate initial void ratio of 0.57, which corresponds to a relative density of 72%. Initial dimensions of the test specimens were recorded; typical dimensions were 13.0 cm in height and 6.24 cm in diameter. A vacuum was applied via the bottom cap of the triaxial assembly to provide suction sufficient to prevent specimen collapse during removal of the split mould and later application of initial confining stress. The split mould was then removed, outer triaxial cell assembled, the triaxial cell filled with water (confining fluid), and an isotropic initial confining stress applied. The vacuum was released and the specimen was fully water saturated by flow of water through the specimen under a low head difference; flow occurred upwards, against gravity, to ensure full saturation.

Following specimen saturation, an initial pore fluid pressure was applied, then confining and pore fluid pressures were simultaneously increased to reach a pre-determined isotropic effective consolidation stress (500 kPa or 1000 kPa) and pore fluid pressure of 9000 kPa. The specimen was then allowed to consolidate under the set effective confining stress until drainage ceased. The pore fluid volume change measurements allowed calculation of specimen void ratios at the end of consolidation.

After consolidation, the specimen was opened to an interface cell (pressurized to 9000 kPa) containing water rich gaseous methane and methane was allowed into the specimen while a known quantity of pore water was drained from the specimen. This procedure produced a partially water saturated medium of known degree of water saturation. Water saturations between 15-20% were used to ensure uniform water distribution. To further promote uniform water distribution, the gas flow direction was reversed and several pressure pluses were applied at the bottom of the specimen, to promote upwards moisture movement.

3.2.2.2 Hydrate formation

Following preparation of the partially water saturated specimen, the specimen was cooled into the hydrate stability zone (5°C) initiating hydrate formation, while the pore gas pressure was maintained constant (at 9000 kPa) by controlling the pressure at the interface cell. Hydrate formation initiated with conversion of capillary held water at grain contacts into hydrate (primary formation phase). The interface cell, containing pressurized gas overlying water, operated as the methane gas source throughout the hydrate formation stage. As such, gaseous methane, which was fed into the specimen, was rich in water vapour because it was allowed to reach saturation at the interface cell. The interface cell was at an elevated temperature (room temperature) relative to the specimen, which was maintained at 5°C . At an elevated temperature (outside the hydrate stability zone) gaseous methane holds a greater mole fraction of water when in aqueous liquid-vapour equilibrium than it holds in the presence of hydrate (within the specimen) at a lower temperature. This reduction in equilibrium water content contained within the gaseous methane associated with cooling drives the hydrate formation into a secondary phase where progressive formation occurs from conversion of vaporous water in methane into hydrate.

The gas volume consumption recorded at the interface cell provides an approximate estimation of the hydrate quantities formed. Generally, obtaining higher hydrate saturations required longer test durations (Table 3.6). Once the target hydrate saturation is achieved, the specimen was left to equilibrate and the hydrate-vapour (H-V) equilibrium achieved.

At the completion of the formation procedures, the specimen was left to equilibrate and H-V equilibrium achieved. The details of mechanisms governing the secondary hydrate formation are discussed in the next section. The data presented in Table 3.6 reveals it was possible to achieve hydrate saturations of about 55% from an initial water content of 15-20%.

A number of preliminary hydrate formation tests were carried out with zero initial water content (dry sand). Hydrate formation with zero initial water content resulted in significantly lower hydrate formation rates. This suggests that hydrate formation from an aqueous form of water is favoured over hydrate formation from condensing water vapour contained within gaseous methane. Once in the presence of hydrate formed during the primary formation phase, the secondary formation reaction appears to continue at a comparatively higher rate. Seemingly, more and more moisture is drawn towards the already formed hydrate. As hydrate accumulation continues, the uniformity of hydrate distribution is expected to be maintained as it is fixed by the initial water distribution and hence by the hydrate distribution of the primary formation phase.

3.3 The concept – Hydrate formation from water saturated gaseous methane

The following explains the underlying concept of secondary hydrate formation from water saturated gaseous methane. Hydrate formation from vapour involves forcing a vapour, which is initially in thermodynamic equilibrium with aqueous liquid (Lw-V), into hydrate vapour (H-V) equilibrium. Our method uses isobaric (constant pressure) cooling of vapour in Lw-V equilibrium to reach H-V equilibrium (Figure 3.4). Note that the numerical representation of different stages and respective pressure/temperature/composition conditions are thus selected to maintain consistency between Figures 3.4, 3.5 and 3.6.

The Phase Rule of Gibbs [Gibbs, 1948] provides the basis for understanding the mechanisms taking place in such a system. It specifies the “degrees of freedom” or the number of independent variables (F) required in defining the state of a system of known number of component (C) and number of coexisting phases (P). The phase rule can be stated as: $F=C-P+2$. The Table 3.1 provides the possible combinations of P and F for a two component system (such as methane-water system). Once F numbers of variables are fixed for the system, all the other variables are fixed as well.

The heterogeneous equilibrium of two or more phases of a two component system can be explained using the Pressure-Temperature-Composition (P-T-X) diagram. The T-X diagram at a given pressure is particularly useful in understanding phase behaviour (Figure 3.5). The following summarizes the representation of various combinations of P and F of Table 3.1 for two or more co-existing phases.

- (a) **P=2, F=2:** The state of a system in two phase equilibrium is determined by the spatial spread of two surfaces in P-T-X space each representing one of the two phases when two state variables are fixed for the system [Kobayashi and Katz, 1949]. For example, at a given temperature T, and a pressure P, the phase composition of the existing phases is fixed by the common intersection of each phase surface with the already fixed constant P/T planes. In Figure 3.5, at a given temperature T, the composition of the aqueous liquid and vapour phases in equilibrium are given by vertical projections of point (2) and (1) respectively, on the composition axis.
- (b) **P=3, F=1:** “Three-phase equilibria are represented by three space curves, each formed by the intersection of two surfaces. The requirement for the uniformity of pressure and temperature for an equilibrium system requires that the space curves for all three-phases must furnish the same projection on the pressure-temperature (P-T) plane” [Kobayashi and Katz, 1949]. Therefore, a plane consisting three space curves for respective phases in equilibrium should be associated with single curvature independent of phase composition in P-T-X space. As such three phase equilibria are represented by lines parallel to X axis on TX and PX diagrams. For such equilibria only one degree of freedom exists. For example, for hydrate-aqueous liquid-vapour (H-Lw-V) three phase equilibrium, at a given pressure there exists unique temperature T (given by the projected intersection of line (6)-(3)-(4)-(5) onto the T axis in Figure 3.5) and composition X (given by vertical projections of points (5), (4), and (6) onto the X axis for Lw, H, and V phases respectively). Therefore, if pressure P is selected as the independent variable, once the

pressure is fixed the other two variables temperature (T) and composition (C) are fixed as well.

- (c) **P=4, F=0:** Four phase equilibrium is represented by quadruple points on the P-T projection of P-T-X space and are in fact projections of “four unique points in space falling on a straight line perpendicular to the P-T plane at their respective phase compositions” [Kobayashi and Katz, 1949]. Each individual point in space is the intersection of three three-phase space curves. These set of curves “when projected on the P-T plane appear as four three-phase curves emanating from a four-phase (quadruple point)” [Kobayashi and Katz, 1949].

The exploration of TX diagrams of Kobayashi and Katz [1949] and the adaptation presented in Figure 3.5 reveals that the hydrate phase coexists with either the aqueous liquid phase or the vapour phase, depending on the relative abundance of water and gas. Consider isobaric cooling (which is represented by the dashed vertical line (1)-(7) of Figure 3.5) of a vapour which is in equilibrium with aqueous liquid at point (1). In the case of our hydrate formation experiments, the system pressure (within the interface cell and the soil specimen) is predetermined (9000 kPa) and maintained at a constant value, while the temperature at the interface cell (where vapour at conditions represented by point (1)) is in equilibrium with room conditions.

The composition of the vapour, which is now governed by the set pressure and temperature regime, is determined by the vertical projection of point (1) onto the composition axis.

Theoretically, at compositions where the mole fraction of water in vapour is less than the mole

fraction corresponding to vertical line (4) – (4') of stoichiometric hydrate composition $CH_4(5.75)H_2O$ (which is given in terms of a mole fraction of 0.852), the H-V equilibrium can be reached at by isobaric sub-cooling of the vapour along the line (1)-(3). Careful observation of the non horizontal boundaries of the Lw-V two-phase region indicates (a) increased dissolved methane mole fraction in water and (b) decreased mole fraction of water in methane associated with cooling as moisture removed from vapour condenses to form aqueous liquid. When the temperature (3) is reached by continuous cooling, hydrate of composition given by (4) forms and coexists with a water of composition given by (5) and a vapour of composition given by (6). The system is now at three-phase H-Lw-V equilibrium. Continuous heat removal at constant temperature results in accumulation of hydrate as more and more vapour is drawn into the soil medium. Once the supply of water rich methane is stopped, the system settles at the imposed temperature of (7) by complete conversion of free water into hydrate followed by further cooling into the H-V two phase region.

The composition of vapour in equilibrium with hydrate is given by the vertical projection onto the X axis at point (8). The composition of hydrate in equilibrium with vapour is given by the vertical line (4)-(4'). Originally Kobayashi and Katz [1949] assumed the hydrate phase composition was fixed with 100% hydrate cage occupancy, however, more recent research [Huo et al., 2003; Sloan, 2003a and 2003b] provide evidence of the non-stoichiometric nature of hydrate formation, noting that unoccupied small cages exist within the hydrate structure. The resulting hydrate number (or the composition) is a function of temperature, pressure, and overall methane composition [Sloan, 2003b]. The effect of non-stoichiometric hydrate occurrence is

neglected in our estimation of hydrate quantities and the stoichiometric hydrate line of Kobayashi and Katz [1949] is assumed.

It is interesting to note that as the vapour cools from (3) to (7), a further decrease in mole fraction of water in methane takes place. The total drop of equilibrium water content in gaseous methane from (1) to (8) (Figure 3.5) represents the driving force that exists for hydrate formation. Figure 3.6 provides a better representation of the drop in moisture content in vapour associated with isobaric cooling. Table 3.2 provides range of experimentally measured values for water content in methane at (1) under Lw-V equilibrium and Table 3.3 provides the range of experimentally measured values for water content in methane under H-V equilibrium. The data set illustrates the reduction of water content in methane associated with cooling.

3.4 Estimation of hydrate quantities formed from isobaric cooling of water saturated vapour

The quantity of hydrate generated from a known initial volume of water saturated methane is calculated by applying the principle of mass balance for methane and water present within a closed system. (Figure 3.7) The initial P/T conditions of water saturated methane, mole fraction of water in methane under Lw-V equilibrium conditions, mole fraction of water in methane under H-V equilibrium conditions, molar volume of water in hydrate phase (or the volume of hydrate lattice per mole of water in hydrate phase), composition of hydrate (or methane to water molar ratio in hydrate phase), and final P/T conditions for the system in H-V equilibrium are required as input parameters in the estimation. Table 3.4 lists useful references cited in literature vital in the determination of some of the aforementioned input parameters. Our estimation

reveals formation of trivial volume fractions of hydrate upon cooling. The Table 3.5 provides the estimate of the hydrate quantity generated per known volume of water saturated methane under Lw-V equilibrium at set P/T conditions. Therefore, it is suggested that continuous feed of water rich methane into the soil media is critical to the success of the formation process. Interestingly, our gas consumption measurements provide a hint of continued hydrate growth even under flow conditions where the flow is allowed to occur through the specimen as a mere consequence of methane/water concentration differences and/or as a requirement to maintain the system pressure as methane is consumed in hydrate formation.

3.5 Hydrate growth habit and distribution deduced from subsequent strength testing of hydrate-bearing specimens

The results of tests (MH A01 – MH 009) where hydrate formation within soil specimens pre-consolidated at effective confining stress of 500 kPa are presented in Table 6. Subsequent to the hydrate formation stage, the test specimens MH 001 – MH 009 were subjected to triaxial compression loading to obtain the strength properties. At the end of the test, hydrate saturation was calculated using the dissociation gas evolution measurements (DGEM) detailed in Chapter 4. The specimens with zero initial degree of water saturation generated comparatively low hydrate saturations. However, the presence of some initial water appeared to have facilitated higher hydrate saturations as can be deduced by comparison of formation duration times and the obtained hydrate saturations (Table 3.6). The strength results can be used to derive indirect evidence of the nature of hydrate distribution within the sediment. The clear correlation obtained between the strength and hydrate saturation at low hydrate saturations (< 40%) is considered as evidence of uniform hydrate distribution (Figure 5.5 of Chapter 5. However, at higher hydrate

saturations ($> 40\%$), the loss of clear correlation between strength and hydrate saturation may be considered as originating from possible non-uniformities in hydrate distribution. The greater stiffness obtained for the tested specimens compared to those obtained for non-cementing habit of hydrate (Yun et al., 2007) suggests possible grain cementation. Based solely on the strength results, a definitive conclusion as to the growth of vapour phase hydrate formation can not be reached; however, further research including microscopic imaging could be employed to understand the pore scale nucleation and growth of hydrate.

3.6 Discussion

As the physical properties of hydrate-bearing sediments are greatly affected by pore space hydrate distribution, we explore the possibilities of obtaining uniform hydrate distributions particularly at higher hydrate saturations. The attempt to obtain uniform hydrate distribution originates by maintaining uniform low initial water distribution within soil pore space and then extends to hydrate formation from water saturated gaseous methane. In accordance with our observations of the hydrate formation process we identify two major factors that determine the degree of success in achieving high hydrate saturations and forming specimens of uniform hydrate distribution representative of the particular growth habit: (1) initial availability of minimal uniformly distributed water content, and (2) continuous feed of water rich methane throughout the formation phase. Our work proves that forming hydrate from water saturated gaseous methane is possible. As suggested by the strength results, employing the method appears to have resulted in uniform hydrate distributions up to saturations of 40%. However, at higher saturations, the strength behaviour suggests possible specimen non-uniformities. Therefore, we

emphasise on the need to perform further research to verify the expected growth morphologies and the uniformity of hydrate distribution.

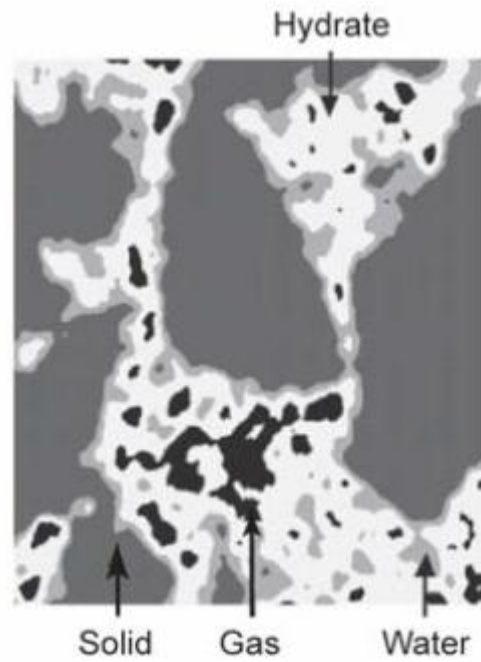


Figure 3.1: X-ray MicroCT imagery showing the distribution of different phases within hydrated sediment

-Mmineral grains (dark grey), gas (black), water (light grey), and hydrate (white) - (Modified from Waite et al, [2009] developed after Jin et al.,[2006])

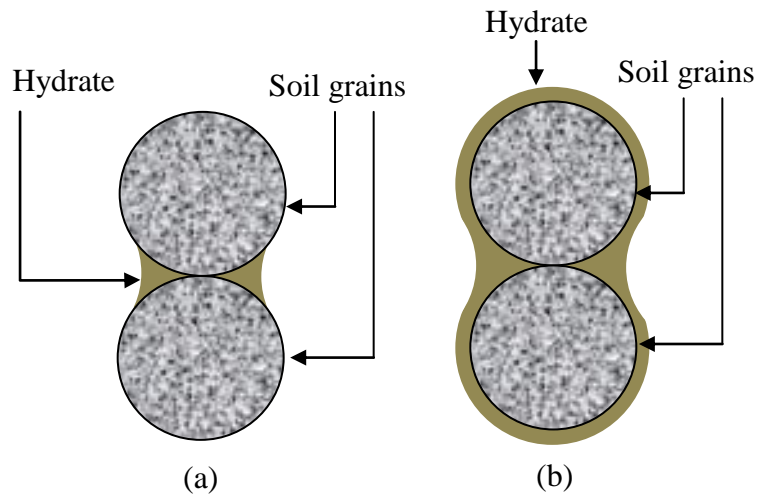
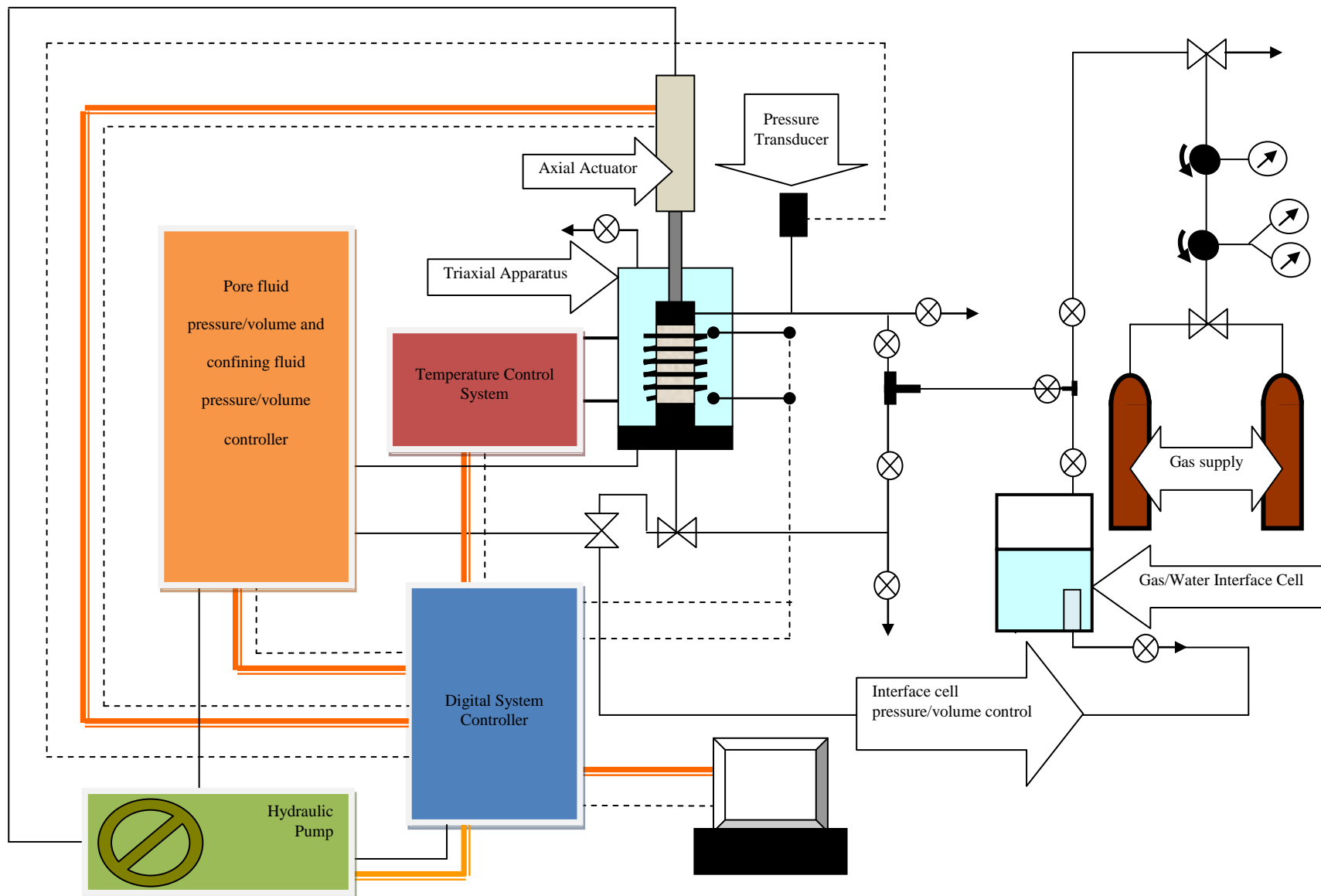


Figure 3.2: Growth habit and growth habit transition; (a) initial conversion of capillary held water into hydrate leading to grain cementing hydrate habit and (b) further hydrate growth from condensing water leading to grain coating hydrate habit








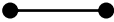

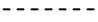


Index	
	Pressure Gauge
	Pressure Regulator
	Three Way Connector
	Stop Valve
	Two Way Valve
	Temperature Sensor
	Fluid Flow
	Data Transfer
	Control Signals
	Personal Computer

Figure 3.3: Triaxial gas hydrate testing system

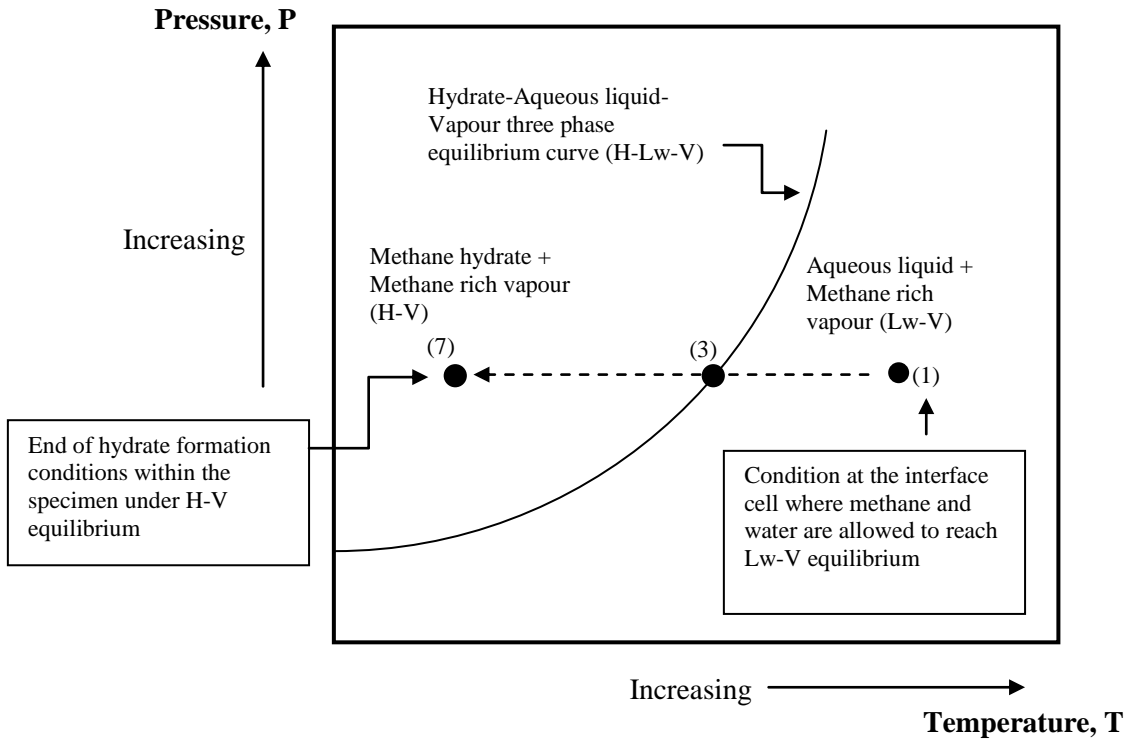


Figure 3.4: The PT Diagram for isobaric cooling of water rich gaseous methane (vapour) into the hydrate stability zone

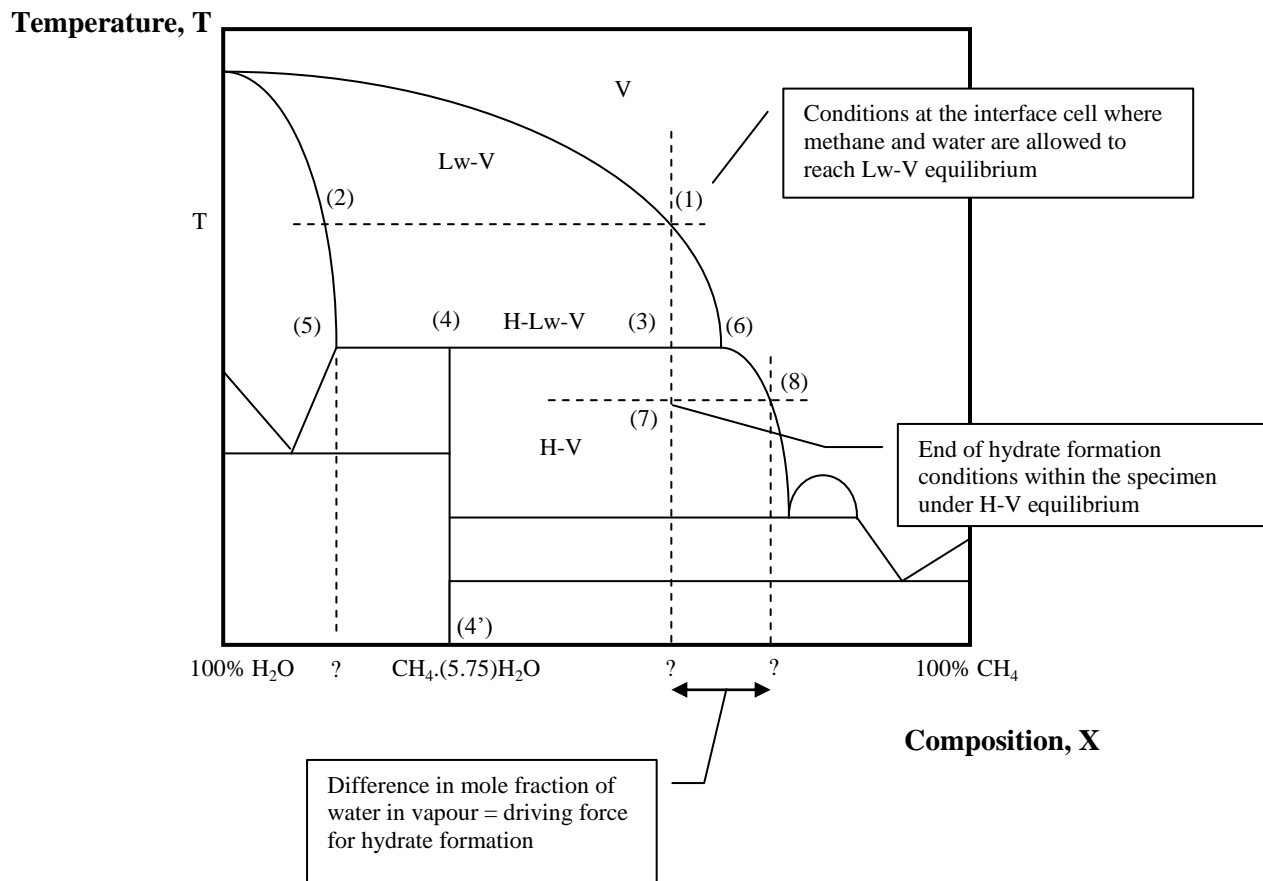


Figure 3.5: Temperature-Composition (T-X) diagram for methane-water binary system at fixed pressure

- [modified after Kobayashi and Katz, 1949]

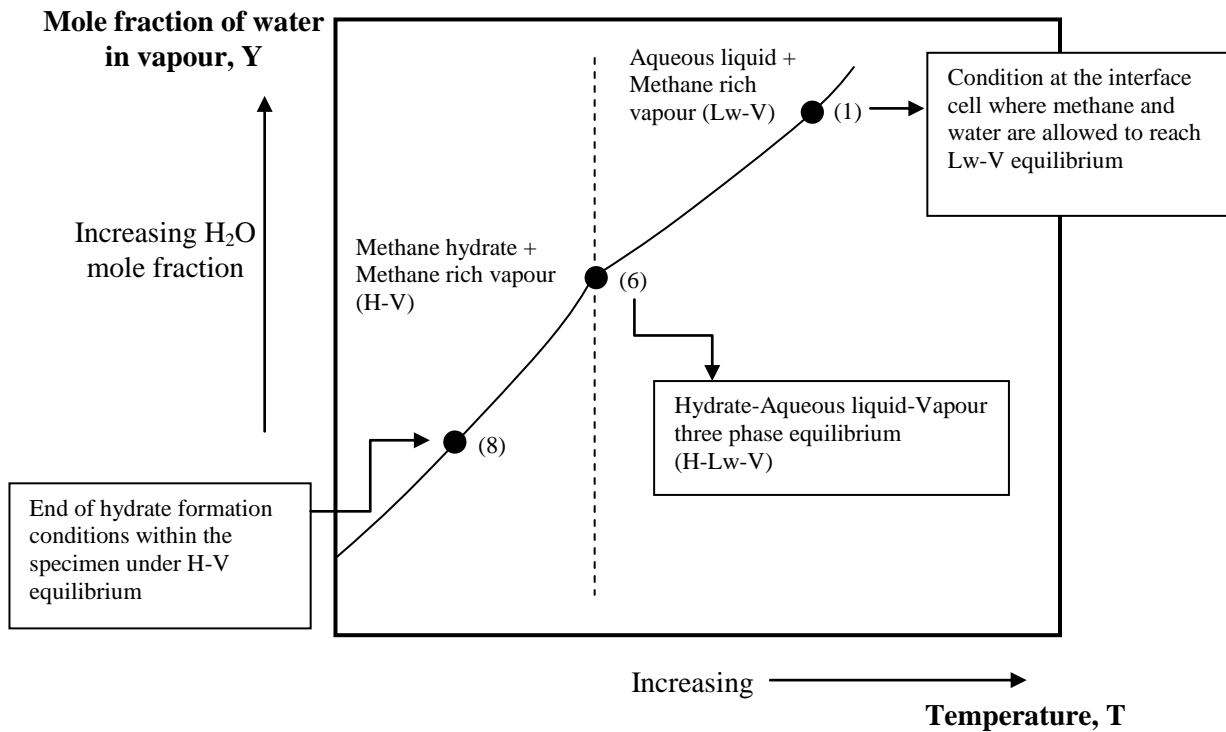


Figure 3.6: The reduction in the water content of gaseous methane associated with isobaric cooling

- As the cooling takes place, moisture is removed from the vapour in the form of condensation in order to maintain the equilibrium moisture content in vapour at a given temperature (solid line (1)-(6)-(8))

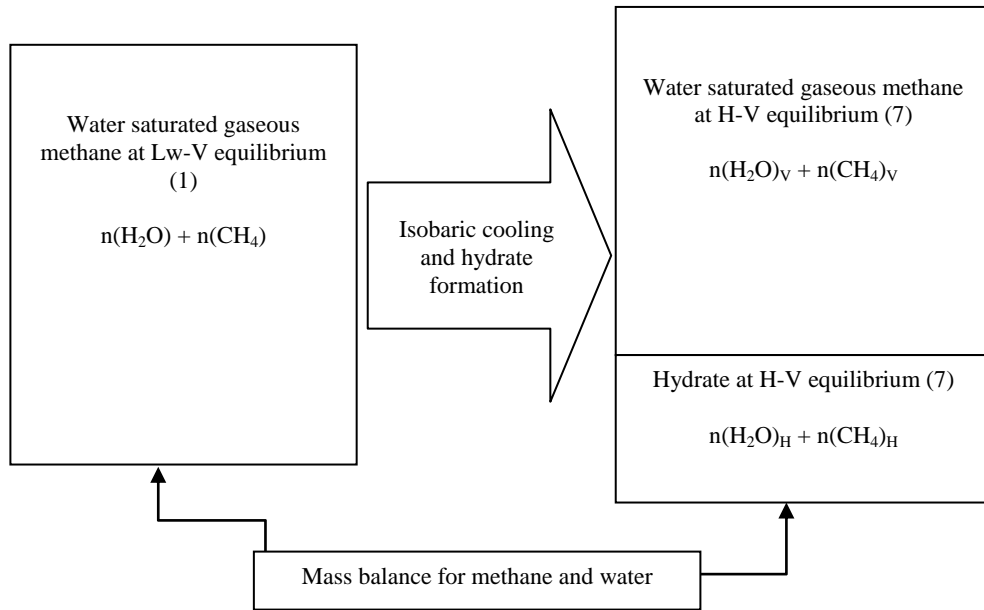


Figure 3.7: Schematic diagram showing application of mass balance for methane and water between the two stages; (1) the system consisting of water saturated gaseous methane (vapour) at Lw-V equilibrium and (2) the system consisting of hydrate and vapour in H-V equilibrium

Table 3.1: Possible combination of number of co-existing phases (P) and number of independent variables (F) for a two component systems in accordance with Gibbs Phase Rule

Components (C)	Number of co-existing phases (P)	Number of independent variables (F)
2	1	3
2	2	2
2	3	1
2	4	0

Table 3.2: Experimentally measured values for water content in methane under Lw-V equilibrium

Pressure (MPa)	Temperature (K)	Mole fraction of water in methane ($\times 10^3$)	Reference
6	293.15	0.470	Oellrich and Althaus [2000]
10	293.15	0.320	Lokken <i>et al.</i> [2008]
10	293.15	0.322	Oellrich and Althaus [2000]
10	283.15	0.168	Lokken <i>et al.</i> [2008]
25.06	303.11	0.371	Chapoy <i>et al.</i> , [2005]

Table 3.3: Experimentally measured values for water content in methane under H-V equilibrium

Pressure (MPa)	Temperature (K)	Mole fraction of water in methane ($\times 10^3$)	Reference
6	283.15	0.251	Oellrich and Althaus [2000]
10	273.15	0.075	Oellrich and Althaus [2000]
25.06	288.11	0.126	Chapoy <i>et al.</i> [2005]

Table 3.4: References for determination of input parameters of the hydrate quantity estimation

	Parameter	References
(a)	Mole fraction of water in methane under Lw-V equilibrium conditions	Duan and Mao [2006] with inputs from Shibue [2003] and Wagner and Pruss [1993] OR Semi-empirical method of Mohammadi et al. [2004] OR CSMGem calculator of Colorado School of Mines – Originally developed by Ballard [2002]
(b)	Mole fraction of water in methane under H-V equilibrium conditions	Semi-empirical method of Chapoy et al. [2010] OR CSMGem calculator of Colorado School of Mines – Originally developed by Ballard [2002]
(c)	Molar volume of water saturated methane under Lw-V equilibrium	Yokoseki [2005] with (a) and (b) above as inputs OR CSMGem calculator of Colorado School of Mines – Originally developed by Ballard [2002]
(d)	molar volume of water in hydrate phase	Ogineko et al. [2006] and Hester et al. [2007]

Table 3.5: Estimated hydrate quantity per known volume of water saturated methane under L-V equilibrium

Equilibrium conditions	(L _w -V)	(H-V)
Temperature (K)	299.15	278.15
Pressure (kPa)	9101.325	9101.325
Volume of hydrate (cc) per 1000 cc of water saturated methane under L-V equilibrium conditions	0.0375	

Table 3.6: Laboratory test results for vapour phase hydrate formation with and without initial water content

Test ID	Initial effective confining stress (kPa)	Hydrate Saturation (%)	Formation Time (hrs)	Initial degree of water saturation	Initial void ratio	Maximum deviator stress (kPa)	Normalized Maximum deviator stress
WS 500	500	0	N/A	100	0.572	3083	N/A
MH A01	500	6.2	70	0	0.569	N/A	N/A
MH A02	500	7.3	67	0	0.573	N/A	N/A
MH 001	500	10.2	72	0	0.579	3273	1.06
MH 002	500	12.7	86	0	0.574	3485	1.13
MH 003	500	27.3	91	17	0.543	3726	1.21
MH 004	500	34.4	101	20	0.550	3927	1.27
MH 007	500	46.3	109	19	0.567	5786	1.88
MH 008	500	51.3	127	20	0.571	7584	2.46
MH 009	500	53.6	116	21	0.541	6157	2.00

Chapter Four: Estimating Pore Space Hydrate Saturation Using Dissociation Gas Evolution Measurements (DGEM) ¹

4.1 Introduction

Geomechanical, acoustic, thermal, and flow properties of gas hydrate-bearing soils are greatly dependent upon the pore space saturation, growth habit, and distribution of hydrates. Therefore, our attempts to correlate presence of hydrate phase with the physical characteristics of such sediments are successful to the extent with which we can accurately determine the saturation, habit, and the distribution of hydrates. Of interest to Chapter 4 is the pore space hydrate saturation; the pore volume fraction of a given sediment occupied by hydrate and its accurate quantification. The accuracy of most saturation estimation methods are affected by growth habit and pore space distribution of hydrate. This chapter presents the details of several methods for hydrate saturation estimation and highlights the usefulness of the dissociation gas evolution measurements (DGEM) method as a reference laboratory method for calibrating and overcoming the challenges associated with other methods. The hydrate saturations values generated by this method depend only on: (1) choice of fundamental physical and chemical laws to accurately represent the methane hydrate system and (2) the bulk hydrate filled pore volume fraction. The calculations associated with the DGEM are based on the concept of mass balance and the volume compatibility properties between two distinct sets of environmental conditions for a closed system.

¹The full citation of this published chapter is: Jayasinghe, A. G., and Grozic, J. L. H. (2013). Estimating Pore Space Hydrate Saturation Using Dissociation Gas Evolution Measurements: In Relevance to Laboratory Testing of Natural or Artificially Synthesised Hydrate-Bearing Soil Specimens, *Journal of Geological Research*, Vol. 2013, Article ID 815841, doi:10.1155/2013/815841. The original article is accessible at: <http://www.hindawi.com/journals/jgr/2013/815841/>. The article is reproduced under the Creative Commons Attribution License, © 2013 A. G. Jayasinghe and J. L. H. Grozic.

The accuracy of the saturation estimations depends on (1) the precision with which the laboratory measurements related to temperature, pressure, and volumetric properties of the system are obtained, and (2) the ability of the physical and chemical laws (models) used in the determination of various parameters to closely represent the true nature of the system. An analysis was performed to evaluate the sensitivity of hydrate saturation to various laboratory measurements associated with the DGEM method, with the intension of understanding the level of accuracy required in the laboratory measurements. The compilation of the available mathematical models used in representing system conditions, and thus generating the methane concentration in different phases, serves as one of the major contributions of the work presented. The evaluation of the sensitivity of hydrate saturation to those models provides insight into the appropriateness of various assumptions associated with DGEM.

The chapter is organized to present the aforementioned in detail as follows. The role of hydrate saturation in determining the host sediment behavior is explained followed by various techniques for determination of hydrate saturation. The laboratory testing procedure is then summarized in relation to application of the DGEM method (The complete experimental procedure is presented in Chapter 2). Measurements of P/T parameters and estimates of volumetric parameters required in the DGEM method of hydrate saturation calculation are then listed. The presentation then proceeds to compile resources available in literature facilitating accurate determination of methane density required in the determination of input parameters to the DGEM method. The analysis performed to evaluate the sensitivity of hydrate saturation to various laboratory measurements associated with the method and to the assumptions of equilibrium states of the system precedes the concluding discussion.

4.2 Hydrate saturation dependency of physical properties

The presence (or more specifically the saturation) of hydrate within the pore space is known to alter the physical properties of host sediment by a great extent. The control of geomechanical (meaning; strength, deformation, and flow) properties of host sediments by hydrates has been a global research focus over the recent past and certainly is gaining more and more interest. The following presents a few experimental investigations of pore space hydrate to illustrate the important effects of hydrate saturation on the physical properties. Understanding of the effects of hydrate saturation highlights the importance of its accurate quantification.

When geomechanical properties of hydrate-bearing sediment are concerned, Ebinuma et al. [2005], Hyodo et al. [2007, 2009, 2011], Kuniyuki et al. [2010], Masui et al. [2005a, 2008a, 2008b] and Miyazaki et al. [2008, 2010, 2011] display hydrate saturation dependency of stress-strain behavior including strength properties such as maximum deviator stress (or peak strength), Young's modulus at 50% of the stress at failure, cohesion, and dilation angle in drained triaxial compression tests. Ghiassian and Grozic [2011] and Winters et al. [2002, 2007] illustrate the hydrate saturation dependency of stress-strain behavior and the excess pore pressure development compared to hydrate free soil under undrained triaxial compression conditions. Yun et al. [2007] illustrates the hydrate saturation dependency of stiffness and strength for Tetrahydrofuran (THF) hydrate under undrained conditions. Strain rate dependency of stress (under uniaxial compression) and creep behavior of hydrate-bearing sediments are investigated by Parameswaran et al. [1989] for frozen specimens of THF hydrate. Cameron and Handa [1990] further the study of Parameswaran et al. [1989] by including the temperature effects on the short and long term strength and deformation behavior. The exact effect of hydrate saturation on the

strength and deformation behavior is detailed by Waite et al. [2009]. The current communication does not wish to duplicate Waite et al. [2009] discussion, but wish to highlight the impact of hydrate saturation on the soil properties to shed light on the importance of its accurate estimation.

Not only strength and deformation properties but also the flow properties of host sediments are altered by the presence of hydrate. According to Kneafsey et al. [2011], Minagawa et al. [2009], and Waite et al. [2009] permeability of hydrated sediments is altered by both the degree of hydrate saturation and the pore scale hydrate distribution. Kumar et al. [2010], and Liang et al. [2011], and Ordonez et al. [2009] are also among the researchers who relate hydrate saturation to host sediment flow properties.

In fact, most physical properties of hydrate sediments, not just geomechanical properties, are affected by the degree of hydrate saturation. These properties include acoustic wave speeds [Chand et al., 2006; Howard et al., 2011; Kleinburg et al., 2003; Priest et al., 2005, 2009; Waite et al., 2008b, 2009; Winters et al., 2004], electrical properties (such as resistivity and dielectric constant) [Kilner and Grozic, 2006; Spangenberg and Kulenkamff, 2006], and thermal properties (such as thermal conductivity) [Waite et al., 2002, 2007, 2009]. Hydrate saturation dependency of some of these properties have lead us to the development of several field and laboratory hydrate detection and quantification techniques. The effectiveness of these techniques greatly depends on pore scale hydrate growth habit and effective medium models of such growth habit used in the interpretation of field or laboratory measurements. Those techniques based on acoustic and electrical properties and other methods of hydrate saturation estimation will later be

discussed in Section 4.3 for effectiveness in comparison to the DGEM method, which is the central of focus for this chapter.

4.2.1 Effective medium models of pore scale hydrate growth habit

As previously described in Chapter 2, a number of different effective medium models for pore scale hydrate growth habits in unconsolidated packing of mineral grains are agreed upon. The Helgerud [2001] classification includes (a) hydrate formation without significant interaction with the frame as a pore filling substance, (b) hydrate formation in the interior of the pores as a part of the load bearing frame, (c) hydrate formation occurring preferentially at grain contacts, acting as cement between particles, and (d) hydrate coating grains more or less uniformly, progressively cementing them as the hydrate volume increases. The hydrate habit models of Winters et al. [2004] treat the hydrate formation at grain contacts or coating the grains within single cementation model.

The choice of effective medium models of hydrate growth habit in the quantification of hydrate saturation is an important decision with regard to certain hydrate saturation quantification methods. Hydrate saturations predicted by both Helgerud [2001] and Winters et al. [2004] are characteristic of speculated hydrate habit model. More recently, Chand et al. [2006] developed a procedure to allow a portion of hydrate saturation to be present as load-bearing cement while the remaining is treated as pore filling inclusions. The predicted hydrate saturations of this approach depend upon the accuracy with which the fraction of cementing hydrate is determined.

4.3 Techniques for determination of the hydrate saturation

The use of acoustic wave speed characteristics, electrical properties including resistivity and dielectric constant, chloride anomalies and associated pore fluid conductivity, imaging methods, pre-formation pore water saturation with the mere assumption of full conversion of water into hydrate, and dissociation gas evolution measurements (DGEM) are among the techniques for quantification of hydrate saturation. However, none of these techniques are without limitations, it is only that some are relatively more effective than the others.

The studies of Priest et al. [2005] and Waite et al. [2008b] and are among the ample evidence found in literature for hydrate saturation dependency of acoustic wave speeds. The acoustic properties, therefore, are used both in the field and laboratory estimation of pore scale hydrate saturation. However, acoustic properties of hydrate-affected sediments are, in fact, largely affected by the pore scale growth habit of hydrate [Howard et al., 2011; Kleinberg et al., 2003; Priest et al., 2009; Waite et al., 2009] as the shear stiffness of the medium is affected by the hydrate growth habit to a varying degree [Waite et al., 2009]. Winters et al. [2004] and Chand et al. [2006] use these phenomena in further analysis of determining growth habit based hydrate saturation (forward model) or hydrate saturation based growth habit (inverse model). Winters et al. [2004] uses P wave measurements to investigate the hydrate growth habit of natural and laboratory synthesized hydrate-bearing specimen at varying hydrate saturations estimated with the use of collection and measurement of dissociation products. The results reflects upon the growth habit dependency of P wave measurements and the need for accurate independent estimate of hydrate saturation in correlating the acoustic wave speeds with hydrate growth habit. On the contrary, Chand et al. [2006] develops an effective medium inversion algorithm for

quantification of hydrate saturation which uses both P and S wave measurements. The degree of grain cementation (which is most certainly governed by many controlling factors including the pre-formation water saturation as discussed previously) is an input parameter to the algorithm. Neither studies provide evidence for capability of acoustic wave speed measurements as a stand-alone technology for hydrate saturation estimation; rather, it requires supporting technology to assess grain scale characteristics. Kleinberg et al. [2003] also agrees that “acoustic properties of hydrate-affected sediments are very sensitive to the growth habit of hydrate”. Howard et al. [2011] also provide evidence for not only hydrate saturation but growth habit dependency of acoustic wave speeds. According to Howard et al. [2011] the pre-formation water saturation determines the growth habit and the low initial water saturations result in acoustic wave velocities attributable to grain coating hydrate habit while, the high initial water saturations generate velocities attributable to hydrates acting as a part of the frame in a load-bearing model. Priest and Best [2005] highlight the need for validating current seismic models against experimental data obtained from laboratory synthesized hydrate-bearing sediment as the early attempts on such validations fail due to several reasons including the incapability of performing proper hydrate saturation quantifications. However, the limitations are not completely derived from growth habit related uncertainties. In fact, for an identified growth form the effective use of acoustics in the hydrate saturation estimation relies on our understanding of the correlation between various sediment properties and stress state with wave speeds (i.e., compression wave velocity v_p and shear wave velocity v_s). “For naturally occurring hydrate-bearing sediments, where the hydrate formation is similar to the excess water method, the v_p / v_s ratio will be dependent on porosity, confining pressure and hydrate saturation and therefore quantification of

hydrate pore saturation from either v_s , v_p , or v_p/v_s ratio would be difficult without a detailed knowledge of sediment properties and stress state” [Priest et al., 2009].

Electrical properties can also be correlated to hydrate saturation and are therefore, used in field and laboratory investigations. The study of Spangenberg and Kulenkampff [2006] experimentally investigates methane hydrate saturation dependency of electrical properties of a glass bead sediment and comments on the difficulties associated with the applicability of the laboratory results in the field hydrate saturation predictions as the accuracy of such predictions depend on a combination of several factors including the cementing or non-cementing grain scale habit of hydrate, grain size distribution, and grain shape distribution. Therefore, it is “advisable to use hydrate content estimations from electrical field measurements with caution as long as the used interpretation methods are not calibrated in the laboratory and verified for their applicability in a natural hydrate-bearing system” (Spangenberg and Kulenkampff, 2006). Further discussion on the limitations of the methods based on electrical resistivity is provided in Waite et al. [2009].

Kilner and Grozic [2006] employ the theory of dielectrics using the time domain reflectometry (TDR) technique and generate a clear correlation between dielectric constant and pore space hydrate saturation. They identify the need to isolate “the effects of individual variables such as: temperature, pressure, salinity, pH, soil type (sands versus clays), grain size, density (porosity and permeability), etc.” in generalizing such correlation for dielectrics and hydrate saturation. No evidence can be found in literature for the use of TDR in field measurements; however, field

application of the method is possible provided that the effect of aforementioned variables on the hydrate saturation measurement is known.

Chloride anomalies seem to generate accurate predictions of hydrate saturation for saline systems when employed in the laboratory under controlled conditions. The inapplicability of this method for systems without access to pore water during formation and for systems with zero salinity remains the disadvantage. Spangenberg et al. [2005] estimates the hydrate saturation with the use of fluid resistivity measurements (or inferred fluid conductivity) combined with fluid conductivity-salt concentration relations to estimate water conversion into hydrate during formation. Other input parameters include hydrate cage occupancy, hydrate density, and specimen pore volume. X-ray diffraction analysis of a portion of the specimen provides an independent estimate of hydrate saturation which is in good agreement with the former estimate.

Modern imaging technology such as x-ray computed tomography (CT) appears to be promising either as stand-alone technology for hydrate saturation estimation at the laboratory or as supporting technology to validate other methods such as those that specifically depend on the pore scale characteristics. Seol et al. [2011] uses x-ray computed tomography observations of hydrated specimens to estimate hydrate saturation and other properties but, with several assumptions. The assumptions are made in relation to hydrate cage occupancy, density of hydrate and gas phases, the host soil skeleton and the degree of relative movement between the particles of the matrix in addition to the assumptions correlating X-ray attenuation and material mass. Density Magnetic Resonance (DMR) measurements are another approach to imaging hydrated sediments. Murray et al. [2006] use DMR measurements for hydrate saturation

estimation in marine sediments and state that accurate estimations are generated conditioned by the use of modern wireline tools of certain specifications to acquire magnetic resonance data.

The DGEM method of hydrate saturation calculation is based on the principle of mass balance and the concept of volume compatibility between two distinct states of a closed system. The method is applicable in the laboratory for determination of hydrate saturation of natural or artificial hydrate-bearing specimens. The method involves obtaining pressure, volume, and temperature (PVT) data for a hydrate-bearing soil specimen within hydrate stability zone, then forcing the specimen to reach elevated temperatures and/or low pressures outside hydrate stability zone resulting in hydrate dissociation, and then repeating PVT measurements allowing determination of phase composition of the system. The accuracy of the predictions relies on the precision with which the PVT data are obtained and the phase composition of system is determined under given state variables.

Despite the modern day technology the use of “a variety of independent estimates of hydrate concentrations, such as resistivity logs, chloride anomalies, and gas evolution measurements (during hydrate dissociation)” combined “with acoustic data” results in “contradictory conclusions regarding the interaction between hydrate and the sediment” [Priest et al., 2005] and is an indication of poorly undertaken hydrate saturation estimates. The discrepancies between hydrate saturations estimated using various techniques are seemingly explained by the uncertainties in the estimated porosities and inaccurate parameter estimates used in corresponding analyses for at least electrical resistivity and P and S wave velocities [Lee and Collett, 2009]. Most methods for hydrate saturation estimation are affected by:

- (1) host sediment characteristics such as porosity, porosity distribution, geological features such as fractures and fracture orientation, intact properties of the soil grains, and stress state;
- (2) pore space consistency (such as existence of free gas) and pore fluid characteristics (such as salinity and presence of other solutes); and
- (3) hydrate growth habit and distribution.

The correlation between the aforementioned and the measured parameter(s) in the hydrate saturation estimation is not clear to the scientific community to the date and/or the determination of the correlation requires employment of secondary measurements/supporting technology.

The challenges may be overcome by employing DGEM in the laboratory as a method of generating reference hydrate saturations in the process of validating saturations generated by other methods it is associated with the following advantages:

- (1) DGEM is based on fundamental physics and chemistry; and
- (2) the estimation depends only on the bulk hydrate filled pore volume fraction.

4.4 Laboratory testing of artificial hydrate-bearing specimens and application of DGEM method for hydrate saturation estimation

The following explains the summary experimental procedure employed at the Geotechnical Gas Hydrate Research Laboratory (GGHRL) at the University of Calgary for synthesis of hydrate-bearing soil specimens and the application of DGEM method for hydrate saturation estimation.

The procedure is also illustrated in Figure 4.1 for hydrate formation in gas rich environment. The complete experimental procedure is presented in Chapter 3.

Step (1)

For laboratory synthesis of artificial methane hydrate-bearing specimens this stage involves preparation of a soil specimen within which hydrates are to be artificially synthesized, assembly of the soil specimen within the testing apparatus, application of P/T conditions under which the hydrates are to be synthesized, and consolidation of the soil specimen.

During this stage measurements are performed to obtain initial specimen dimensions (height and diameter). For the case of laboratory synthesized hydrate specimens, the mass of dry soil occupying the specimen is also obtained. These measurements facilitate the estimation of the volume of void space, V_{vo} of the specimen. Any volume change of the specimen during consolidation is recorded and V_{vo} is corrected accordingly.

Step (2)

For laboratory synthesis of artificial methane hydrate-bearing specimens the second step involves hydrate formation within the soil specimen. Formation in water rich environment generally involves continuous feed of methane dissolved water into the specimen. Formation in gas-rich environment generally involves continuous feed of methane-the hydrate former into the partially water saturated specimen. It should be noted that there are other methods of hydrate synthesis at the laboratory which are associated with slightly different procedures. However, the

completion of hydrate formation, if attempted in a water rich environment, will result in two distinct phases; hydrate and gas dissolved water (equation (4.1)). As opposed to aforementioned, hydrate formation, if attempted in a gas rich environment, upon completion will result in two distinct phases; hydrate and vapour (equation (4.2)). In either case, incomplete formation will result in all three phases; hydrate, gas dissolved water, and vapour (equation (4.3), Figure 4.2) to be present in the system while the system is assumed to be at a given temperature and pressure within the hydrate stability zone where the actual temperature at a minute locality within the hydrate forming media can be approximated to the enforced temperature without significant loss of accuracy. The P/T conditions of the system at the end of hydrate formation stage are herein after referred to as *pre-dissociation temperature* and *pre-dissociation pressure*. The equation (4.1) assumes that the soil specimen is at hydrate-aqueous liquid (H-Lw) two phase equilibrium while the equation (4.2) assumes that the soil specimen is at hydrate-vapour (H-V) two phase equilibrium. The measured values of pre-dissociation temperature and pressure are used to determine the methane concentration of different phases (i.e., M_H , M_{w_o} , and M_{G_o}) as detailed in Section 4.4.3. The series of tests for which the results are presented in this thesis involved hydrate formation in gas-rich environment arriving at H-V two phase equilibrium under the pre-dissociation conditions.

Step (3)

During this stage the hydrated soil specimen was subjected to triaxial compression test at constant mass. Other destructive tests and/or non-destructive tests (e.g., acoustic, thermal, or flow property measurements, computer tomography or electron scanning to generate hydrate

distribution profiles) may also be performed. During such a testing procedure the soil specimen may or may not be allowed to undergo deformation and/or volume change.

Step (4)

At the end of testing mentioned in Step (3), hydrates are allowed to dissociate, and the dissociation products are collected at a separate gas/water collector cell. The dissociation may have been induced either by increasing the system temperature or by depressurization or by a combination of both. Dissociation of hydrates will result in two distinct phases to be present within the system; gas dissolved water, and vapour (Figure 4.2). Complete collection of any gas trapped within the host sediment at the gas/water collector is ensured by flooding the soils specimen with water. The system including the host soil specimen, gas/water collector, and the connection tubing in-between are all then allowed to reach aqueous liquid-hydrate (Lw-H) two phase equilibrium under P/T conditions outside hydrate stability zone. These P/T conditions of the system are referred to as *post-dissociation* conditions hereinafter and are usually represented by the ambient room temperature and moderate to low pressures. The measured values of post-dissociation temperature and pressure are used to determine the methane concentration of different phases (i.e., M_{wf} and M_{Gf}) as detailed in Section 4.4.3. Other laboratory measurements associated with this stage are used to determine the volumetric parameters including $V_{Gf(GWC)}$, V_{ext} , V_{WTotal} , and $V_{Gi(GWC)}$ and the details are presented in Section 4.4.2.

The principle of mass balance when applied between the pre and post-dissociation conditions of the system appear in following forms for (1) complete formation in water rich environment, (2)

complete formation in gas rich environment, and (3) incomplete formation in either water or gas rich environments.

$$M_H V_H + M_{W_o} V_{W_o} = M_{W_f} V_{W_f} + M_{G_f} V_{G_f} \quad (4.1)$$

$$M_H V_H + M_{G_o} V_{G_o} = M_{W_f} V_{W_f} + M_{G_f} V_{G_f} \quad (4.2)$$

$$M_H V_H + M_{W_o} V_{W_o} + M_{G_o} V_{G_o} = M_{W_f} V_{W_f} + M_{G_f} V_{G_f} \quad (4.3)$$

The mass balance equations, when coupled with volume compatibility equations derived from the Figure 4.1 results in the following relationships for the hydrate saturation respectively.

$$V_H = \frac{V_{G_f} M_{G_f} - V_{W_o} M_{W_o} + V_{W_f} M_{W_f}}{(M_H - M_{W_o})} \quad (4.4)$$

$$V_H = \frac{V_{G_f} M_{G_f} - V_{W_o} M_{G_o} + V_{W_f} M_{W_f}}{(M_H - M_{G_o})} \quad (4.5)$$

$$V_H = \frac{V_{G_f} M_{G_f} - V_{W_o} M_{G_o} + V_{W_f} M_{W_f} - V_{W_{Tot}} (M_{W_o} - M_{G_o})}{(M_H - M_{G_o}) - \frac{V_l}{V_e} (M_{W_o} - M_{G_o})} \quad (4.6)$$

The following sub-sections discuss measurements and estimates that are required to be performed in the hydrate saturation estimation in order to obtain the volume and concentration (or density) components that appear in equations (4.4)-(4.6). It should be noted that methane-water binary system has been considered hereinafter for the presentation of DGEM for hydrate saturation estimation. The intension is to provide the reader with an understanding of the system at pre and post-dissociation conditions, and with a guide to sources of information available in

literature allowing proper calculations of the properties of each phase of the system. The challenges associated with each measurement or parameter estimation are also discussed.

4.4.1 Measured parameters

The measured parameters include the direct measurements of P/T state variables for system at pre and post dissociation conditions and are used in conjunction with estimates of methane density in the hydrate saturation calculation. These parameters include the following:

- (1) Pre-dissociation temperature
- (2) Pre-dissociation pressure (gauge)
- (3) Post-dissociation temperature: if the system is allowed to reach thermodynamic equilibrium with the room conditions the post-dissociation temperature is the same as ambient room temperature. However, ensuring the system reaches thermodynamic equilibrium with the environment or within the two-phase aqueous liquid-vapour (Lw-V) system itself is a matter of extreme practical difficulty. This issue is later discussed in more detail with relevance to estimation of total aqueous phase volume of the system V_{wf} at post dissociation conditions.
- (4) Post-dissociation pressure (gauge)
- (5) Ambient room temperature
- (6) Ambient pressure: The ambient pressure is used coupled with gauge pressure measurements in arriving at system state variables under pre and post dissociation conditions and can be obtained using an absolute pressure transducer. Alternatively, local weather reports may be used to obtain this parameter. Ambient pressure is mentioned as

one of the top two contributors to error in hydrate saturation calculation by Lee and Collett [2009] with respect to their gas evolution measurements of pressure cores.

4.4.2 Estimates of volumetric parameters

The volumetric parameters are derived from multiple laboratory measurements performed during a typical test and are used as inputs with equations (4.4), (4.5), and (4.6) in the hydrate saturation estimation. These parameters include the following:

- (1) Volume of voids V_{Vo} within the hydrated host sediment under pre-dissociation conditions immediately prior to testing such as those mentioned in Step (3) of Section 4.4: This is usually estimated with specimen dimensions (height and diameter), grain density of soil, and mass of dry soil occupying the specimen. The V_{Vo} for a laboratory synthesized hydrate specimen is corrected for any specimen volume changes occurring due to consolidation etc. between the time of measurement of specimen dimensions and reaching the pre-test conditions within the hydrate stability zone.
- (2) Total gas phase volume $V_{Gf(GWC)}$ of the system at completion of the collection of gas/water products from hydrate dissociation: This is usually estimated with height and diameter of a gas column of a gas/water collection assembly.
- (3) Total volume of hydrate forming gas filled elements external to the immediate boundaries of the specimen V_{ext} for which the material mass present within is forced into the

gas/water collector during collection of dissociation products: The method of estimating such volume component needs to be given proper attention during planning of experimental procedure. For the tests carried out at the GGHRL at University of Calgary the gas volume associated with material external to the specimen boundaries arise only from the quantity of gas present within the specimen end caps and connection tubing between the specimen top cap and the gas/water collector. This quantity is carefully determined from mass of water occupying the corresponding volume at full water saturation, density of water, ambient temperature, and pressure.

- (4) Total aqueous phase volume V_{wf} of the system under post-dissociation conditions (which includes the soil specimen, gas/water collector, and the connection tubing in between) at completion of collection of gas/water products from hydrate dissociation: Theoretically, V_{wf} is the initial volume of water present within the system corrected for P/T differences between the initial and post-dissociation conditions plus the total inflow minus the total outflow. The above quantity is given by the net summation of the following components:
- (1) the volume of water available at pre-dissociation conditions immediately prior to testing corrected for P/T differences between the pre and post-dissociation conditions
 - (2) volume of water generated from hydrate dissociation calculated at post-dissociation P/T conditions
 - (3) volume inflow in to the specimen (if any) during the collection of dissociation products at the gas/water collector
 - (4) volume of water initially present within connection tubing (if any) between the specimen and the gas/water collector corrected for P/T differences between initial and post-dissociation conditions
 - (5) volume

of water initially present within the gas/water collector corrected for P/T differences between initial and post-dissociation conditions (6) volume of water displaced from gas/water collector (if any) during collection of dissociation products. The component (6) is valid only in the case of a water displacement column type collector with the assumption that displaced water would not carry away significant quantity of hydrate forming gas (methane) in dissolved form. The fact that methane dissolves in water at very slow rates at neat ambient conditions especially when no significant agitation of the aqueous liquid body is present may even lead to difficulties in justifying the efforts needed to estimate V_{wf} under practical circumstances. Further, such a system cannot be expected to reach thermodynamic Lw-V equilibrium within a reasonable time span for any efforts of quantification to be justifiable. Therefore, V_{wf} may be abandoned from the hydrate saturation calculation.

(5) Initial volume of water V_{wTot} available for hydrate formation: This quantity is ideologically estimated at pre-dissociation or hydrate forming P/T conditions before substantial or preferably any mixing of water and hydrate forming gas takes place. For laboratory synthesized hydrate this quantity can be estimated from initial soil moisture content or from water saturated specimen pore volume minus displaced pore water volume associated with gas introduction (corrected for P/T differences between initial and pre-dissociation conditions). Estimation of this quantity is needed only when the complete formation of hydrate cannot be guaranteed under pre-dissociation conditions immediately prior to testing. Determining this quantity for natural hydrate-bearing

specimens of core samples could be extremely challenging, instead, it would be more practical to determine the specimen consistency at pre-dissociation conditions immediately prior to testing. Lee and Collett [2009] address the issues with determining the specimen consistency. Seemingly, Lee and Collett [2009] assume that the specimen pore space is completely occupied by hydrate and free water neglecting the possible presence of free gas within the specimen.

- (6) Initial gas phase volume $V_{Gi(GWC)}$ at the gas/water collector: Absence or presence of such volume component depends on the design of the gas/water collector: (1) if the gas/water collector is designed in the form of a water displacement column with no initial air/gas within, no such volume component exists; (2) if the gas/water collector is designed in the form of a pressure vessel with no flow out during collection of dissociation products, an initial gas volume of $V_{Gi(GWC)}$ may present within the collector. In the latter case the initial gas volume component may be determined with the use of height and diameter of the gas column. The hydrate saturation calculation presented herein considers no existence of initial gas volume within the collector.

4.4.3 Estimates of methane density and volume of hydrate bond water

Estimates of methane density and volume of hydrate bond water are required as inputs with the use of equations (4.4), (4.5), or (4.6) in the hydrate saturation estimation. The following outlines the methods for estimating five different methane density values at various P/T conditions in and out the hydrate stability zone of methane-water binary system. Various thermodynamic and empirical models are assumed for the methane-water binary system in the estimation of these

parameters. In addition to the density parameters, the molar volumes of water in the aqueous liquid (V_l) and hydrate (V_e) phases are estimated. The range of applicability and limitations of the models used in the calculation process are presented in Table 4.3. The recommended options for methane density calculations are provided. The choices made as to the use of these different models in the estimation of hydrate saturation for the tests conducted at GGHRL of University of Calgary and presented in this thesis are also denoted.

(1) The molar volume of water V_l is determined either at post-dissociation T and P or at pre-dissociation T and P with the use of water density obtained from Lide [2007] and molar mass of water. This quantity is used in the hydrate saturation calculation to estimate the volume of water generated as a dissociation product or consumed during hydrate formation V_{WH} which is estimated with the following relationship.

$$V_{WH} = V_l \frac{V_H}{V_e} \quad (4.7)$$

If the volume of hydrate bond water V_{WH} is used in the hydrate saturation calculation with relevance to the system consistency at post-dissociation conditions, the post-dissociation T and P are applicable to V_l . Otherwise, pre-dissociation T and P should be used.

(2) Molar volume of water in the hydrate lattice V_e

The molar volume of water in the hydrate phase is used as a secondary input in the estimation of methane density in the hydrate phase. The volume of hydrate lattice per mole of water at pre-

dissociation T and P (or the molar volume of water in the hydrate phase) V_e is determined considering the hydrate lattice geometry. The fitted model of Hester et al. [2007] expresses the lattice parameter $[a]$ as a function of temperature:

$$\frac{[a] - a_o}{a_o} = \exp \left(\begin{array}{l} a_1[T - T_o] \\ + \frac{a_2}{2}[T - T_o]^2 \\ + \frac{a_3}{3}[T - T_o]^3 \end{array} \right) - 1 \quad (4.8)$$

where, a_o is the lattice parameter at a reference temperature T_o .

At a reference temperature of 298.15 K, it is shown that all hydrates of a given structure can be fitted using the above expression. For structure I hydrates, the model constants, $a_1 = 1.1280E - 04$, $a_2 / 2 = 1.8003E - 07$, and $a_3 / 3 = -1.5898E - 11$. The only guest dependent parameter a_o (Å) at 298.15 K could be extrapolated with adequate accuracy using the relationship developed by Ogienko *et al.* [2006] for the temperature range of 86-267 K for cubic structure I methane hydrate.

$$a_o = \left(\begin{array}{l} 11.835(11) - 1.12(116) \times 10^{-4} T_o \\ + 2.47(56) \times 10^{-6} T_o^2 \end{array} \right) \quad (4.9)$$

The molar volume of water in the hydrate phase V_e is then determined as follows for a structure I unit cell of 46 water molecules.

$$V_e = \frac{[a]^3 \times (6.02214179 \times 10^{23} \text{ mol}^{-1})}{46} \quad (4.10)$$

The model developed by Hester et al. [2007] fits significantly well with the experimental data of Shpakov et al. [1998] and those of Ogienko et al. [2006]. Shpakov et al. [1998] also presents a prediction model for V_e , however, the predictions appear to deviate from their experimental results as the temperature increases. Alternatively, Sun and Duan [2007] presents an equation (equation (4.11)) for the determination of V_e as a function of T and P although, the origin and the particulars of derivation of the expression are not clear.

$$V_e(T, P) = [1.820 + 2.217 \times 10^{-5} T + 2.242 \times 10^{-6} T^2] \frac{10^{-30} N_A}{N_W} \times \exp[-3.5 \times 10^{-4} (P - 0.1) + 7.07 \times 10^{-6} (P - 0.1)^{1.5}] \quad (4.11)$$

(3) The hydrate number n_k and methane concentration in the hydrate phase M_H

The maximum amount of methane that can occur in methane hydrate is fixed by the clathrate geometry. Most commonly, methane forms hydrates of molecular structure called Structure I. The cubic unit cell of structure I hydrate consists of 46 water molecules forming 2 small cavities and 6 large cavities. When all cavities are occupied by methane the composition is $CH_4 \cdot 5.75H_2O$ where 5.75 is referred to as the hydrate number, n_k . However, gas clathrate hydrates are known to be non-stoichiometric compounds and are stable at range of values of hydrate numbers [Huo

et al., 2003]. In fact different cage occupancies are obtained at different formation temperatures and pressures [Jager, 2001; Sloan, 1998; Sum et al., [1997]; Sun and Duan, 2007] and at different overall methane compositions [Huo et al., 2003; Sloan, 2003a]. According to the predictions of Sun and Duan [2007], “the occupancy fraction of methane both in small cage and large cage increases with increasing temperature and pressure” at H-Lw equilibrium. Table 4.1 summarises hydrate numbers generated by a number of independent experimental studies by Galloway et al. [1970], Handa [1986], Handa and Stupin [1992], Sum et al. [1997], Uchida et al. [1999], Seo et al., [2002], and Circone et al. [2005]. Fair amount of variability can be identified as associated with the experimentally derived values of n_k and correlating hydrate number with formation conditions does not appear to be possible with the limited experimental data.

Alternatively, the model of Sun and Duan [2007] allows computing the hydrate cage occupancy at given P/T conditions over the H-Lw region. The CSMGem calculator of Colorado School of Mines [originally developed by Ballard, 2002] also proves to be a useful tool in generating small and large cage occupancies under H-V, hydrate-aqueous liquid-vapour (H-Lw-V), and H-Lw equilibrium conditions for a given system at known P/T allowing subsequent calculation of n_k . However, commenting on the relative accuracy of the predictions of Sun and Duan [2007] and CSMGem are beyond the scope of this research. The hydrate number n_k is used in the hydrate saturation calculation to determine the Methane concentration in the hydrate phase under pre-dissociation conditions.

The moles of methane in the hydrate phase under pre-dissociation conditions are determined using the following relationship with the approximated or estimated n_k as an input variable.

$$M_H = \left(\frac{1}{n_k} \right) \left(\frac{1}{V_e} \right) \quad (4.12)$$

(4) Vapour phase methane concentration under H-V equilibrium M_{Go}

Determination of vapour phase methane concentration within the H-V region of CH_4-H_2O system requires computation of vapour phase composition (i.e., mole fraction of methane) and the molar volume of the vapour at a given P/T condition. The equilibrium vapour phase composition can be derived from the moisture content measurements in methane in the presence of hydrate performed by Chapoy et al. [2005, 2010], Folas et al. [2007], Lokken et al. [2008], Kosyakov et al. [1979], Oellrich and Althause [2000], Youssef et al. [2009], Aoyagi et al. [1980], Aoyagi et al. [1979], and Sloan et al. [1976], Song et al. [2004], and Zhang et al. [2011]. The moisture content data range over P/T regions of 240-280 K and 3.4-10.4 MPa. Moisture content data is usually presented in literature in terms of ppm (parts per million or more specifically the number of moles of methane present per million moles of the methane-water mixture) [Chapoy et al., 2010; Youssef et al., 2009] or in terms of lbm/MMCF (pound mass per million cubic feet) at a reference pressure and a temperature (which are usually 14.7 psia and 60°F). Using the above in the calculation of methane concentration per unit volume of vapour phase requires the use of an appropriate Equation of State (EoS) capable of generating the molar volume of vapour phase at the corresponding pre-dissociation T/P conditions at which the test is conducted and at the reference T/P conditions (60°F and 14.7 psia). Many of the equations of state for methane-water system are applicable over the Lw-V region but not in the presence of hydrate. Duan et al. [1992a] provides a hint of the difficulties associated with accommodating the complex volumetric and phase behaviour in the presence of hydrates in to the formulation of

an EoS. Therefore, the methane concentration in vapour phase needs to be calculated by approximating an existing pure component EoS. As such we recommend the use of the pure component EoS for methane developed by Duan et al. [1992b] in the determination of M_{Go} . Alternatively, the CSMGem calculator can also be used to determine M_{Go} . The vapour phase methane concentration is thus calculated by approximating $MV_{V(CH_4+H_2O)@(H-V)}$ with pure component (methane) molar volume under hydrate forming conditions (equation 4.13).

$$M_{Go} = \frac{y_{CH_4}}{MV_{V(CH_4+H_2O)@(H-V)}} \quad (4.13)$$

(5) Aqueous phase methane concentration under H-Lw equilibrium M_{wo}

Methane solubility in water in equilibrium with its hydrate has been researched by many [Davie et al., 2004; Hashemi et al., 2006; Lu et al., 2008; Servio and Englezos, 2002; Sun and Duan, 2007; Zatsepina and Buffett, 1997]. In the absence of hydrate methane solubility increases with decreasing temperature and increasing pressure, however, in the presence of hydrate the solubility decreases with decreasing temperature and increasing pressure [Lu et al., 2008; Servio and Englezos, 2002; Zatsepina and Buffett, 1997]. The peak in the hydrate solubility corresponds to the three phase H-Lw-V equilibrium temperature at a given pressure [Zatsepina and Buffett, 1997]. The pressure dependency of the solubility profile could be considered insignificant in the presence of hydrates [Davie et al., 2004]. However, according to Lu et al. [2008] the pressure effect on solubility in the presence of hydrate is small at low temperatures than at high temperatures, also, the relative change in solubility over the same magnitude of pressure change increases with pressure. The model developed by Zatsepina and Buffette [1997] investigates the

effects of temperature, pressure, and salinity on methane solubility. However, “the model of Zatsepina and Buffette [1997, 1998] underestimated CH_4 solubility in water and underestimated the salting-out effect of electrolyte on CH_4 solubility both at vapour-aqueous liquid (V-Lw) equilibrium and at H-Lw equilibrium” [Sun and Duan, 2007]. Davie et al. [2004] fits theoretical calculations of Zatsepina and Buffette [1997] with a simple equation. Hashemi et al. [2006] presents an improved model to predict solubilities in pure water at H-Lw and H-Lw-V equilibrium. The results closely match the experimentally derived values of Servio and Englezos [2002]. The effects of capillarity and salinity are also taken into account in the predictions of the model Sun and Duan [2007]. The model requires temperature, pressure, salinity, and pore radius as the inputs. It is noteworthy that the pore radius effects are negligible for coarse grained sediments and the aforementioned fact is visible in the model predictions for radii greater than 300 nm. The model results over the H-Lw region and along the H-Lw-V boundary have been verified against experimental data of Servio and Englezos [2002], Kim et al. [2003], and Seo et al. [2002] for solubility in pure water. Lu et al. [2008] using Raman spectroscopy measures methane concentrations in pure water in equilibrium with structure I hydrate. A relationship for mole fraction x_{CH_4} of methane in water is derived as a function of temperature (T in K) and pressure (P in MPa).

$$x_{CH_4} = \exp\left(\frac{11.0464 + 0.023267P}{-(4886.0 + 8.0158P)/T}\right) \quad (4.14)$$

The predictions obtained using equation (4.14) is in good agreement with the measured values given by Servio and Englezos [2002] and values predicted by Sun and Duan [2007].

Determination of aqueous phase methane concentration requires the knowledge of aqueous phase molar volume at the given P/T in addition to methane solubility (i. e. mole fraction). The CSMGem calculator proves to be a useful tool as it is capable of generating both the methane mole fraction and the molar volume of aqueous phase and thus M_{wo} can be calculated as follows.

$$M_{wo} = \frac{x_{CH_4}}{MV_{Lw(CH_4+H_2O)}@(H-Lw)} \quad (4.15)$$

The aqueous phase methane concentration under H-Lw equilibrium is not included in the subsequent sensitivity analysis as the sensitivity analysis is carried out for hydrates formed within gas rich environment.

(6) Aqueous phase methane concentration under Lw-V equilibrium M_{wf}

Both experimental studies and mathematical derivations for methane solubility in water in the absence of hydrate phase could be cited in literature [Ben-Naim and Yaacobi, 1974; Claussen and Polglase, 1952; Duan and Mao, 2006; Duan et al., 1992c; Hashemi et al., 2006; O’Sullivan and Smith, 1970; Price, 1979; Sultanov et al., 1972; Sun and Duan, 2007; Wiesenburg and Guinasso, 1979; Yamamoto et al., 1976]. Hashemi et al. [2006] predicts solubilities in pure water at Lw-V equilibrium in addition to that at H-Lw and H-Lw-V equilibrium. The predictions are verified against experimental values presented by Servio and Englezos [2002]. The model developed by Duan et al. [1992c] predicts methane solubility for a system at a given temperature/pressure/salinity condition and the results are verified against experimental results of Claussen and Polglase [1952], O’Sullivan and Smith [1970], Sultanov et al. [1972], Ben-Naim

and Yaacobi [1974], Yamamoto et al. [1976], Price [1979], Wiesenburg and Guinasso [1979]. However, introducing a more recent model with better accuracy Duan and Mao [2006] affirm that “all of the published models, including the Duan model [1992c], are found to possess intolerable deficiencies”. Duan and Mao [2006] model is capable of predicting the liquid phase density (g/cc) in addition to methane solubility in terms of molality allowing the calculation of the number of moles of methane present per unit volume of liquid. The model presented by Sun and Duan [2007] could also be used to generate more accurate predictions provided that the temperature, pressure, salinity, and pore radius are known. The predictions over the Lw-V region have been verified for solubility in pure water against data of Servio and Englezos [2002], Kim et al. [2003], and Seo et al. [2002]. The model of Chapoy et al. [2004] can also be used to generate accurate aqueous phase methane mole fractions over the temperature range of 275-313 K and pressures up to 18 MPa. Alternatively, the CSMGem calculator is also capable of generating both the methane mole fraction and the molar volume of aqueous phase. M_{wf} can thus be determined as follows with a suitable choice of aforementioned mathematical models.

$$M_{wf} = \frac{x_{CH_4}}{MV_{Lw(CH_4+H_2O)}@(Lw-V)} \quad (4.16)$$

The sensitivity of the hydrate saturation to the aqueous phase methane concentration under Lw-V equilibrium at post-dissociation P/T conditions was omitted from the sensitivity analysis in accordance with the arguments presented on the determination of the corresponding aqueous phase volume V_{wf} .

(7) Vapour phase methane concentration under Lw-V equilibrium, M_{Gf}

Determination of vapour phase methane concentration under Lw-V equilibrium requires determination of both (1) vapour phase mole fraction of methane, y_{CH_4} and (2) molar volume of vapour in equilibrium with the aqueous phase, $MV_{V(CH_4+H_2O)@(Lw-V)}$. The mole fraction of methane in vapour can be determined by using the model developed by Duan and Mao [2006]. The method requires inputs from Shibue [2003] and Wagner and Pruss [1993]. Alternatively, the semi-empirical method of Mohammadi et al. [2004] can also be used to determine the mole fraction of methane in vapour. The aqueous phase methane concentration which is required as an input in the above calculation procedures are considered negligible. Greater accuracy can be obtained by using the model of Chapoy et al. [2004] to determine aqueous phase methane mole fractions over the temperature range of 275-313 K and pressures up to 18 MPa. According to Duan and Mao [2006] the model results of Chapoy et al. [2004] closely represents experimental measurements over the aforementioned P/T range. The molar volume of vapour in equilibrium with the aqueous phase can be determined using the model presented by Sun et al. [2003], and the CSMGem calculator. Both the model of Sun et al. [2003] and CSMGem could be used to predict the vapour phase composition for the $CH_4 - H_2O$ system too. The CSMGem calculator generates the phase composition and molar volume at given P/T conditions for methane and water in Lw-V equilibrium at corresponding feed compositions. If the mole fraction of methane and the molar volume of the vapour are known the vapour phase methane concentration can be computed as follows.

$$M_{Gf} = \frac{y_{CH_4}}{MV_{V(CH_4+H_2O)}@(Lw-V)} \quad (4.17)$$

The Table 4.2 illustrates the use of the estimates of volumetric properties and methane density in the hydrate saturation calculation at measured P/T conditions immediately prior to testing (within hydrate stability zone) or at final system equilibrium (outside hydrate stability zone) for three different scenarios; (a) complete hydrate formation is achieved in a water rich environment allowing no free gas to be present immediately prior to testing (b) complete hydrate formation is achieved in a gas rich environment allowing no free water to be present immediately prior to testing (c) incomplete hydrate formation in either water or gas rich environment leaving all three H-Lw-V phases in the system.

4.5 A sensitivity analysis for DGEM

A sense of accuracy for a given measurement or method of estimation involving several measurements and assumptions can only be developed through a proper sensitivity analysis. The sensitivity of the DGEM estimated hydrate saturation were investigated against the measurements during a typical test, estimates of volumetric properties, and assumptions associated with the DGEM method. For the purpose of performing the sensitivity analysis, measurements for a typical test conducted at the GGHR at the University of Calgary was combined with the hydrate saturation estimation detailed as per section (b) of Table 4.2 for formation of hydrates in gas-rich environment.

4.5.1 Sensitivity of hydrate saturation to direct temperature measurements, absolute pre and post-dissociation pressures and estimates of volumetric parameters

The Table 4.4 illustrates the sensitivity of the hydrate saturation to number of test parameters. It should be noted that most of the test parameters are “secondary” as they are derived from multiple “primary” laboratory measurements. Preferably, the sensitivity of hydrate saturation is evaluated against the secondary parameters but not against the primary measured parameters.

The objective is to allow the use of more than one method in deriving the secondary parameters at the laboratory. As such the sensitivities presented herein would be more meaningful and useful to the reader.

The sensitivities presented in Table 4.4 are based on functional tables developed by calculating the hydrate saturation at different values of a test parameter within the mentioned range of validity. The functional tables were converted into graphical form and empirical equations were developed by fitting linear trend-lines. Therefore, it should be noted that although we have retained nine-digit accuracy for the sensitivity derived from the constants of an empirical equation, the equation itself is by no means this accurate. The accuracy of the sensitivity calculation is therefore, limited by the uncertainty in the estimation of hydrate saturation which is attributed to the uncertainties of various mathematical models used and the assumptions made during the process of estimation. However, this does not underestimate the usefulness of sensitivity values presented in Table 4.4 (given a calculation procedure) as it is very important in any experiment to know the “uncertainty” or the “estimated amount by which the observed or calculated value of a quantity may differ from the true value” [Zebrowski, 1979] due to errors in measurement. Errors in measurement could either be systematic (occurring due to errors in

calibration or inappropriate use of a measuring instrument) or random (occurring due to uncontrolled variables such as minor fluctuations in environmental conditions or due to specimen variations).

Provided that appropriate measuring instruments under existing environmental conditions are used during the test, the total uncertainty in the measurement (test parameter) can be calculated considering the “accuracy” and the “precision” of the instruments. The ‘accuracy’ of an instrument is related to the instrument calibration and the physical standards against which the instrument is calibrated and is defined as “a certification of how closely” an instrument “be expected to agree with its calibration standard” [Zebrowski, 1979]. “The precision of an instrument is the index of its discriminating ability. It is usually stated as the instrument’s smallest scale division” [Zebrowski, 1979]. It should also be noted that certain test parameters depend on more than one measured quantity (e.g. Initial volume of soil voids). In such situations, the error analysis should consist of error propagation calculations as well. Once the total uncertainty of the measurement is calculated, the sensitivity values presented can be used to calculate the corresponding uncertainty that should be expected in the estimated hydrate saturation. The performed sensitivity analysis provided valuable input in to re-evaluating the accuracy of the experimental measurement at the GGHR of University of Calgary. With the renewed accuracy of our measurements, our hydrate saturation estimates carry only about $\pm 2\%$ error.

4.5.2 Sensitivity to estimates of methane density

Based on our previous presentation of available resources for methane density estimations, the following models were chosen to generate methane density estimates for hydrates formed in gas-rich environment: EoS of Duan et al. [1992b], CSMGem Calculator of Colorado School of Mines, Duan and Mao [2006] model, and the Ideal Gas Law. The Ideal Gas Law is used here only as a method associated with minimal computational effort. The hydrate saturations obtained with the use of Ideal Gas Law can then be compared with those obtained by employing the other models to generate a feel for the value of extra effort associated with those other models.

4.5.2.1 Methane density of the hydrate phase - Hydrate number n_k

The sensitivity of the hydrate saturation to the hydrate number was investigated by computing the hydrate saturation for a typical test over a range of hydrate numbers from 5.75 to 6.00 at formation conditions given by a temperature of 278.15 K and pressure of 9101.325 kPa. The resulting functional table was then used to develop an empirical correlation by fitting a linear trend-line. A sensitivity of 0.01234504 change in hydrate saturation per percentage change in hydrate number was derived. The range of hydrate numbers over which the sensitivity was evaluated extend beyond the range of experimentally determined hydrate numbers at the stated P/T conditions. However, with very little amount of experimental data and our modest understanding of the factors governing the hydrate cage occupancy uncertainties still exist as to the adequacy of the range of hydrate numbers selected for the analysis. However, compared to the sensitivities of hydrate saturation to other parameters subjected to investigation, the derived sensitivity to hydrate number appears less significant.

4.5.2.2 Methane density of vapour phase under the H-V equilibrium at pre-dissociation conditions M_{Go}

The application of DGEM in hydrate saturation estimation for hydrates formed in gas-rich environment assumes H-V equilibrium under pre-dissociation conditions. The hydrate saturation at the above assumption of two-phase H-V equilibrium conditions was evaluated by determining hydrate saturation with the use of CSMGem calculator, the EoS developed by Duan et al. [1992b], and the Ideal Gas Law. The use of Duan model and Ideal Gas Law neglects the presence of moisture in vapour. Apparently, CSMGem calculator too seems to be neglecting the presence of moisture and hence the vapour is approximated to a single component pure CH₄ system. If CSMGem is assumed to accommodate the presence of moisture in gas phase, the mere comparison of the hydrate saturation values obtained by CSMGem and Duan et al. [1992b] may suggest that the sensitivity to the assumption of moisture free gas phase appears to have little effect over the hydrate saturation. However, the difference between the CSMGem and Duan et al. [1992b] based predictions cannot be completely attributed to the consideration of presence or absence of moisture in the gas phase, as there could be other differences between the two calculation procedures contributing to the difference in predicted saturations. As such the available resources do not allow us to investigate the effects of possible existence of non-equilibrium conditions within the system or the treatment of water-hydrocarbon interaction. The hydrate saturations obtained are presented in Table 4.5. The calculations were performed at pre-dissociation temperature of 278.15 K and pressure of 9101.325 kPa. It is also interesting to note that the results generated with the use of Ideal Gas Law deviate greatly from the rest and highlights the usefulness of other methods at high pressures and low temperatures as the real gases stray from ideal conditions.

4.5.2.3 Methane density of vapour phase under Lw-V equilibrium at post-dissociation conditions at the gas/water collector M_{Gf}

The application of DGEM assumes Lw-V two phase equilibrium under the post-dissociation conditions. As such we investigate the sensitivity of the hydrate saturation against the assumption of moisture free gas phase in equilibrium with aqueous liquid. If the vapour phase water content in methane is neglected assuming gaseous phase of pure CH₄ within the gas/water collector the molar volume of methane under the post-dissociation conditions can be calculated using the Ideal Gas Law or the EoS of Duan et al. [1992b]. The approaches such as the model developed by Duan and Mao [2006] and CSMGem accommodates the effect due to the presence of moisture in the vapour phase. The CSMGem calculator is calibrated for water-hydrocarbon systems by regressing water-hydrocarbon interaction parameters available in GPA Thermodynamic Database [1996]. The hydrate saturations obtained with the use of aforementioned at post-dissociation temperature of 296.15 K and pressure of 445.325 kPa are presented in Table 4.6. The results show a moderate sensitivity to the treatment of water-hydrocarbon interaction in the gaseous phase. At the test P/T conditions there exists a difference of only 1.62 in percentage hydrate saturation between the two Duan models. Interestingly, the hydrate saturation generated by the Ideal Gas Law appears to be in good agreement with those other methods. Therefore, it is suggested that under conditions of high temperature and low pressure a model such as Ideal Gas Law which is associated with the least computation effort can be employed in the saturation calculation without significant accuracy.

4.5.2.4 Methane density of vapour phase under the Lw-V equilibrium for the material mass present within total volume of hydrate forming gas filled elements external to the immediate boundaries of the specimen $M_{G_{ext}}$

When hydrate dissociation products are collected and post-dissociation gas P/T/V measurements are performed at separate gas/water collector external to the hydrated specimen, a quantity of gas external to the specimen and present within such elements as connection tubing between the specimen and the collector may enter into the collector resulting in an overestimation of the moles of methane generated from hydrate dissociation. Therefore this quantity of gas should be estimated and detached from the hydrate saturation calculation. Under the prevailing conditions at GGHRL of University of Calgary, such connection tubing consists of vapour saturated gaseous methane at formation pressure and room temperature. A similar procedure to previously mentioned (for vapour phase methane density under Lw-V equilibrium at the gas/water collector) was followed to check the sensitivity to the assumption of Lw-V two phase equilibrium in the determination of the quantity of gas within respective external volume under corresponding P/T conditions. The results are shown in Table 4.7 for a typical test at a (room) temperature of 299.15 K and a pressure of 9101.325 kPa. Similar to the previous case of estimating M_{Gf} , the fact that whether or not the gaseous phase is saturated with water does not appear to have no significant impact over the estimated hydrate saturation. However, as opposed to the hydrate saturations obtained for vapour phase under post-dissociation conditions at the gas/water collector, the use of Ideal Gas Law results in significant overestimation of hydrate saturation. This is due to the fact that real gases deviate from ideal conditions at high pressures. The results indicate the necessity for approximating the actual test conditions with appropriate models of adequate accuracy.

4.6 Discussion

The use of DGEM method for estimation of hydrate saturation proves to be a useful methodology as the estimated quantities are independent of intact sediment characteristics, pore space consistency, hydrate growth habit, and hydrate distribution. The calculation is based on the principle of mass balance for methane and volume compatibility of the phases present within the system. However, the task is not less challenging as the accuracy of the estimation greatly depends on (1) the degree of care we exert in performing numerous measurements in the laboratory, (2) selection of measuring devices and apparatus to generate adequate level of accuracy, and (3) how well the hydrated soil system is modelled with physical and chemical equilibrium conditions that are assumed. Therefore, we perform a sensitivity analysis highlighting the need for minimizing measurement errors, and evaluating the consequences of assumed equilibrium conditions not being representative of the true nature of the system. The key findings of the sensitivity analysis on various laboratory measurements can be summarized as follows:

- P/T measurements of the system components contained within the laboratory are critical, particularly when large quantities of methane are present at low density (specifically at high temperatures and low pressures).
- Volume measurements in the system components are critical when the methane density is at its greatest (high pressure and low temperature).

Laboratory experiments should therefore pay attention to the aforementioned in the selection of measuring devices and apparatus in order maintain appropriate levels of accuracy in testing.

Under the assumed equilibrium pre and post dissociation conditions, estimation of methane density in hydrate, aqueous liquid, and vapour phases require the use of various theoretical models. As such we focus on developing a resource information base for hydrate saturation estimates illustrating the current state of knowledge in related hydrate sciences. In this effort we have attempted suggesting the use of those models that are validated against experimental data in many situations as possible. The key findings of the sensitivity analysis for hydrates formed in gas-rich environment at the assumed equilibrium conditions of the system under which methane density of different phases are estimated suggests that neglecting the water content in vapour phase, as done with the use of single component models, does not appear to result in significant change in the estimated hydrate saturations. It, therefore, appears that the consequences of assumed equilibrium conditions not being representative of the true nature of the system to have no significant impact on the estimated hydrate saturations. As a result, the DGEM method for hydrate saturation estimation yields results representative of true hydrate saturation present within a given sediment, provided that adequate care is exerted at the laboratory to minimize measurement errors. Additionally, the analysis presented in Section 4.5.2 extends to investigate when and where it is appropriate to use models such as Ideal Gas Law (which are associated with minimal computational effort) and caution the use of ideal approximation of moist gaseous methane when conditions stray from ideal conditions.

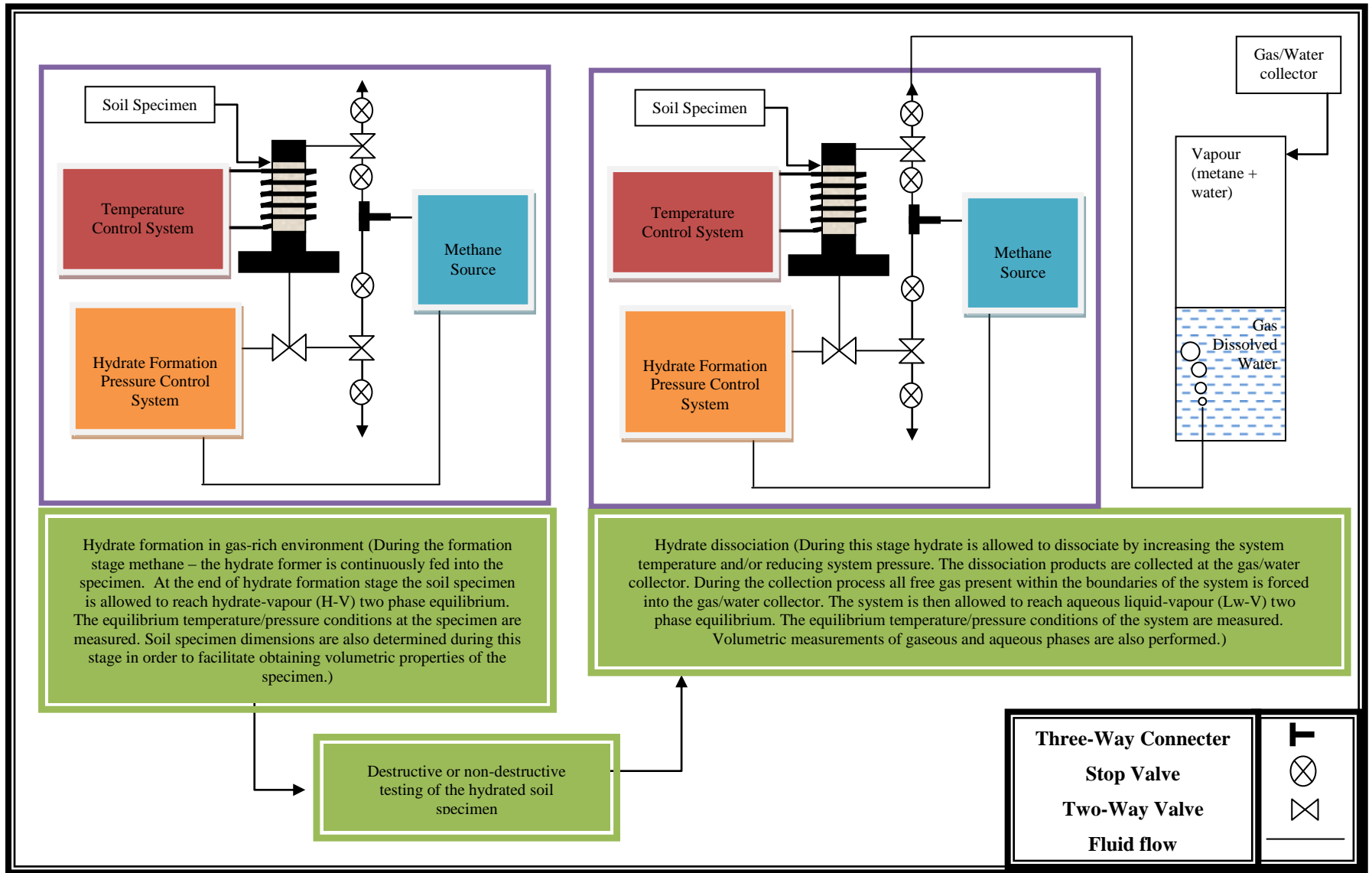


Figure 4.1: Hydrate formation in gas-rich environment, subsequent testing, and measurements to facilitate application of DGEM for hydrate saturation estimation

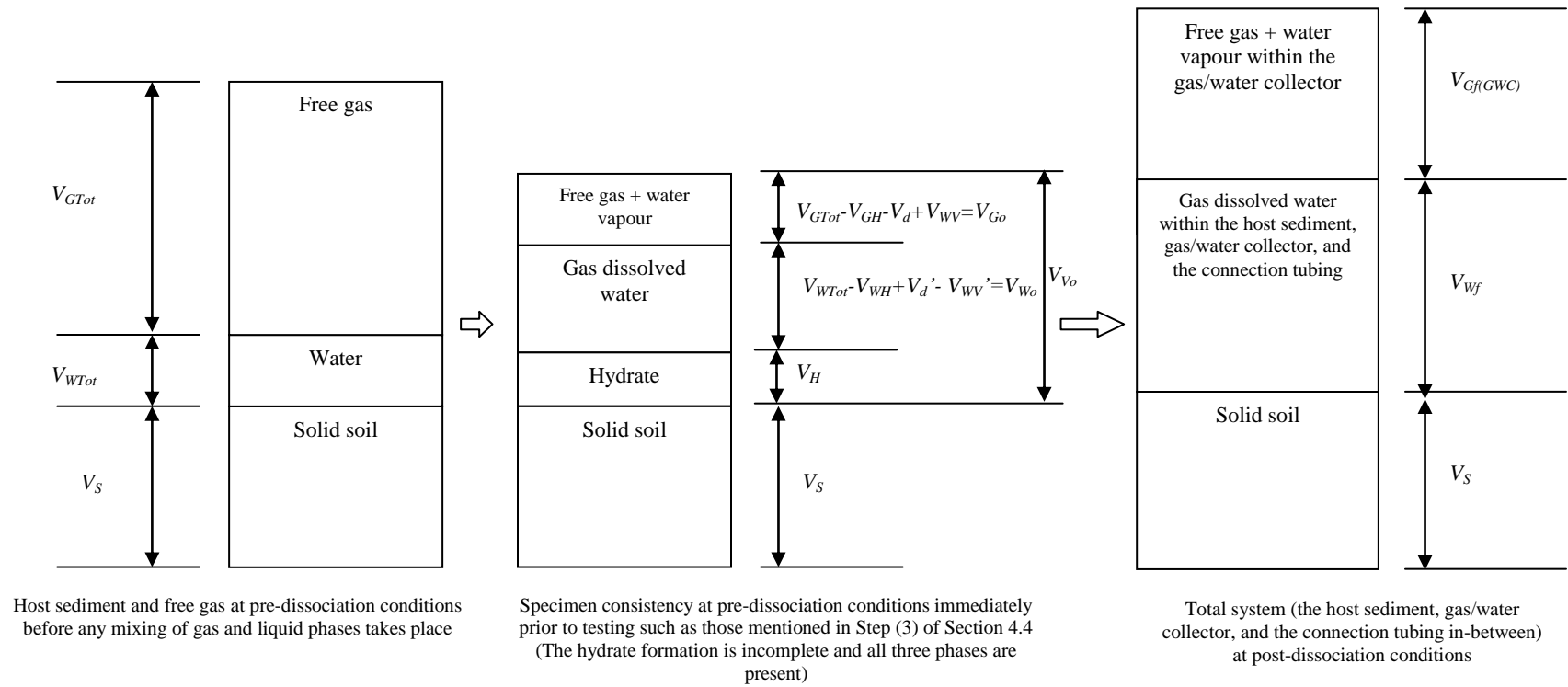


Figure 4.2: System consistency at pre and post-dissociation conditions

Table 4.1: References for experimental determination of hydrate number, n_k

Reference	Temperature /pressure conditions	Hydrate number	Remarks
Handa [1986]	253.0 \pm 0.5 K 3.40 \pm 0.10 Mpa	6.00	Determines hydrate number for bulk hydrate using gas evolution measurements upon dissociation
Handa and Stupin [1992]	263.0-276.2 K 2.64-5.26 Mpa	5.94	Determines hydrate number for hydrate formed within 70Å silica gel-pores
Sum et al. [1997]	273.65-276.65 K at corresponding three phase equilibrium pressure	6.04 \pm 0.03	Determines the hydrate number over a range of temperatures for bulk hydrate at corresponding three phase equilibrium pressure
Uchida et al. [1999]	273.2-278.4 K 3.0-7.0 Mpa	6.2 \pm 0.2	Determines the hydrate number for bulk hydrate over a range of temperatures and pressures
Seo et al. [2002]	274.15 K 10.0 Mpa	6.00	Determines the hydrate number for bulk hydrate at the given temperature and pressure
Circone et al. [2005]	263-285 K 1.9-9.7 Mpa	5.99 \pm 0.07	Determines an average hydrate number along the three phase equilibrium boundary for bulk methane hydrate using gas evolution measurements upon dissociation over a range of temperatures and pressures
Galloway et al. [1970]	283-288.5 K 7.10-13.17 Mpa	5.84-6.34	Determines the hydrate number with \pm 15.6% average maximum relative uncertainty over a range of temperatures and pressures

Table 4.2: Hydrate saturation estimation with the use of simple and complex primary estimates at measured P/T conditions

(a) complete hydrate formation is achieved in a water rich environment allowing no free gas to be present immediately prior to testing such as those mentioned in Step (3) of Section 4.4 (b) complete hydrate formation is achieved in a gas rich environment allowing no free water to be present immediately prior to testing (c) incomplete hydrate formation in either water or gas rich environment leaving all three H-Lw-V phases in the system

Principle of mass balance for methane/hydrate saturation	M_H	M_{W_o}	V_{W_o}	M_{G_o}	V_{G_o}	M_{W_f}	V_{W_f}	$M_{G_f}V_{G_f} = n_{G_f}$	$V_{W_{Tot}}$
<p>(a) At completion of hydrate formation in water rich environment:</p> $M_H V_H + M_{W_o} V_{W_o} = M_{W_f} V_{W_f} + M_{G_f} V_{G_f}$ $V_H = \frac{M_{G_f} V_{G_f} - V_{W_o} M_{W_o} + V_{W_f} M_{W_f}}{(M_H - M_{W_o})}$	$M_H = \frac{1}{n_k V_e}$	Calculated assuming two phase H-Lw equilibrium under pre-dissociation conditions	$V_{W_o} = V_{V_o} - V_H$ (V_{V_o} is experimentally determined)	N/A	$V_{G_o} = 0$	Calculated assuming two phase Lw-V equilibrium under post-dissociation conditions	Experimentally determined	$n_{G_f} = n_{G_f(GWC)} - n_{ext}$ $n_{G_f(GWC)} = V_{G_f(GWC)} / V_{M_f}$ $n_{ext} = V_{ext} M_{W_{ext}}$ $M_{W_{ext}}$ is calculated assuming two phase Lw-V equilibrium at P/T conditions applicable to material mass present within V_{ext} . Gas saturated water within connection tubing is at hydrate forming (or pre-dissociation pressure) and ambient room temperature. V_{ext} is experimentally determined.	N/A

Principle of mass balance for methane/ hydrate saturation	M_H	M_{W_o}	V_{W_o}	M_{G_o}	V_{G_o}	M_{W_f}	V_{W_f}	$M_{G_f}V_{G_f} = n_{G_f}$	$V_{W_{Tot}}$
<p>(b) At completion of hydrate formation in gas rich environment:</p> $M_H V_H + M_{G_o} V_{G_o} = M_{W_f} V_{W_f} + M_{G_f} V_{G_f}$ $V_H = \frac{M_{G_f} V_{G_f} - V_{W_o} M_{G_o} + V_{W_f} M_{W_f}}{(M_H - M_{G_o})}$	$M_H = \frac{1}{n_k V_e}$	N/A	$V_{W_o} = 0$	Calculated assuming two phase H-V equilibrium under pre-dissociation conditions	$V_{G_o} = V_{V_o} - V_H$ (V_{V_o} is experimentally determined)	Calculated assuming two phase Lw-V equilibrium under post-dissociation conditions	Experimentally determined	$n_{G_f} = n_{G_f(GWC)} - n_{ext}$ $n_{G_f(GWC)} = V_{G_f(GWC)} / V_{M_f}$ $V_{M_f} = 1 / M_{G_f}$ $n_{ext} = \frac{V_{ext}}{V_{M_{ext}}}$ $V_{M_{ext}} = 1 / M_{G_{ext}}$ $M_{G_{ext}}$ is calculated assuming two phase Lw-V equilibrium at P/T conditions applicable to material mass present within V_{ext} . Vapour within V_{ext} is at hydrate forming (or pre-dissociation pressure) and ambient room temperature. V_{ext} is experimentally determined.	N/A

Principle of mass balance for methane/hydrate saturation	M_H	M_{W_o}	V_{W_o}	M_{G_o}	V_{G_o}	M_{W_f}	V_{W_f}	$M_{G_f}V_{G_f} = n_{G_f}$	$V_{W_{Tot}}$
<p>(c) For hydrate formation in gas rich environment where the formation is incomplete leaving all H-Lw-V phases in the system:</p> <p>$M_H V_H + M_{W_o} V_{W_o} + M_{G_o} V_{G_o} = M_{W_f} V_{W_f} + M_{G_f} V_{G_f}$</p> <p>Thermodynamic state of the system is difficult to define</p> $V_H = \frac{M_{G_f} V_{G_f} - V_{W_o} M_{G_o} + V_{W_f} M_{W_f} - V_{W_{Tot}} (M_{W_o} - M_{G_o})}{(M_H - M_{G_o}) - \frac{V_f}{V_e} (M_{W_o} - M_{G_o})}$	$M_H = \frac{1}{n_k V_e}$	Calculated assuming two phase H-Lw equilibrium under pre-dissociation conditions	$V_{W_o} = (V_{W_{Tot}} - V_{W_H})$ (neglecting the change in water volume due to gas dissolution + change in water volume due to evaporation into the gas phase) Volume of water consumed in the hydrate formation $V_{W_H} = \frac{V_f V_H}{V_e}$	Calculated assuming two phase H-V equilibrium under pre-dissociation conditions	$V_{G_o} = V_{V_o} - V_H - V_{W_o}$ (V_{V_o} is experimentally determined)	Calculated assuming two phase Lw-V equilibrium under post-dissociation conditions	Experimentally determined	$n_{G_f} = n_{G_f(GWC)} - n_{ext}$ $n_{G_f(GWC)} = V_{G_f(GWC)} / V_{M_f}$ $V_{M_f} = 1 / M_{G_f}$ $n_{ext} = \frac{V_{ext}}{V_{M_{ext}}}$ $V_{M_{ext}} = 1 / M_{G_{ext}}$ $M_{G_{ext}}$ is calculated assuming two phase Lw-V equilibrium at P/T conditions applicable to material mass present within V_{ext} . Vapour within V_{ext} is at hydrate forming (or pre-dissociation pressure) and ambient room temperature. V_{ext} is experimentally determined.	Experimentally determined

Table 4.3: Resources for determination of hydrate bond water and methane concentration

The volume of hydrate bond water V_{WH}
(1) Molar volume of water in aqueous liquid V_l
Lide [2007] – Density of water at a given temperature (pressure effect on water density is neglected) – Recommended and used in this study
(2) Molar volume of water in the hydrate phase V_e
<p>(a) Hester et al. [2007] – Recommended and used in this study – (Theoretical) – Lattice parameter a at a given temperature (pressure effect on hydrate density neglected) – fits with experimental data of Shpakov et al. [1998] and Ogienko et al. [2006] with an average difference of 0.004 Å which is falling within the measurement error of experimental data Ogienko et al. [2006] – (Experimental/Theoretical) lattice parameter at a reference temperature, a_o (pressure effect on hydrate density neglected) – T range = 86-267 K</p> <p>(b) Shpakov et al. [1998] – (Experimental/Theoretical) lattice parameter a at a given temperature by fitting to experimental data (pressure effect on hydrate density neglected) – T range = 80-210 K – Predictions deviate from experimental data with increasing temperature</p> <p>(c) Sun and Duan [2007] – (Theoretical) V_e at a given temperature and a pressure</p>
The hydrate number n_k for estimation of methane concentration in the hydrate phase M_H
<p>(a) Regression of experimental data – not recommended as limited amount of experimental data is available</p> <p>(b) CSMGem [Ballard, 2002] – Recommended and used in this study – (Theoretical) – Verified against experimental data available at Gas Processors Association (1996), Thermodynamic Database Version 2.0 – Predictions of n_k at temperature/pressure/composition conditions over (H-V), (H-Lw-V), and (H-Lw) phase regions</p> <p>(c) Sun and Duan [2007] – (Theoretical) – Predictions of n_k at P/T conditions over (H-Lw) two phase region</p>

**Table 4.3: Resources for determination of hydrate bond water and methane concentration
.....contd.**

Vapour phase methane concentration under H-V equilibrium M_{Go}
(1) Mole fraction of methane in vapour at a given temperature and a pressure
Regression of experimental data – Chapoy et al. [2005, 2010], Folas et al. [2007], Lokken et al. [2008], Kosyakov et al. [1979], Oellrich and Althause [2000], Youssef et al. [2009], Aoyagi et al. [1979, 1980], Sloan et al. [1976], Song et al. [2004], and Zhang et al. [2011] – T range = 240-280 K and P range = 3.4-10.4 MPa
(2) Molar volume of vapour at given temperature and a pressure
The use of an EoS for vaporous methane-water system in the presence of hydrate - Not available
(3) Estimation of M_{Go} with the use of a pure component EoS for CH_4 (neglecting the presence of moisture and the effects of hydrate phase) – <i>Recommended and used in this study</i>
(a) CSMGem [Ballard, 2002] – (Theoretical) – Verified against experimental data available at Gas Processors Association (1996), Thermodynamic Database Version 2.0 – Predictions of M_{Go} at temperature/pressure/composition conditions over (H-V) phase region (b) Duan et al. [1992b] – (Theoretical) – T range = 0-1000° C (273.15-1273.15 K) and pressures up to 8000 bar (800 MPa) assuming a pure system consisting of CH_4

**Table 4.3: Resources for determination of hydrate bond water and methane concentration
.....contd.**

Aqueous phase methane concentration under Lw-V equilibrium M_{wf}
<p>(a) Chapoy et al. [2004] – Recommended – (Experimental/Theoretical) – T range = 257-313 K and pressures up to 18 MPa – Predictions of the thermodynamic model verified against experimental data</p> <p>(b) CSMGem [Ballard, 2002] – Recommended – (Theoretical) – Verified against experimental data available at Gas Processors Association (1996), Thermodynamic Database Version 2.0</p> <p>(c) Duan et al. [1992c] – Not recommended over the T range of 273-283 K according to Duan and Mao [2006] – (Theoretical)</p> <p>(d) Duan and Mao [2006] – Recommended and used in this study – (Theoretical) – Predictions verified against experimental data, T range = 273-523 K and pressures up to 2000 bar (200 MPa) – Obtains experimental accuracy – Salinity effects over methane solubility taken into consideration</p> <p>(e) Hashemi et al. [2006] – (Theoretical) – Verified against experimental data of Servio and Englezos [2002] over the P/T ranges of 278.7-284.4 K and 35-65 bar (3.5-6.5 MPa)</p> <p>(f) Sun and Duan [2007] – (Theoretical) – Verified against experimental data – Salinity and capillary effect over methane solubility taken in to consideration</p>

**Table 4.3: Resources for determination of hydrate bond water and methane concentration
.....contd.**

Vapour phase methane concentration under Lw-V equilibrium M_{Gf}
(1) Mole fraction of methane in vapour at a given temperature and a pressure
<p>(a) CSMGem [Ballard, 2002] – Recommended and used in this study – (Theoretical) – Verified against experimental data available at Gas Processors Association (1996), Thermodynamic Database Version 2.0</p> <p>(b) Duan and Mao [2006] with inputs from Shibue et al. [2003] and Wagner and Pruss [1993] – Recommended and used in this study – T range = 273-523 K and pressures up to 2000 bar (200 MPa), predictions verified against experimental data of Olds et al. [1942], Sultanov et al. [2005], Mohammadi et al. [2004], Rigby and Prausnitz [1968] for both non saline and saline systems</p> <p>(c) Mohammadi et al. [2004] with dissolved mole fraction of methane in aqueous phase calculated using Chapoy et al. [2004] – (Experimental/Theoretical) – Verified against experimental data over the temperature range of 273.15-377.59 K and pressures up to 1000 bar (100 MPa)</p> <p>(d) Sun et al. [2003] – (Theoretical) – Accurate predictions in the T range of 273-383 K and pressures up to 1000 bar (100 MPa)</p>
(2) Molar volume of vapour at given temperature and a pressure
<p>(a) CSMGem [Ballard, 2002] – Recommended and used in this study – (Theoretical)– Verified against experimental data available at Gas Processors Association (1996), Thermodynamic Database Version 2.0</p> <p>(b) Duan and Mao [2006] – Recommended and used in this study – (Theoretical) – T range = 273-523 K and pressures up to 2000 bar (200 MPa)</p> <p>(c) Sun et al. [2003]] – (Theoretical) – Accurate predictions in the T range of 273-383 K and pressures up to 1000 bar (100 MPa)</p>

Table 4.4: Sensitivity of hydrate saturation to direct temperature measurements, absolute pre and post-dissociation system pressures, and estimates of volumetric parameters:

The absolute pressures are obtained by combination of gauge and ambient pressures. The volume of gas collected at the gas/water collector $V_{Gf(GWC)}$ is obtained with the use of measured height and diameter of the gas column. The volume of hydrate forming gas filled elements external to the specimen for which the material mass within is forced into the gas/water collector during collection of dissociation products V_{ext} is predetermined using mass of water occupying the corresponding volume at full water saturation, density of water, ambient temperature and pressure. The pore volume of the hydrated host sediment V_{Vo} is obtained with the use of specimen dimensions (including height and the diameter), grain density, and mass of dry soil.

Test parameter	Sensitivity in terms of the change in hydrate saturation	Units	Range of validity ^a
Pre-dissociation temperature (K) within the hydrated specimen	0.73480982	K ⁻¹	274.15-283.15 K
Post dissociation temperature at the gas/water collector (K)	0.92676320	K ⁻¹	290.15-297.15 K
Ambient room temperature (K)	0.15316374	K ⁻¹	293.15-303.15 K
Pre-dissociation pressure (Absolute) (kPa)	0.01702934	kPa ⁻¹	9026.325-9276.325 kPa
Post dissociation pressure (absolute) at the gas/water collector (kPa)	0.59329482	kPa ⁻¹	400-470 kPa
Volume of gas collected at the gas/water collector, $V_{Gf(GWC)}$ (cc)	0.04929067	cc ⁻¹	5295-5357.5 cc
Volume of hydrate forming gas filled elements external to the specimen for which the material mass within is forced into the gas/water collector during collection of dissociation products, V_{ext} (cc)	1.14748275	cc ⁻¹	21-26 cc
Pore volume of the hydrated host sediment immediately prior to testing such as that mentioned in Step (3) of Section 4.4, V_{Vo} (cc)	1.60985040	cc ⁻¹	143-148 cc
^a Within the range of validity hydrate saturation calculated as per section (b) of the Table 4.2 exhibits a linear relationship with the test parameter			

Table 4.5: Sensitivity of hydrate saturation to the choice of vapour phase EoS under pre-dissociation conditions at H-V equilibrium

Description	Molar volume of methane (cc/mol)	Hydrate saturation (%)
CSMGem	210.13	47.7
EoS of Duan et al. [1992b]	206.8594	46.2
Ideal Gas Law	254.1026	60.2

Table 4.6: Sensitivity of hydrate saturation to the choice of vapour phase EoS under post-dissociation conditions at Lw-V equilibrium

Description	Molar volume of methane (cc/mol)	Hydrate saturation (%)
Vapour saturated gas phase using Duan and Mao [2006]	5520.98	44.6
EoS of Duan et al. [1992b]	5486.85	46.2
CSMGem	5523.34	44.4
Ideal Gas Law	5529.29	44.2

Table 4.7: Sensitivity of hydrate saturation to the choice of vapour phase EoS at Lw-V equilibrium for quantity of gas present within such elements external to the immediate boundaries of the specimen for which the material present within is forced into the gas/water collector during collection of dissociation products

Description	Molar volume of methane (cc/mol)	Hydrate saturation (%)
Vapour saturated gas phase using Duan and Mao [2006]	236.03	46.2
EoS of Duan et al., [1992b]	235.69	46.2
CSMGem	239.33	46.6
Ideal Gas Law	273.29	49.9

Chapter Five: Triaxial compression strength of methane hydrate-bearing coarse granular media

5.1 Introduction

Of interest to this chapter is the behavior of hydrate-cemented coarse granular sand under triaxial compression conditions. An experimental program was carried out with the use of laboratory reconstituted specimens of 20/30 grading Ottawa sand at an initial void ratio of 0.57 corresponding to a relative density of 72%. One of the objectives of the investigation was to study the hydrate saturation dependency of strength (defined by the maximum deviator stress) and stiffness (i.e., initial tangential stiffness defined by the Young's modulus and secant stiffness defined by the secant modulus or the Young's modulus at 50% stress at failure). A set of triaxial tests under constant mass conditions were carried out (at various hydrate saturations ranging from 0 to 80%) after consolidation at an effective confining stress of 500 kPa or 1000 kPa. This allowed investigating the initial effective confining stress dependency of strength and stiffness of hydrate-bearing soils – which was the second objective of the experimental program. At the time of triaxial compression, a typical hydrated specimen consisted of hydrate and vapour (i.e. water saturated gaseous methane) in its pore space. No free water was expected to be present within the specimens during this stage of the test given the particular hydrate formation method presented in Chapter 3 was followed. The comparison of the present results with those published in literature then led to differentiation of behaviour between sediments consisting of cementing habit of hydrate (as in the case of present research) and sediments consisting of pore filling/load bearing habit of hydrate (as published in literature). The comparison met the requirements of the

third objective of the work – investigating the growth habit dependency of strength and stiffness of hydrate-bearing sediments.

The Chapter is organised to present geomechanical properties of hydrate-bearing sediments and their characterization, a literature review of experimental investigations on geomechanical properties of hydrate-bearing sediments, the present experimental procedure in summary, a comprehensive analyses of observations, followed by the results including the initial effective confining stress/hydrate saturation/hydrate habit dependency of strength/stiffness. Based on the results, the possible grain-scale mechanisms taking place under triaxial compression of hydrate-cemented soils and the differences in the mechanisms that should be expected for non-cementing hydrate habits are postulated and discussed.

5.2 Geomechanical properties of hydrate-bearing sediments and the characterisation

Geomechanical properties of hydrate-bearing sediments are greatly altered by the presence of hydrates. However, the exact nature of hydrate influence on sediment properties is not fully understood. The geomechanical properties play a major role in determining the short and long term sediment behaviour related to drilling and methane production, reservoir subsidence, and in understanding mechanisms that lead to slope instability issues associated with shallow hydrated sediments. Sediment strength and deformation characteristics under application of loading are critical inputs for analysis of potential failure around wells [Rustqvist and Moridis, 2007]. The slides and slumps on the continental slope and rise of South West Africa, slumps on the U. S. Atlantic continental slope, and submarine slides on the Norwegian continental margin are among many historical evidence that exhibit a possible connection between hydrate boundaries and geo-

hazards [Grozic, 2010]. The possible mechanisms that lead to slope instability in these sediments include those that are associated with adverse changes in pressure or temperature causing partial dissociation of hydrate such as lowering of sea level, increase in ocean temperature, and erosion or local slumping [Grozic, 2010; McIver, 1982; Nixon and Grozic, 2007; Sultan et al., 2004]. Characterization of the mechanical properties of hydrate-bearing sediments are based on non-destructive field measurements including seismic and electric methods, direct sampling and subsequent laboratory measurements of natural hydrate-bearing cores, or laboratory tests on artificially synthesised hydrate-bearing specimens. The field measurement of seismic and electric properties are affected by a complex interplay of host sediment properties, pore fluid consistency, hydrate saturation, distribution and growth habit [Priest et al., 2005, 2009; Spangenberg and Kulenkampff, 2006]. Direct sampling is significantly affected by alterations to in-situ stress conditions and hydrate dissociation related issues during sampling and core transfer [Waite et al., 2009; Yun et al., 2006]. As such laboratory synthesis and subsequent testing of hydrate-bearing sediments is an important method of gaining fundamental knowledge about these complex materials provided that host sediment properties, intact hydrate properties, quantity and the spatial variation of hydrate present within sediment pore space, and the nature of hydrate and sediment grain interaction are known.

5.2.1 Early investigations of geomechanical properties of hydrate-bearing sediments

The majority of our knowledge of the geomechanical properties of hydrate-bearing sediments is fairly recent. Segoo and Wittebolle [1984] tested the mechanical behaviour of Freon 12 hydrate-bearing specimens in a modified triaxial cell and demonstrated a remarkable increase in strength and stiffness in the presence of hydrate.

Drained conditions: Following the aforementioned early investigations, Ebinuma et al. [2005], Hyodo et al. [2007, 2009, 2011], Kuniyuki et al. [2010], Masui et al. [2005, 2008a, 2008b] and Miyazaki et al. [2008, 2010, 2011] investigated hydrate saturation dependency of stress-strain behavior including strength properties such as peak strength, Young's modulus at 50% of the stress at failure, cohesion, and dilation angle under drained triaxial compression conditions for methane hydrate-bearing sediments. The aforementioned forms a reasonably comprehensive set of tests on drained strength contributing to understanding of methane production and reservoir subsidence related issues of hydrated sediments. The tests were performed on soil specimens consisting artificially synthesized hydrates from ice-seeding or hydrate pre-mixing methods. The details of different methods of laboratory hydrate synthesis and their implications on the physical properties are presented in Chapter 2.

Undrained or constant mass conditions: The understanding of the strength of hydrate-bearing sediments under undrained conditions (where pore pressure dissipation of incompressible pore fluid is completely obstructed) and under constant mass conditions (where drainage of pore fluid including gas and water is completely obstructed but partial pore fluid pressure dissipation due to compressibility of the free gas occupying the pore space is allowed) are particularly important in relevance to loading of subsurface strata due to offshore constructions and slope instability issues. The undrained strength of methane hydrate-bearing sediments was first investigated by Winters et al. [2002, 2007a] with focus on acoustic, shear strength, permeability, and electrical resistance properties prior to and after hydrate formation. The study used soil specimens containing natural hydrates and soil specimens containing artificial hydrates formed in the laboratory using the partial water saturation method. Their work showed that physical properties

greatly depend on the amount of hydrate present in sediment, its distribution within the pore space, and the concentration at specific locations. The strength of hydrate-bearing specimens was found to be much higher than that of specimens containing no hydrates [Winters et al., 2002]; the presence of solid hydrate in pore voids caused dilation with an increase in strength and negative pore pressure development during undrained shear. The strength (of hydrated sediments formed by employing partial water saturation method) was further investigated by Ghiassian and Grozic [2011], who illustrated the hydrate saturation dependency of stress-strain behavior and the excess pore pressure development under undrained conditions. Yun et al. [2007] also investigated the hydrate saturation dependency of stiffness and strength for Tetrahydrofuran (THF) hydrate-bearing specimens under constant mass conditions. However, complete understanding of the behavior of hydrated sediments during shear deformation under conditions of hindered drainage has not yet been achieved, further research effort is required.

5.3 Experimental procedure

The experimental procedure consists of several steps:

- (1) preparation of hydrate host sediment by dry pluviation of sand;
- (2) water saturation of the sand specimen;
- (3) ramping up of pore and confining fluid pressures;
- (4) consolidation;
- (5) partial pore fluid replacement by gaseous methane;
- (6) hydrate formation;
- (7) shearing under triaxial compression; and
- (8) hydrate dissociation and collection of dissociation products.

The detailed procedures for Steps (1) through (6) are presented in Chapter 3. The Step (8) is detailed in Chapter 4 in relevance to dissociation gas evolution measurements method for hydrate saturation estimation. Therefore, the following is focused on detailing the Step (7) – shearing under triaxial compression with summary information of the other steps.

20/30 grading Ottawa sand was used to prepare all test specimens of dimensions 13.0 cm in height and 6.24 cm in diameter at 0.57 initial void ratio, which corresponds to a relative density of 72%. The sand specimens were completely water saturated and allowed to consolidate under an effective confining stress of either 500 kPa or 1000 kPa and at a pore water pressure of 9000 kPa. Upon consolidation gaseous methane was introduced into the specimens replacing a pre-determined volume of pore water. Hydrates were then allowed to form at a temperature of 5°C and a gas pressure of 9000 kPa. Upon completion of hydrate formation process, the specimens were subjected to shearing under triaxial compression. The test conditions are given in Table 5.1.

5.3.1 Specimen consistency immediately prior to shearing

Immediately prior to shearing, a typical hydrated soil specimen consisted of hydrate and vapour (i.e. water saturated gaseous methane) in its pore space.

5.3.2 Shearing at constant mass under triaxial compression conditions

The standard *consolidated undrained (CU) test* serves as a baseline method for the triaxial compression testing carried out within the scope of this research. The first stage of the test involves application of all-round stress with drainage permitted, ensuring the sample is fully consolidated under the applied all-around stress. This stage refers to the Step (4) of the

experimental procedure followed. The second stage of the CU test involves shearing the specimen by application of deviator stress with no drainage allowed (i.e., under undrained conditions). This stage refers to the Step (7) of the experimental procedure followed. In the case of the hydrate-bearing specimens subjected to testing, fully undrained conditions did not exist as the specimen pore space consisted of considerable amount of free gas, and hence partial pore gas pressure dissipation was expected due to compressibility of free gas. However, the pore space constituents were not allowed to change during shearing and therefore, the tests may be described as performed under *constant mass* conditions.

Deviator stress was applied at a constant strain rate of 1%/min. The confining fluid pressure was maintained constant throughout the shearing stage and the confining fluid volume displacement was recorded facilitating the calculation of specimen volume change during the shearing stage. The axial load, axial deformation, and the pore fluid (gas) pressure response were also recorded. The Figure 5.1 presents a schematic diagram of the triaxial apparatus.

Upon completion of shearing, temperature was increased to induce hydrate dissociation and all dissociation products (gas/water) were collected at a separate gas/water collector. The pressure, temperature, and volume measurements of the dissociation products were then used to calculate the hydrate saturations of the respective specimens. The methodology for determination of hydrate saturation is detailed in Chapter 4. At the end of gas/water collection process, test specimen was isolated from the gas/water collector and an instant vacuum was applied at the bottom of the specimen to preserve the features of the failed specimen during subsequent release of confining pressure, draining of confining fluid, and disassembly of the triaxial cell. Visual

observations were then carried out to identify the features such as shear bands. Shear bands were observed particularly at higher hydrate saturations.

The test specimens for water saturated reference tests were performed following standard procedure of the CU test. The specimens were prepared by employing the same procedure listed above for hydrate-bearing specimens except the partial pore fluid replacement by methane introduction (Step 5), and hydrate formation (Step 6) were omitted. The shearing was performed under *undrained conditions* subsequent to consolidation of test specimens at either one of the initial effective confining stresses; 250 kPa, 500 kPa, and 1000 kPa.

The consolidated undrained/constant mass triaxial compression tests carried out on water saturated and hydrate-bearing soil specimens are listed with the respective conditions under which the tests are carried out in Table 5.1.

5.4 Pore fluid pressure response and volume change during undrained shearing of water saturated soil specimens

5.4.1 Pore fluid pressure response

The change in pore pressure (Δu) caused by the respective changes in the major and minor principal stresses $\Delta\sigma_1$ and $\Delta\sigma_3$ are given by the following equation developed by Skempton [1954].

$$\Delta u = B[\Delta\sigma_3 + A(\Delta\sigma_1 - \Delta\sigma_3)] \quad (5.1)$$

where $\Delta u = \Delta u_a + \Delta u_d$ (5.2)

Δu_a is the pore pressure development during application of all around confining stress and is expressed as:

$$\Delta u_a = B\Delta\sigma_3 \quad (5.3)$$

Δu_d is the pore pressures development during deviatoric loading stage of the test and is expressed as:

$$\Delta u_d = BA(\Delta\sigma_1 - \Delta\sigma_3) \quad (5.4)$$

In the case of consolidated undrained triaxial test, the shearing stage or the deviator stress application stage involves shearing of a soil specimen under constant confinement, and hence the excess pore water pressure development during shearing can be expressed using the equation 5.4 with substitution of constant $\Delta\sigma_3$ applicable for the test.

The parameters A and B are known as the Skempton's pore pressure coefficients and the B parameter is expressed as follows:

$$B = \frac{1}{1 + \frac{nC_v}{C_c}} \quad (5.5)$$

$$\text{or } B = \frac{1}{\alpha + \frac{nC_v}{C_c}} \quad (5.6)$$

and,

$$\alpha = \text{Biot's effective stress coefficient; } \alpha = 1 - \frac{C_s}{C_c}$$

C_s = compressibility of the soil mineral

n = porosity of the soil material,

C_v = compressibility of the pore fluid (water in the case of saturated soil), and

C_c = compressibility of the soil structure

The B parameter is expressed as presented by equation (5.5) with the assumption of Terzaghi's simple effective stress law: $\Delta\sigma' = \Delta\sigma - \Delta u$. The B parameter is expressed as presented by equation (5.6) with the assumption of Biot's expression for effective stress: $\Delta\sigma' = \Delta\sigma - \alpha\Delta u$.

The coefficient B greatly depends on the relative compressibility of pore space, soil structure, and the mineral grains [Bishop and Henkel, 1962]. For water saturated soil, where the relative compressibility of pore space to soil structure is considered insignificant, the ratio C_v/C_c approaches zero. Also, as the relative compressibility of the mineral grains to that of soil structure may well be considered as negligible, the ratio C_s/C_c approaches zero. As such the value of Biot's effective stress coefficient α tends towards unity (1) and so does the coefficient B . The measured values of the B for the water saturated test specimens WS 250, WS 500, and WS 1000 are given in Table 5.2.

The coefficient $A = \frac{1}{3}$ for elastic materials. However, soil material can hardly be described as elastic. In the case of soil, the coefficient A is reflective of stress-strain behaviour of the soil structure. A is positive for initially loose packing of particulate material, which are expected to undergo compression upon deviatoric loading. A is negative for dense dilative material. The value of A at a given point on the stress-strain curve also depends on the proportion of failure stress applied [Bishop and Henkel, 1956; Skempton, 1954]. Therefore, it appears no unique value of A exists for a given soil material. With relevance to the present study, the A parameter for water saturated test specimens was determined experimentally at 5% strain with the use of measured pore pressure response. The values obtained are presented indicating the dilative background volumetric behaviour of dense sand (Table 5.2).

5.4.2 Volume change

Theoretically, when incompressible mineral grains and pore water is assumed, water saturated specimens do not undergo volume change during application of deviatoric stress under undrained conditions. However, in reality, minute quantity of volume change should be expected, the accurate measurement of which is generally hindered since the relative magnitude of volume change compared to the measurement error associated with measuring devices and mechanisms is not significant.

5.5 Pore fluid pressure response and volume change during shearing of hydrate-bearing soil specimens under constant mass conditions

As previously mentioned, the hydrate-bearing soil specimens subjected to testing consisted of *hydrate* and water saturated *gaseous methane* in the pore space. Presence of no free water in the

pore space should be expected when the specific experimental procedure adopted is considered. Hence, pore fluid pressure response during shear is referred to *pore gas pressure* response. Due to compressibility of the pore space consequential of the presence of free gas, the change in pore fluid pressure originating in response to shearing should be expected to undergo partial dissipation. Thus, it is also expected that the hydrate-bearing specimens undergo volume change in response to shearing.

The analysis of pore fluid pressure response of hydrate-bearing specimens requires appropriate modifications to Biot's α and Skempton's B parameters. The theoretical predictions of the volume change can then be made for hydrate-bearing soils considering volume compatibility of the constituents (i.e., *soil, hydrate, and free gas*) within a hydrated soil specimen.

5.5.1 Biot's effective stress parameter α for hydrate-bearing soil

As previously mentioned the Biot's effective stress coefficient for hydrate-free sediment is given as $\alpha = 1 - \frac{C_s}{C_c}$, where C_s is the compressibility of the soil mineral and C_c is the compressibility of the soil structure (or the skeleton). In the case of hydrate-cemented soils, appropriate modifications to C_s and C_c should be considered in the theoretical determination of Biot's α coefficient.

5.5.1.1 The aggregated compressibility of the solid constituents C'_s

The compressibility of the soil mineral C_s , should preferably be substituted with the aggregated compressibility of all solid constituents C'_s (i.e., mineral grains and solid ice like hydrate). In

hydrate-cemented soil systems, soil grains and hydrate behave as an aggregated crystal. In this case, the compressibility of the crystalline aggregate is not accurately represented by the simple volumetric average of compressibility of the two phases: soil and hydrate. The equation 5.7 expresses the aggregate compressibility according to Hill's [1952] theoretical study on the elastic behaviour of a crystalline aggregate. Priest et al. [2005] estimates compressional and shear wave velocities (v_p and v_s) with the use of Hill's [1952] expression for aggregated compressibility of hydrate-cemented soil over a range of hydrate saturations. The estimated values of velocity are found to be comparable with independent measurements of v_p and v_s performed over the range of hydrate saturations. This observation proves the applicability of equation 5.7 for hydrate-cemented soils. The aggregated bulk modulus of the solid constituents K'_s (which is the inverse of the aggregated compressibility of the solid constituents C'_s) is thus calculated with the use of Hill's averaging method as follows facilitating the determination of the compressibility of the solid phase with the effects of hydrate taken into account.

$$K'_s = \frac{1}{C'_s} = \frac{1}{2} \left[\sum_{i=1}^N \psi_i K_i + \left(\sum_{i=1}^N \psi_i / K_i \right)^{-1} \right] \quad (5.7)$$

where,

N = number of distinct solid constituents (= 2 including soil mineral and hydrate)

ψ_i = the volumetric fraction of the i^{th} constituent in the solid phase and

K_i = the bulk modulus of the i^{th} constituent

5.5.1.2 The compressibility of the soil skeleton (or the hydrate-cemented solid framework) C_c

The compressibility of the soil skeleton is given by the inverse of bulk modulus or the (skeletal stiffness) of the soil framework K_c . The skeletal stiffness K_c is generally expressed as follows.

$$K_c = \frac{1}{C_c} = \frac{E}{3(1-2\mu)} \quad (5.8)$$

where,

E = Young's modulus and

μ = Poisson's ratio

In hydrate research, the skeletal stiffness K_c is often considered to be better represented by

$$K_c = \frac{1}{C_c} = \frac{2(1+\mu)}{3(1-2\mu)} G \quad (5.9)$$

with independent measurements/estimations of shear modulus G .

Santamarina et al. [2010] and Waite et al. [2009] brings into greater attention the fact that G is dependent upon the sediment's fabric properties, and the nature of inter-granular contacts.

Particularly, in the presence of hydrate, G becomes significantly dependent on the degree of hydrate saturation and the pore scale hydrate habit. In the case of sediments where the hydrate formation cements the sediment grains at the grain contacts, as in the case of specimens

subjected to testing under present research, hydrate formation becomes the primary control of G and therefore of the skeletal stiffness [Dvorkin et al, 2000]. As such the ability to accurately determine G is immensely important in determining the compressibility of the solid (soil-hydrate) framework of hydrate-cemented soils. Often, the use of acoustic wave speed measurements is suggested. The shear modulus G is related to shear wave velocity v_s as follows [Priest et al., 2005; Santamarina et al., 2010].

$$v_s = \sqrt{\frac{G}{\rho}} \quad (5.10)$$

where,

ρ = mass density of the soil-hydrate medium

However, it should be noted that according to Lambe and Whitman [1979], the shear modulus G obtained for small strain conditions as aforementioned provides only an upper bound to the value of G applicable to large strain conditions.

Nevertheless, the measurement of acoustic properties of hydrate-bearing soils, remains beyond the scope of the present research. Therefore the compressibility of the solid framework, C_c was determined using the equation 5.8.

The Poisons ratio μ can be evaluated from the measured axial and lateral strains during deviator stress application stage of the triaxial compression test. Since, lateral strain measurements were

not performed as a part of laboratory testing of the present research, an approximated value of $\mu = 0.2$ was used in the aforementioned calculation of Biot's α coefficient. This assumption is based on the observation of Lambe and Whitman [1979] that the Poisson's ratio varies with strain and typically has values of about 0.1 to 0.2 during early stages of loading of sand associated with elastic deformation.

The Biot's α coefficient for the test specimens was therefore, determined with (1) the aggregated compressibility of the solid constituents C'_s determined from equation (5.7) and (2) the compressibility of the solid framework C_c determined using the equation (5.8) with the use of experimentally obtained E and the approximated value of $\mu (=0.2)$. The calculated values of Biot's α coefficient are presented in the Table 5.3. The typical values of constituent compressibility used with equation 5.7 are presented in Table 5.4(a) and (b).

5.5.1.3 An effective stress law for hydrate-bearing soils

The calculated values of Biot's α coefficient for hydrate-bearing soils range between 0.947 and 0.996. Therefore, the effective stress coefficient for hydrate-bearing soils can well be approximated to unity (1). As a result, the Terzaghi's simple effective stress law is applicable for tested hydrate-bearing soils.

$$\sigma' = \sigma - u_g \quad (5.11)$$

where,

σ' = effective stress

σ = total stress and

u_g = the pore gas pressure

5.5.2 Pore pressure coefficient B for hydrate-bearing soil

The pore pressure coefficient B can be determined with the use of Biot's effective stress coefficient α as determined in the previous section and the compressibility of the solid framework C_c determined using the equation (5.8) upon appropriate modifications to compressibility of the pore fluid C_v to represent hydrate-bearing soil. The hydrate-bearing soil specimens subjected to testing in the present study consisted of solid hydrate and free gaseous methane in the pore space. As mentioned in relation to determination of the Biot's α coefficient, the hydrate is considered as a solid constituent. Therefore, the pore space compressibility is determined solely by pore gas compressibility C_g and is expressed as follows.

$$C_v = C_g S_g \quad (5.13)$$

where;

$$C_g = -\frac{1}{V_g} \frac{\Delta V_g}{\Delta P} \text{ at constant temperature } T; \Delta \text{ denotes change in gas volume } V_g \text{ or pressure } P$$

and S_g = degree of gas saturation

The gas compressibility value used in the calculations is given in Table 5.4(c).

The definition of porosity n of the hydrate-bearing soil material in relevance to determination of B should also be modified accordingly to include free gaseous methane as the only pore space constituent and is expressed as follows.

$$n = \frac{V_g}{V_s + V_H + V_g} \quad (5.13)$$

The calculated values of coefficient B are presented in the Table 5.5. It can be seen that the values of B obtained for hydrate-bearing soils are significantly low and are governed by the high compressibility of the pore space occupied by gaseous methane.

5.5.3 Pore pressure coefficient A for hydrate-bearing soils

The Skempton's pore pressure coefficient A for the tested specimens can be calculated using the pore fluid pressure measurements performed during deviatoric loading. For specimens at low hydrate saturations ($< 40\%$), the coefficient was calculated at 2-5% strain in order to capture the pore pressure development behaviour prior to reaching at maximum deviator stress. The values are presented in Table 5.6.

As will be discussed later in Section 5.7.4, the maximum deviator stress and the pre-peak stress-strain behaviour obtained for specimens with high hydrate saturations ($> 40\%$) do not reflect the properties of the soil medium under the applied loading and boundary conditions, but are considerably affected by hydrate strength. The properties of the soil medium, specifically,

negative pore pressure development indicating dilative background volumetric tendency are apparent only in the post-peak region at these hydrate saturations. Also, the corresponding deviator stress response in the post-peak region, is not representative of the pore pressure response and its resultants (i.e. development of negative pore pressure, increase of effective stress, and increase of frictional resistance to shearing) as further hydrate breakage/de-bonding related loss of cohesion is greater than any increase in frictional resistance. The resultant is a net decrease in deviator stress. Therefore, the calculation of A parameter either as applicable to pre-peak region or as applicable to post-peak region for the specimens consisting of high hydrate saturations is apparently not meaningful.

In overall, the discussion of pore fluid pressure response of hydrate-bearing soils provided in Sections 5.5.1, 5.5.2, and 5.5.3 can be summarized as follows. In general, for a material whose background volumetric tendency is dilative, a deviator stress increment under undrained/constant mass conditions causes a negative pore pressure change and hence the net pore pressure reduces upon further deviator stress increase. However, in the presence of free gas when the medium is associated with a low B value as in the case of our hydrate-bearing specimens, the Skempton's equation (Equation 5.4) for pore pressure generation suggests development of smaller negative pore pressure change upon application of deviator stress increment, relative to the case of a specimen consisting of no free gas. Volume expansion should then be expected as the medium does not generate an increment of effective stress adequate to prevent volume expansion during deviatoric loading. Hindered negative pore pressure development and associated hindered development of effective stress may eventually lead to strain softening of deviator stress as less and less resistance to shearing is developed as the shearing continues.

Some evidence can be found in gas hydrate literature: according to Winters et al. [2007] the presence of free gas within the pore space during constant mass shear is reported to greatly reduce the tendency for negative pore pressure development of hydrate-bearing sediments resulting in decreased shear strength development; Yun et al.[2007] also suggests possibility of specimen volume expansion due to inadequate pore space water saturation as associated with observed larger lateral strains in triaxial compression of their hydrated soil specimens at constant mass.

5.5.4 Experimental measurement of volume change in response to shearing

The total specimen volume change during the shearing stage of the consolidated undrained triaxial test can be measured by means of tracking the volume displacement of the confining fluid (water). Specifically, the calculation can be performed taking into consideration (1) the fluid volume received by the cell pressure intensifier in the event of specimen volume expansion or (2) the fluid volume pushed out from the cell pressure intensifier into the confining cell surrounding the soil specimen in the event of specimen volume reduction. A correction should be made to the calculated volume change for volume of fluid displaced into the cell pressure intensifier due to intrusion of the axial loading ram into the triaxial confining cell during application of deviator stress. However, in relevance to testing of hydrate-bearing specimens, the accurate measurement of volume change is hindered due to existence of many obstacles including temperature variations/gradients within the confining fluid volume tracking system, possible gas migration through membranes surrounding the soil specimen, and creep in the triaxial confinement cell etc. Therefore, the volume change measurements performed during the present research was considered as of low reliability and was exempted from the subsequent

analysis of the test results. The following methods are recommended for volume change measurements to address the aforementioned challenges with respect to hydrate-bearing soils.

- (a) Direct measurement of strain using axial and lateral strain gauges – Despite the difficulty in fixing suitable deformation indicators due to low strength of soil specimens [Bishop and Henkel, 1962], the use of axial strain gauges and multiple lateral measurement gauges to capture non uniform strains resulting from end resistance can be employed to obtain a specimen volume change measure independent of uncertainties related to that obtained by tracking the confining fluid displacement.
- (b) Use of digital imaging techniques – Imaging technology such as those suggested by Macari et al. [1997] presents a way of eliminating limitations such as those related to measuring radial strains with strain gauges placed at discrete points (commonly at the middle, at a third, and at two thirds along the height of the specimen) and later use of averaging methods to correlate the deformation measured at discrete points to that of total specimen. The method of Macari et al. [1997] involved video recording of a soil specimen throughout a triaxial test using two cameras placed to capture perpendicular view of specimen, selection of discrete individual images for further analysis, and computer aided volume estimation. Application of proper correction for magnification due to presence of confining fluid in the line of vision between the specimen and the video camera was also considered.

5.5.5 Predicting volume change response to shearing for hydrate-bearing soil

The specimen volume change during shearing can be calculated considering the volume compatibility for a hydrated soil specimen. The following inputs are required for the calculation:

- (a) initial pore gas volume V_g
- (b) initial pore gas pressure P (which is the measured initial pore fluid pressure u in the triaxial test) and
- (c) the change in pore gas pressure ΔP due to application of an increment of deviator stress (which is the measured pore fluid pressure change Δu in the triaxial test)

Then, according to volume compatibility of the system:

$$\begin{pmatrix} \text{Specimen} \\ \text{Volume} \\ \text{Change} \end{pmatrix} = \begin{pmatrix} \text{Volume} \\ \text{Change in} \\ \text{the Gaseous} \\ \text{Phase} \end{pmatrix} + \begin{pmatrix} \text{Volume} \\ \text{Change in} \\ \text{the Soil and} \\ \text{Hydrate} \\ \text{Phases} \end{pmatrix} \quad (5.14)$$

If the soil and solid hydrate phases are considered to be incompressible, then

$$\begin{pmatrix} \text{Volume} \\ \text{Change in} \\ \text{the Soil and} \\ \text{Hydrate} \\ \text{Phases} \end{pmatrix} = 0 \quad (5.15)$$

Therefore, the specimen volume change in response to deviator stress increment is given by the volume change in the gaseous phase. The gaseous phase volume change can be calculated with a use of a suitable EOS for methane. The Ideal Gas Law (IGL) may be employed or an EOS such as Duan et al. [1992b] may be used to obtain better accuracy. If the Duan et al. [1992b] model is used, the specimen volume change ΔV can be calculated as follows.

$$\Delta V = \left(\frac{V_{m(P+\Delta P, T)}}{V_{m(P, T)}} \right) V_g - V_g \quad (5.16)$$

where,

$V_{m(P,T)}$ = molar volume of methane at initial pore gas pressure P and temperature T (obtained from Duan et al. [1992b] EOS)

$V_{m(P+\Delta P,T)}$ = molar volume of methane at pore gas pressure $P + \Delta P$ and temperature T (obtained from Duan et al. [1992b] EOS)

5.6 Undrained response of water saturated specimens –observations and analysis

5.6.1 Typical behaviour of undrained water saturated specimens

The typical undrained behaviour of dense saturated sand under triaxial compression is characterised by the following features:

- (a) strain hardening of deviator stress in response to shear;
- (b) initial effective confining stress dependency of deviator stress at failure – greater the initial effective confining stress, the and higher the deviator stress at failure; and
- (c) initial effective confining stress dependency of excess pore pressure development – greater the initial effective confining stress, the higher the initial positive pore pressure response (contractive volumetric tendency), and the smaller the later negative pore pressure response (dilative volumetric tendency).

Undrained shearing of saturated sand ultimately results in arriving at a steady state characterised by deformation at constant stresses, volume, and velocity [Poulos, 1981; Castro et al., 1982].

Dense (dilative) materials initially develop positive excess pore pressure (indicative of contraction tendency); then reach at a point of maximum pore pressure (point of phase

transformation); and undergo reduction of pore pressure afterwards (indicative of dilative tendency) as the steady state is reached at large strains [Negussey et al., 1987]. This behaviour is illustrated in Figure 5.2. The point of phase transformation can also be characterised as the point at which the stress path turns its direction in $p' - q$ space.

5.6.2 Observations and analysis of undrained response of water saturated specimens

The features of the observed behaviour of the specimens tested are presented in Table 5.7.

The undrained triaxial compression behaviour of water saturated sand specimens subjected to testing are representative of a dense packing of particulate granular material (Figure 5.3). The deviator stress response to constant rate strain (1%/min) illustrates strain-hardening behaviour. At all three effective confining stresses (250 kPa, 500 kPa, and 1000 kPa) phase transformation occurs very early during loading (at axial strains $< 1\%$). Upon phase transformation, the shear resistance continues to increase as the development of negative pore pressures lead to increased effective stress. Failure occurs at strains between 10-13% in all cases. The tests yield a mobilised friction angle of 31.51° at the maximum deviator stress (Figure 5.3). At higher initial effective confining stresses, the specimens develop greater secant (E_{50}) and initial tangential stiffness (Table 5.7).

The pore fluid pressure response is representative of dense material of which the background volumetric tendency is dilative. Close observation of the pore pressure development allows identification of potential signs of dissolved gas exsolution from pore water such as the drop in the rate of negative pore pressure development (Figure 5.3) initiating between 5-7% axial strains. The crossing of excess pore pressure curves may have resulted from the differences in the degree

of gas exsolution between the specimens, and the resulting differences in the negative pore pressure development. The tests were conducted at initial back pressures of 1050 kPa, 1050 kPa, and 1070 kPa at respective effective confining stresses of 250 kPa, 500 kPa, and 1000 kPa. Apparently, the imposed initial back pressure was insufficient to prevent dissolved gas exsolution at all negative pore pressures that developed for the test specimens at the respective density and initial confining stress. Therefore, the negative pore pressure response at larger strains was omitted from further analysis.

Consequently, it is difficult to determine if the observed mild softening of deviator stress at larger strains (Figure 5.3) occurring associated with the reduced rate of negative pore pressure development is indicative of the material reaching at a steady state or is resulting from a mere counter-effect of reduced negative pore pressure development. When free gas is present within the pore space (due to gas exsolution), resulting in B values between zero (0) and unity (1), the Skempton's equation suggests development of smaller negative pore pressure change relative to the case of fully saturated soils upon application of deviator stress increment. Hindered negative pore pressure development and associated hindered development of effective stress can eventually lead to strain softening of deviator stress as less and less resistance to shearing is developed as the shearing continues. Therefore, there exists little confidence with regard to using the end of test state of the tests to derive the steady state friction angle which is considered a material parameter constant for a given sand [Negussey et al., 1987]. However, it is shown experimentally (Figure 5.4) that the friction angle mobilized at undrained phase transformation and the friction angle mobilized at steady state are identical [Negussey et al., 1987]. Therefore, a steady state friction (or friction at phase transformation) represented by an angle of 24.21° was

obtained for the sand using the measurements at phase transformation (Figure 5.5). The findings of the analysis of the behaviour of the water saturated specimens are summarised in Table 5.8.

To eliminate dissolved gas exsolution in the case of undrained tests on dense material, where negative pore pressure development is expected, the initial pore water pressure and the confining pressure under which shearing initiates should be obtained by incrementing the back pressure and confining pressure adequately beyond the pressures at which back pressure saturation is carried out upon completion of a successful B-Test. During the increment of back pressure and confining pressure, the effective confinement may be kept constant; further consolidation of the specimen may be carried out at the final pressures if the effective confinement is allowed to change during pressure increment. It is also recommended to flush carbon dioxide gas through the specimen before flushing de-aired water during specimen saturation stage in order to obtain better pore saturation.

5.7 Response of hydrate-bearing specimens to shearing under constant mass - observations and analysis

The observations made on the stress-strain behaviour of the hydrate-bearing specimens tested are presented under three headings; (1) response of hydrate-bearing specimens at low hydrate saturations (< 40%) consolidated at 500 kPa initial effective confining stress, (2) response of hydrate-bearing specimens at low hydrate saturations (< 40%) consolidated at 1000 kPa initial effective confining stress, and (3) response of hydrate-bearing specimens at high hydrate saturations (> 40%). The 40% limit of hydrate saturation for distinguishing the behaviour is selected upon careful evaluation of overall observations. Particularly, strength (the maximum

deviator stress) dependency on hydrate saturation starts showing lack of correlation and scatter around hydrate saturation of 40%. The features of the observed behaviour of the specimens tested are presented in Table 5.7.

At set values of host specimen void ratio of dense packing, initial effective confining stress, and pore fluid pressure (i.e., gas pressure in the case of present study), the strength-deformation behaviour of hydrate-bearing cemented specimen under constant mass conditions is differentiated from the behaviour of the water saturated non-hydrated host specimen under undrained conditions mainly by three factors: (1) compressibility of the pores space relative to that of water saturated non-hydrated specimen, (2) cementation of soil grains due to the presence of hydrate at mineral grain contacts, and (3) densification of the soil material due to hydrate pore space occupancy.

The effects of relative pore space compressibility were discussed previously (Section 5.5.2) and can be summarized as (a) the presence of free gas within pore space of hydrate-bearing soil resulting in a low value for Skempton's pore pressure coefficient B , (b) development of smaller negative pore pressure change and hence hindered effective stress development compared to water saturated non-hydrated specimen upon application of deviator stress increment, (c) volume expansion of the hydrate-bearing specimen as the medium does not generate an increment of effective stress adequate to prevent volume expansion during deviatoric loading, and (d) hindered development of effective stress leading to strain softening of deviator stress at larger strains as less and less resistance to shearing is developed as shearing continues.

The effects of grain cementation due to presence of hydrate are particularly visible in the form of greater stiffness and tendency for aggregate scale dilation [Waite et al., 2009 after Yun et al., 2007]. Under constant mass conditions, tendency for aggregate scale dilation results in greater tendency for development of negative pore pressure – an opposite effect to which is resulting due to pore space compressibility.

The effects of densification due to pore space presence of hydrate should be expected to be visible in the form of greater strength compared to a water saturated non-hydrated specimen, and increased dilative volumetric tendency [Waite et al., 2009 after Yun et al., 2007] resulting in greater negative pore pressure development upon application of deviator stress increment under constant mass conditions – an opposite effect to which is resulting due to pore space compressibility.

The grain scale model for shear strength of hydrate-bearing sediments presented in Waite et al [2009] modified after Yun et al. [2007] (Figure 5.6) presents the aforementioned graphically. Experimental evidence for aforementioned can also be found in Winters et al. [2002, 2007] and Ghiassian and Grozic [2011].

5.7.1 Observations of hydrate-bearing sediment behaviour in summary

The initial effective confining stress/hydrate saturation dependency of strength/stiffness observed in the stress-strain response of the hydrate-bearing specimens tested under triaxial compression are characterized by the following features.

(a) The specimens at hydrate saturation $< 40\%$ exhibit:

- strain hardening response to shear (with mild softening at larger strains);
- smaller initial positive pore pressure response (contractive volumetric tendency) compared to water saturated non-hydrated specimens, and tendency for positive pore pressure development decreasing with increasing hydrate saturation;
- smaller or similar rate of later negative pore pressure development compared to water saturated non-hydrated specimens (dilative volumetric tendency) , and tendency for negative pore pressure development increasing with hydrate saturation;
- increased strength (maximum deviator stress) at higher initial effective confining stress;
- greater initial tangential stiffness at greater initial effective confining stress, lack of correlation between secant stiffness and initial effective confining stress; and
- increased strength and stiffness with increasing hydrate saturation.

(b) The specimens at hydrate saturations $> 40\%$ exhibit:

- brittle behaviour in stress-strain response;
- significantly higher peak stress and initial tangential stiffness and secant stiffness relative to the tests performed at low saturations; and
- lack of clear correlation of peak stress and stiffness with initial effective confining stress and hydrate saturation.

The following sections discuss the behaviour listed above in detail.

5.7.2 Response of hydrate-bearing specimens at low hydrate saturations (< 40%) consolidated at 500 kPa initial effective confining stress to shearing at constant mass

The observed stress strain behaviour at low hydrate saturations (< 40%) for specimens MH 001, MH 002, MH 003, and MH 004 at respective hydrate saturations of 10.2% , 12.7%, 27.3%, and 34.4% is presented in Figure 5.7. The stress-strain behaviour can be identified as strain hardening; mild softening of deviator stress at larger strains can be identified for MH 001 and MH 002 which are at the low end of the range of hydrate saturations. As explained previously, mild strain softening can be explained as attributed to effects of pore space compressibility (i.e., reduced tendency for negative pore pressure development, hindered development of effective stress and shear resistance) being predominant over the effects of hydrate cementation and densification (i.e., increased tendency for development of negative pore pressure, effective stress, and shear resistance).

For all hydrate saturations, the maximum deviator stress appears to increase with increasing hydrate saturation (Figure 5.8). The initial tangential stiffness also shows a general increasing trend with hydrate saturation (Figure 5.9).

The observed pore pressure behaviour (Figure 5.7(b)) supports the observed deviator stress response to shearing. The pore fluid pressure response is representative of dense material of which the background volumetric tendency is dilative. It can be observed that the rate of negative pore pressure development for hydrate-bearing specimens is less than that for non-hydrated water saturated specimen. This can be attributed to the effects of pore space compressibility (i.e. partial dissipation of pressure) due to the presence of free gas. However, the rate of negative pore

pressure development has generally increased with increasing hydrate saturation (except in the case of MH 004). This is explained by the increasing degree of difficulty against volumetric deformation caused by hydrate densification taking place with increasing hydrate saturation becoming more predominant (resulting in a material of greater dilative volumetric tendency) over the pore space compressibility effects. The test MH 004 later develops a higher rate of negative pore pressure development representative of its higher hydrate saturation compared to the other tests. The initial behaviour of the test may have originated from a specimen specific irregularity.

In all cases, the hydrate-bearing specimens show insignificant positive pore pressure response compared to the water saturated non-hydrated specimens at the beginning of the deviatoric loading stage (corresponding to the contractive volumetric tendency), indicating that hydrate has stiffened the soil skeleton.

5.7.3 Response of hydrate-bearing specimens at low hydrate saturations (< 40%) consolidated at 1000 kPa initial effective confining stress to shearing at constant mass

The observed stress strain behaviour at low hydrate saturations (< 40%) and 1000 kPa initial effective confining stress for specimens MH 005, and MH 006 at respective hydrate saturations of 22.6% and 38.8% are presented in Figure 5.10. It should be noted that the actual pore pressure response of test MH 006 is unknown due to connectivity issues originating from hydrate plugging of connection tubing between specimen pore space and the pressure measuring device (the pore gas pressure during the shearing stage of the test was measured with a transducer

connected and placed closely to the top cap of the triaxial specimen). Behaviour similar to that of specimens consolidated at 500 kPa initial effective confining stress is observed with (a) strain hardening with mild softening at larger strains resulting from damping of negative pore pressure due to pore space compressibility, (b) lower tendency for initial positive pore pressure development representative of hydrate stiffened soil skeleton of low contractive volumetric tendency, and (d) later pore fluid pressure response representative of dilative volumetric tendency (Figure 5.10). The maximum deviator stresses occur at strains between 9-11%. The hydrate saturation dependency of the deviator stress at failure (Figure 5.8) and stiffness (Figure 5.9) are observed, indicating higher strength and stiffness at higher hydrate saturations. The initial rate of later negative pore pressure development of MH 005 is apparently equal to that of the water saturated non-hydrated soil specimen which is an indication of hydrate cementation and densification effects being predominant over the pore space compressibility effects at the particular hydrate saturation.

Comparison of maximum deviator stress and stiffness of these tests with the respective parameters obtained for those consolidated at 500 kPa initial effective confining stress indicates the initial effective confining stress dependency of strength (Figure 5.8) and stiffness (Figure 5.9). Greater strength (maximum deviator stress at failure) and initial tangential stiffness is obtained at higher initial effective confining stress.

5.7.4 Response of hydrate-bearing specimens at high hydrate saturations (> 40%) to shearing at constant mass

The maximum deviator stress and stiffness of specimens containing hydrate saturations > 40% are in general significantly higher than that of specimens with low saturations. The characteristic feature of stress-strain behaviour at these saturations is the brittle behaviour shown by most of the specimens (MH 008, MH 009, MH 010, MH 011, MH 012, and MH 013) with strain softening of deviator stress occurring subsequent to arriving at a peak stress (Figure 5.12, Figure 5.13, Figure 5.14, Figure 5.15, Figure 5.16, and Figure 5.17). Over the range of hydrate saturation > 40%, moderate to high negative pore pressures are developed during shearing compared to the previous cases; generally, larger negative pore pressures are developed at higher hydrate saturations as should be expected due to hydrate cementation and densification. The maximum rate of negative pore pressure response is generally reached after the peak in deviator stress.

Neither the maximum deviator stress nor the stiffness show a clear correlation with hydrate saturation or the initial effective confining stress (Figures 5.8 and 5.9). It is, however, interesting to note that the residual/ultimate strength of tested specimens (Figure 5.18) generally falls within a strength band of positive gradient showing a general increase in residual/ultimate strength with hydrate saturation. It can be hypothesised that the lack of correlation of peak strength with hydrate saturation is originating from factors such as non-uniformities in spatial distribution of hydrate, and whether the failure takes place following hydrate breakage or hydrate-mineral debonding (which is determined by the relative magnitude of intact strength of hydrate and hydrate–mineral bonding strength). Both intact hydrate strength and hydrate-mineral bonding strength

are complex functions of many variables including the properties of the mineral substrate, hydrate former, P/T conditions at which hydrate formation is carried out, and hydrate habit etc. [Hyodo et al., 2002; and Jung and Santamarina 2011]. Therefore, the strength behaviour becomes difficult to predict with the knowledge of hydrate saturation alone.

Irrespective of lack of correlation seen, the observed behaviour (i.e., brittle failure followed by reaching at a residual strength which is generally increasing with hydrate saturation) can be explained as related to peak strength being determined by intact hydrate strength and/or hydrate-mineral bonding strength at these hydrate saturations [Yun et al, 2007]. As can be seen in the case of many specimens, the peak strength is generally reached after initial positive pore pressure development (indicative of contract volumetric tendency) and some negative pore pressure development (indicative of dilative volumetric tendency) eventually causing hydrate breakage or de-bonding. Hydrate breakage or de-bonding (at peak) results in sudden loss of cohesion which is visible in the form of an abrupt drop in strength. Hydrate de-bonding at the hydrate-grain interface (interface shearing) should be expected to result in greater dilative volumetric tendency than in the case of hydrate breakage (or hydrate shearing). A graphical presentation of the aforementioned can be found in Figure 5.6 after Waite et al. [2009]. Most of our tests for which the pore gas pressure measurement is available (MH 009, MH 010, MH 011 and MH 013) show a further increase in the rate of negative pore pressure development corresponding to greater dilative volumetric tendency at the respective strains in the post-peak region. The rate of negative pore pressure development reaches a peak at 2%, 2.6%, 1.4%, and 4.7% strain for the aforementioned specimens respectively. Therefore, it is possible to expect hydrate-mineral de-bonding to take place rather than hydrate breakage under the corresponding test P/T conditions

and surface properties of Ottawa sand used for testing. However, verification of the aforementioned awaits technology development such as integration of grain scale visual imaging techniques into triaxial testing.

The increased tendency for negative pore pressure development observed in the post-peak region may also be viewed as an attempt to overcome naturally present grain interlocking and hydrate added resistance to deformation. The strength of soil material is a combination of cohesive resistance and effective stress dependent frictional resistance. The aforementioned tendency for negative pore pressure development (in the post-peak region) resulting in greater effective stress, however, is aligned with reduction of strength as previously mentioned. The observation can be explained as increased frictional resistance due to increased effective stress being not adequate to overcome loss of cohesive strength resulting from hydrate de-bonding. However, as clearly visible in the case of specimen MH 013 (Figure 5.17), continuous development of frictional strength later overcomes the loss of cohesive strength resulting in overall strength regain.

Further as our specimens are consisting of free gas in the pore space, development of negative pore pressure adequate to prevent volume change is hindered. Therefore the specimens overcome resistance to deformation leading to failure, reaching at residual strengths and development of shear planes.

Shearing could be expected to generate heat due to frictional resistance causing localized dissociation of hydrates at the respective sliding planes. However, the measured global P/T conditions associated with the series of hydrate-bearing tests indicated that the specimens

remained within the hydrate stability zone for methane-water system throughout application of deviatoric loading. Whether the amount of frictional heat generated under the respective P/T conditions and deformation rates is adequate to initiate hydrate dissociation would be an interesting subject for future research and integration of new technologies such as thermal imaging to obtain visual evidence of such behaviour is recommended. Although little evidence is found in literature on frictional melting of hydrates, such evidence is available on frictional melting of water ice-which is considered a close analogy for hydrates. It is shown that the quantity of frictional heat and resultant melting is deformation rate and temperature dependent [Bowden and Tabor, 1950; Evans et al., 1976; Marmo et al., 2005]. Upon generation of such frictional heating, continuous hydrate dissociation is not expected as hydrate dissociation is an endothermic process which results in temperature reduction in the locality leading to self-preservation of hydrate. Localized hydrate dissociation may initially produce a lubricating effect at the shearing surface. Also, it may partially reduce the greater dilative volumetric tendency existing in the presence of hydrate and could be considered as a secondary reason for reduced later tendency for negative pore pressure development. The ultimate/residual strength is apparently representative of the hydrate saturation (Figure 5.18). The residual strength generally increases with hydrate saturation.

Detection of frictional heat generation as mentioned above originates with the early observations of Bowden and Tabor [1959] which demonstrated that small sparkling points of light occurred at the interface between glass or quartz surfaces sliding relative to each other in the dark. This is recognized as due to friction between grains generating heat [Loung, 1986] and the technique, infrared thermography, a non-destructive method of observing the energy dissipation ability of

granular material is used successfully to detect heat generated by friction between grains of sheared sand [Luong, 1896; Luong, 2007]. The method has been used most successfully at stress states beyond the characteristic state for drained shearing under application of cyclic or vibratory loading. In the case of triaxial compression test, the characteristic state refers to the stress state at which the transformation in deformation mechanism from compression to dilation takes place for a granular assembly of grains which is also characterised by zero rate of change in volumetric strain under drained conditions. “Within the subcharacteristic domain below the characteristic threshold” (characteristic state), “the intergranular contacts remain stable” and continuous loading causes small slip and greater “entanglement” and “tightening of constituent grains” resulting in relatively small quantity of heat generation [Luong, 2007]. However, beyond the characteristic state, the “intergranular contacts become unstable, leading to significant sliding caused by interlocking breakdown” and significantly large quantities of frictional heat is dissipated [Luong, 2007]. The application of the method under monotonic loading and constant mass conditions as relevant to the present research is not documented; however, it would be interesting to investigate the possible use of this technology as relevant to testing of present study since it would provide visual evidence of hydrate dissociation due to frictional heat suggested above.

5.7.5 End of test visual observations of test specimens

Visual observations of the specimens were performed at the end of each test to identify modes of failure. These observations provided evidence of shear banding for the tests MH 008, MH 009, MH 010, MH 012, and MH 013. The photographs of the sheared specimens or deformation band scars left on the membranes are presented in Figure 5.19. A vacuum was applied at the bottom of

the specimens in order to preserve the features of the deformed specimen, immediately prior to releasing the confining pressure at the end of respective tests. The photographs were taken once the confining cell was removed. Shear banding provides evidence of volume change during constant mass shearing of the test specimens. Slight increase in strength observed towards the end of certain tests (as in the case of MH 009) may be attributed to failure mode resulting in restricted movement of failed soil wedge (Figure 5.19 (b)).

The measured inclination of the shearing plane (θ) to the direction of minor principal stress varied approximately from 54° to 65° . With the assumption of the classical Mohr-Coulomb solution for the orientation of the failure plane, the mobilised friction angle (ϕ) for the respective specimens can be calculated using the relation $\theta = 45^\circ + \phi/2$. The obtained values of mobilised friction angle that vary between 18° and 40° are presented in Table 5.9. However, it should be noted that only limited information of the specimen deformation mechanism can be obtained from end of test visual observations. Use of technology such as Computer Tomographic (CT) scanning when performed at multiple stages during loading allows obtaining greater details of initiation and development of strain localisation [Alshibli et al., 2006; and Kneafsey et al., 2010]. Use of scanning electron microscopy (SEM) can further deepen the investigation allowing identification of grain scale features within and in the vicinity of deformation zones [Sulem and Outfroukh, 2006]. However, integration of these technologies (particularly SEM) with hydrate-bearing soil testing systems awaits further technological advancement mainly due to requirements of maintaining P/T conditions suitable for ensuring hydrate stability.

5.8 The stress path plots

5.8.1 The definition of stress path

“A stress path is a locus of points of maximum shear stress experienced by an element in going from one state of stress to another” [Lambe, 1967]. When the effective stress path is considered, the maximum shear stress q is given by $q = (\sigma'_1 - \sigma'_3) / 2$ at the stress state $p' = (\sigma'_1 + \sigma'_3) / 2$. An illustration is provided in Figure 5.20 with an explanation of the integration of the Mohr-Coulomb failure criterion in the $p' - q$ space. The presentation of our test data in the $p' - q$ space further highlights the differences in stress-strain behaviour between water saturated sand specimens and hydrate-bearing specimens. It also provides direction for future research to further our understanding of hydrate-bearing soils.

5.8.2 $p' - q$ plots for hydrate-bearing specimens

The $p' - q$ plots where $q = (\sigma_1 - \sigma_3) / 2$ and $p' = (\sigma'_1 + \sigma'_3) / 2$, for all test specimens are provided in Figure 5.21 categorised using the initial effective confining stress and hydrate saturation. The specimens with relatively higher hydrate saturation generally marks higher shear strength at failure (denoted by solid green circles of Figure 5.21(a)). The hydrate saturation appears to increase the density of the granular packing resulting in higher strength.

The dashed blue line represents the steady state obtained using the conditions at phase transformation for the water saturated reference tests performed at the corresponding initial effective confining stress. The dashed red line represents the Mohr-Coulomb failure criterion for the non-cohesive water saturated sand specimens. The gradient of the line relates to the

mobilised friction angle as given by $\tan \beta = \sin \phi'$. Integration of Mohr-Coulomb failure criterion suggests that the points of maximum shear stress at failure (corresponding to maximum deviator stress) obtained for a given soil at different initial effective confining stress (ECS) lie on a straight line on the $p' - q$ plot (denoted by dashed green line in Figure 5.21 (a)). When zero cohesion is assumed for sand, the maximum shear stress at failure is given by $q_f = \sin \phi' p'_f$. It appears that our hydrate-bearing tests generally do not plot on this line of zero cohesion. Therefore, if the friction angle is assumed to be unaffected by the presence of hydrate, it can be concluded that hydrate adds cohesion to the granular material. This can only be verified by performing triaxial compression tests at given host sediment void ratio and constant hydrate saturation at varying initial effective confining stress to determine if the mobilised friction angle at the respective hydrate saturation has changed from that of non-hydrated specimen. The magnitude of hydrate added cohesion can be determined as given by the intercept of the plot ($= c' \cos \phi'$). Repeating the aforementioned set of experiments at various hydrate saturations would also allow the determination of the correlation between hydrate saturation and the mobilised friction angle. According to Soga et al. [2006] and Waite et al. [2009], the friction angle is independent of hydrate saturation resulting in the increased strength reported in the presence of hydrate being completely attributed to hydrate added cohesion. The experimental verification of the aforementioned is suggested for future research.

5.9 Results

The following section summarises the findings of this research as to the initial effective confining stress/hydrate saturation dependency of strength/stiffness. Also, it presents a

comparison of the present work to the findings of Yun et al. [2007] and Santamarina and Ruppel [2008].

5.9.1 Strength and stiffness dependency on initial effective confining stress

(a) Strength versus initial effective confining stress

- The observations reveal a positive relationship between strength and effective confining stress at low hydrate saturations (< 40%). Greater strength is obtained at greater initial effective confinement.
- The observations reveal no clear correlation between strength and effective confining stress at high hydrate saturations (> 40%).
- The strength of hydrate-bearing sediment at low hydrate saturations is hypothesised to be predominantly determined by a combination of (a) frictional resistance between mineral grains and (b) hydrate-added cohesion (due to cementation) and/ or frictional resistance (due to densification of the soil material). The frictional resistance determined by the mineral contact stress is related to the effective confinement. Thus the hypothesised strength behaviour justifies the observed correlation between strength and initial effective confining stress.
- However, at high hydrate saturations, it is hypothesised that strength is predominantly determined by the intact hydrate strength and/or hydrate-mineral bonding strength, the degree to which the strength is influenced by the effective confinement depends upon the degree to which the intact hydrate strength and/or hydrate-mineral bonding strength is affected by the effective confinement. Such evidence of intact hydrate strength and/or hydrate-mineral bonding strength dependency on effective confinement is hardly

addressed in existing literature. However, the intact hydrate strength is known to be governed by the formation pore fluid pressure [Hyodo et al., 2002] which is a constant (9000 kPa) for the entire set of specimens subjected to testing under this research.

Therefore, there exists only little possibility that the hydrate strength is determined by the initial effective confinement; hence the above hypothesis of strength behaviour at high hydrate saturations justifies the lack of correlation between strength and effective confinement.

(b) Stiffness versus initial effective confining stress

- The observations reveal greater initial tangential stiffness at confining stress at low hydrate saturations (< 40%). However, no clear correlation between secant stiffness and effective confining stress is observed both at low (< 40%) and high hydrate saturations (> 40%).
- The stiffness of hydrate-bearing particulate soil material can be considered as determined by the packing density of the host sediment, grain interlocking between the mineral particles, and hydrate cementation. Of above factors, the packing density is influenced by the effective confinement; thus stiffness may expect to be influenced by effective confinement. However, at the initial void ratio of 0.57 (corresponding to a relative density of 72%) it appears that the differences in stiffness between the specimens tested at 500 kPa and 1000 kPa initial effective confinement are only visible at low hydrate saturations where the hydrate cementation effects on stiffness are not so predominant.

5.9.2 Strength and stiffness dependency on hydrate saturation

(a) Strength versus hydrate saturation

- The observations reveal a positive relationship between strength and hydrate saturation at low hydrate saturations ($< 40\%$). Greater strength is obtained at greater hydrate saturations.
- The observations reveal no clear correlation between strength and hydrate saturation at high hydrate saturations ($> 40\%$). However, significantly higher strengths than that obtained at low saturations are reported.
- At low saturations, increase in the degree of hydrate saturation results in greater volumetric tendency for dilation (due to hydrate added resistance to deformation resulting from densification and cementation). A dilative sediment undergoing shearing under constant mass conditions develop negative pore fluid pressures. Consequently, the effective confinement on the sediment increases and thus is the strength.
- At high hydrate saturations ($> 40\%$) peak strength is governed by intact hydrate strength and/or hydrate-mineral bonding strength and therefore shows a poor correlation between strength and hydrate saturation. However, the residual/ultimate strength shows a positive correlation with hydrate saturation; the underlying mechanisms are revisited under Section 5.10.

(b) Stiffness versus hydrate saturation

- The observations reveal a positive relationship between stiffness and hydrate saturation at low hydrate saturations ($< 40\%$). Greater stiffness is obtained at greater hydrate saturations. This could be attributed to increased cementing effect with increasing hydrate

saturation. The initial tangential stiffness is better correlated with hydrate saturation than secant stiffness.

- The observations reveal no clear correlation between stiffness and hydrate saturation at high hydrate saturations (> 40%). However, significantly higher stiffness than that obtained at low saturations is reported. The factors such as special variability in hydrate distribution may have resulted in a poor correlation between stiffness and hydrate saturation.

In overall, the strength/stiffness behaviour is consistent with the speculations made in Chapter 3 of the grain cementing/coating growth habit of hydrate relevant to the hydrate formation method followed in the preparation of the test specimens. The grain scale mechanisms underlying the behaviour are revisited in Section 5.7.

5.9.3 Comparison to previous work

The Figure 5.22 explores the strength-hydrate saturation correlation for hydrate-bearing sand specimens, including the data of present study and those of Yun et al. [2007]. Both the data sets exhibit similar non-linear trend of increasing strength with increasing hydrate saturation. It should be noted that the results of Yun et al. [2007] are obtained for THF hydrates with pore water saturation, where pore filling to load bearing habits of hydrate can be expected. The hydrate formation method employed in the present study results in grain cementing habit of hydrate formation. Further information of these different hydrate habits were presented in Chapter 2. The strength results of the present work generally plot above those of Yun et al. [2007]. The differences in strength between the two studies may be originating from differences

in host sediment properties and differences in hydrate habit. Comparison of the non-hydrated specimen strengths of the two studies reveals a possible influence of host sediment differences.

A comparison of stiffness-strength correlation (Figure 5.23) reveals greater differences between the two formation habits. The cementing habit (this study) generates greater stiffness, particularly at higher hydrate saturations.

From Figures 5.22 and 5.23, there is an indication that stiffness of hydrate-bearing sediments is greatly influenced by the hydrate habit (or in other words, the degree of inter-particle bonding due to hydrate cementation); while, the strength of hydrate-bearing sediments does not show a significant difference between the two formation habits.

The comparison of our results to previous work is further extended to compare our results with those predicted by the Santamarina and Ruppel [2008] model with the intention of generating further understanding of the underlying mechanisms of strength/stiffness behaviour.

Santamarina and Ruppel [2008] developed an expression for undrained shear strength of hydrate-bearing sediments based on their observation of experimental data generated by Yun et al. [2007] for sand specimens consisting THF hydrate and water in the pore space. Their observations can be listed as follows: (a) at low hydrate saturations the strength is determined by effective stress controlled particle frictional resistance, (b) the contribution of intact hydrate strength and/or hydrate-mineral bonding strength increases non-linearly with increasing hydrate saturation, and (c) the effects of pore space presence of hydrate are more pronounced at lower host sediment

porosities. The model captures these observations and is given by equation 5.17. The model parameters a and b were obtained by fitting the model results to experimental data of Yun et al. [2007].

$$S_u = a(\sigma'_3)_o + bq_h \left(\frac{S_h}{n} \right)^2 \quad (5.17)$$

S_u is the undrained shear strength (MPa); $(\sigma'_3)_o$ is the initial effective confining stress (MPa); q_h is the hydrate strength (= 8 MPa, after Durham et al., 2005); S_h is the hydrate saturation ($0 < S_h < 1$); n is the porosity of the medium; a is a model coefficient which captures friction and pore pressure generation in sediments; and “ b is a model coefficient which captures the hydrate’s ability to contribute to sediment strength and thus “reflect the formation method/habit of hydrate in a given soil” [Santamarina and Ruppel, 2008].

Comparison of our results to those predicted by the above expression with the fitted model coefficients $a = 1.55$ and $b = 0.14$ (derived for F110 Ottawa Sand) are shown in Figure 5.24. The predicted versus measured strength of present study and Yun et al. [2007] is given in Figure 5.25. It should be noted that the values of a and b of Santamarina and Ruppel [2008] model are obtained by fitting the model to experimental data of Yun et al. [2007] for THF hydrates of pore filling to load bearing hydrate habits. In general, for most of our test specimens, the measured strength appears to be greater than the predicted strength. The difference could be attributed to one or many of the following factors: (1) the general error associated with the model predictions

(note that the data of Yun et al. [2007] also exhibits similar scatter about the trend of model predicted strength), (2) mismatch of the fitted values of the model coefficients with the host sediment properties and hydrate-cemented nature of sand subjected to testing in the present study, and (3) mismatch of model assumptions with the properties of hydrate-cemented sands of the present study originating from differences between the nature of the hydrate-sediment interaction (or the hydrate growth habit) of the two studies. In the following discussion we explore the contribution of the aforementioned factors (2) and (3) to the differences between the predicted and the observed strength.

Multiple linear regression analysis was employed to calibrate the Santamarina and Ruppel [2008] model to best fit our data set with the intension of eliminating undesirable influence of mismatching model coefficients in the interpretation of the observations. As a result an $a = 2.30$ and $b = 0.12$ was obtained. The Figure 5.26 and Figure 5.27 illustrate the better fit obtained with the use of calibrated model.

Santamarina and Ruppel [2008] model the contribution of hydrate to strength of aggregated material as equal to $bq_h \left(\frac{S_h}{n} \right)^2$, and expect the parameter b to be reflective of the formation method/habit of hydrate. Careful observation of the equation suggests that for a given sediment of known porosity n , the contribution of hydrate to strength is a function of the degree of hydrate saturation S_h and the hydrate strength q_h . The hydrate strength obtained after Durham et al. [2005] represent the hydrate breakage strength in shear. As such it appears that the

expression represents pore filling or load bearing habits of hydrate where the grain cementing nature of hydrate (or hydrate-mineral bonding effect) is insignificant. As observed in Figure 5.26 and Figure 5.27 the data fit of the present study with the Santamarina and Ruppel [2008] model suggests that the influence of potential hydrate-grain cementation on the strength is not significant up to 50% hydrate saturation. However, at higher hydrate saturations our results deviate from behaviour of sediments with pore filling to load bearing hydrate habit, and the model is incapable of capturing the behaviour at these hydrate saturations.

Interestingly, if the model calibration is performed at each different initial effective confining stress (500 kPa and 1000 kPa) to generate 2 sets of values for a and b ($a = 3.10$ and $b = 0.08$ at 500 kPa effective confinement and $a = 2.45$ and $b = 0.05$ 1000 kPa effective confinement), a noticeable improvement in the predicted strength can be obtained (Figure 5.28). Therefore it appears that differentiating between the initial effective confinement in the calibration of the model constants help isolating the hydrate saturation effects on the model predicted strength.

5.10 Behaviour of hydrate-cemented soils in summary

The following concludes the presentation of the finding of this research in summary with grain-scale mechanisms underlying the observed strength/stiffness behaviour of hydrate-cemented sediments under constant mass shearing. The understanding of the mechanisms taking place at particle level is then used to predict the variations of strength/stiffness behaviour that should be expected with non-cementing hydrate growth habits. In overall the above comparison of our results with Yun et al. [2007] and Santamarina and Ruppel [2008] suggest that the differences in strength behaviour between pore filling/load bearing and cementing hydrate habits are more

prominent at high hydrate saturations. According to analysis of our experimental results, at high hydrate-saturations the strength is governed by intact hydrate strength and/or hydrate-mineral bonding strength.

(a) Grain-scale mechanisms at low hydrate saturations ($< 40\%$) can be summarised as follows:

- Particles develop frictional resistance in response to shearing
- Deformation and particle re-arrangement is restricted due to cohesion induced by hydrate cementation at grain contacts and accumulation on grain surfaces. Thus, stiffer response and greater volumetric tendency for dilation compared to non-hydrated sediments should be expected.
- Increased volumetric tendency for dilation results in greater tendency for negative pore pressure generation under constant mass shearing and therefore, increased strength compared to non cementing sediments should be expected.

(b) Grain-scale mechanisms at high hydrate saturations ($> 40\%$) can be summarised as follows:

- The development of frictional resistance upon application of loading is hindered within the hydrate stiffened aggregated body of particulate soil material. Particularly the initial contractive volumetric tendency is low.
- Further development of resistance to applied loading develops with appearance of dilative volumetric tendency. In the case of constant mass shearing with pore space consisting of free gas, volumetric change is allowed. However deformation is restricted

within the hydrate stiffened body. Resistance to applied loading is borne by the hydrate mass, which later fails upon reaching at intact hydrate strength and/or hydrate- mineral bonding strength. According to our observations, hydrate failure marks a peak in the stress-strain curve.

- Hydrate failure results in sudden loss of cohesion. The failure strength is thus governed by the intact hydrate strength and/or hydrate-mineral bonding strength. Generally, greater stiffness than that at low saturation should be expected.
- Upon hydrate breakage or de-bonding, dilative volumetric tendency further increases as mineral grain interlocking and hydrate-induced resistance to deformation is attempted to overcome. This is visible in the form of increasing rate of negative pore pressure development in the post-peak region.
- As in the case of our test specimens where the pore space is compressible, volumetric deformation takes place by overcoming the resistance to deformation with dissipation of negative pore pressure. Localised zones of deformation may appear and the material reaches residual/ultimate strength which is predominantly governed by the hydrate saturation.

In the case of non-cementing hydrate growth habits the following variations of the strength/stiffness behaviour should be expected under constant mass shearing.

- In the case of non-cementing hydrates, the effect of hydrate pore space presence can be identified as densification of the soil structure. Therefore, the soil behaves as a material of greater density than that given by the void ratio of the soil mineral grain packing.

- At low saturations where the hydrate added cohesion is low for cementing hydrates, no significant difference in strength should be expected between cementing and non-cementing growth habits. In other words the strength is determined by hydrate saturation but not by the growth habit.
- Less stiff response should be expected with non-cementing hydrates as hydrate cementation added resistance to deformation is non-existent.
- At high hydrate saturations the strength is determined by intact hydrate strength (but not by hydrate-mineral bonding strength). Also, dependant upon the hydrate formation methodology, un-reacted water may present surrounding the grains and within hydrate masses. Such features can also affect the strength of uncemented sediments as over pressurization of trapped water can promote hydrate breakage as negative global pore fluid pressures develop in response to shearing under constant mass.
- At very high hydrate saturations where the particulate body tend to behave as an aggregated body, the stiffness of non-cementing hydrate-bearing sediment may expect to be as comparable to that of cementing hydrates.

5.11 Remarks

The following few remarks upon review of experimental program presented in this thesis are presented with the intention of providing guidance for future research. First, we identify the need to develop experimental methods to properly isolate the hydrate effects on soil behaviour under undrained triaxial conditions from drained effects due to pore space presence of free gas and resulting pressure dissipation. Achieving complete water saturation of hydrate-cemented specimens will require overcoming challenges present due to:

- low permeability of hydrate-cemented media
- possibilities of hydrate de-bonding from grain surfaces or grain contacts and being carried away as particulate matter from the specimen affecting hydrate saturation
- hydrate dissolution or reformation depending upon the dissolved methane concentration in percolating water and P/T conditions.

Secondly, further triaxial compression testing may be performed for a given soil material to study the comparative behaviour between the cases of undrained with no pore space presence of free gas, constant mass with pore space presence of free gas, and drained. Thirdly, we identify the need to integrate thermal/visual imaging techniques to further facilitate grain scale studies.

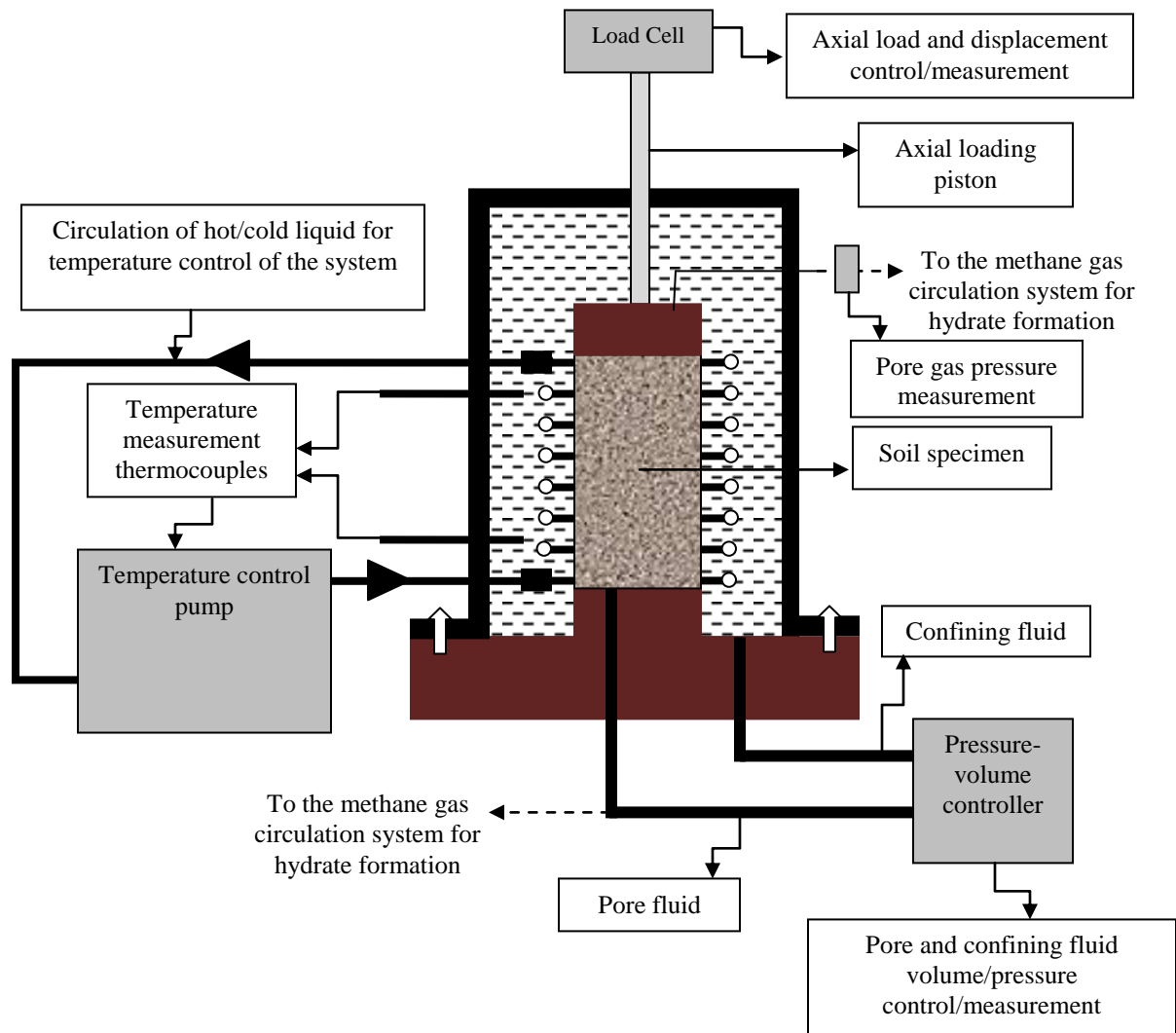


Figure 5.1: High pressure and low/high temperature capable triaxial soil testing apparatus

-The axial load, axial deformation, confining fluid pressure/volume and pore gas pressure are measured during a typical triaxial test at constant mass for hydrate-bearing soil consisting of hydrate and free gas within its pore space. The system temperature is maintained constant within the hydrate stability zone during the test.

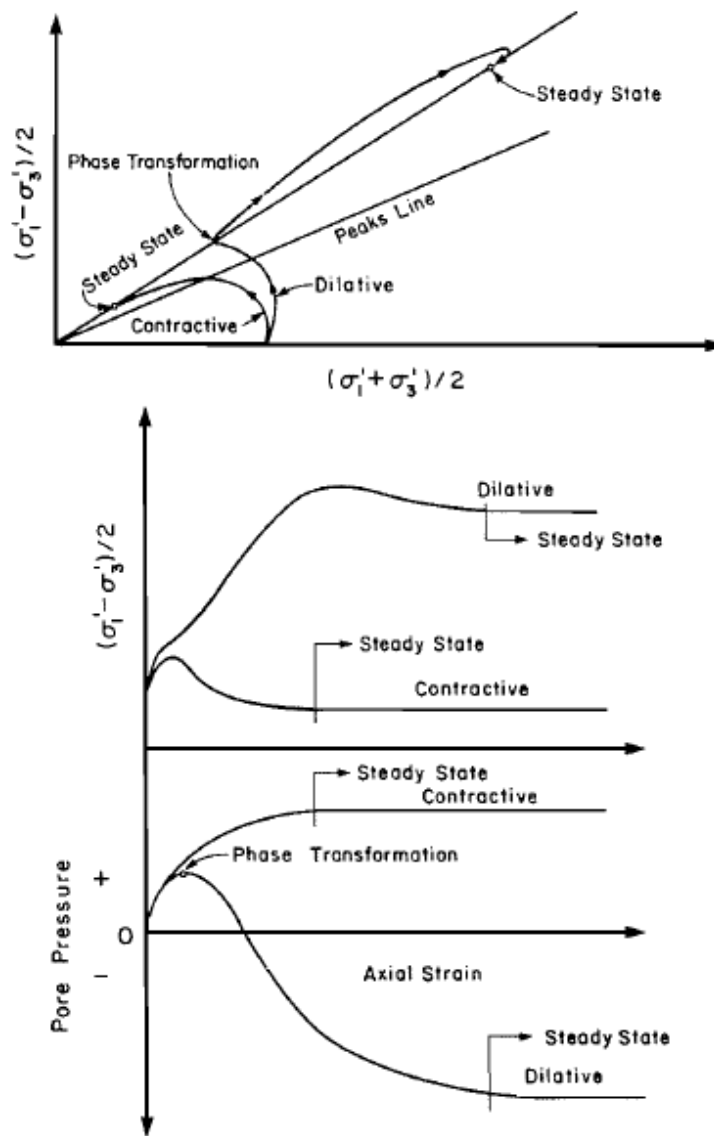
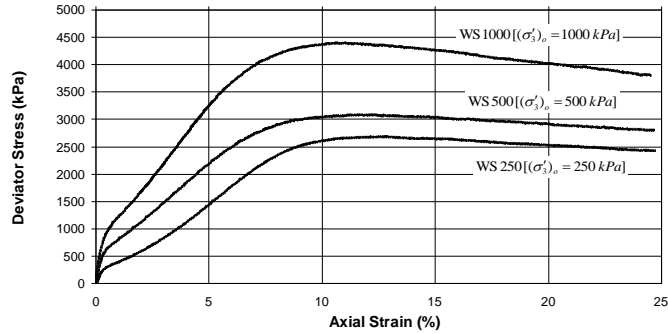


Figure 5.2: Phase transformation and steady states during undrained shear

- (Adopted from Negussey et al., 1987) - Dense (dilative) materials initially develop positive excess pore pressure (indicative of contraction tendency); then reach at a point of maximum pore pressure (point of phase transformation); and undergo reduction of pore pressure afterwards (indicative of dilative tendency) as the steady state is reached at large strains

(a)



(b)

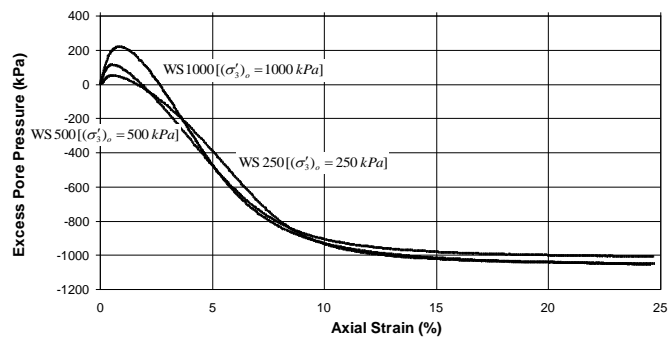


Figure 5.3: (a) Deviator stress and axial strain and (b) pore fluid pressure response to deviatoric loading as measured on water saturated sand specimens at different initial effective confining stresses

Close observation of the pore pressure development allows identification of potential signs of dissolved gas exsolution from pore water. The crossing of excess pore pressure curves may have resulted from the differences in the degree of gas exsolution between the specimens, and the resulting differences in the negative pore pressure development.

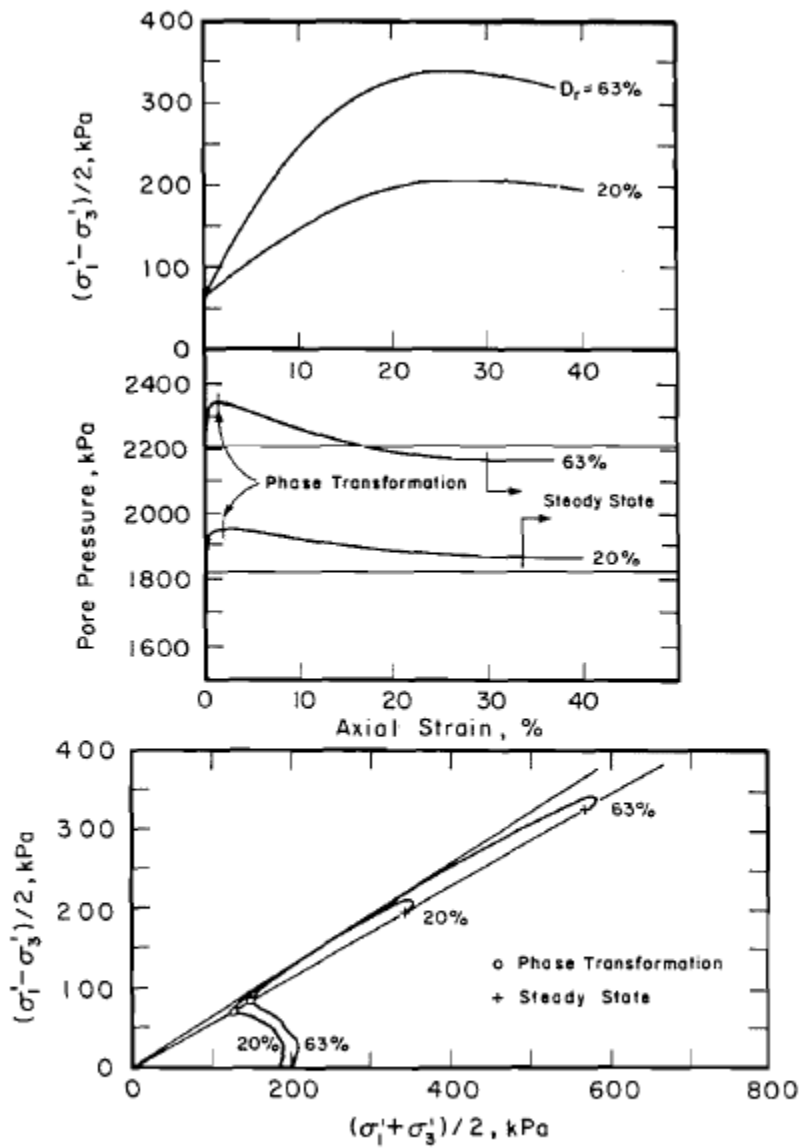


Figure 5.4: The identity of the friction angle mobilized at undrained phase transformation and at the friction angle mobilized at steady state

- (Adopted from Negussey et al., 1987 based on the experimental results obtained for dilative Brenda Mine tailings)

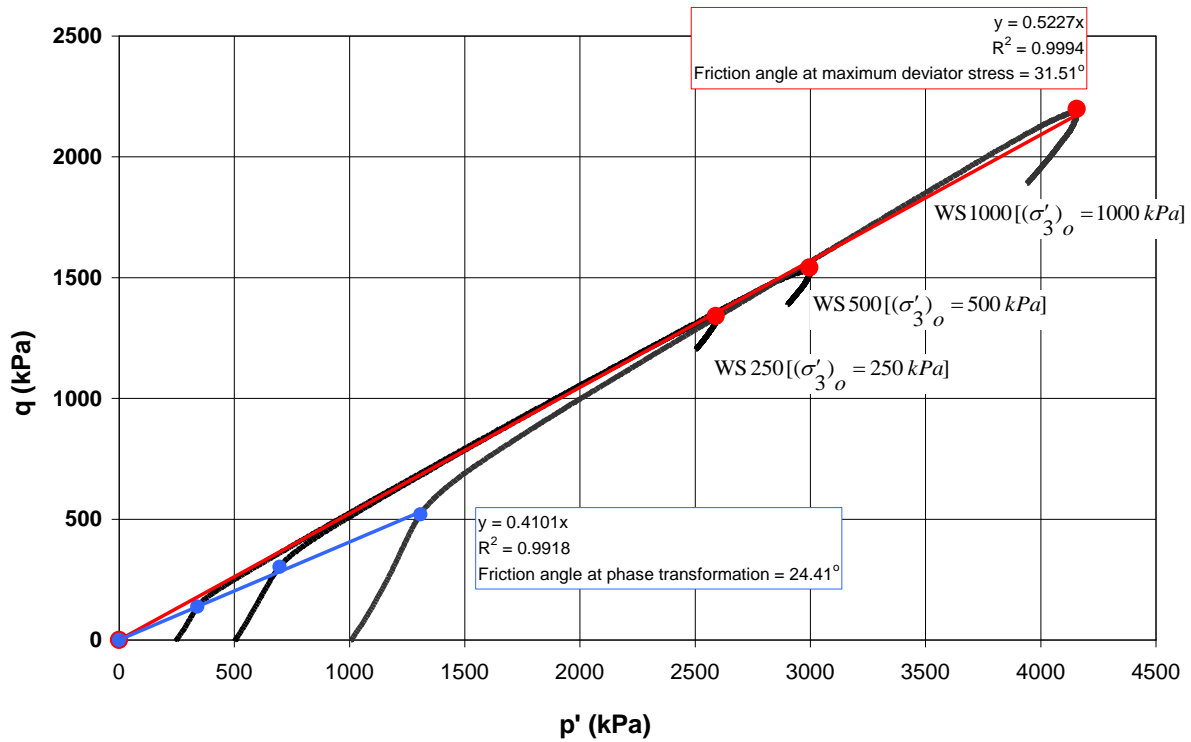


Figure 5.5: $p' - q$ plots for water saturated sand specimens at different initial effective confining stresses [$q = (\sigma'_1 - \sigma'_3)/2$ and $p' = (\sigma'_1 + \sigma'_3)/2$]

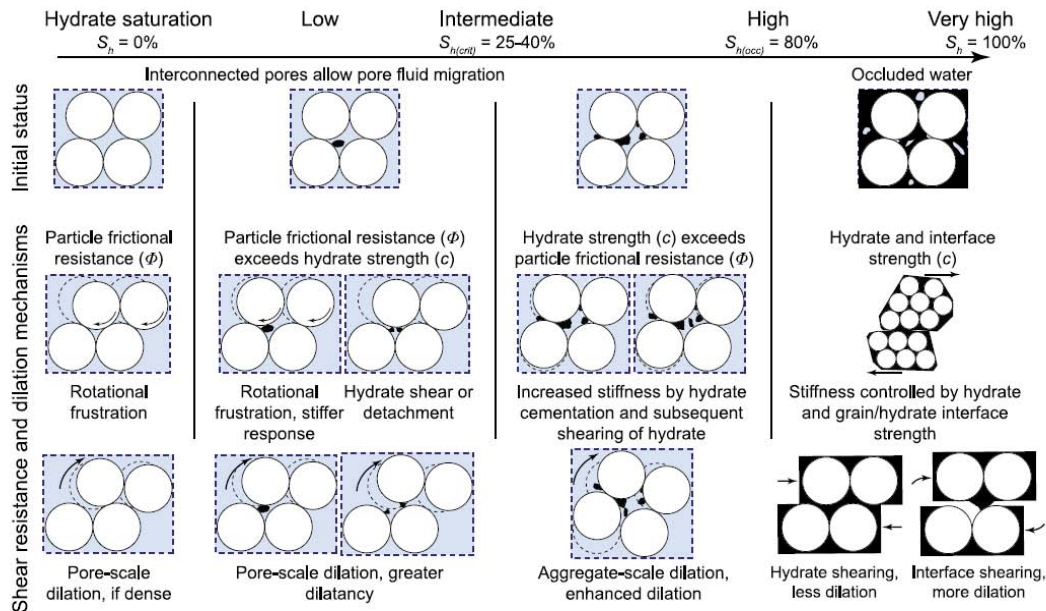
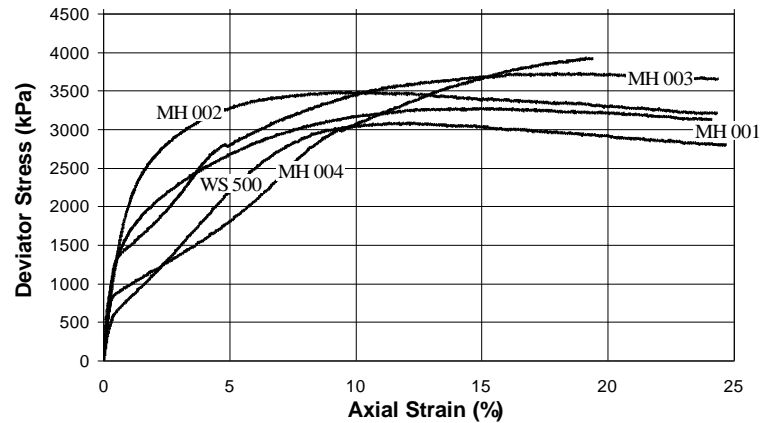


Figure 5.6: Grain scale mechanisms governing stress-strain behaviour of hydrate-bearing sediments

- (Adopted from Waite et al. [2009] developed based on experimental results obtained for THF hydrate-bearing sand specimens by Yun et al. [2007]) - The sediment grains are indicated as white circles, hydrate as black, and water as blue. At low hydrate saturations (0 to 40%), the model suggests that the shear strength is mainly determined by the frictional resistance between the soil grains. Stiffness is expected to increase with hydrate saturation. At moderate hydrate saturations (40 to 80%), it is suggested that a stiffer response should be expected with increased dilation taking place at aggregate scale, and hydrate cementation induced cohesion exceeds the frictional resistance between soil grains. At very high hydrate saturations (> 80%), it is suggested that soil behaves more like a continuum the shear strength, stiffness, and the overall stress-strain behaviour of which is determined by intact hydrate strength and/or hydrate-mineral bonding strength. According to Hyodo et al. [2002] and Jung and Santamarina [2011], both intact hydrate strength and hydrate-mineral bonding strength are complex functions of many variables

including the properties of the mineral substrate, hydrate former, P/T conditions at which hydrate formation is carried out, and hydrate habit etc. Therefore, the behaviour becomes difficult to predict.

(a)



(b)

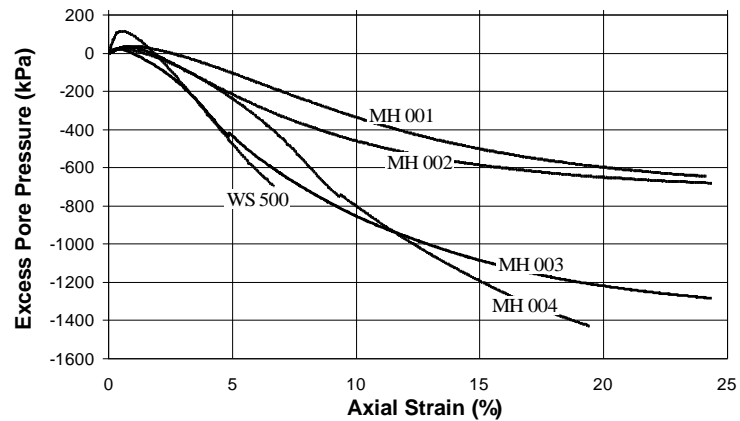


Figure 5.7: (a) Deviator stress and axial strain and (b) pore fluid pressure response to deviatoric loading as measured on hydrate-bearing specimens at low hydrate saturations (<40%) at 500 kPa initial effective confining stress

The lower tendency for initial positive pore pressure generation appears to increase with increasing hydrate saturation. Also the rate of negative pressure development has generally increased with increasing hydrate saturation as should be expected with increasing tendency for background volumetric deformation that exists with hydrate densification of the soil medium.

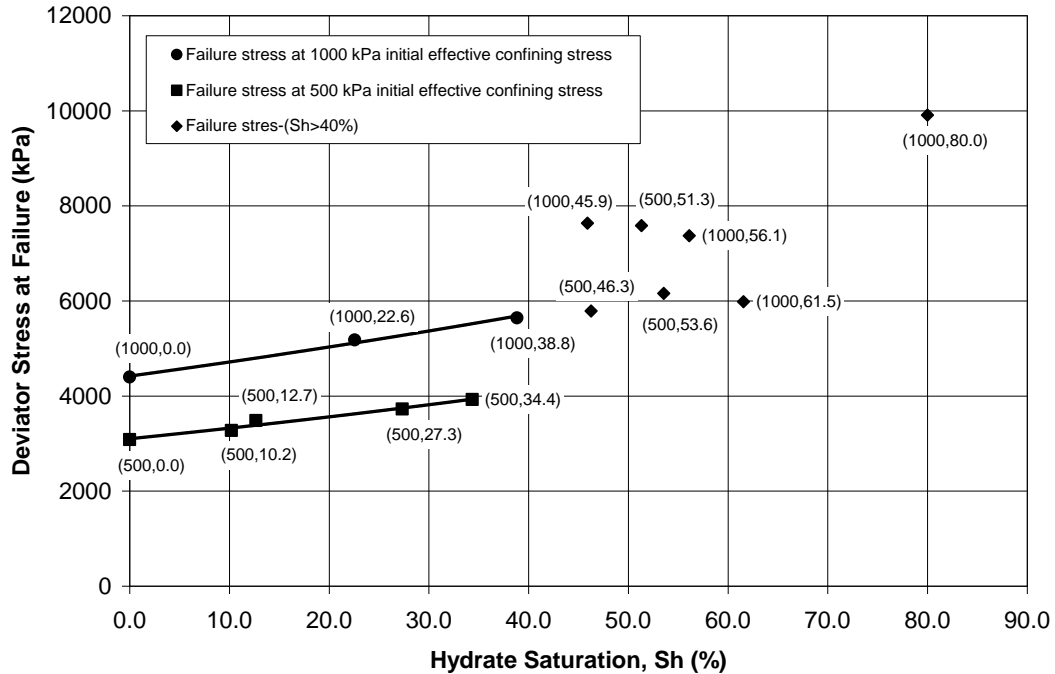
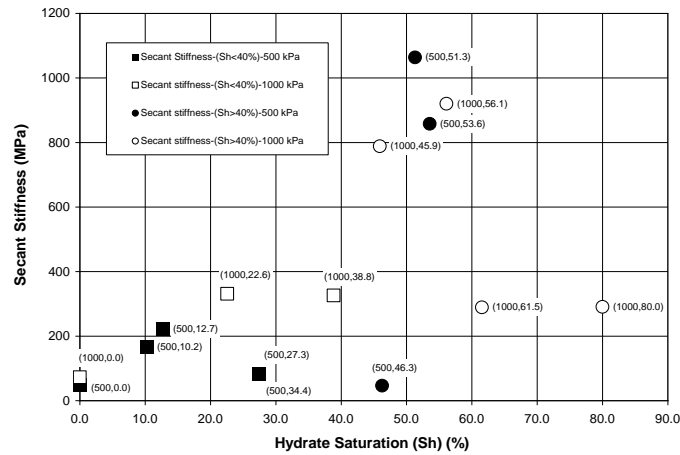


Figure 5.8: Hydrate saturation dependency of deviator stress at failure at different initial effective confining stress (ECS)

- The solid line joining the solid squares illustrates the trend at 500 kPa initial ECS for hydrate saturations < 40%. The solid line joining the solid circles illustrates the trend at 1000 kPa initial ECS. At higher hydrate saturations, the plot of data points (solid diamonds) illustrates the loss of clear correlation of deviator stress at failure with initial ECS and hydrate saturation. The data points are labelled with initial ECS in kPa and hydrate saturation appearing within parenthesis () respectively. Refer to Figure 5.18 for the variation of residual/ultimate strength at high hydrate saturations (> 40%) with initial ECS.

(a)



(b)

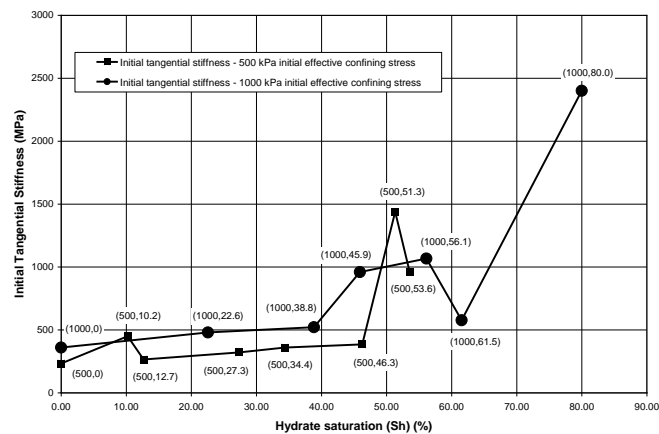
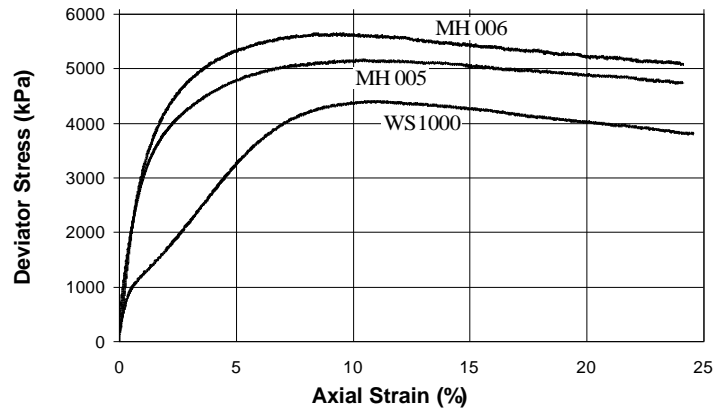


Figure 5.9: Hydrate saturation dependency of secant stiffness at different initial effective confining stress (ECS), and (b) hydrate saturation dependency of initial tangential stiffness at different initial effective confining stress (ECS)

- The higher the hydrate saturation, the greater the stiffness. Apparently, stiffness only slightly affected by the initial ECS. The data points are labelled with initial ECS in kPa and hydrate saturation appearing within parenthesis () respectively.

(a)



(b)

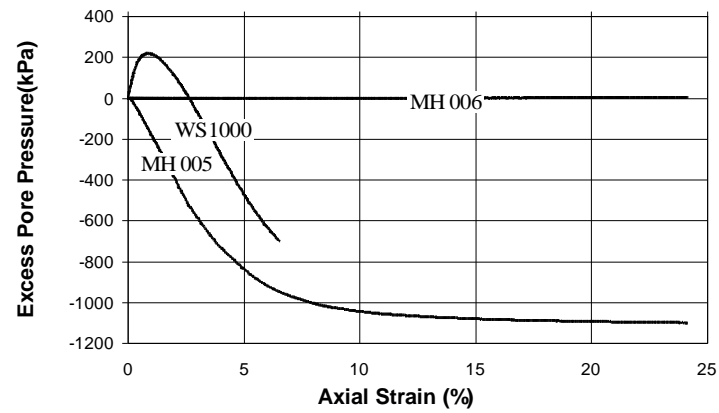


Figure 5.10: (a) Deviator stress and axial strain, (b) pore fluid pressure response and (c) volume change behaviour in response to deviatoric loading as measured on hydrate-bearing specimens at low hydrate saturations (<40%) at 1000 kPa initial effective confining stress

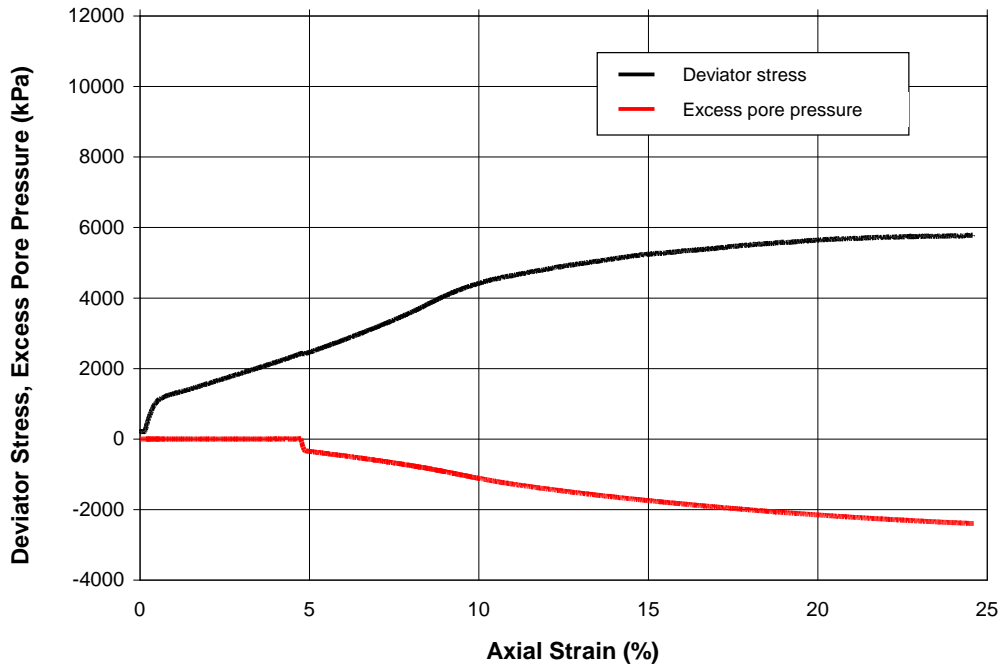


Figure 5.11: Deviator stress and excess pore fluid pressure for test MH 007 (at hydrate saturation of 46.3%) during shearing at 500 kPa initial ECS

- During shearing, the pore fluid pressure was monitored using an external pore pressure transducer connected to the top cap of the triaxial specimen. The zero response of pore pressure development observed in the early portion of this test may have been caused by a hydrate plug between the specimen and the pressure transducer. As the pore pressure within the specimen drops in response to deviatoric loading under constant mass conditions, the hydrate plug appears to be removed by the differential pressure opening the specimen to the pressure transducer and allowing subsequent monitoring of negative pore pressure development.

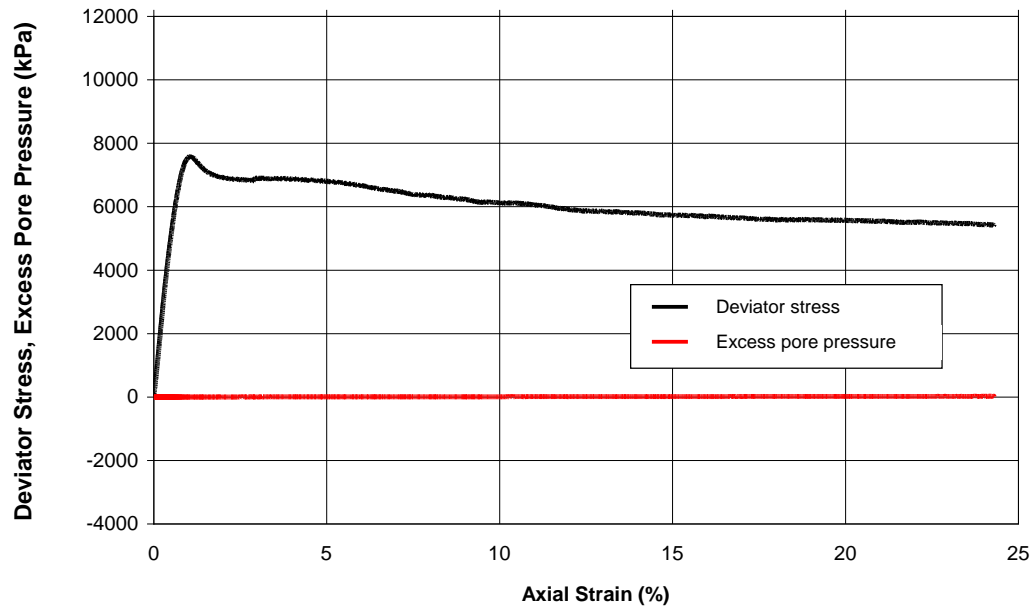


Figure 5.12: Deviator stress and excess pore fluid pressure for test MH 008 (at hydrate saturation of 51.3%) during shearing 500 kPa initial ECS

- The zero response of pore pressure development observed in this test may have been caused by a hydrate plug between the specimen pore space and the pore pressure measuring transducer connected to the top cap of the specimen. The deviator stress response is characterised by brittle failure, which features reaching at a peak (representative of hydrate breakage/de-bonding strength), sudden loss of strength (due to loss of hydrate added cohesion), and reaching at a residual (representative of hydrate saturation). Volumetric change may have taken place in the post-peak region leading to strain localization and appearance of shear bands. The final deformed form of the specimen is given in Figure 5.19(a).

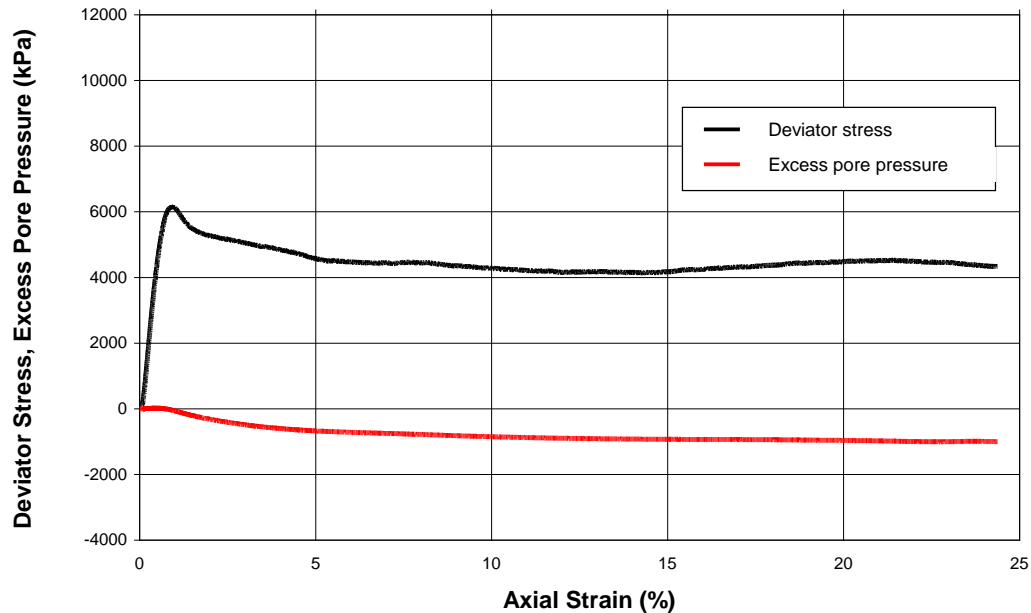


Figure 5.13: Deviator stress and excess pore fluid pressure for test MH 009 (at hydrate saturation of 53.6%) during shearing at 500 kPa initial ECS

The deviator stress response is characterised by brittle failure, which features reaching at a peak (representative of hydrate breakage/de-bonding strength), sudden loss of strength (due to loss of hydrate added cohesion), and reaching at a residual (representative of hydrate saturation). The post-peak negative pore pressure development (indicating dilative background volumetric tendency) is not adequate to generate adequate increase in effective stress to overcome strength reduction due to loss of cohesion. The maximum rate of negative pore pressure development is observed at 2% strain corresponding to stresses in the post-peak region. Upon later dissipation of pore pressure, the specimen develops shear bands. The final deformed form of the specimen is given in Figure 5.19(b).

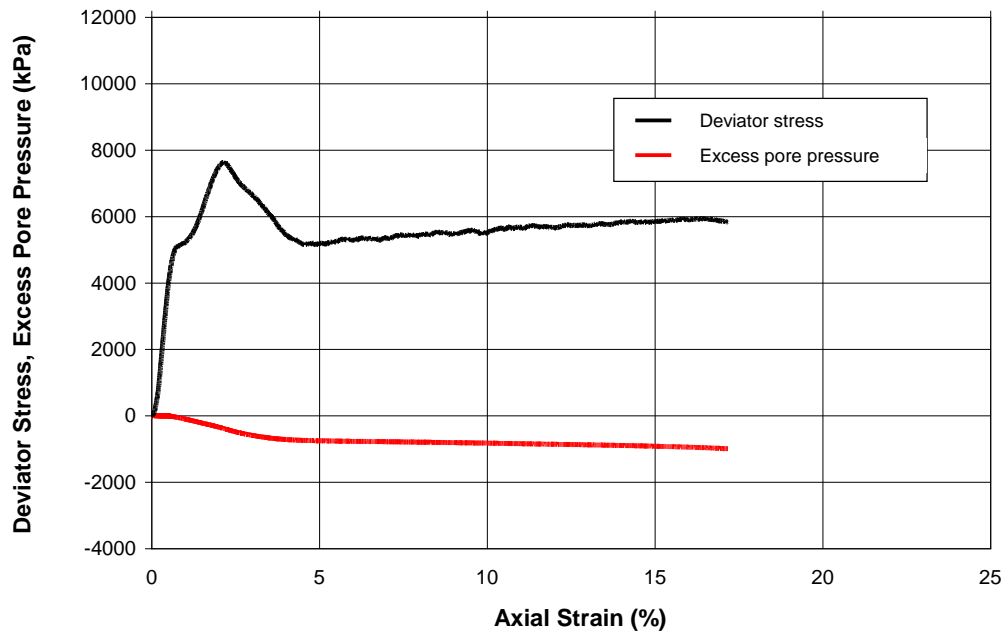


Figure 5.14: Deviator stress and excess pore fluid pressure for test MH 010 (at hydrate saturation of 45.9%) during shearing at 1000 kPa initial ECS

The deviator stress response is characterised by brittle failure, which features reaching at a peak (representative of hydrate breakage/de-bonding strength), sudden loss of strength (due to loss of hydrate added cohesion), and reaching at a residual (representative of hydrate saturation). The post-peak negative pore pressure development (indicating dilative background volumetric tendency) is not adequate to generate adequate increase in effective stress to overcome strength reduction due to loss of cohesion. The maximum rate of negative pore pressure development is observed at 2.6% strain corresponding to stresses in the post-peak region. Upon later dissipation of pore pressure, the specimen develops shear bands. The final deformed form of the specimen is given in Figure 5.19(c).

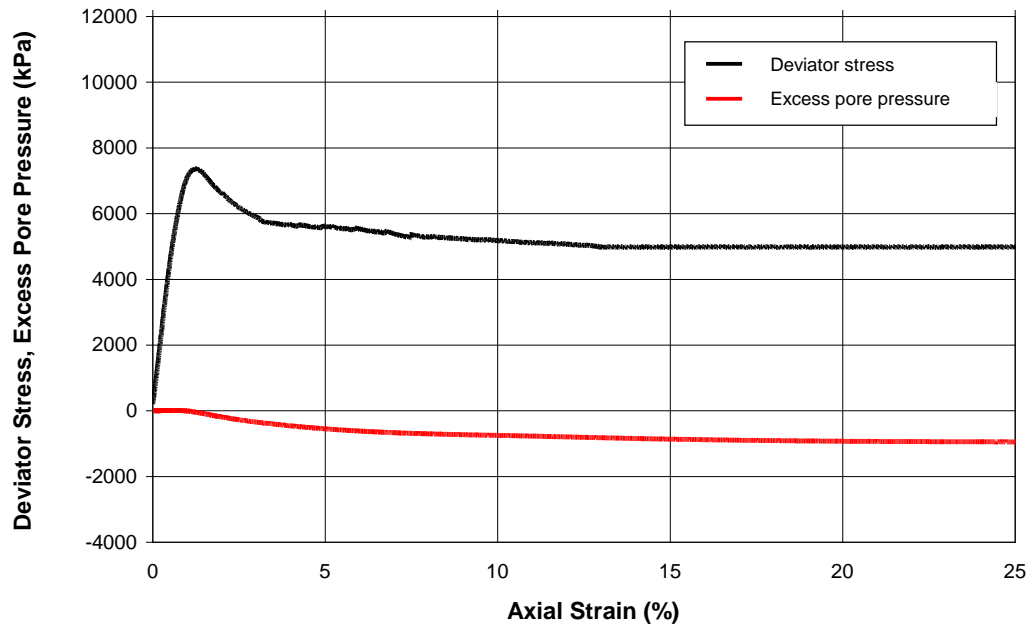


Figure 5.15: Deviator stress and excess pore fluid pressure for test MH 011 (at hydrate saturation of 56.1%) during shearing at 1000 initial ECS

The deviator stress response is characterised by brittle failure, which features reaching at a peak (representative of hydrate breakage/de-bonding strength), sudden loss of strength (due to loss of hydrate added cohesion), and reaching at a residual (representative of hydrate saturation). The post-peak negative pore pressure development (indicating dilative background volumetric tendency) is not adequate to generate adequate increase in effective stress to overcome strength reduction due to loss of cohesion. The maximum rate of negative pore pressure development is observed at 1.4% strain corresponding to stresses in the post-peak region.

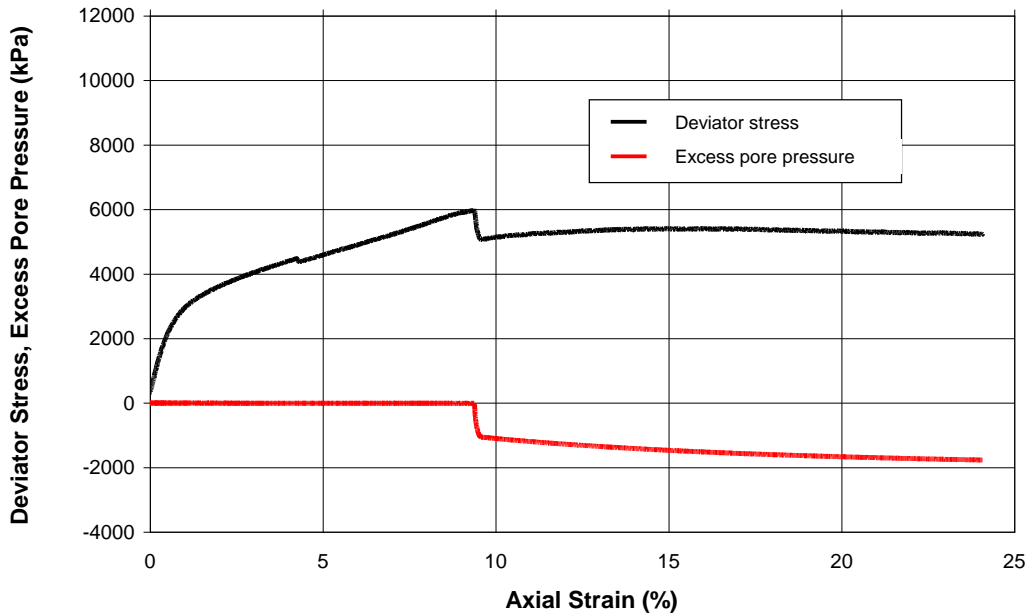
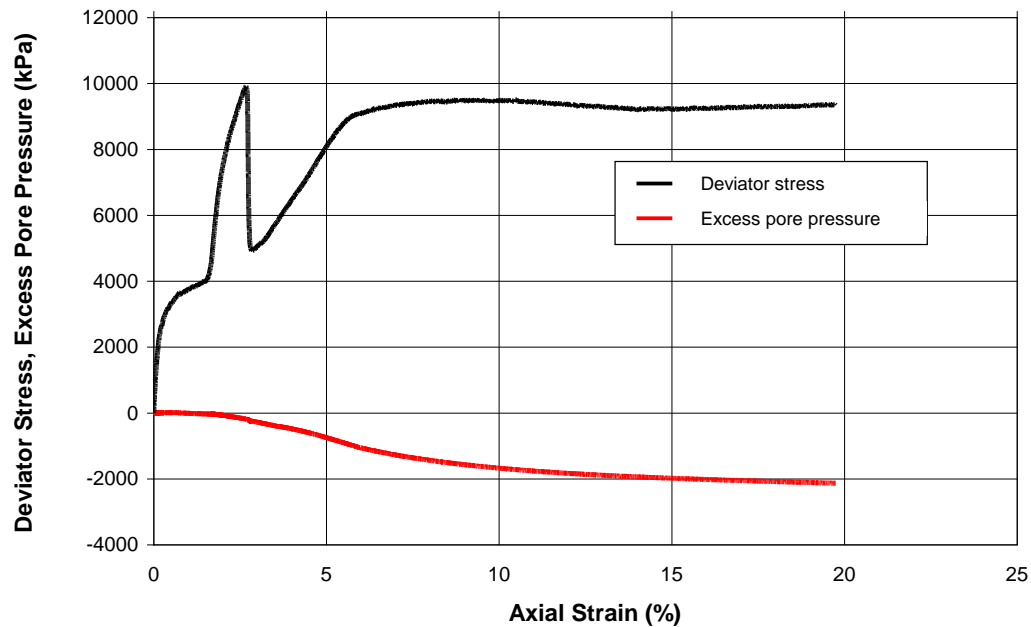


Figure 5.16: Deviator stress and excess pore fluid pressure for test MH 012 (at hydrate saturation of 61.5%) during shearing at 1000 kPa initial ECS

The specimen develops shear bands and the final deformed form of the specimen is given in Figure 5.19(d). The pore pressure response for initial portion of the test is not available, possibly due to hydrate plugging of connection tubing between the specimen pore space and the pressure measuring transducer. The test appears to have disturbed by later hydrate unplugging.



Figure

5.17: Deviator stress and excess pore fluid pressure for test MH 013 (at hydrate saturation of 80%) during shearing at 1000 kPa initial ECS

The deviator stress response is characterised by brittle failure, which features reaching at a peak (representative of hydrate breakage/de-bonding strength), sudden loss of strength (due to loss of hydrate added cohesion), and reaching at a residual (representative of hydrate saturation). A significant amount of post-peak frictional strength regain is observed with the development of negative pore pressure. Upon later pore pressure dissipation the specimen develops shear bands and Figure 5.1(e) shows the band scars left on the specimen membrane. The maximum rate of negative pore pressure development is observed at 4.7% strain corresponding to stresses in the post-peak region.

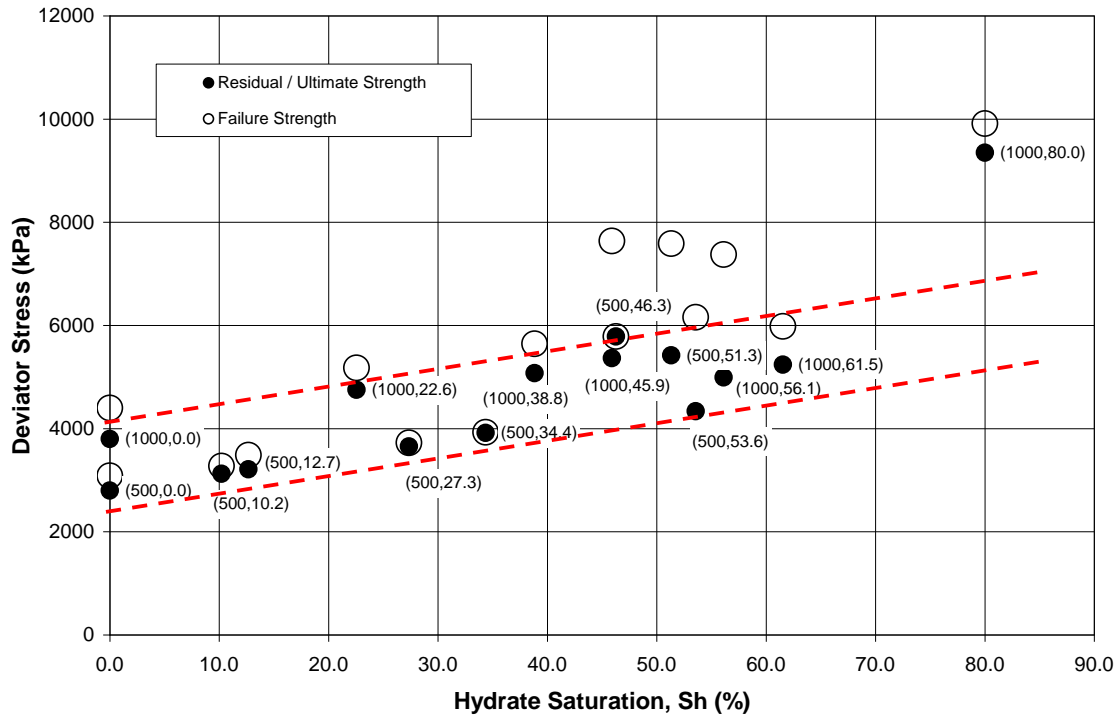


Figure 5.18: Hydrate saturation dependency of failure stress and residual strength

- The variation of residual/ultimate strength of the test specimens with hydrate saturation reveals that for majority of the tested specimens the residual/ultimate strength falls within a strength band of positive gradient (the region enclosed by the red dashed lines). This is an indication of greater residual/ultimate strength obtained at higher hydrate saturations. The trend is similar to that expected for strain-hardening material at increasing density. The brittle behaviour at higher hydrate saturations is indicated by the greater difference between the peak (open circles) and residual strengths (solid circles). All data points for residual strength (solid circles) are labelled with initial effective confining stress (ECS) in kPa and hydrate saturation appearing within parenthesis () respectively. Note that at higher hydrate saturations neither the failure strength nor the residual strength illustrates strong correlation with initial ECS.

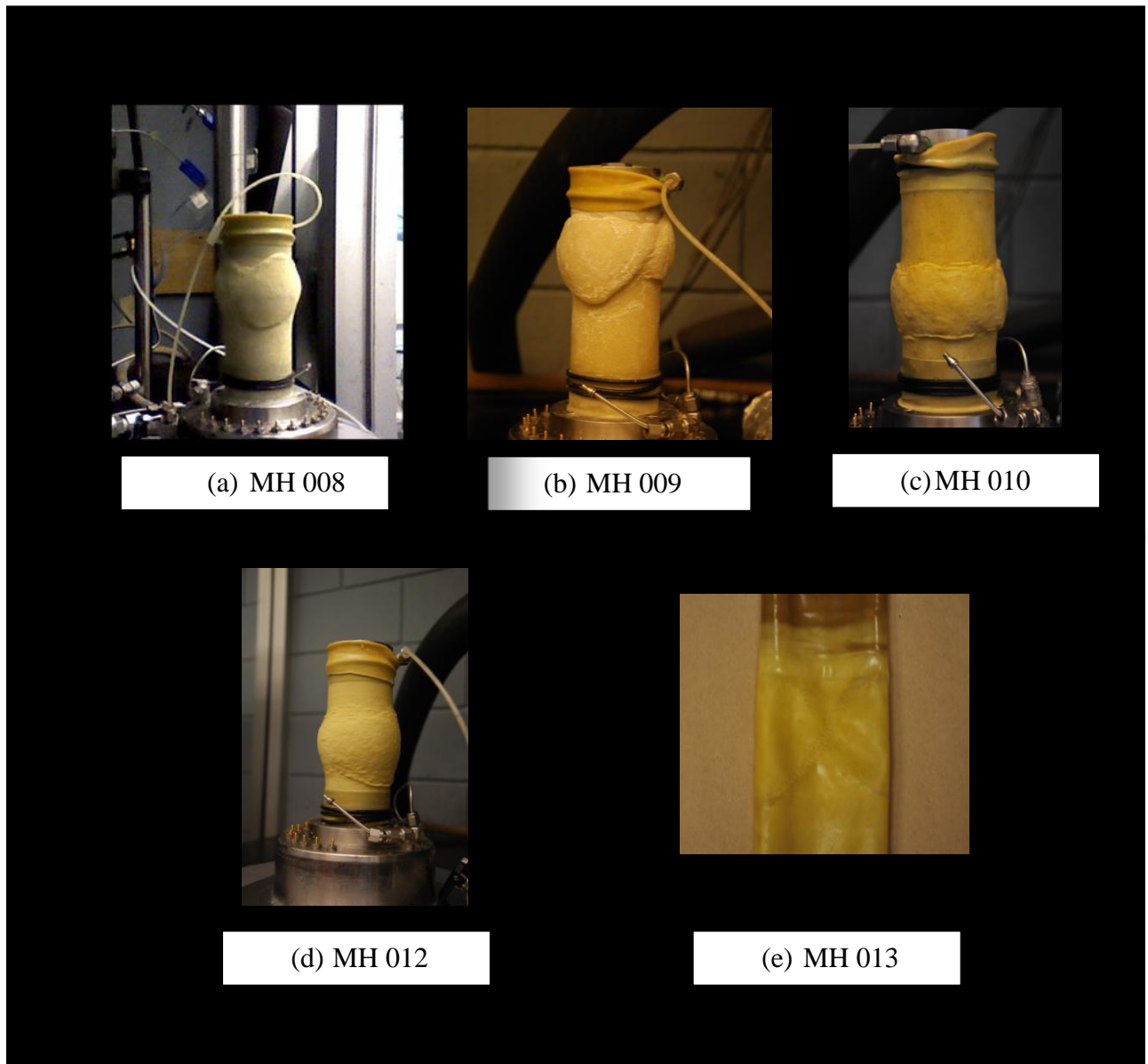
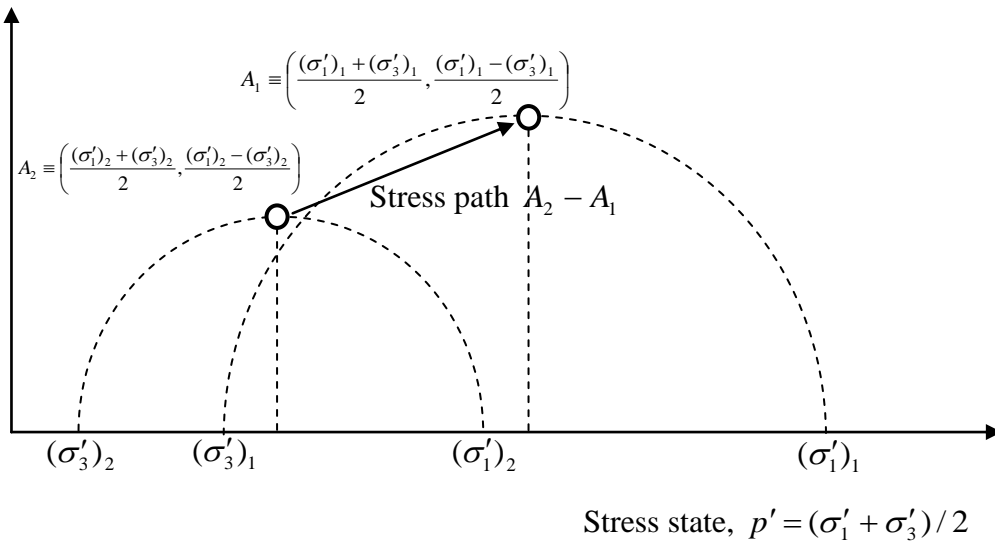
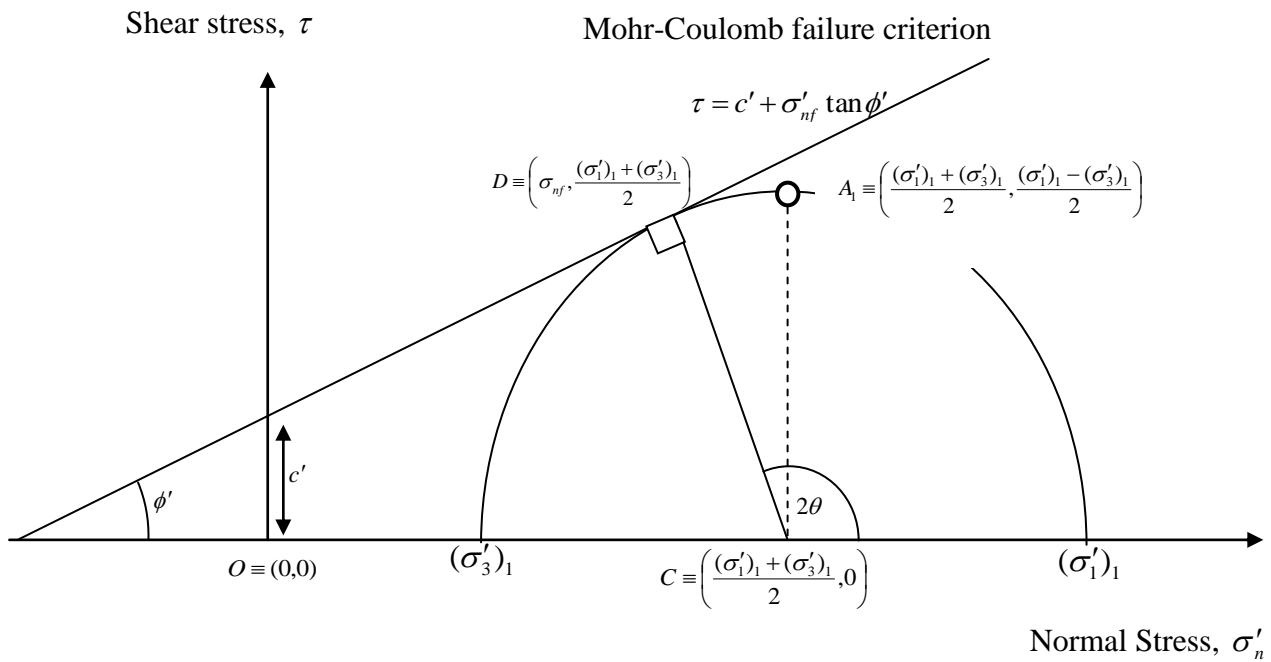


Figure 5.19: Photographs of sheared specimens and deformation band scars left on specimen membrane

Maximum shear stress, $q = (\sigma'_1 - \sigma'_3) / 2$



(a)



(b)

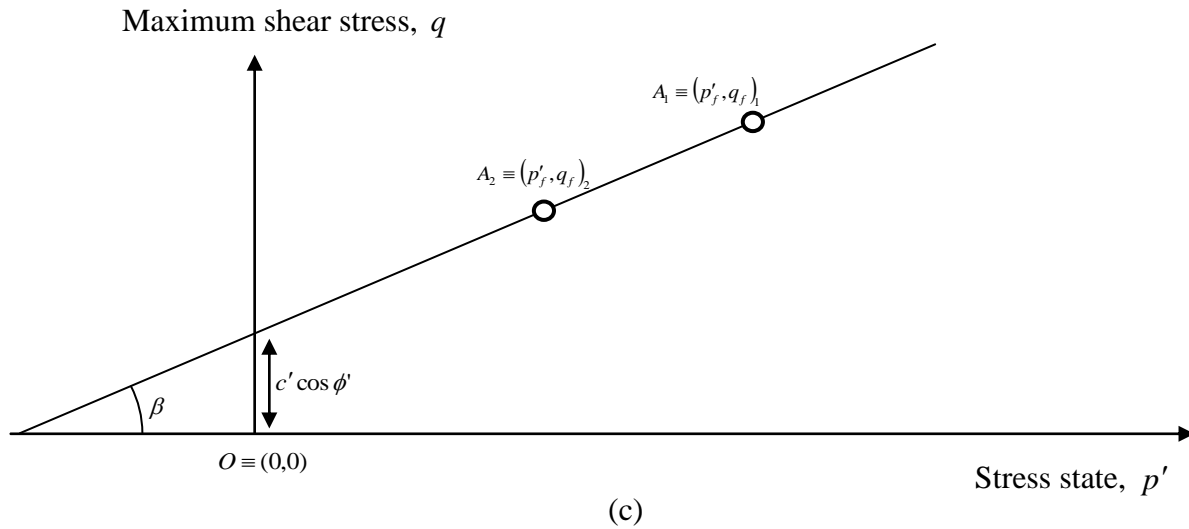
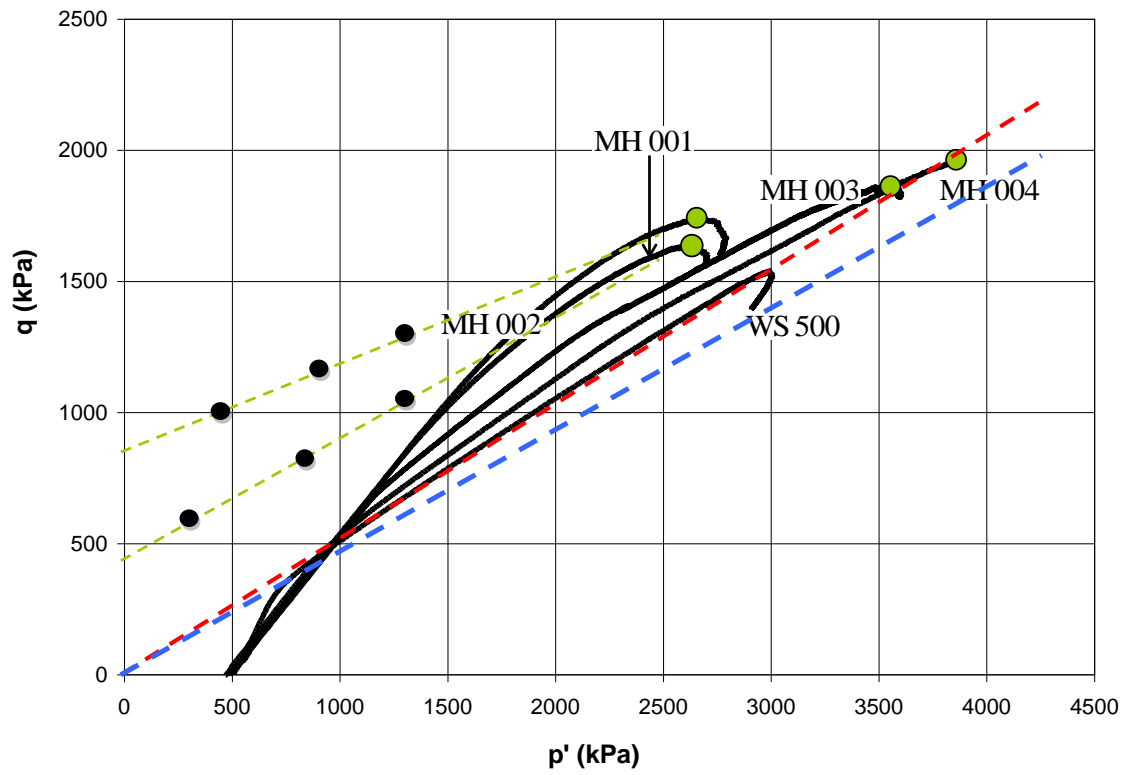
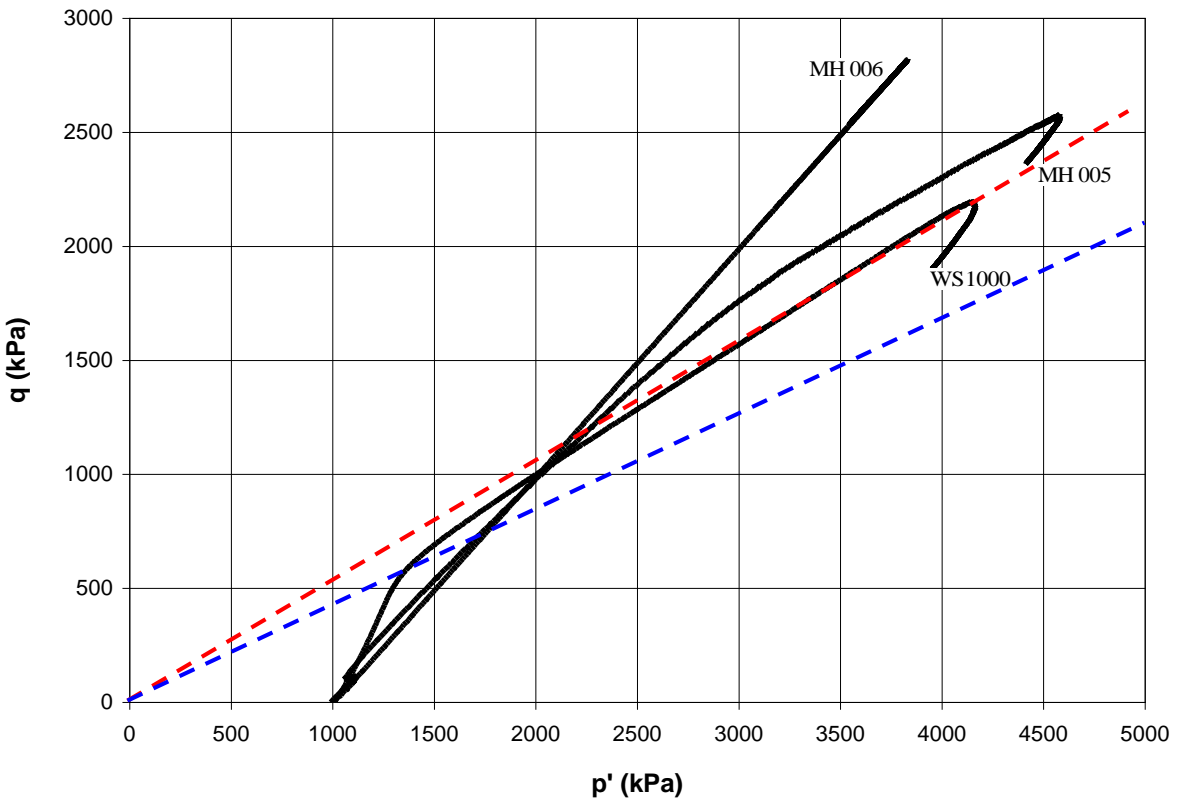


Figure 5.20: The stress path plot and the Mohr-Coulomb failure criterion

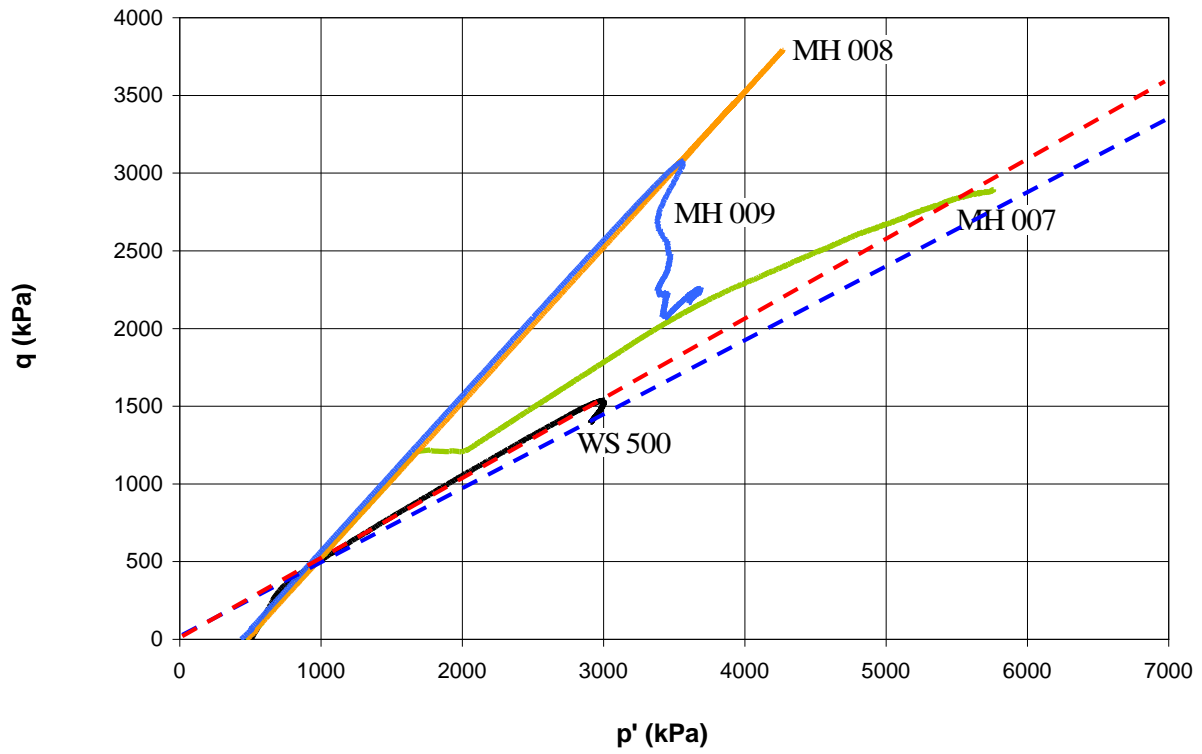
(a) The stress path $A_2 - A_1$, (b) The Mohr's Circle and the Mohr-Coulomb failure criterion – The coordinates of a point on the perimeter (e.g. D) gives the normal shear stress and the mobilised shear stress on a plane of inclination θ to the direction of minor principal stress. The point D represents the shear and the normal stresses on the failure plane corresponding to the maximum shear stress given by $q_f = [(\sigma'_1)_1 - (\sigma'_3)_1]/2$ or maximum deviator stress)/2 (in the case of triaxial testing) and the stress state $p'_f = [(\sigma'_1)_1 + (\sigma'_3)_1]/2$. The maximum shear stress mobilises on a plane of inclination 45° to the minor principal stress and is represented by point A_1 . The geometry of the plot suggests $CD = OC \sin \phi' + c' \cos \phi'$. The equation can also be written as $q_f = p'_f \sin \phi' + c' \cos \phi'$. (c) The plot of maximum shear stress at failure obtained for different stress states (for different tests) on the $q - p'$ plane. Integration of the Mohr-Coulomb failure criterion suggests that the gradient of the plot is given by $\tan \beta = \sin \phi'$ and the intercept of the plot is given by $c' \cos \phi'$.



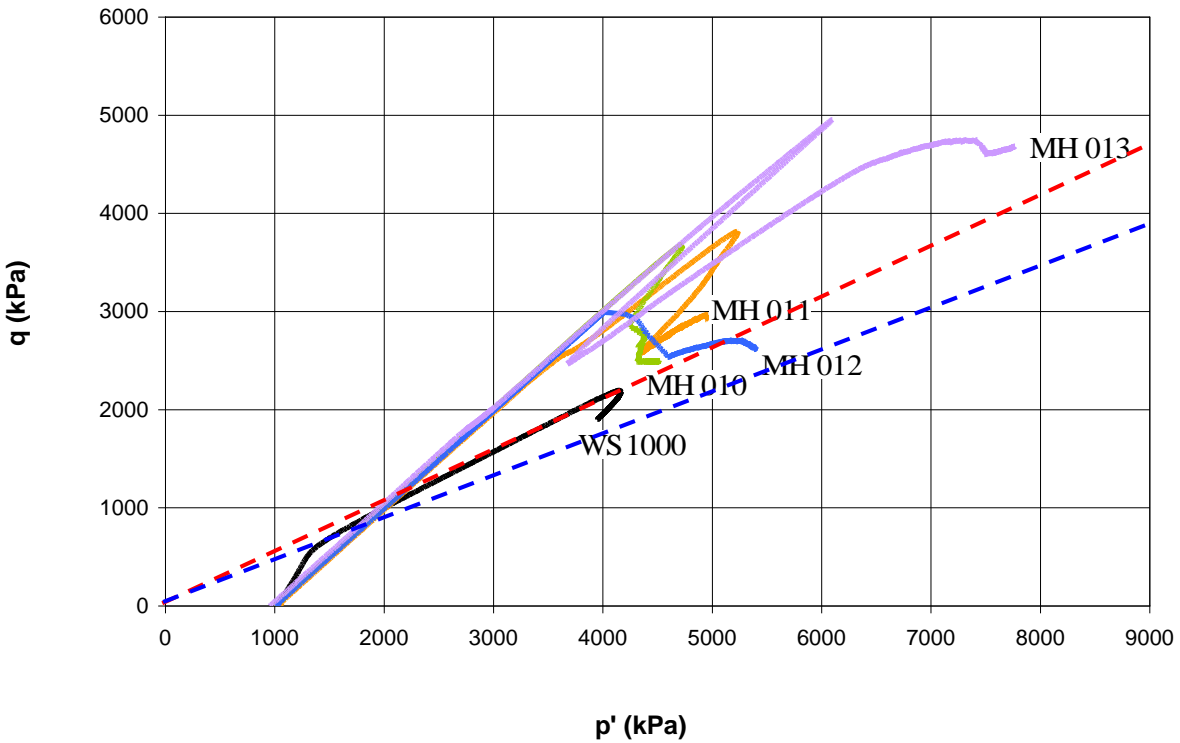
(a) $p' - q$ plots for hydrate-bearing specimens at low hydrate saturations (<40%) at 500 kPa initial effective confining stress [$q = (\sigma'_1 - \sigma'_3)/2$ and $p' = (\sigma'_1 + \sigma'_3)/2$]



(b) $p' - q$ plots for hydrate-bearing specimens at low hydrate saturations (<40%) at 1000 kPa initial effective confining stress [$q = (\sigma'_1 - \sigma'_3) / 2$ and $p' = (\sigma'_1 + \sigma'_3) / 2$]



(c) $p' - q$ plots for hydrate-bearing specimens at high hydrate saturations (>40%) at 500 kPa initial effective confining stress [$q = (\sigma'_1 - \sigma'_3)/2$ and $p' = (\sigma'_1 + \sigma'_3)/2$]



(d) $p' - q$ plots for hydrate-bearing specimens at high hydrate saturations ($>40\%$) at 1000 kPa initial effective confining stress [$q = (\sigma'_1 - \sigma'_3)/2$ and $p' = (\sigma'_1 + \sigma'_3)/2$]

Figure 5.21: $p' - q$ plots for hydrate-bearing specimens

The dashed blue line represents the steady state obtained using the conditions at phase transformation for the water saturated reference tests performed at the corresponding initial effective confining stress. The dashed red line represents the Mohr-Coulomb failure criterion for the non-cohesive water saturated sand specimens. The gradient of the line relates to the mobilised friction angle as given by $\tan \beta = \sin \phi'$. The failure shear strength of each hydrated specimen is denoted by a solid green circle in (a).

Each set of dashed green line and the solid black circles in (a) represents a possible outcome of performing the experiments at varying initial effective confining stress and constant hydrate saturation. According to Soga et al. [2006] and Waite et al. [2009], the friction angle is independent of hydrate saturation in which case the dashed green lines plot parallel to the Mohr-Coulomb failure criterion for water saturated specimens (dashed red line). The experimental verification of the aforementioned is suggested for future research.

(Note: The actual pore pressure response of MH 006 and MH 008 are unknown due to connectivity issues between the pore space and pore pressure measuring transducer potentially arising from hydrate blockage of connection tubing. Therefore, the effective stress paths of the tests are not available.)

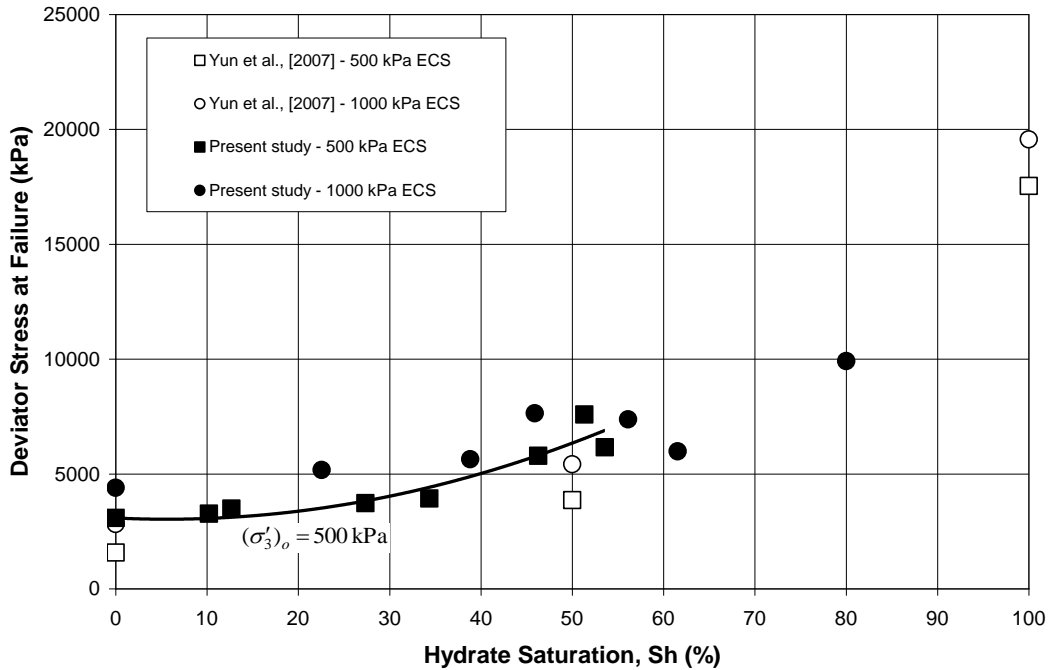


Figure 5.22: Comparison of hydrate saturation dependency of failure strength of the present study for cementing habit of hydrates (solid circles and squares) with that of Yun et al. [2007] for pore-filling to load bearing habit of hydrates (open circles and squares) - The solid line represents the general trend at 500 kPa initial effective confining stress (ECS) fitted to data of present study.

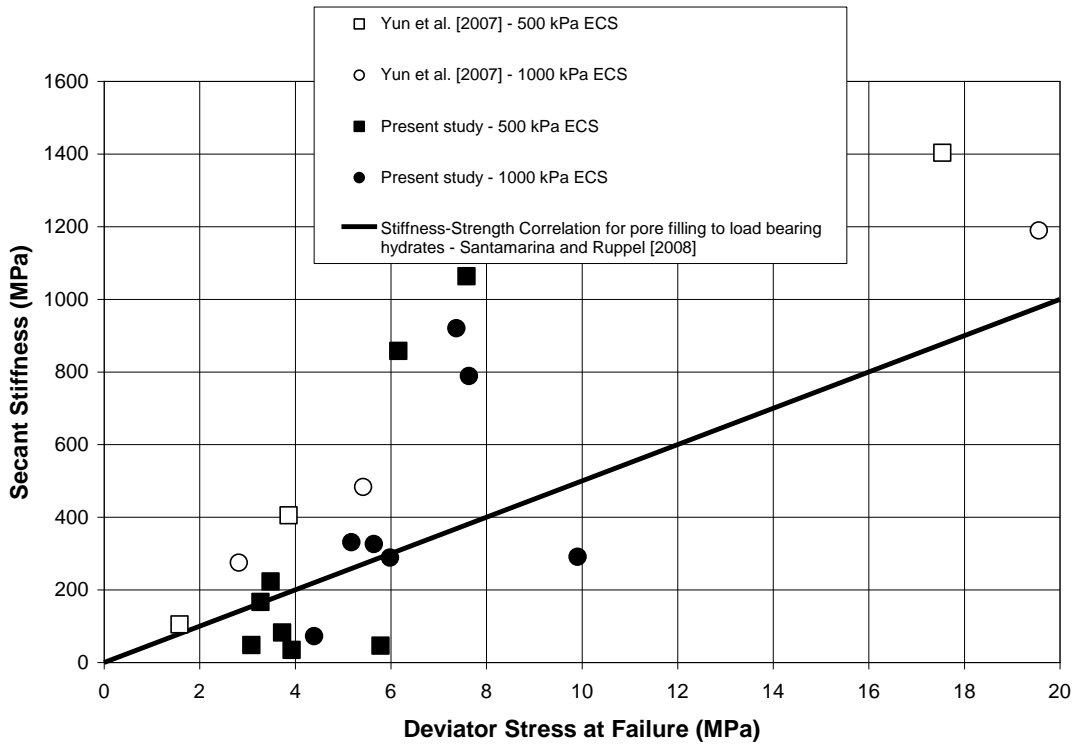


Figure 5.23: Comparison of strength-stiffness correlation for the present study for cementing habit of hydrates (solid circles and squares) with that obtained by Yun et al. [2007] for pore-filling to load bearing habit of hydrates (open circles and squares) - The solid line represents the strength-stiffness correlation of Santamarina and Ruppel [2008] developed by fitting to the data of Yun et al. [2007].

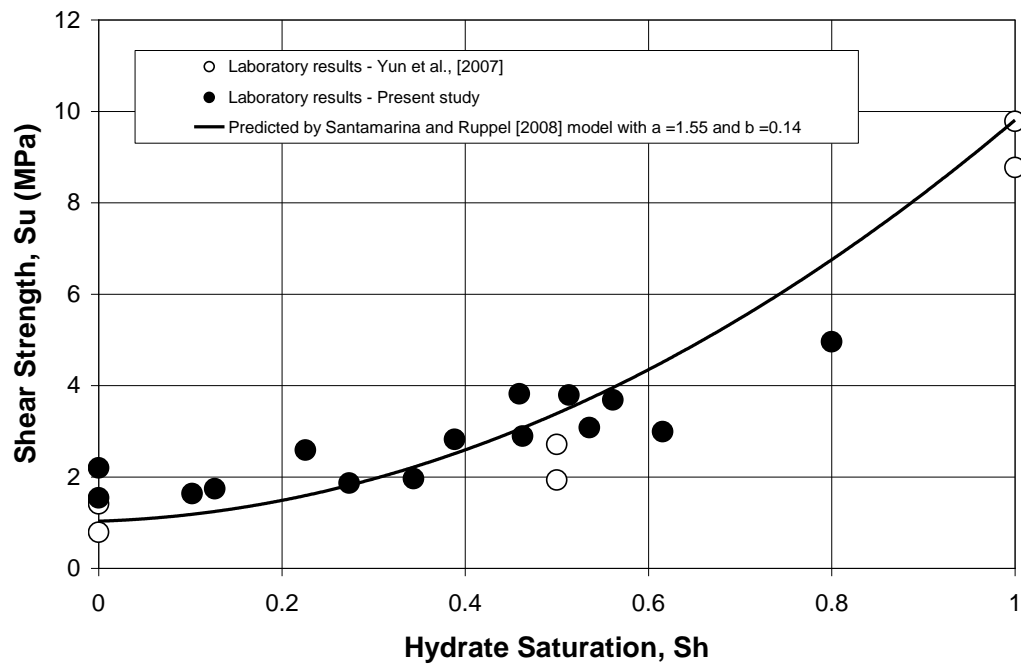


Figure 5.24: Comparison of shear strength at constant mass obtained in the present study (solid circles) with the data of Yun et al. [2007] (open circles)

- The solid line represents the undrained strength predicted by Santamarina and Ruppel [2008] model with a and b parameters obtained by fitting to data of Yun et al.[2007].

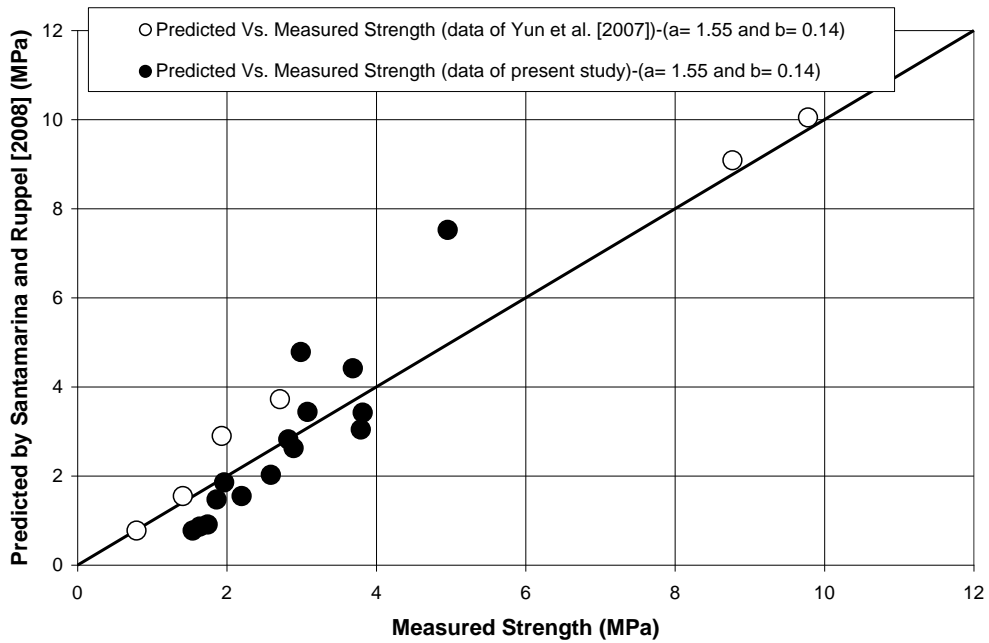


Figure 5.25: The predicted undrained strength by Santamarina and Ruppel [2008] model versus measured strength of present study (solid circles) and measured undrained strength of Yun et al. [2007] (open circles)

- In general, for most of our test specimens, the measured strength appears to be greater than the predicted strength.

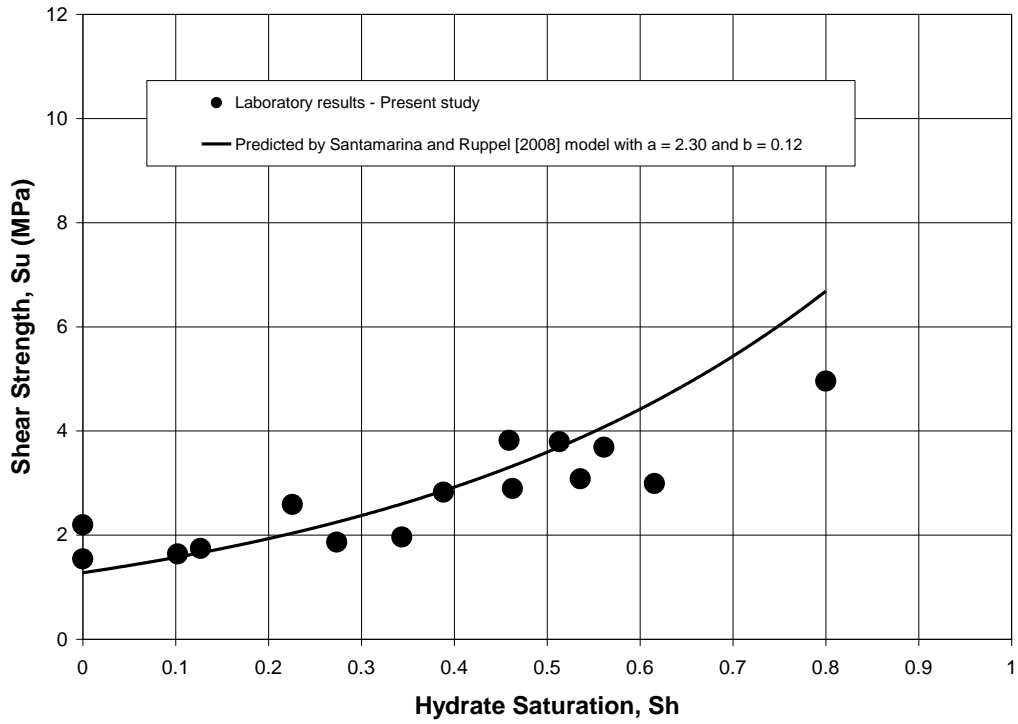


Figure 5.26: Comparison of measured shear strength of present study (solid circles) with that predicted by Santamarina and Ruppel [2008] model with a and b parameters obtained by fitting to data of present study

- An improved fit was obtained compared to the Figure 5.24.

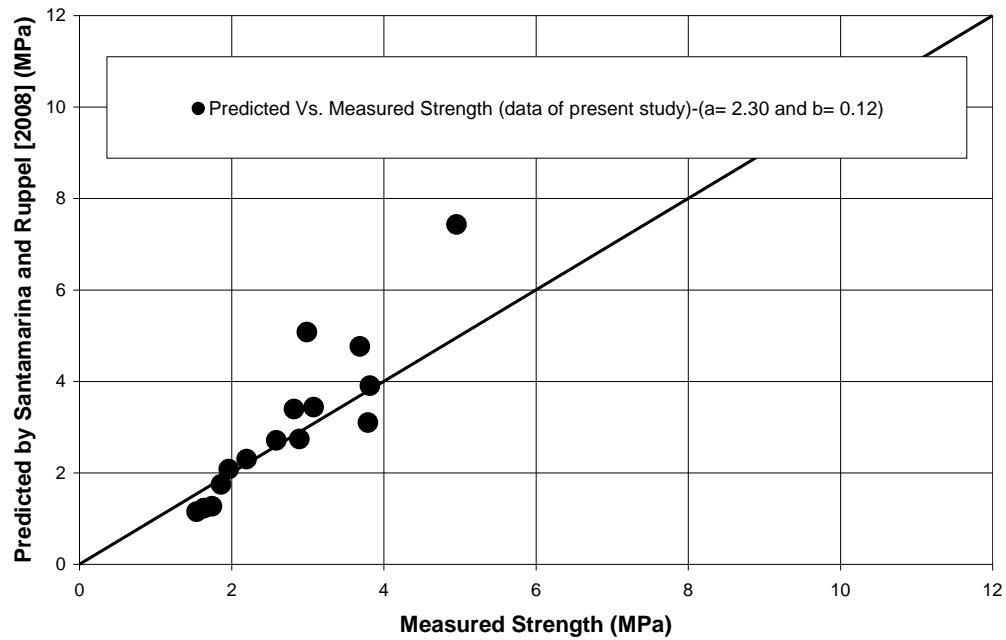


Figure 5.27: The predicted strength by Santamarina and Ruppel [2008] model versus the measured strength of present study (solid circles)

- The model parameters a and b used in the prediction were calibrated using the data of present study. An improved fit relative to that observed in Figure 5.25 was obtained.

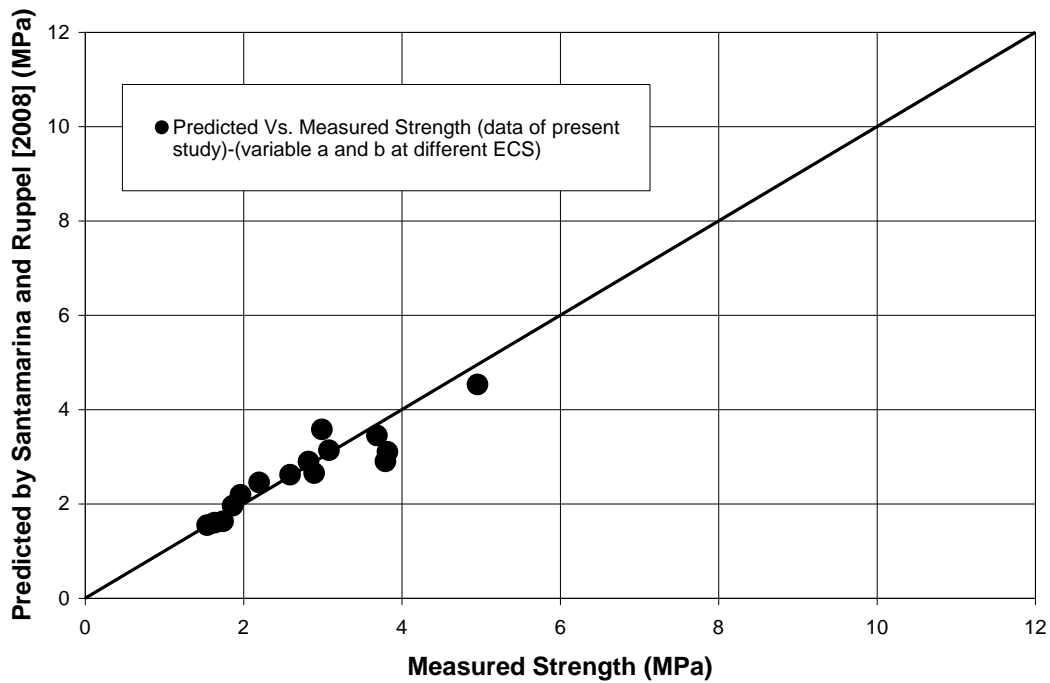


Figure 5.28: The predicted strength by Santamarina and Ruppel [2008] model versus the measured strength of present study (solid circles)

- The model calibration was performed at each different initial effective confining stress (ECS) (500 kPa and 1000 kPa) to generate two sets of values for a and b ($a = 3.10$ and $b = 0.08$ at 500 kPa ECS and $a = 2.45$ and $b = 0.05$ at 1000 kPa ECS), a noticeable improvement relative to that observed in Figure 5.27 was obtained. This indicates there is an influence of effective confinement on the predicted hydrate contribution to strength, which has not been taken into account in the present form of Santamarina and Ruppel [2008] model.

Table 5.1: Test conditions for water saturated non-hydrated specimens and hydrate-bearing specimens

Test ID	Constant confining pressure during shearing (kPa)	Pore fluid pressure immediately prior to shearing (kPa)	Initial effective confining stress (kPa)	Void ratio at the end of consolidation	Hydrate Saturation (%)	Hydrate Formation P/T conditions (Note: sheared under same P/T conditions)	
						Pore fluid pressure (kPa)	Temperature (° C)
WS 250	1300	1050	250	0.539	0	N/A	N/A
WS 500	1550	1050	500	0.561	0	N/A	N/A
WS 1000	2070	1070	1000	0.553	0	N/A	N/A
MH 001	9500	9000	500	0.568	10	9000	5
MH 002	9500	9000	500	0.566	13	9000	5
MH 003	9500	9000	500	0.531	27	9000	5
MH 004	9500	9000	500	0.538	34	9000	5
MH 005	10000	9000	1000	0.530	23	9000	5
MH 006	10000	9000	1000	0.573	39	9000	5
MH 007	9500	9000	500	0.562	46	9000	5
MH 008	9500	9000	500	0.564	51	9000	5
MH 009	9500	9000	500	0.532	54	9000	5
MH 010	10000	9000	1000	0.551	46	9000	5
MH 011	10000	9000	1000	0.540	56	9000	5
MH 012	10000	9000	1000	0.568	62	9000	5
MH 013	10000	9000	1000	0.530	80	9000	5

Table 5.2: Skempton's pore pressure parameters *A* and *B* for water saturated specimens

Test ID	Constant confining pressure during shearing (kPa)	Pore fluid pressure immediately prior to shearing (kPa)	Initial effective confining stress (kPa)	Skempton's pore pressure coefficient B (Measured)	Deviator stress at 5% strain (kPa)	Excess Pore fluid pressure at 5% strain (kPa)	The multiple of pore pressure parameters AB	Skempton's pore pressure coefficient A
WS 250	1300	1050	250	0.970	1345	-354	-0.263	-0.271
WS 500	1550	1050	500	0.973	2074	-434	-0.209	-0.215
WS 1000	2070	1070	1000	0.981	3026	-384	-0.127	-0.129

Table 5.3: Biot's Effective stress coefficient for hydrate-bearing specimens

Test ID	Hydrate Saturation (%)	Initial effective confining stress (kPa)	Aggregated compressibility of the solid constituents (soil and hydrate) (Mpa ⁻¹) C _s	Compressibility of hydrate-cemented soil skeleton (Mpa ⁻¹) C _c	Biot's effective stress coefficient $\alpha = (1-C'_s/C_c)$
MH 001	10.21	500	2.81E-05	4.00E-03	0.993
MH 002	12.67		2.86E-05	6.79E-03	0.996
MH 003	27.34		3.10E-05	5.61E-03	0.994
MH 004	34.36		3.23E-05	5.00E-03	0.994
MH 007	46.27		3.47E-05	4.68E-03	0.993
MH 008	51.32		3.57E-05	1.25E-03	0.971
MH 009	53.56		3.55E-05	1.88E-03	0.981
MH 005	22.56	1000	3.01E-05	3.75E-03	0.992
MH 006	38.84		3.35E-05	3.45E-03	0.990
MH 010	45.91		3.45E-05	1.88E-03	0.982
MH 011	56.12		3.61E-05	1.69E-03	0.979
MH 012	61.54		3.76E-05	3.12E-03	0.988
MH 013	80.00		4.00E-05	7.50E-04	0.947

Table 5.4: Typical values of constituent compressibility

Specimen constituents	Compressibility of the specimen constituents (Mpa ⁻¹)	References
(a) Soil mineral grains	2.78E-05	Stroll and Kan [1981], Hovem and Ingram [1979]; Stern et al. [1985], Turgut and Yamamoto [1990]
	2.50E-05	Ogushwitz et al. [1985]
	2.63E-05	Richardson et al. [2002] - Used in the calculations
	2.13E-05	Richardson et al. [2002]
	2.73E-05	Waite et al. [2000] - As reported in Priest et al. [2005]
(b) Solid methane hydrate	1.30E-04	Waite et al. [2000] - As reported in Priest et al. [2005] - Used in the calculations
(c) Gaseous methane	1.31E-01	At the relative pressure of 9000 kPa and temperature 5° C calculated with the use of Duan et al. [1992b] - Used in the calculations

Table 5.5: The calculated values of pore pressure coefficient B for hydrate-bearing specimens

Test ID	Hydrate Saturation (%)	Initial effective confining stress (kPa)	Aggregated compressibility of the solid constituents (soil and hydrate) (Mpa^{-1}) C'_s	Compressibility of hydrate-cemented soil skeleton (Mpa^{-1}) C_c	Pore space compressibility C_v (= Gas compressibility) (Mpa^{-1})	Biot's effective stress coefficient $\alpha = (1-C'_s/C_c)$	Skempton's Pore Pressure coefficient B
MH 001	10.21	500	2.81E-05	4.00E-03	1.306E-01	0.993	0.086
MH 002	12.67		2.86E-05	6.79E-03	1.306E-01	0.996	0.142
MH 003	27.34		3.10E-05	5.61E-03	1.306E-01	0.994	0.146
MH 004	34.36		3.23E-05	5.00E-03	1.306E-01	0.994	0.143
MH 007	46.27		3.47E-05	4.68E-03	1.306E-01	0.993	0.156
MH 008	51.32		3.57E-05	1.25E-03	1.306E-01	0.971	0.052
MH 009	53.56		3.55E-05	1.88E-03	1.306E-01	0.981	0.082
MH 005	22.56	1000	3.01E-05	3.75E-03	1.306E-01	0.992	0.097
MH 006	38.84		3.35E-05	3.45E-03	1.306E-01	0.990	0.106
MH 010	45.91		3.45E-05	1.88E-03	1.306E-01	0.982	0.070
MH 011	56.12		3.61E-05	1.69E-03	1.306E-01	0.979	0.078
MH 012	61.54		3.76E-05	3.12E-03	1.306E-01	0.988	0.147
MH 013	80.00		4.00E-05	7.50E-04	1.306E-01	0.947	0.077

Table 5.6: The calculated values of pore pressure coefficient A for hydrate-bearing specimens at low hydrate saturations (< 40%)

Test ID	Hydrate Saturation (%)	Initial effective confining stress (kPa)	Axial strain (%)	Skempton's pore pressure parameter A
MH 001	10.21	500	5	-0.47
MH 002	12.67		5	-0.47
MH 003	27.34		5	-1.10
MH 004	34.36		5	-0.94
MH 005	22.56	1000	2	-1.08
MH 006	38.84			*
*Pore pressure measurement not available				

Table 5.7: Triaxial compression strength of non-hydrated and hydrated specimens at different initial effective confining stress and hydrate saturations

Test ID	Initial effective confining stress (kPa)	Hydrate Saturation (%)	Formation P/T conditions (Note: sheared under same P/T conditions)		Pore fluid pressure immediately prior to shearing (kPa)	Constant confining pressure during shearing (kPa)	Pore space consistency during shearing (Gas: G, Water: W, Hydrate: H)	Initial void ratio	Void ratio at the end of consolidation
			Pore fluid pressure (kPa)	Temperature (°C)					
WS 250	250	0	1050	5	1050	1300	W	0.548	0.539
WS 500	500	0	1050	5	1050	1550	W	0.572	0.561
WS 1000	1000	0	1070	5	1070	2070	W	0.560	0.553
MH 001	500	10.2	9000	5	9000	9500	GH	0.579	0.568
MH 002	500	12.7	9000	5	9000	9500	GH	0.574	0.566
MH 003	500	27.3	9000	5	9000	9500	GH	0.543	0.531
MH 004	500	34.4	9000	5	9000	9500	GH	0.550	0.538
MH 005	1000	22.6	9000	5	9000	10000	GH	0.546	0.530
MH 006	1000	38.8	9000	5	9000	10000	GH	0.589	0.573
MH 007	500	46.3	9000	5	9000	9500	GH	0.567	0.562
MH 008	500	51.3	9000	5	9000	9500	GH	0.571	0.564
MH 009	500	53.6	9000	5	9000	9500	GH	0.541	0.532
MH 010	1000	45.9	9000	5	9000	10000	GH	0.565	0.551
MH 011	1000	56.1	9000	5	9000	10000	GH	0.551	0.540
MH 012	1000	61.5	9000	5	9000	10000	GH	0.577	0.568
MH 013	1000	80.0	9000	5	9000	10000	GH	0.545	0.530

Table 5.7: Triaxial compression strength of non-hydrated and hydrated specimens at different initial effective confining stress and hydrate saturations-results....contd.

Test ID	Hydrate Saturation (%)	Maximum deviator stress (kPa)	Secant Stiffness, E ₅₀ (MPa)	Initial tangential stiffness (Mpa)	Residual / Ultimate deviator stress (kPa)	Maximum negative excess pore pressure developed in response to shearing (kPa)
WS 250	0	2682	28	122	2417	-1025
WS 500	0	3083	48	233	2798	-1014
WS 1000	0	4397	73	360	3799	-1052
MH 001	10.2	3273	167	450	3123	-638
MH 002	12.7	3485	223	265	3211	-666
MH 003	27.3	3726	82	321	3653	-1276
MH 004	34.4	3927	35	360	3915	-1398
MH 005	22.6	5177	331	480	4752	-1052
MH 006	38.8	5643	326	521	5075	-14
MH 007	46.3	5786	46	385	5784	-2371
MH 008	51.3	7584	1063	1439	5419	20
MH 009	53.6	6157	858	960	4334	-947
MH 010	45.9	7636	789	960	5363	-1020
MH 011	56.1	7373	920	1067	4992	-1018
MH 012	61.5	5982	289	577	5237	-1774
MH 013	80.0	9910	291	2400	9348	-2086

Table 5.8: Summary results for water saturated specimens

Material	Test	Peak friction angle (degrees)	Friction angle at phase transformation = steady state friction angle (degrees)
Ottawa 20/30 grading sand at initial void ratio of 0.57 and corresponding relative density of 72%	Consolidated undrained triaxial compression	31.51°	24.21°

Table 5.9: Mobilised friction angle and the measured inclination of the shearing plane

Test ID	Hydrate Saturation (%)	Initial effective confining stress (kPa)	Measured inclination of the shearing plane to the direction of minor principal stress (θ)	Mobilised friction angle assuming Mohr-Coulomb solution (ϕ)
MH 008	22.56	500	54	18.00
MH 009	38.84		60	30.00
MH 010	45.91	1000	60	30.00
MH 012	61.54		65	40.00
MH 013	80.00		60	30.00

Chapter Six: Conclusions and Recommendations

6.1 Conclusions

This thesis is focused on introducing a novel formation procedure to artificially synthesise representative hydrate-bearing sediments in the laboratory and investigating the behaviour of hydrate-bearing sediments under triaxial compression conditions. Additionally, attention had been paid to accurately estimating the hydrate saturations. The findings have led to several conclusions, which are presented below in relevance to the main findings of the Chapters 2, 3, 4, and 5.

Methane Hydrates in Porous Soil Media-A Review - Chapter 2

- Natural hydrate-bearing cores are greatly disturbed by the sample handling and specimen preparation process. Particularly, freezing causes the greatest damage to the soil skeleton and the pore structure while, depressurization and subsequent re-pressurization alters hydrate distribution. Therefore, the use of laboratory synthesised hydrate-bearing specimens is necessary in the study of hydrate-bearing sediments. More importantly, the ability to form specimens representative of the hydrate habit which is of interest to the study is of immense importance in our attempt to better understand the physical properties of these sediments.
- Artificial hydrate-bearing sediments formed with the use of initially partial water saturated specimens are believed to be of grain cementing habit. Review of water migration characteristics during formation suggests that evenness of hydrate distribution may be obtained at low initial water saturations followed by rapid formation with

simultaneous nucleation at multiple sites. Post formation water saturation of these sediments may lead to hydrate de-bonding from grain contacts resulting in pore filling to load bearing hydrate habits. The review of hydrate formation process presented in Chapter 2 provided insight into planning the laboratory formation procedure of the present study.

Laboratory Synthesis of Methane Hydrate-Bearing Sediment – A novel method for laboratory synthesis of methane hydrate-bearing sediment from water saturated gaseous methane - Chapter 3

- Hydrate formation from water saturated gaseous methane within initially partial water saturated sand specimens apparently results in grain cementing and/or coating hydrate habit.
- Two major factors were identified as determining the degree of success as to achieving high hydrate saturations and forming specimens of uniform hydrate distribution representative of grain cementing and/or coating growth habit: (1) initial availability of minimal uniformly distributed water content, and (2) continuous feed of water rich methane throughout the formation phase.
- The formation procedure employed in the present study proves the possibility of obtaining higher hydrate saturations compared to those obtained from other existing procedures. As evident from the results uniform spatial distribution of hydrates was obtained only at low hydrate saturations. Further research at grain scale may be employed to confirm the deduced growth habit and the uniformity of hydrate distribution.

Estimating Pore Space Hydrate Saturation Using Dissociation Gas Evolution Measurements (DGEM) - Chapter 4

The investigation of the sensitivity of hydrate saturation to various measurements performed in the laboratory revealed:

- P/T measurements of the system components at the laboratory are critical, particularly when large quantities of methane are present at low density (specifically at high temperatures and low pressures).
- Volume measurements in the system components are critical when the methane density is at its greatest (high pressure and low temperature).

The key findings of the sensitivity analysis on the use of different mathematical models to generate methane densities representative of the true nature of the methane-water system revealed:

- Alternatives to ideal approximation such as Duan *et al.* [1992b] and CSMGem calculator of Ballard [2002] should be used when conditions stray from ideal conditions. Therefore, the Ideal Gas Law should be employed with caution.
- Neglecting the water content in vapour phase, as done with the use of single component models for methane such as Duan *et al.*, [1992b], does not appear to have significant impact on the estimated hydrate saturation.

Triaxial Compression Strength of Methane Hydrate-Bearing Coarse Granular Media -

Chapter 5

The series of laboratory tests on the triaxial compression behaviour of artificially synthesised methane hydrate-bearing sand to investigate the initial confining stress and hydrate saturation dependency of strength and stiffness led to the following conclusions:

- At low hydrate saturations (<40%), the strength of hydrate-bearing sediments is affected by initial effective confinement and hydrate saturation; greater strength is obtained at greater initial effective confinement and higher hydrate saturations.
- At low hydrate saturations (<40%), the stiffness of hydrate-bearing sediments is affected by initial effective confinement and hydrate saturation; greater stiffness is obtained at greater initial effective confinement and higher hydrate saturations.
- The stress-strain behaviour at high hydrate saturations (> 40%), exhibits brittleness and seemingly represents an altered strain hardening behaviour.
- At high hydrate saturations (> 40%), hydrate-bearing sediments develop greater strength, however, it is difficult to deduce a clear correlation between strength, initial effective confinement, and saturation.
- Also, at high hydrate saturations (> 40%), hydrate-bearing sediments develop greater stiffness, however, it is difficult to deduce a clear correlation between stiffness and saturation.
- The stiffness of hydrate-bearing sediments at high hydrate saturations does not appear to be significantly affected by initial effective confinement.

The in depth investigation of grain scale mechanisms of shearing and comparison of our results to those obtained for non-cementing hydrates revealed:

- At low saturations the strength is mainly governed by frictional resistance to shearing. However, evidence of hydrate induced cohesion is also available.
- At high saturations the peak strength is governed by the intact hydrate strength and/or hydrate-mineral bonding strength.
- At high saturations the residual strength is predominantly governed by the hydrate saturation.
- Stiffness is greatly determined by the hydrate habit; cementing and/or grain coating habit showing greater stiffness at low saturations. At high saturations stiffness of non-cementing hydrates may expect to be as comparable to that of cementing hydrates only if the saturation is as high as such that the particulate body tend to behave as an aggregated body.

6.2 Significance

This research marks the single most comprehensive laboratory investigation of triaxial compression strength of methane hydrate-bearing sediments at constant mass undertaken to date.

The work presented in this thesis has made a significant contribution to the advancement of hydrate knowledge in the form of the very findings that it presents and also in the form of directions it provides for future research. Specifically, the knowledge of soil behaviour at constant mass is important in evaluating the potential risks associated with short and long term sediment behaviour related to drilling and methane production, reservoir subsidence, and mechanisms that lead to slope instability issues associated with shallow hydrated sediments. The

experimental investigation observes the shear failure of these sediments under loading conditions with restricted pore pressure dissipation. Further, as can be deduced from the observations of pore pressure development, it also suggests of another kind of failure; failure due depressurisation (or negative excess pore pressure development) which brings a portion of the sediment outside the hydrate stability boundary thus inducing dissociation.

6.3 A path forward

The work presented in this thesis has taken our understanding of the behaviour of hydrate-bearing sediments a step forward. However, understanding the mechanics of these sediments still require significant study. As such, continuous deployment of research effort is needed on both experimental and numerical aspects for the development of hydrate sciences. The following areas of potential future development are identified based on the experience gained throughout the years working towards the presentation of this work:

1. Experimental methods

- a. Improvements in experimental methods to isolate the nature of hydrate habit, including overcoming limitations such as possible pore space compressibility
- b. Incorporation of advanced technology (such as microscopic imaging) with conventional methods of geomechanical testing to better understand the particle level mechanisms

2. Further experimental investigation such as:

- a. Triaxial compression testing to verify the hypothesised behaviours.

- b. Isotropic loading and unloading tests to better understand the pore pressure development, potential induced hydrate dissociation, and after-effects on pore pressure development and volume change behaviour.

- 3. Further experimental investigations on micro and macro scale hydrate growth habits/morphologies achieved with different specimen preparation techniques, and comparison to formation of natural hydrates

- 4. Further experimental investigations on the hydrate-mineral bonding strength and compressive/tensile strength of intact hydrate

- 5. Investigations on the effects of host sediment properties, formation P/T conditions, and subsequent changes to the P/T conditions in relevance to all aforementioned experimental investigations

- 6. Further improvements to numerical correlation of geomechanical properties and the pore space presence of hydrate
 - a. By inclusion of mathematical expression of hydrate-sediment interaction (or the formation habit effects)

 - b. By inclusion of potential deterministic factors of intact hydrate compressive/tensile strength (such as confining pressure and temperature)

References

- Andersen, G. R., C. W. Swan, C. C. Ladd, and J. T. Germaine (1995), Small-strain behavior of frozen sand in triaxial compression, *Can. Geotech. J.*, 32, 428–451.
- Alshibli, K. A., Batiste, S. N., & Sture, S. (2003). Strain localization in sand: plane strain versus triaxial compression. *Journal of Geotechnical and Geoenvironmental Engineering*, 129(6), 483-494.
- Aoyagi, .K, K. Y. Song, E. D. Sloan, P. B. Dharmawardhana, and K. Riki (1979), Improved measurements and correlation of the water content of methane gas in equilibrium with hydrate, paper presented at the 1979 Annual Convention, Gas Processors Association, 25-28.
- Aoyagi, K, K. Y. Song, R. Kobayashi, E. D. Sloan, and P. B. Dharmawardhana (1980), The water content and correlation of the water content of methane in equilibrium with hydrates, Report no. 45, Gas Processors Association, Tulsa, OK.
- ASTM Standard C-778-12, Standard Specification for Standard Sand, American Society for Testing and Materials (ASTM), West Conshohocken, PA.
- Ballard, A. L. (2002), A non-ideal hydrate solid solution model for a multi-phase equilibria program, PhD Thesis, Chemical and Petroleum-Refining Engineering, Colorado School of Mines, Colorado, USA.
- Ben-Naim, A., and M. Yaacobi (1974), Effects of solutes on the strength of hydrophobic interaction and its temperature dependence, *Journal of Physical Chemistry*, 78, 170-175.

Berge, L. I., K. A. Jacobsen, and A. Solstad (1999), Measured acoustic wave velocities of R11 (CCl₃F) hydrate samples with and without sand as a function of hydrate concentration, *Journal of Geophysical Research*, 104, 15, 415-424, doi: 10.1029/1999JB900098.

Bishop, A. W., & Henkel, D. J. (1962). *The measurement of soil properties in the triaxial test*, 2nd Edition, Edward Arnold (Publishers) Ltd., London, United Kingdom.

Boswell, R., and T. Collett (2006), The gas hydrates resource pyramid, *Fire in the Ice: Methane Hydrate Newsletter*, fall, pp. 5–7, Office of Fossil Energy, Natl. Energy Technol. Lab., U.S. Dep. of Energy, Washington, D. C.

Bowden, F. P. and Tabor, D. (1959). *Friction and Lubrification*, Dunod, Paris.

Buffett, B., and O. Zatsepina (2000), Formation of gas hydrate from dissolved gas in natural porous media, *Marine Geology*., 164, 69–77, doi:10.1016/S0025-3227(99)00127-9.

Cameron, I., Y. P. Handa, and T. H. W. Baker (1990), Compressive strength and creep behaviour of hydrate-consolidated sand, *Canadian Geotechnical Journal*, 27, 255-258.

Castro, G., Poulos, S. J., France, J. W., and Enos, J. L. (1982). Liquefaction induced by cyclic loading. Report submitted to National Science Foundation, Washington, DC.

Chand, S., T. A. Minshull, J. A. Priest, A. I. Best, C. R. I. Clayton, and W. F. Waite (2006), An effective medium inversion algorithm for gas hydrate quantification and its application to laboratory and borehole measurements of gas hydrate-bearing sediments, *Geophysical Journal International*, 166, 543-552.

Chapoy, A., C. Coquelet, and D. Richon (2005), Corrigendum to “Revised solubility data and modeling of water in the gas phase of the methane/water binary system at temperatures

from 283.08 to 318.12 K and pressures up to 34.5 MPa” [Fluid Phase Equilibria 214 (2003) 101-117], Fluid Phase Equilib., 230, 210-214.

Chapoy, A., H. Haghghi, R. Burgass, and B. Tohidi (2010), Gas hydrates in low water content gases: Experimental measurements and modelling using the CPA equation of state, Fluid Phase Equilib., 292, 9-14.

Chapoy, A., A. H. Mohammadi, D. Richon, and B. Tohidi (2004), Gas solubility measurement and modeling for methane-water and methane-ethane-n-butane-water systems at low temperature conditions, Fluid Phase Equilib., 220, 113-121.

Cho, G., J. Dodds, and J. Santamarina (2005). Particle shape effects on packing density, stiffness and strength: Natural and crushed sands. Internal report- Georgia Institute of Technology.

Cho, G., J. Dodds, and J. C. Santamarina (2006). Particle shape effects on packing density, stiffness, and strength: natural and crushed sands. Journal of Geotechnical and Geoenvironmental Engineering, 132, 5, 591-602.

Chuvilin, E. M., T. Ebinuma, Y. Kamata, T. Uchida, S. Takeya, J. Nagao, and H. Narita (2003), Effects of temperature cycling on the phase transition of water in gas-saturated sediments, Can. J. Phys., 81, 343–350, doi:10.1139/p03-028.

Circone, S., S. H. Kirby, and L. A. Stern (2005), Direct measurement of methane hydrate composition along the hydrate equilibrium boundary, Journal of Physical Chemistry B, 109, 9468-75.

Clarke, M. A., M. Pooladi-Darvish, and P. R. Bishnoi (1999), A Method to Predict Equilibrium Conditions of Gas Hydrate Formation in Porous Media, Ind. Eng. Chem. Res., 38, 2485-2490.

Claussen, W. F., and M. F. Polglase (1952), Solubilities and structures in aqueous aliphatic hydrocarbon solutions, *Journal of the American Chemical Society*, 74, 4817-4819.

Claypool, G. W., and I. R. Kaplan (1974), *Natural Gases in Marine Sediments*, pp. 99-139, Plenum, New York, USA:

Clennell, M. B., M. Hovland, J. S. Booth, P. Henry, and W. J. Winters (1999), Formation of natural gas hydrates in marine sediments: 1. Conceptual model of gas hydrate growth conditioned by host sediment properties, *J. Geophys. Res.*, 104, 22, 985-23, 003, doi:10.1029/1999JB900175.

Collett, T. S. (2002), Energy resource potential of natural gas hydrates, *AAPG Bull.*, 86, 1971–1992.

Davie, M. K., O.Y. Zatsepina, and B. A. Buffett (2004), Methane solubility in marine hydrate environments, *Marine Geology*, 203, 177-184.

Duan, Z., and S. Mao (2006), A thermodynamic model for calculating methane solubility, density and gas phase composition of methane-bearing aqueous fluids from 273 to 523 K and from 1 to 2000 bar, *Geochimica et Cosmochimica Acta*, 70, 3369-3386.

Duan, Z., N. Moller, and J. H. Weare (1992a), An equation of state for the CH₄-CO₂-H₂O system: II. Mixtures from 50 to 1000 °C and 0 to 1000 bar, *Geochimica et Cosmochimica Acta* 56, 2619-2631.

Duan, Z., N. Moller, J. Greenberg, and J. H. Weare (1992b), An equation of state for the CH₄-CO₂-H₂O system: I. Pure systems from 0 to 1000°C and 0 to 8000 bar, *Geochimica et Cosmochimica Acta*, 56, 2605-2617.

- Duan, Z., N. Moller, J. Greenberg, and J. H. Weare (1992c), The prediction of methane solubility in natural waters to high ionic strength from 0 to 250°C and from 0 to 1600 bar, *Geochimica et Cosmochimica Acta*, 56, 1451-1460.
- Durham, W. B., L. A. Stern, S. H. Kirby, and S. Circone (2005), Rheological comparisons and structural imaging of sI and sII end-member gas hydrates and hydrate/sediment aggregates, paper presented at Fifth International Conference on Gas Hydrates, pp. 607– 614, Tapir Acad, Trondheim, Norway.
- Dvorkin, J., M. B. Helgerud, W. F. Waite, S. H. Kirby, and A. Nur (2000), Introduction to physical properties and elasticity models, in *Natural Gas Hydrate: In Oceanic and Permafrost Environments*, edited by M. D. Max, pp. 245–260, Kluwer Acad., Dordrecht, Netherlands.
- Eaton, M., D. Mahajan, and R. Flood (2007), A novel high-pressure apparatus to study hydrate-sediment interactions, *Journal of Petroleum Science and Engineering*, 56, 101-107.
- Eaton, M. W., K. W. Jones, and D. Mahajan (2009), Mimicking natural systems: methane hydrate formation – decomposition in depleted sediments, *The Geological Society, London, Special Publications*, 319, 121-130.
- Ebinuma, T., Y. Kamata, H. Minagawa, R. Ohmura, J. Nagao, and H. Narita (2005), Mechanical properties of sandy sediment containing methane hydrate, paper presented at Fifth International Conference on Gas Hydrates, Tapir Acad., Trondheim, Norway, 958–961.
- Fernandez, A. L., and J. C. Santamarina (2001), Effect of cementation on the small-strain parameters of sands, *Can. Geotech. J.*, 38, 191–199, doi:10.1139/cgj-38-1-191.

Folas, G. K., E. W. Froyna, J. Lovland, G. M. Kontogeorgis, and E. Solbraa (2007), Data and Prediction of water content of high pressure nitrogen, methane, and natural gas, *Fluid Phase Equilib.*, 252, 162-174.

Galloway, T. J., W. Ruska, P. S. Chappellear, and R. Kobayashi (1970), Experimental Measurement of hydrate numbers for methane and ethane and comparison with theoretical values, *Ind. Eng. Chem. Fundam.*, 9(2), 237-243.

Gas Processors Association (1996), *Thermodynamic Database Version 2.0*, Oklahoma State University, OK, USA.

Ghiassian, H., and J. L. H. Grozic (2011), Undrained Triaxial Testing Of Methane Hydrate Bearing Soil Specimens, paper presented at 7th International Conference on Gas Hydrates, Edinburgh, Scotland, United Kingdom.

Gibbs, J. W. (1948), *The collected works of J. Willard Gibbs, Thermodynamics*, (1(1), Yale U. Press, New Haven, CN.

Grozic, J. L. H. (2010). Interplay between gas hydrates and submarine slope failure. *Advances in Natural and Technological Hazards Research, Special Issue Submarine Mass Movements and Their Consequences*, Vol. 28, pp 11-30.

Grozic, J. L. H., and H. Ghiassian (2010). Undrained shear strength of methane hydrate-bearing sand: Preliminary laboratory results, *Proceedings 6th Canadian Permafrost Conference and 63rd Canadian Geotechnical Conference*, Calgary.

Gupta, A., J. Lachance, E. D. Sloan, and C. A. Koh (2008), Measurements of methane hydrate heat of dissociation using high pressure differential scanning calorimetry, *Chem. Eng. Sci.*, 63,5848–5853, doi:10.1016/j.ces.2008.09.002.

- Hammerschmidt, E.G. (1934), Formation of gas hydrates in natural gas transmission lines, *Industrial and Engineering Chemistry*, 8, 851-855.
- Handa, Y. P. (1986), Compositions, enthalpies of dissociation, and heat capacities in the range 85 to 270 K for clathrate hydrates of methane, ethane, and propane, and enthalpy of dissociation of isobutene hydrate, as determined by a heat-flow calorimeter, *J. Chem. Thermodynamics*, 18, 915-921.
- Handa, Y. P., and D. Stupin (1992), Thermodynamic properties and Dissociation Characteristics of Methane and Propane Hydrates in 70-Å-Radius silica gel pores, *J. Phys. Chem.*, 96, 8599-8603.
- Hashemi, S., A. Macchi, S. Bergeron, and P. Servio (2006), Prediction of methane and carbon dioxide solubility in water in the presence of hydrate, *Fluid Phase Equilibria*, 246, 131-136.
- Helgerud, M. B. (2001), Wave speeds in gas hydrate and sediments containing gas hydrate: A laboratory and modeling study, Ph.D. thesis, Stanford University, California, USA.
- Hester, K. C., Z. Huo, A. L. Ballard, C. A. Koh, K. T. Miller, and E. D. Sloan (2007), Thermal expansivity of sI and sII clathrate hydrates, *Journal of Physical Chemistry B*, 111, 8830-8835.
- Hill, R., (1952). The elastic behaviour of crystalline aggregate. *Proc. Phys. Soc. London, Sect. A*, 65, 349-354.
- Howard, J. J., K. C. Hester, J. C. Stevens, and M. B. Rydzy (2011), Ultrasonic velocity measurements during experimental CH₄ hydrate formation and CO₂ exchange, paper presented at 7th International Conference on Gas Hydrates, Edinburgh, Scotland, United Kingdom.

Huo, Z., K. Hester, E. D. Sloan Jr., and K. T. Miller (2003), Methane hydrate nonstoichiometry and phase diagram, *AICHE J.*, 49, 1300-1306.

Hvorslev, M. J. (1969), Physical properties of remoulded cohesive soils, Vicksburg: U.S. Army Engineer Waterways Experiment Station, Translation 69-5.

Hyodo, M., A. F. L. Hyde, Y. Nakata, N. Yoshimoto, M. Fukunaga, K. Kubo, Y. Nanjo, T. Matsuo, and K. Nakamura (2002), Triaxial Compressive Strength of Methane Hydrate, Paper presented at the 12th International Offshore and Polar Engineering Conference, Kitakyushu, Japan.

Hyodo, M., Y. Nakata, N. Yoshimoto, and T. Ebinuma (2005), Basic research on the mechanical behavior of methane hydrate sediments mixture, *Soils Found.*, 45, 75–85.

Hyodo, M., Y. Narita, N. Yoshimoto, and R. Orense (2007), Shear behaviour of methane hydrate-bearing sand, paper presented at Sixteenth International Offshore and Polar Engineering Conference, Lisbon, Portugal.

Hyodo, M., Y. Nakata, N. Yoshimoto, R. Orense, and J. Yoneda (2009), Bonding strength by methane hydrate formed among sand particle. *Powders and Grains*, paper presented at 6th International Conference on Micromechanics of Granular Media, 79-82.

Hyodo, M., J. Yoneda, Y. Nakata, and N. Yoshimoto (2011), Strength and dissociation property of methane hydrate bearing sand, paper presented at 7th International Conference on Gas Hydrates, Edinburgh, Scotland, United Kingdom.

Jager, M. D. (2001), High pressure studies of hydrate phase inhibition using Raman spectroscopy, Ph.D. thesis, Colorado School of Mines, Colorado, USA.

Jardine, R. J., A. Gens, D. W. Hight, and M .R. Coop (2004), Developments in understanding soil behaviour, The Skempton Conference: Proceedings of a Three Day Conference on Advances in Geotechnical Engineering, Organised by the Institution of Civil Engineers and Held at the Royal Geographical Society, London, UK.

Jayasinghe, A. G., and Grozic, J. L. H. (2013). Estimating Pore Space Hydrate Saturation Using Dissociation Gas Evolution Measurements: In Relevance to Laboratory Testing of Natural or Artificially Synthesised Hydrate-Bearing Soil Specimens, Journal of Geological Research, Vol. 2013, Article ID 815841, doi:10.1155/2013/815841.

Jayasinghe, A and J. L. H. Grozic (2008), Modelling Dissociation Behaviour of Methane Hydrate in porous soil media, paper presented at Sixth International Conference on Gas Hydrates, Chevron, Vancouver, BC, Canada.

Jin, S., J. Nagao, S. Takeya, Y. Jin, J. Hayashi, Y. Kamata, T. Ebinuma, and H. Narita (2006), Structural investigation of methane hydrate sediments by microfocus X-ray computed tomography technique under high-pressure conditions, Jpn. J. Appl. Phys., 45, L714- L716, doi:10.1143/JJAP.45.L714.

Jung, J. W., and J. C. Santamarina (2011), Hydrate adhesive and tensile strengths, Geochem. Geophys. Geosyst., 12, Q08003, doi:10.1029/2010GC003495.

Katsuki, D., R. Ohmura, T. Ebinuma, and H. Narita (2007), Methane hydrate crystal growth in a porous medium filled with methane-saturated liquid water, Philosophical Magazine, 87, 1057-1069.

Katsuki, D., R. Ohmura, T. Ebinuma, and H. Narita (2006), Formation, growth and ageing of clathrate hydrate crystals in a porous medium, Philosophical Magazine, 86, 1753-1761.

- Kilner, J. R., and J. L. H. Grozic (2006), Determination of synthetic hydrate content in sand specimens using dielectrics, *Canadian Geotechnical Journal*, 43(6), 551-562.
- Kim, Y. S., S. K. Ryu, S. O. Yang, and C. S. Lee (2003). Liquid water–hydrate equilibrium measurements and unified predictions of hydrate-containing phase equilibria for methane, ethane, propane, and their mixtures. *Industrial & Engineering Chemistry Research*, 42, 2409–2414.
- Klapproth, A., K. S. Techmer, S. A. Klapp, M. M. Murshed, and W. F. Kuhs (2007), Microstructure of gas hydrates in porous media, in *Physics and Chemistry of Ice: Proceedings of the 11th International Conference on the Physics and Chemistry of Ice*, edited by W. F. Kuhs, pp. 321–328, R. Soc. of Chem., London.
- Kleinberg, R. L., C. Flaum, D. D. Griffin, P. G. Brewer, G. E. Malby, and E. T. Peltzer, J. P. Yesinowski (2003), Deep Sea NMR: Methane hydrate growth habit in porous media and its relationship to hydraulic permeability, deposit accumulation, and submarine slope stability. *Journal of Geophysical Research*, 108(B10), 2508, doi: 10.1029/2003JB002389.
- Kleinberg, R., and D. Griffin (2005), NMR measurements of permafrost: Unfrozen water assay, pore-scale distribution of ice, and hydraulic permeability of sediments, *Cold Reg. Science Technol.*, 42, 63 – 77.
- Kneafsey, T. J., Y. Seol, A. Gupta, and L. Tomutsa L (2011), Permeability of laboratory-formed methane-hydrate-bearing sand: Measurements and observations using X-Ray computed tomography, *SPE Journal*, March 2011, 78-94.
- Kneafsey, T. J., L. Tomutsa, L. Moridis, Y. Seol, B. Freifeld, C. E. Taylor, and A. Gupta (2005), Methane hydrate formation and dissociation in a partially saturated sand—Measurements and observations, in *Fifth International Conference on Gas Hydrates*, pp. 213–220, Tapir Acad., Trondheim, Norway.

Kneafsey, T. J., L. Tomutsa, G. J. Moridis, Y. Seol, B. M. Freifeld, C. E. Taylor, and A. Gupta (2007), Methane hydrate formation and dissociation in a partially saturated core-scale sand sample, *Journal of Petroleum Science and Engineering*, 56, 108-126.

Kneafsey, T. J., Rees, E. V. L., Nakagawa, S., and Kwon, T. H. (2010), Examination of Hydrate Formation Methods: Trying to Create Representative Samples, http://www.netl.doe.gov/technologies/oil-gas/publications/Hydrates/2010Reports/ESD05-048_HydrateFormationMethods.pdf

Kneafsey T. J. And S. Nakagawa (2011), Repeated Methane hydrate Formation and Dissociation in a Partially Water Saturated Sand: Impact on Hydrate Heterogeneity and Sonic-Frequency Seismic Properties., Paper Presented at 7th International Conference on Gas Hydrates (ICGH 2011), Edinburgh, Scotland, United Kingdom.

Kobayashi, R., and D. Katz (1949), Methane hydrate at high pressure, *Petroleum Transactions-AIME*, 66-70.

Koh, C. A. and Sloan, E. D. (2007), Natural gas hydrates: Recent advances and challenges in energy and environmental applications. *AIChE J.*, 53: 1636–1643. doi: 10.1002/aic.11219

Kono, H. O., and B. Budhijanto (2002), Modeling of gas hydrate formation processes by controlling the interfacial boundary surfaces, paper presented at the 4th International Conference on Gas Hydrates, Jpn. Natl. Oil Corp., Yokohama, Japan, 19–23 May.

Kosyakov, N. E., B. I. Ivchenko, and P. P. Krishtopa (1979), Solubility of moisture in compressed argon, methane, and helium at low temperatures, *Zhurnal Prikladnoi Khimi*, 52(4), 922-923.

Kumar, A., B. Maini, P. R. Bishnoi, M. Clarke, O. Zatsepina, and S. Srinivas (2010), Experimental determination of permeability in the presence of hydrates and its effect on

the dissociation characteristics of gas hydrates in porous media, *Journal of Petroleum Science and Engineering*, 70, 114-122.

Kuniyuki, M., M. Akira, A. Kazuo, S. Yasuhide, Y. Tsutomu, and O. Seisuke (2010). Strain-rate dependence of triaxial compressive strength of artificial methane-hydrate-bearing sediment, *International Journal of Offshore and Polar Engineers*, 20 (4), 256-264.

Kvenvolden, K. A. (1993), Gas Hydrates - Geological Perspective and Global Change, *Reviews of Geophysics*, 31, 173-187.

Kwon, T. H., G. C. Cho, and J. C. Santamarina (2008), Gas hydrate dissociation in sediments: Pressure-temperature evolution, *Geochem. Geophys. Geosyst.*, 9, Q03019, doi:10.1029/2007GC001920.

Lambe, T. W. (1967). Stress path method. *ASCE Journal of the Soil Mechanics and Foundations Division*, November, 309-331.

Lambe, W. T., and Whitman, R. V. (1979). *Soil Mechanics*. John Wiley & Sons.

Lee, J. Y, Yun, T. S., Santamarina, J. C., Ruppel, C. (2007). Observations related to tetrahydrofuran and methane hydrates for laboratory studies of hydrate-bearing sediments. *Geochem. Geophys. Geosyst.*, 8(10).

Lee, M. W., and T. S. Collett (2009), Gas hydrate saturations estimated from fractured reservoir at Site NGHP-01-10, Krishna-Godavari Basin, India, *Journal of Geophysical Research*, 114: B07102, doi: 10.1029/2008JB006237.

Liang, H., Y. Song, Y. Chen, and Y. Liu (2011), The measurement of permeability of porous media with methane hydrate, *Petroleum Science and Technology*, 29, 79-87.

Lide, D. R. (2007), CRC Handbook of Chemistry and Physics 88 ed., CRC Press Inc., Boca Raton, Florida.

Lokken, T. V., A. Bersas, K. O. Christensen, C. F. Nygaard, and E. Solbraa (2008), Water content of high pressure natural gas: Data, prediction and experience from field, paper presented at International Gas Union Research Conference, Paris, France.

Luong, M. P. (2007). Introducing infrared thermography in soil dynamics, *Infrared Physics & Technology*, 49, 306-311.

Luong, M. P. (1986). Characteristic threshold and infrared vibrothermography of sand. *ASTM geotechnical testing journal*, 9(2), 80-86.

Lu, W., I. M. Chou, and R. C. Burruss (2008), Determination of methane concentrations in water in equilibrium with sI methane hydrate in the absence of a vapor phase by in situ Raman spectroscopy. *Geochimica et Cosmochimica Acta*, 72, 412-422.

Macari, E. J., Parken, J. K., & Costes, N. C. (1997). Measurement of volume changes in triaxial tests using digital imaging techniques. *ASTM geotechnical testing journal*, 20(1), 103-109.

MacDonald, G. T. (1990), Role of methane clathrate in past and future climates, *Climate Change*, 16, 247-281.

Madden, E. M., S. Ulrich, P. Szymcek, S. McCallum and T. Phelps (2009), Experiment formation of massive hydrate deposits from accumulation of CH₄ gas bubbles within synthetic and natural sediments, *Marine and Petroleum Geology*, 26, 369-378.

Majorowicz, J., and J. Safanda, K. Osadetz (2012), Inferred gas hydrate and permafrost stability history models linked to climate change in the Beaufort-Mackenzie Basin, Arctic Canada, *Climate of the Past*, 8 (2), 667-682.

- Makogon, I.F. (1981), *Hydrates of natural gas*, PennWell Books, Tulsa, Okla.
- Masui, A., H. Haneda, Y. Ogata, and K. Aoki (2005a), The effect of saturation degree of methane hydrate on the shear strength of synthetic methane hydrate sediments, the paper presented at Fifth International Conference on Gas Hydrates, Tapir Acad., Trondheim, Norway, 657–663.
- Masui, A., H. Haneda, Y. Ogata, and K. Aoki (2005b), Effects of Methane Hydrate Formation on Shear Strength of Synthetic Methane Hydrate Sediments, Paper presented at the 5th International Offshore and Polar Engineering Conference, Seoul, Korea.
- Masui, A., K. Miyazaki, H. Haneda, Y. Ogata, and K. Aoki (2008a), Mechanical properties of natural gas hydrate bearing sediments retrieved from eastern Nankai trough, paper presented at OTC 19277, OTC 2008, Houston, Texas, USA.
- Masui, A., K. Miyazaki, H. Haneda, Y. Ogata, and K. Aoki (2008b), Mechanical characteristics of natural and artificial gas hydrate bearing sediments, paper presented at Sixth International Conference on Gas Hydrates, Chevron, Vancouver, BC, Canada.
- Minagawa, H., R. Ohmura, Y. Kamata, J. Nagao, T. Ebinuma, H. Narita, and Y. Masuda (2009), Water permeability of porous media containing methane hydrate as controlled by the methane-hydrate growth process, in *Natural gas hydrates—Energy resource potential and associated geologic hazards*, edited by T. Collett, A. Johnson, C. Knapp, and R. Boswell, pp 734-739, AAPG Memoir 89, Tulsa, O. K.
- Miyazaki, K., A. Masui, H. Haneda, Y. Ogata, K. Aoki and T. Yamaguchi (2008), Variable-Compliance-Type Constitutive Model For Methane Hydrate Bearing Sediment, paper presented at 6th International Conference on Gas Hydrates, Vancouver, British Columbia, Canada.

- Miyazaki, K., A. Masui, Y. Sakamoto, and N. Tenma (2010a), Effect of confining pressure on triaxial compressive properties of artificial methane hydrate bearing sediments, Offshore Technology Conference, Houston, Texas, USA.
- Miyazaki, K., A. Masui, K. Aoki, Y. Sakamoto, T. Yamaguchi, and S. Okubo (2010b), Strain-Rate Dependence of Triaxial Compressive Strength of Artificial Methane-Hydrate-Bearing Sediment, International Journal of Offshore and Polar Engineering, 20 (4), 256-264.
- Miyazaki, K., A. Masui, Y. Sakamoto, K. Aoki, N. Tenma, and T. Yamaguchi (2011), Triaxial compressive properties of artificial methane-hydrate-bearing sediment, Journal of Geophysical Research, 116, B06102, doi:10.1029/2010JB008049.
- Mohammadi, A. H., A. Chapoy, B. Tohidi, and D. Richon (2004), A semi empirical approach for estimating the water content of natural gases, Ind. Eng. Chem. Res., 43, 7137-7147.
- Moridis, G. J., and T. S. Collett (2003), Strategies for Gas Production from Hydrate Accumulations under various Geologic Conditions, Report LBNL-52568, Lawrence Berkeley National Laboratory, Berkeley, CA.
- Murray D. R., R. L. Kleinberg, B. K. Sinha, M. Fukuhara, O. Osawa, T. Endo, and T. Namikawa (2006), Saturation, acoustic properties, growth habit, and state of stress of a gas hydrate reservoir from well logs. Petrophysics, 47(2), 129-137.
- Nabeshima, Y., Y. Takai, and T. Komai (2005), Compressive strength and density of methane hydrate, 6th 2005 International Society of Offshore and Polar Engineers, Ocean Mining Symposium, ISOPE OMS-2005, 197-200, Changsha, China.
- Negusse, D., Wijewickreme, W. K. D., and Vaid, Y. P. (1987). Constant volume friction angle of granular materials. Canadian Geotechnical Journal, 25(1), 50-55.

Nimblett, J., and C. Ruppel (2003), Permeability evolution during the formation of gas hydrates in marine sediments, *J. Geophys. Res.*, 108(B9), 2420, doi:10.1029/2001JB001650.

Nishio, S., E. Ogisako, and A. Denda (2011), Geotechnical properties of seabed ground in East Nankai Trough, paper presented at the 7th International Conference on Gas Hydrates, Edinburgh, Scotland, United Kingdom.

Nixon, M. F., and J. L. H. Grozic (2007), Submarine slope failure due to gas hydrate dissociation: A preliminary quantification, *Can. Geotech. J.*, 44, 314–325, doi:10.1139/T06-121.

Oellrich, L. R., and K. Althaus (2000), GERG-Water Correlation (GERG Technical Monograph TM14) Relationship between water content and water dew point keeping in consideration the gas composition in the field of natural gas, *Fortschritt-Berichte VDI, Reihe 3-Nr. 679*.

Ogienko, A. G., A. V. Kurnosov, A. Y. Manakov, E. G. Larionov, A.I. Ancharov, M. A. Sheromov, and A. N. Nesterov (2006), Gas hydrates of argon and methane synthesized at high pressures: composition, thermal expansion, and self-preservation, *Journal of Physical Chemistry B*, 110, 2840-2846.

Ohmura, R., W. Shimada, T. Uchida, Y. H. Mori, S. Takeya, J. Nagao, H. Minagawa, T. Ebinuma, and H. Narita (2004), Clathrate hydrate crystal growth in liquid water saturated with a hydrate-forming substance: variations in crystal morphology, *Philosophical Magazine*, 84 (1), 1-16.

Olds, R. H., Sage, B. H., Lacey, W. H., (1942), Phase equilibria in hydrocarbon systems: composition of the dew-point gas of the methane–water system., *Ind. Eng. Chem. Res.*, 34, (10), 1223–1227.

Ordonez, C., J. L. H. Grozic, and J. Chen (2009), Hydraulic conductivity of Ottawa sand specimens containing R-11 gas hydrates, paper presented at 62nd Canadian Geotechnical Conference, Halifax, NS, Canada.

O'Sullivan, T. D., and N. O. Smith (1970), The solubility and partial molar volume of nitrogen and methane in water and in aqueous sodium chloride from 50 to 125°C and 100 to 600 atm, *Journal of Physical Chemistry*, 74, 1460-1466.

Parameswaran, V. R., M. Paradis, and Y. P. Handa (1989), Strength of frozen sand containing tetrahydrofuran hydrate, *Canadian Geotechnical Journal*, 26, 479-483.

Price, L. C. (1979), Aqueous solubility of methane at elevated pressures and temperatures, *AAPG bulletin*, 632, 1527-1533.

Priest, J. A., A. Best, and C. R. Clayton (2005), A laboratory investigation into the seismic velocities of methane gas hydrate-bearing sand, *J. Geophys. Res.*, 110 (13), B04102, doi:10.1029/2004JB003259.

Priest, J. A., E. V. L. Rees, and C. R. I. Clayton (2009), Influence of gas hydrate morphology on the seismic velocities of sands, *J. Geophys. Res.*, 114, B11205, doi:10.1029/2009JB006284.

Priest, J., A. Sutaniya and C. Clayton (2011), Impact of hydrate formation and dissociation on the stiffness of a sand, paper presented at the 7th International Conference on Gas Hydrates (ICGH 2011), Edinburgh, Scotland, United Kingdom.

Poulos, S. J. (1981). The steady state of deformation. *ASCE Journal of Geotechnical Engineering Division*, 107(GT5), 553-562.

- Reagan, M. T., and G. J. Moridis (2007), Oceanic gas hydrate instability and dissociation under climate change scenarios, LBNL-62999, *Geophys. Res. Lett.*, 34, L22709, doi: 10.1029/2007GL031671.
- Reagan, M. T., G. J. Moridis, S. M. Elliott, and M. Maltrud (2011), Simulation of arctic gas hydrate dissociation in response to climate change: Basin-scale assessment, in *Arctic Technology Conference 2011*, Society of Petroleum Engineers, 1038-1051.
- Rempel, A.W., and B. A. Buffett (1997), Formation and accumulation of gas hydrate in porous media, *Journal of Geophysical Research*, 102, B5, 10151-10164.
- Rees, E. V. L., T. J. Kneafsey, and S. Nakagawa (2011), Geomechanical Properties of synthetic hydrate bearing sediments, Paper presented at the 7th International Conference on Gas Hydrates (ICGH 2011), Edinburgh, Scotland, United Kingdom.
- Rigby, M., Prausnitz, J. M., (1968), Solubility of water in compressed nitrogen, argon and methane, *J. Phys. Chem.*, 72 (1), 330–334.
- Ruppel, C. (2011), Methane hydrates and contemporary climate change, *Nat. Educ. Knowl.*, 2(12), 12.
- Santamarina, J. C., K. A. Klein, and M. A. Fam (2001), *Soils and Waves: Particulate Materials Behavior, Characterization and Process Monitoring*, 488 pp., John Wiley, New York.
- Santamarina, J. C., and C. Ruppel (2008), The impact of hydrate saturation on the mechanical, electrical, and thermal properties of hydrate-bearing sand, silts, and clay, paper 5817 presented at the 6th International Conference on Gas Hydrates, Chevron, Vancouver, B. C., Canada.

- Sego, D. C. and R. J. Wittebolle (1984), Engineering behaviour of a sand containing gas hydrates, Proceedings of. Cold Regions-Engineering Speciality Conference, 589-601, Montreal, Canada.
- Seo, Y., H. Lee, and B. Ryu (2002), Hydration number and two-phase equilibria of CH₄ hydrate in the deep ocean sediments, Geophysical Research Letters, 29(8), No. 1244.
- Seol, Y., E. Myshakin, and T. Kneafsey (2011), Quantitative applications of X-Ray CT observations for core-scale hydrate studies, Paper presented at 7th International Conference on Gas Hydrates, Edinburgh, Scotland.
- Servio, P., and P. Englezos (2002), Measurement of dissolved methane in water in equilibrium with its hydrate, Journal of Chemical & Engineering Data, 47, 87-90.
- Shpakov, V. P., J. S. Tse, C. A. Tulk, B. Kvamme, and R. Belosludov (1998), Elastic moduli calculation and instability in structure I methane clathrate hydrate, Chemical Physics Letters, 282, 107-114.
- Shibue, Y. (2003), Vapor pressures of aqueous NaCl and CaCl₂ solutions at elevated temperatures, Fluid Phase Equilib., 213, 39-51.
- Sia, C. W. (2013), Experiment investigation of gas hydrate formation habit in porous media using permeability and thermal conductivity measurements, Ph. D. Thesis, Department of Chemical and Petroleum Engineering, University of Calgary, Calgary, Alberta.
- Skempton, A. W. (1954), The pore-pressure coefficients A and B, Geotechnique, 4, 143-147.
- Sloan, E. D. (1998), Clathrate Hydrates of Natural Gas, 2nd edition, Marcel Dekker, New York, USA.

- Sloan, E. D., F. M. Khoury, and R. Kobayashi (1976), Water content of methane gas in equilibrium with hydrates, *Industrial & Engineering Chemistry Fundamentals*, 15(4), 318-323.
- Sloan, E. D. (2003), Clathrate hydrate measurements: microscopic, mesoscopic, and macroscopic, *J. Chem. Thermodynamics* 35, 41-53.
- Sloan, E. D. (2003), Fundamental principles and applications of natural gas hydrates, *Nature*, 426(20), 353-359.
- Soga, K., Lee, S. L., Ng, M. Y. A., and Klar, A. (2006). Characterisation and engineering properties of methane hydrate soils. *Proceedings of the 2nd International Workshop on Characterisation and Engineering Properties of Natural Soils*, 4, 2591-2642.
- Song, K. Y., M. Yarrison, and W. Chapman (2004), Experimental low temperature water content in gaseous methane, liquid ethane, and liquid propane in equilibrium with hydrate at cryogenic conditions, *Fluid Phase Equilib.*, 224, 271-277.
- Song, Y., F. Yu, Y. Li, W. Liu and J. Zhao (2010), Mechanical property of artificial methane hydrate under triaxial compression, *Journal of Natural Gas Chemistry*, 19, 246-250.
- Spangenberg, E., and J. Kulenkampff (2006), Influence of methane hydrate content on electrical sediment properties, *Journal of Geophysical Research*, 33, L24315, doi: 10.1029/2006GL028188.
- Spangenberg, E., B. Beeskow-Strauch, M. Luzi, R. Naumann, and J. M. Schicks (2008), The process of hydrate formation in clastic sediments and its impact on their physical properties, *Proceedings of the 6th international conference on Gas Hydrates*, Vancouver, BC, Canada.

- Spangenberg, E., J. Kulenkampff, R. Naumann, and J. Erzinger (2005), Pore space hydrate formation in a glass bead sample from methane dissolved in water, *Geophys. Res. Lett.*, 32, L24301, doi:10.1029/2005GL024107.
- Stern, L. A., S. H. Kirby, and W. B. Durham (1996), Peculiarities of methane clathrate hydrate formation and solid-state deformation, including possible superheating of water ice, *Science*, 273, 1843–1848, doi:10.1126/science.273.5283.1843.
- Stern, L. A., S. H. Kirby, and W. B. Durham (1998), Polycrystalline methane hydrate: Synthesis from superheated ice, and low-temperature mechanical properties, *Energy Fuels*, 12, 201–211, doi:10.1021/ef970167m.
- Sulem, J. and Outfroukh, H. (2006). Shear banding in drained and undrained triaxial tests on a saturated sandstone: Porosity and permeability evolution, *International Journal of Rock Mechanics and Mining Sciences*, 43, 292-310.
- Sultan, N., P. Cochonat, J. P. Foucher, and J. Mienert (2004), Effect of Gas Hydrate Melting on Seafloor Slope Instability, *International Journal of Marine Geology*, 213, 379-401.
- Sultan, N. (2007), Comment on “Excess pore pressure resulting from methane hydrate dissociation in marine sediments: A theoretical approach” by Wenyue Xu and Leonid N. Germanovich, *J. Geophys. Res.*, 112, B02103, doi:10.1029/2006JB004527.
- Sultanov, R. C., V. E. Skripka, and A. Y. Namiot (1972), Solubility of methane in water at high temperatures and pressures (in Russian), *Gazova Promyshlennost*, 17, 6-7.
- Sum, A. K., R. C. Burruss, and E. D. Sloan (1997), Measurement of clathrate hydrates via Raman spectroscopy, *Journal of Physical Chemistry B*, 101, 7271-7377.

- Sun, R., and Z. Duan (2007), An accurate model to predict the thermodynamic stability of methane hydrate and methane solubility in marine environments. *Chemical Geology*, 244, 248-262.
- Sun, R., Z. Huang, and Z. Duan (2003), A new equation of state and Fortran 77 program to calculate vapor-liquid equilibria of CH₄-H₂O system at low temperatures, *Computers and Geosciences*, 1291-1299.
- Ting, J. M., R. T. Martin, and C. C. Ladd (1983), Mechanisms of strength for frozen sand, *J. Geotech. Eng.*, 109(10), 1286–1302.
- Tohidi, B., R. Anderson, M. B. Clennell, R. W. Burgass, and A. B. Biderkab (2001), Visual observation of gas-hydrate formation and dissociation in synthetic porous media by means of glass micromodels, *Geology*, 29 (9), 867-870.
- Uchida, T., T. Hirano, T. Ebinuma, H. Narita, K. Gohara, S. Mae, and R. Matsumoto (1999), Raman spectroscopic determination of hydration number of methane hydrates, *AIChE J.*, 45(12), 2641-2645.
- Van der Waals, J.H., J.C. Platteeuw (1959) Validity of the Clapeyron's Equation for phase equilibria involving clathrates. *Nature*, 183-462.
- Wagner, W., and A. Pruss (1993), International equations for the saturation properties of ordinary water substance. Revised according to the international temperature scale of 1990. addendum to *J. Phys. Chem. Ref. Data* 16, 893 (1987), *J. Phys. Chem. Ref. Data*, 22, 783-787.
- Waite, W. F., B. J. de Martin, S. H. Kirby, J. Pinkston, and C. D. Ruppel (2002), Thermal conductivity measurements in porous mixtures of methane hydrate and quartz sand, *Geophys. Res. Lett.*, 29(24), 2229, doi:10.1029/2002GL015988.

- Waite, W. F., L. A. Stern, S. H. Kirby, W. J. Winters, and D. H. Mason (2007), Simultaneous determination of thermal conductivity, thermal diffusivity and specific heat in sI methane hydrate, *Geophys. J. Int.*, 169, 767–774, doi:10.1111/j.1365-246X.
- Waite, W. F., J. C. Santamarina, D. D. Cortes, B. Dugan, D. N. Espinoza, J. Germaine, J. Jang, J. W. Jung, T. J. Kneafsey, H. Shin, K. Soga, W. J. Winters, and T. S. Yun (2009), Physical properties of hydrate-bearing sediments, *Rev. Geophys.*, 47, RG4003, doi:10.1029/2008RG000279.
- Waite, W. F., T. J. Kneafsey, W. J. Winters, and D. H. Mason (2008a), Physical property changes in hydrate-bearing sediment due to depressurization and subsequent repressurization, *Journal of Geophysical Research*, 113, B07102, doi:10.1029/2007JB005351.
- Waite, W. F., J. P. Osegovic, W. J. Winters, M. D. Max, and D. H. Mason (2008b), Seeding hydrate formation in water-saturated sand with dissolved-phase methane obtained from hydrate dissolution: a progress report, paper presented at the 6th International conference on Gas Hydrates (ICGH 2008), Vancouver, BC, Canada.
- Wiesenburg, D. A. and N. L. Guinasso (1979), Equilibrium solubilities of methane, carbon monoxide and hydrogen in water and seawater, *Journal of Chemical & Engineering Data*, 24, 356-360.
- Winters, W. J., I. A. Pecher, J. S. Booth, D. H. Mason, M. K. Relle, and W. P. Dillon (1999), Properties of samples containing natural gas hydrate from the JAPEx/JNOC/GSC Mallik 2L-38 gas hydrate research well, determined using Gas Hydrate And Sediment Test Laboratory Instrument (GHASTLI), in *Geological Survey of Canada, Bulletin 544*, edited by S. R. Dallimore et al., pp. 241-250, Canadian Government Publication Centre, Ottawa.

- Winters, W. J., W. F. Waite, D. H. Mason, W. P. Dillon, and I. A. Pecher (2002), Sediment properties associated with gas hydrate formation. Proceedings of the Fourth International Conference on Gas Hydrates, pp. 722-727, Yokohama.
- Winters, W. J., I. A. Pecher, W. F. Waite, and D. H. Mason (2004), Physical properties and rock physics models of sediment containing natural and laboratory-formed methane gas hydrate, *American Mineralogist*, Volume 89, 1221–1227.
- Winters, W. J., W. F. Waite, D. H. Mason, L. Y. Gilbert, and I. A. Pecher (2007), Methane gas hydrate effect on sediment acoustic and strength properties, *Journal of Petroleum Science and Engineering*, 56, 127–135.
- Winters, W. J., W. F. Waite, D. H. Mason, and P. Kumar (2008), Physical properties of repressurized samples recovered during the 2006 national gas hydrate program expedition offshore India, paper 5531 presented at the 6th International Conference on Gas Hydrates, Chevron, Vancouver, B. C., Canada.
- Yamamoto, S., J. B. Alcauskas, and T. E. Crozier (1976), Solubility of methane in distilled water and seawater, *Journal of Chemical & Engineering Data*, 21, 78-80.
- Yokoseki, A. (2005), Methane gas hydrate viewed through unified solid-liquid-vapor equation of state, *International Journal of Thermophysics*, 26(3), doi:10.1007/s10765-005-5575-5.
- Yoneda, J., M. Hyodo, Y. Nakata, N. Yoshimoto, Y. Imamura and N. Tenma (2011), Localized deformation of Methane Hydrate-bearing sand by Plane Strain Shear Tests, paper presented at 7th International Conference on Gas Hydrates, Edinburgh, Scotland, United Kingdom.
- Youssef, Z., A. Barreau, P. Mougín, J. Jose, and I. Mokbel (2009), Measurements of hydrate dissociation temperature of methane, ethane, and CO₂ in the absence of any aqueous phase

and prediction with the cubic plus association equation of state, *Industrial and Engineering Chemistry Research*, 48, 4045-4050.

Yun, T. S., F. M. Francisca, J. C. Santamarina, and C. Ruppel (2005), Compressional and shear wave velocities in uncemented sediment containing gas hydrate, *Geophys. Res. Lett.*, 32, L10609, doi:10.1029/2005GL022607.

Yun, T. S., G. A. Narsilio, J. C. Santamarina, and C. Ruppel (2006), Instrumented pressure testing chamber for characterizing sediment cores recovered at in situ hydrostatic pressure, *Marine Geology*, 229, 285-293.

Yun, T. S., J. C. Santamarina, and C. Ruppel (2007), Mechanical properties of sand, silt, and clay containing tetrahydrofuran hydrate, *Journal of Geophysical Research*, vol. 112, B04106, doi:10.1029/2006JB004484.

Yun T. S., and J. C. Santamarina (2011), Hydrate growth in granular materials: implications to the hydrate bearing sediments, *Geoscience Journal*, 15(3), 265-273, doi: 10.1007/s12303-011-0025-9.

Zatsepina, O. Y., and B. A. Buffett (1997), Phase equilibrium of gas hydrate: implications for the formation of hydrate in the deep sea floor, *Geophysical Research Letters*, 24(13), 1567-1570.

Zatsepina, O. Y., and B. A. Buffett (1998), Thermodynamic conditions for the stability of gas hydrate in the seafloor, *Journal of Geophysical Research-B: Solid Earth*, 103, 24127-39.

Zebrowski, E (1979), *Fundamentals of Physical Measurement*, Rohnbach P, editor. Wadsworth Publishing Company, Inc., Belmont, CA, USA.

Zhang, L., R. Burgass, A. Chapoy, and B. Tohidi (2011), Measurement and modeling of water content in low temperature hydrate-methane and hydrate-natural gas systems, *J. Chem. Eng. Data*, 56, 2932-2935.

Zhong, Y., and R. E. Rogers (2000), Surfactant effects on gas hydrate formation, *Chem. Eng. Sci.*, 55, 4175 – 4187, doi:10.1016/S0009-2509(00)00072-5.